MOMENT REDISTRIBUTION BEHAVIOUR OF SFRC MEMBERS WITH VARYING FIBRE CONTENT

By

Arno Wilhelm Möhr

Thesis presented in fulfilment of the requirements for the degree of Master of Science in Engineering at Stellenbosch University

Supervisor:

Prof. W.P. Boshoff

March 2012

DECLARATION

By submitting this thesis electronically, I declare that the entirety of the work contained therein is my own, original work, that I am the owner of the copyright thereof (unless to the extent explicitly otherwise stated) and that I have not previously in its entirety or in part submitted it for obtaining any qualification.

Date: .....

Signature: .....

SUMMARY

Steel fibre reinforced concrete (SFRC) is the most prominent fibre reinforced concrete composite that was engineered to enhance the material's post-cracking behaviour. In certain situations it is utilised to replace conventional reinforcement and considered to be more cost-efficient.

The purpose of this research is to characterise the moment redistribution behaviour of a statically indeterminate SFRC structure with varying volumes of fibres, with the focus on the development of the moment redistribution accompanied by the rotation of the plastic hinges at the critical sections in the structure.

The material properties were characterised with a series of experimental tests. The compression behaviour was obtained with uniaxial compression tests while the uniaxial tensile behaviour was obtained with an inverse analysis performed according to flexural test results. These properties were utilised to derive a theoretical moment-curvature relation for each SFRC member which supplied the basis for the characterised moment-rotation behaviour and the finite element analyses (FEA) performed on the statically indeterminate structure. Experimental tests were conducted on the statically indeterminate structure in laboratory conditions to validate the theoretical findings.

For the different SFRCs the material properties in compression were similar, while it resulted in an increased tensile resistance with an increase in the volume steel fibres. The theoretical moment-curvature and moment-rotation responses also indicated an increased structural capacity and member ductility with an increase in the volume fibres.

From the finite element analyses the computational moment redistribution-plastic rotation relations were obtained. It was found that the final amount of moment redistribution decreased with an increase in the fibre volume, but that the rotational capacity increased.

It was found that the experimental moment-curvature and moment-rotation results correlate well with the theoretical predictions. Also, unexpected structural behaviour was observed, but the issue was addressed with applicable computational analyses which confirmed the possible causes. It was concluded that the computational moment redistribution approximations were reasonably accurate. A parameter study indicated that the crack band width differed among the different SFRC members.

OPSOMMING

Staal vesel versterkte beton (SVVB) is die mees vooraanstaande vesel versterkte beton mengsel wat ontwikkel is om die materiaalgedrag na kraakvorming te verbeter. In sekere situasies kan dit gebruik word om konvensionele staal te vervang en lei soms to koste vermindering .

Die einddoel van die studie is om die moment herverdeling gedrag te karaktiseer vir ‘n statiese onpebaalbare SVVB struktuur deur die invloed van verskillende volumes vesels en die rotasie kapasiteit by die kritieke posisies in ag te neem.

Die materiaal eienskappe was geidentifiseer met ‘n reeks eksperimentele toetse. Die druk gedrag was geïdentifiseer deur eenassige druktoetse, terwyl die eenassige trek gedrag bekom is met die implementasie van ‘n inverse analise van die uitgevoerde buig toetse. Hierdie eienskappe is gebruik om die teoretise moment-kromming verhouding vir elke mengsel te bekom. Hierdie verhoudings word as die basis bestempel vir die teoretiese moment-rotasie verhouding en die eindige element analises (EEA) wat op ‘n staties onbepaalbare struktuur toegepas is. Eksperimentele toetse is op hierdie voorgestelde struktuur toegepas om die teoretiese verwagtings te verifieer.

Dit is gevind dat die druk gedrag ooreenstem tussen die verskillende mengsels, alhoewel ‘n toename in die trek kapasiteit ervaar is met ‘n toename in die volume vesels. Die teoretiese moment-kromming en moment-rotasie verwantskappe stel ook voor dat die strukturele kapasiteit en duktiliteit toeneem met ‘n toename in die volume vesels.

Die teoretiese moment herverdeling-plastiese rotasie verwantskapppe is verkry deur middel van die eindige element analises. Dit is gevind dat die aantal moment herverdeling by faling afgeneem het vir ‘n toename in die volume vesels, maar dat dit to ‘n groter rotasie kapasiteit gelei het.

Van die eksperimentele resultate is dit afgelei dat die teoretiese moment-kromming en moment-rotasie verwantskappe goeie benaderings voorstel. Sekere invloede van die opstelling het daartoe gelei dat onverwagte strukturele gedrag bekom is, maar die moontlike invloede is verifieer met eindige element analises. Dit is afgelei dat die teoretiese beramings van die moment herverdeling gedrag redelik akkuraat is. ‘n Parameter studie het getoon dat die kraak spasiëring verskil tussen mengsels met verskillende volumes vesels.

ACKNOWLEDGEMENTS

I would like to thank Prof. Billy Boshoff for the guidance he provided me as my study leader. His persistence to push me to my limit has ensured me to always deliver my best efforts.

I would also like to express my gratitude towards Mr. Johan van der Merwe and Mr. Dion Viljoen from the workshop. Their assistance in preparing the necessary molds and their innovative and practical knowledge is greatly appreciated.

I would also like to express my gratitude towards Mr. Charlton Ramat for his assistance in the concrete laboratory.

Finally I would like to thank all of my colleagues, for the past two years would have been quite dull without their frequent conversations and visits at the prestigious coffee machine.

NOTATIONS

α	Softening angle in the concrete crushing zone
c	Neutral axis depth at ultimate moment
d	Effective depth of section
δ	Displacement / Ratio of the redistributed moment to the elastic bending moment
ε	Strain
$\Delta\varepsilon$	Material ductility
ε_{crack}	Strain value at which cracking initiates
ε_{crush}	Strain value at which concrete crushing commences
ε_{peak}	Strain value corresponding with peak of curve
ϑ	Rotation
$\Delta\vartheta$	`Size of small rotation / member ductility
ϑ_p	Plastic rotation
κ	Curvature
$\Delta\kappa$	Sectional ductility
k	Height factor
k_u	Neutral axis depth
ρ	Radius of curvature
ρ_{eff}	Effective reinforcement ratio
σ	Stress
σ_{crack}	Stress value at which cracking initiates
σ_{crush}	Stress value at which concrete crushing commences
σ_{peak}	Stress value corresponding with peak of curve
dA	Small area across the cross section
b	Width of cross section

E	E-modulus (material stiffness)
F	Internal horizontal force
h	Height of cross section
I	Moment of inertia for the cross section
k_h	Size factor according to RILEM TC 162-TDF
K_{cs}	Axial stiffness of centre support
L	Span length
L_p	plastic hinge length
L_{soft}	Length of the concrete crushing zone at the compression surface
M	Bending moment
M_{elast}	Bending moment according to linear elastic law
M_{red}	Redistributed bending moment
P	Applied lateral force
s	Distance between flexural cracks
t	Concrete cover
Δx	Size of small element
Δ_v	Vertical displacement
y	Vertical distance on cross-section
y_c	Depth of compression zone
y_t	Depth of tension zone
Z	Value for moment arm

ABBREVIATIONS

2D	Two-dimensional
3PBT	Three point bending test
BMD	Bending moment diagram
CBW	Crack band width
CMOD	Crack mouth opening displacement
COV	Coefficient of variance
DOF	Degree of freedom
FE	Finite element
FRC	Fibre reinforced concrete
HPFRC	High performance concrete composite
LVDT	Linear variable displacement transducer
MR	Moment redistribution
NA	Neutral axis
NAD	Neutral axis depth
OPC	Ordinary Portland Cement
SCC	Self compacting concrete
SFRC	Steel fibre reinforced concrete
SFRCC	Steel fibre reinforced concrete composite
SLS	Serviceability limit state
TI	Toughness index
ULS	Ultimate limit state

TABLE OF CONTENTS

CHAPTER 1

INTRODUCTION

1.1. Background

Concrete is the most widely used structural material around the world. This is due to two major advantages, namely its high compressive strength and its ability to be cast in any shape or form. Another feature is that it can be manipulated to suit most environmental conditions whilst providing optimal performance. Concrete also has a major setback, which is that it is a brittle material and has little tensile resistance. Thus this composite is susceptible to cracking behaviour in the tensile regions. In order to overcome this setback, conventional steel bars have been utilised in the tensile regions to provide the required tensile strength and to control the crack development. It should be mentioned that the steel is also implemented in compression zones and at sections that are susceptible to shear effects in order to provide extra capacity.

Structural engineers strive to provide effective and economical designs with a lasting durability (Löfgren, 2005). Due to the high cost of steel and labour in European countries, another means of providing tensile reinforcing has been developed. A viable solution was the use of steel fibres to provide the tensile reinforcing for specific applications (Schumacher, 2006). Although the fibres are more expensive than conventional steel per volume of concrete, it provides the opportunity to

reduce the labour costs immensely when used without conventional steel. This is as that there is no need to place any steel before casting commences, which could be time consuming.

Steel fibres are used to increase the residual tensile strength and to enhance the post-cracking behaviour of a concrete composite (Schumacher, 2006). The major characteristic of a steel fibre reinforced concrete (SFRC) composite is that it improves the member's durability, ductility and is utilised to limit the crack development of the composite (Schumacher, 2006). SFRCs has been readily used in slabs on grade, tunnel linings, structures susceptible to earth quakes (ductility aspect) and in precast situations (Schumacher, 2006).

During the last few decades thousands of experimental tests has been conducted to study the feasibility of the member's structural behaviour and thus far it has been concluded that SFRCs provide promising results, e.g. increased toughness and durability (Löfgren, 2005). Thus far the design of SFRCs has been conducted with the use of journal articles and model codes, such as FIB (FIB, 2010), RILEM TC 162-TDF (2003), DIN, etc. Unfortunately designers are hesitant to use these guidelines as they would rather base their calculations on published standardised design codes.

A structural phenomenon that is utilised by designers of reinforced concrete structures to their advantage is moment redistribution (MR) in statically indeterminate structures. Moment redistribution is utilised to ensure that the amount of steel in hogging and sagging regions comply with a cost-effective design, with a decrease in the probability of steel congestion and to ensure simpler steel layouts. The allowable amount of moment redistribution is prescribed in structural design codes for conventional concrete design, but has not been considered for SFRCs. This phenomenon could have a major influence in the structural design process for a situation when conventional steel is implemented in conjunction with steel fibres.

1.2. Aim, Scope and Limitations

The aim of this study is to provide insight on the moment redistribution behaviour of SFRCs and to determine whether the allowable amount currently prescribed for conventional concrete structures are valid for the design of steel fibre reinforced concrete structures.

In this study moment redistribution behaviour is considered for SFRC members with different volumes of fibres, 0.5%, 0.75% and 1.0%. Another aspect that is investigated is the influence of the volume of fibre on the ductility of the member which in turn influences the structural behaviour of a

statically indeterminate structure. Theoretical moment-curvature and moment-rotation models are derived for each SFRC member, which are implemented in computational analyses. This is used to determine the moment-rotation behaviour in relation to the rotational behaviour of the critical sections.

For this study the theoretical models are derived according to Euler flexural assumptions (Hibbeler, 2005), while the shear behaviour is not included. The structural behaviour is only considered for a volume of fibres ranging from 0.5 to 1.0%. The results are obtained from a statically indeterminate structure, which is considered to be representative of the global behaviour. The load application is limited to point loads at midspan. It is important to note that the study is only based on the Ultimate Limit State (ULS) design and that the Serviceability Limit State (SLS) is not considered.

1.3. Outline of Contents

The sequence of the methods used to obtain the required results is schematically illustrated in Figure 1.1.

In Chapter 2 a theoretical background is given on typical SFRC behaviour and the structural components involved in the moment redistribution phenomenon.

In Chapter 3 the material properties is characterised. This is done by performing compression and flexural tests, accompanied by an inverse analyses procedure.

In Chapter 4 the theoretical moment-curvature and moment-rotation models is derived. A computational analysis is also conducted to predict the moment redistribution behaviour for each SFRC member.

In Chapter 5 the theoretical derived models are evaluated with laboratory tests. Problems that occurred during the test procedure are reported and addressed.

In Chapter 6 a parameter study is conducted on the crack band width value, which influences the results obtained from the theoretical models.

Chapter 7 reports the final conclusions and future prospects.

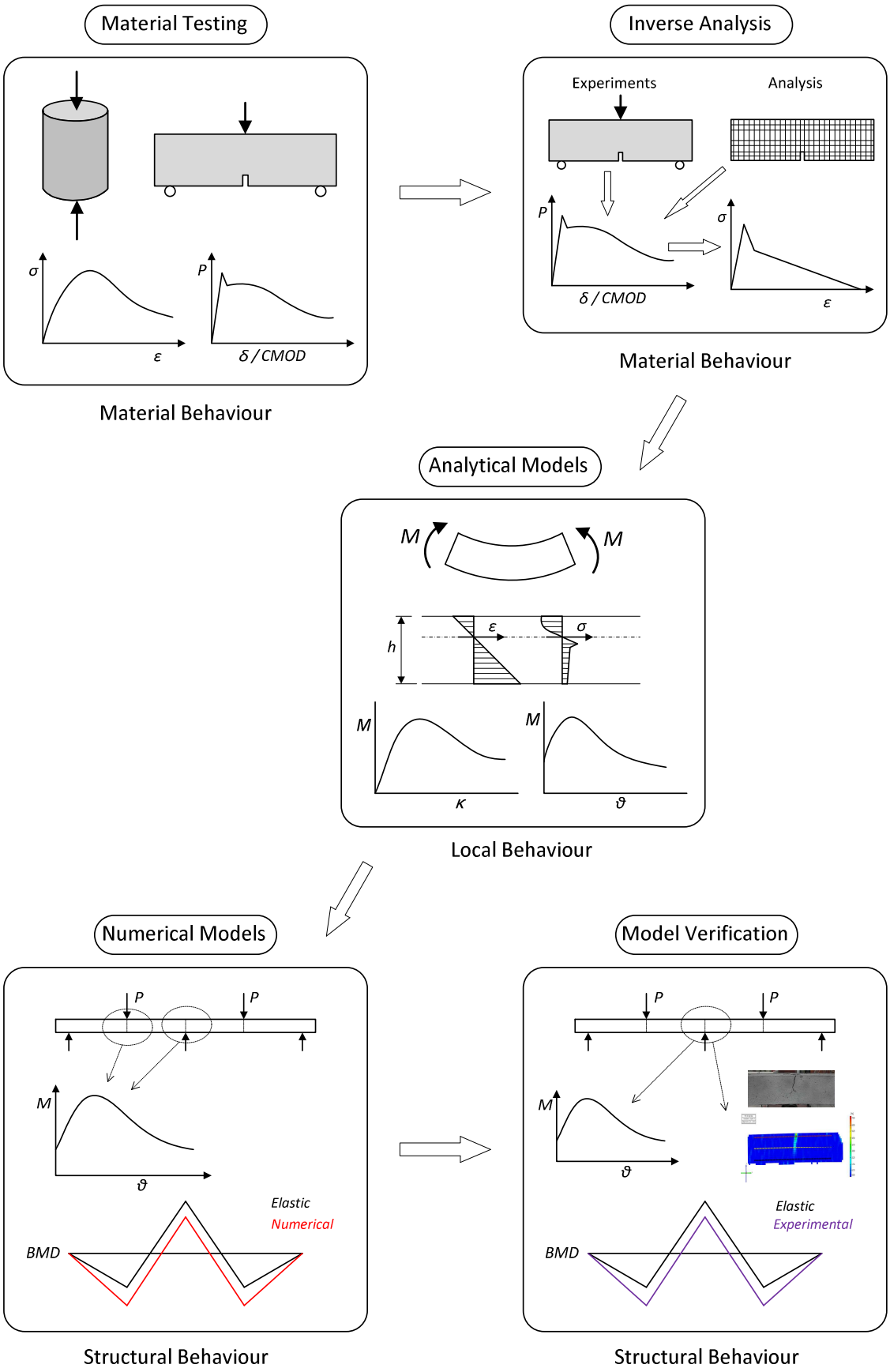

Figure 1.1 Schematic representation of the content outline.

CHAPTER 2

BACKGROUND STUDY

2.1. Fibre reinforced concrete

Fibre reinforced concrete (FRC) is a composite material that is characterised by an enhanced post-cracking tensile residual strength due to the fibre reinforcement mechanisms provided by fibres bridging the crack surfaces (di Prisco, et al, 2009). Fibre reinforced building materials date back ages as it was first implemented in a structural sense in the form of clay bricks containing straw (Brandt, 2008).

During the last three decades, a wide research has been performed on material properties of FRC, both at fresh and hardened state (di Prisco, et al, 2004). Research on the structural response of FRC elements was mainly developed during the last two decades (Di Prisco *et al*, 2004 and Brandt, 2008). As a consequence, there is still a lack of international Building Codes for structural design for FRC elements and this may explain the limited utilisation of FRC among practitioners, even though a number of design guidelines were recently developed. In fact, clear and simple design rules from building codes are required by designers, who hardly accept voluntary added responsibility by adopting guidelines or, even worse, research results available in scientific papers.

Early design considerations were produced by ACI 544 (ACI, 1996) and ACI 318 (ACI, 2008) while RILEM TC162-TDF produced design guidelines for typical structural elements (Vandewalle, *et al*. 2003).

The principles discussed in RILEM TC162-TDF are mainly related to steel fibre reinforced concrete (SFRC) having a softening post-cracking behaviour in uniaxial tension (Figure 2.1) even though it can be extended to hardening materials. Recently the new Draft FIB Model Code (FIB, 2010) was published, which includes design models for SFRC elements. These design models are mainly based on the principles discussed in RILEM TC162-TDF.

2.1.1. Effects of fibres

Fibres can be used on a micro- or macro-scale, with the latter used to enhance the performance on a structural level, while the former is used for material enhancement. Fibres are used to produce composite materials with different material responses, which can be referred to as strain softening or strain hardening materials.

Strain softening (deflection softening) refers to a material which exhibits a decreasing stress level after the cracking, whereas a strain (or deflection) hardening material increases its load-bearing capacity after cracking, and additionally more but smaller cracks are produced. Strain softening/hardening refers to a direct tensile response while deflection softening/hardening refers to a flexural response (Naaman & Reinhardt, 2006 and Jansson, 2008). This is further explained in Figure 2.1. The response is influenced by the fibre geometry, material properties and the dosage in the concrete mix.

As mentioned before, the focus of this research is on the use of steel fibres. Steel fibres are available in many shapes and lengths with different diameter sizes. The typical shapes are shown in Figure 2.2, with the hooked steel fibres utilised most as they provide the best results (Brandt, 2008). The effectiveness is related to the pull-out response of the fibres, but will not be discussed.

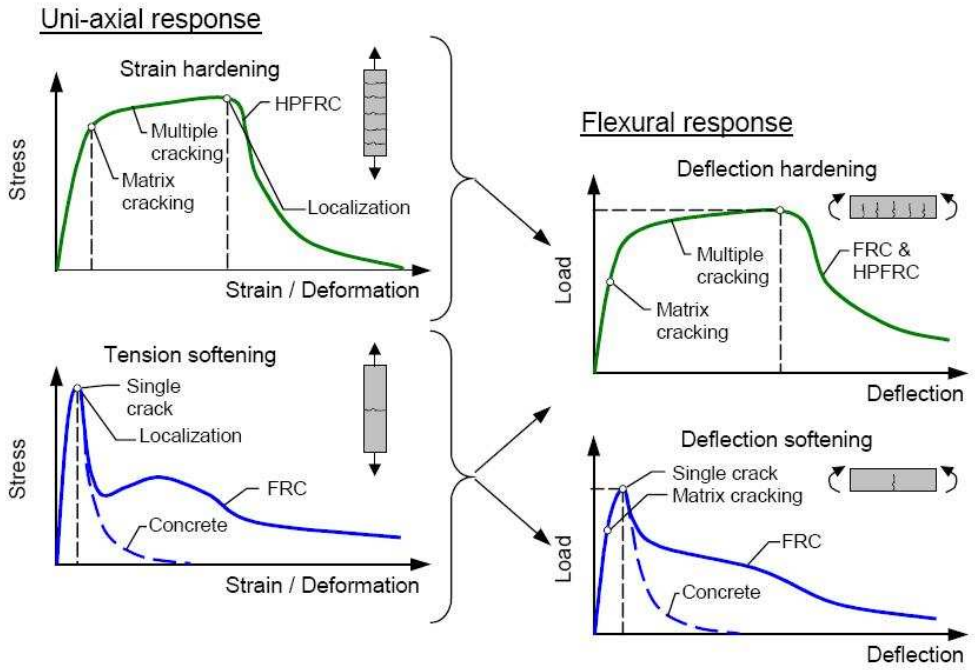

Figure 2.1 Characterisation of the tensile and flexural behaviour (Löfgren, 2005:54).

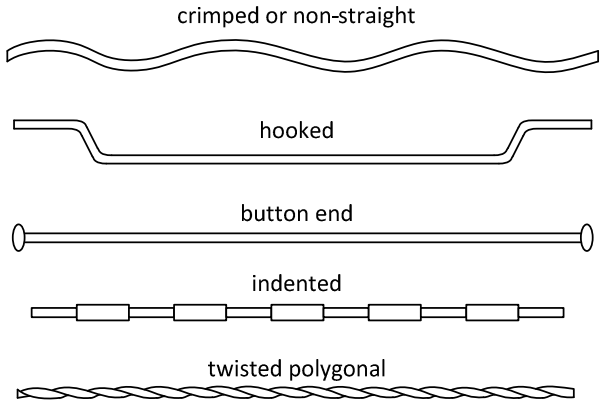

Figure 2.2 Schematic examples of steel fibre shapes (Brandt, 2008).

The advantages of the use of steel fibres include (BEKAERT, 2004)

- Ductile concrete with a high load bearing capacity,
- Efficient crack control,
- Durability,

- Quick and easy application,
- and Efficient and cost-effective solution.

Typical applications for steel fibres are in (BEKAERT, 2004)

- Concrete floors,
- Tunnelling and underground structures,
- and Prefabricated applications.

Steel is an elasto-plastic material with the same material properties in tension and compression. Therefore it is effective to use with concrete to supply extra support in tension and/or compression. Steel has a high Young's-modulus (E ≈ 210 GPa) with the characteristic of tension hardening. A major concern is the effect of oxidation (rust) on the durability of steel.

Steel fibres are used structurally with the intention that it provides the required tensile strength after cracking occurs. Thus, it provides a post-cracking mechanism. The idea is that the fibres pull-out rather than to fracture, as it can be shown that the fracture energy is higher in such a case.

2.1.2. Modelling tensile behaviour

Concrete is a brittle material and therefore has little tensile strength. In conventional concrete, steel bars are added in the tensile zones to supply the required tensile strength. Steel reinforcing is a versatile material as could provide extra support in tension and/or compression. As far as design codes are concerned the tensile response of concrete is so small that it is ignored, with the steel bars supplying the only form of tensile strength.

For steel fibre reinforced concrete (SFRC) the tensile behaviour of the whole composite (evenly distributed fibres) is altered, opposed to conventional steel bars that only supply the tensile reinforcement at specific sections (Figure 2.3). Thus, the material property for the composite's tensile behaviour is altered in the post-crack region, which signifies that a modified stress-strain diagram could be supplied for the fibre reinforced composite.

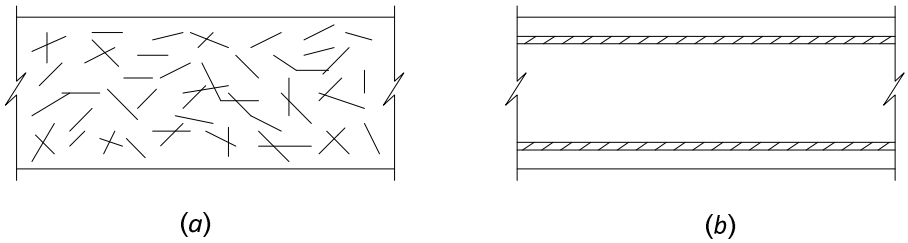

Figure 2.3 Schematic presentation of (a) randomly distributed fibres in FRC vs (b) conventionally reinforced concrete.

2.1.2.1. FIB Model Code and RILEM TC 162-TDF

RILEM TC 162-TDF (2003) has provided a model to predict the cross sectional capacity for SFRC (Figure 2.4), according to the ultimate limit state for bending and axial force. The model uses the mechanical properties obtained from standard three point bending tests to define a representative tensile behaviour.

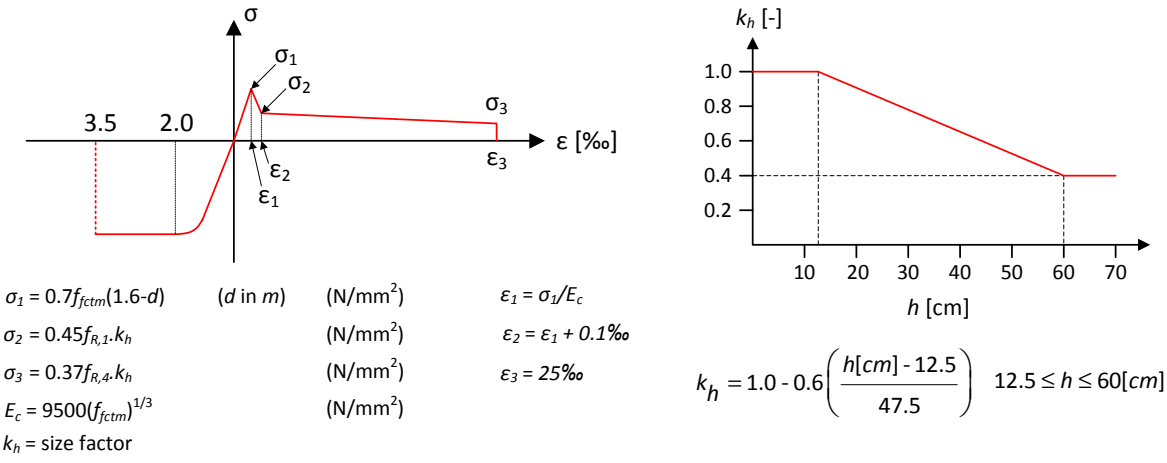

Figure 2.4 Stress-strain diagram and size factor according to RILEM TC 162-TDF (2003:562).

At first the method was developed without the use of the size factor, but after comparing the predictions of the design method with that of experimental results of structural elements with various sizes it was found that the design method severely overestimates the carrying capacity (RILEM TC 162-TDF, 2003).

The following assumptions were used in assessing the ultimate resistance of a cross-section (RILEM TC 162-TDF, 2003:561-562) using Figure 2.4 as a reference:

- Plane sections remain plane and perpendicular to the neutral axis.
- The stresses in the SFRC in tension as well as compression are derived from the stress-strain diagram shown in Figure 2.4 and explained in the appendix of the model code (RILEM TC 162-TDF, 2003).
- The stresses in the reinforcement (bars) are derived from an idealised bi-linear stress-strain diagram.
- For cross sections subjected to pure axial compression, the compressive strain in SFR-concrete is limited to -0.002. For cross sections not fully in compression, the limiting compressive strain is taken as -0.0035. In intermediate situations, the strain diagram is defined by assuming that the strain is -0.002 at a level $^{3}/_{7}$ of the height of the compressed zone, measured from the most compressed face (BS EN 1992-1-1:2004).
- For SFRC which is additionally reinforced with bars, the strain is limited to 0.025 at the position of the reinforcement.
- To ensure enough anchorage capacity for the steel fibres, the maximum crack width in the ultimate limit state is restricted to 3.5mm. If crack widths larger than 3.5mm are used, the residual flexural tensile strength corresponding to that crack width and measured during the bending test has to be used to calculate σ_3. It is recommended that this value, which replaces $f_{R,4}$, should not be lower than 1 MPa.

2.1.2.2. Tensile Model Parameters

The RILEM code provides an indication of the shape for the uniaxial tensile stress-strain relationship. The prescribed shape indicates deflection softening, as is expected for conventional SFRC. It is therefore assumed that the tensile relationship has a multi-linear response, with a crack initiating at a cracking stress (σ_{crack}) with a corresponding cracking strain (ε_{crack}), as shown in Figure 2.5. The remainder of the response (softening region) can be described with more stress-strain points (ε_i,σ_i). The complete uniaxial tensile response is determined using an inverse analysis, which is discussed in Section 3.4.1.

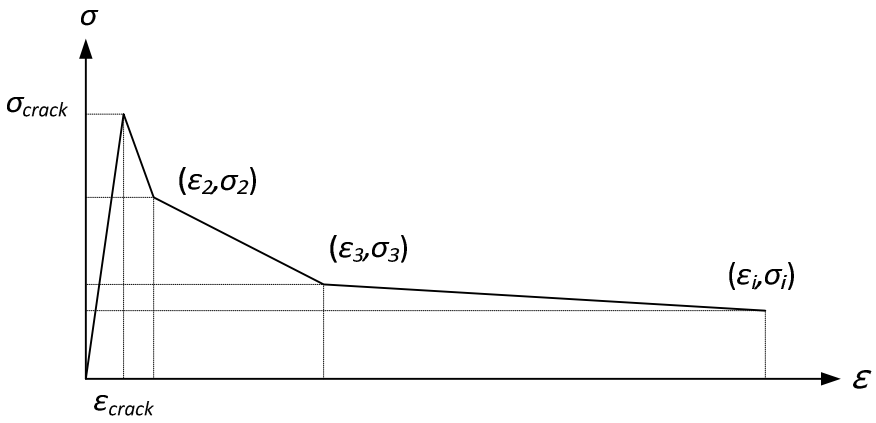

Figure 2.5 Presentation of multi-linear tensile response for FRC.

2.1.3. Modelling compressive behaviour

The principal feature of concrete is the compressive response and therefore models have been developed to predict the compressive stress-strain relationship, e.g. Eurocode 2 (2004). From a design perspective simple compression models are utilised, which have fixed shapes, but certain characteristics such as concrete strength (cylinder or cube) and *E*-modulus (material stiffness) define the overall behaviour.

An analytical model to predict the complete stress-strain relationship of fibre-reinforced mortar, taking into account the fibre shape, volume fraction and fibre geometry, has been proposed by Fanella and Naaman (1985:479).

Ezeldin and Balaguru (1992:415-27) proposed an analytical expression for generating the stress-strain curve of SFRC based on the expression proposed by Careira and Chu (1985:800) for uniaxial compression of unreinforced concrete. A dimensionless material parameter, β, is determined from the stress-strain curve of a compression test. The proposed equation to determine the parameter β, is derived for hooked end steel fibres.

These compression models will not be used directly in the research, but it does give an approximation of the expected shape for SFRC in uniaxial compression. Figure 2.6 shows the result obtained from compression tests of cylinders with 1% volume fraction fibres versus that of unreinforced concrete (König & Kützing, 1999).

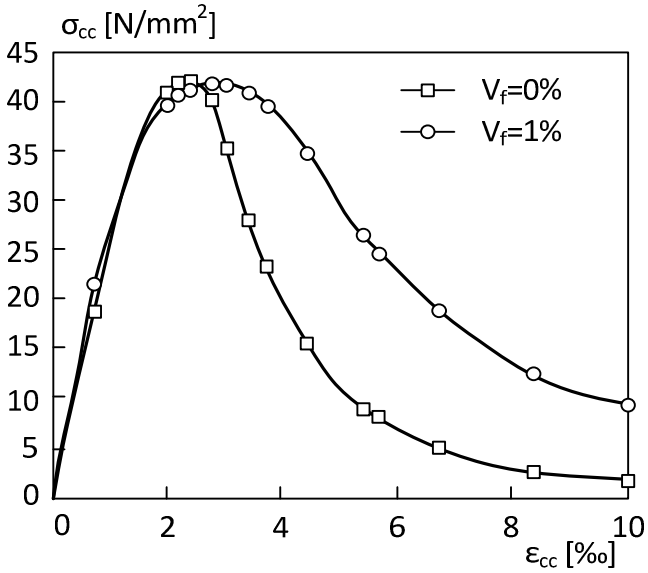

Figure 2.6 Typical behaviour of SFRC in compression (König & Kützing, 1999:255).

2.1.3.1. Effect of addition of fibres on compressive behaviour

The following characteristics have been observed on the compressive behaviour of SFRC compared to conventional concrete:

- There is an increase in toughness. Toughness is characterised as the area under the stress-strain curve (Nataraja *et al*., 1999:385).
- Concrete strength will not be greatly affected (König & Kützing, 1999:255).
- An increase in ductility has been found. The area under the post-peak curve is higher for that of plain concrete, meaning the confinement is increased. An increase in confinement causes an increase in the ductility.
- An increase in ability to resist spalling has also been found (Nataraja *et al*., 1999:383).

2.1.3.2. Compressive Model Parameters

The mentioned models provided an indication of what to expect for the compressive behaviour, as shown in Figure 2.7. The main features of the predicted stress-strain relation are the crushing strength (σ_{crush}), crushing strain (ε_{crush}), the *E*-modulus and the Toughness Index (*TI*). The toughness

index is calculated using the area under the normalised stress-strain curve from a zero strain up to 0.5 of the peak strength in the post-peak region.

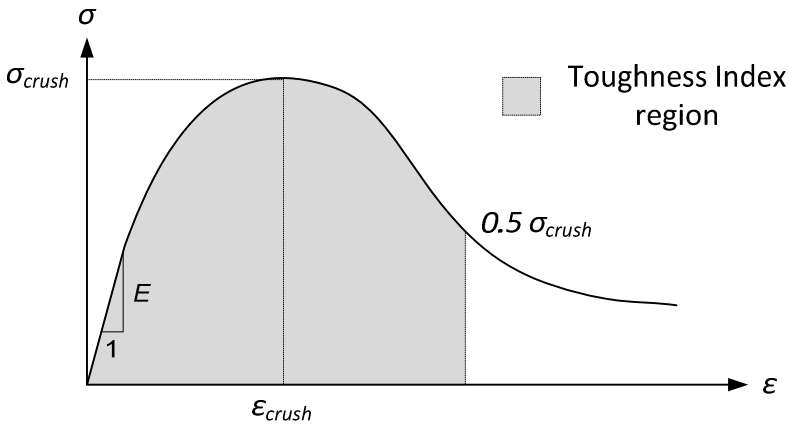

Figure 2.7 Presentation of the main parameters for the compressive response for SFRC.

2.2. Flexural behaviour

In the previous sections the uniaxial behaviour of concrete in tension and compression has been discussed. Most concrete structures are however not subjected to uniaxial behaviour only. Bending is a form of structural behaviour that occurs when a slender member is subject to a transverse load, causing it to move out of plane. This out of plane movement causes bending stresses in a structural member that consist of tensile and compressive regions.

A significant flexural characteristic is the bending moment-curvature relationship, as it can be used to define the structural behaviour for a cross-section in a structural member.

2.3. Moment redistribution

In Section 2.1 the uniaxial behaviour of compression and tension has been discussed for structural members. In this section, Moment Redistribution (MR), which is a structural behaviour in statically indeterminate structures, is discussed.

It is possible to use a distribution of moments and forces different from that given by linear elastic structural analysis if the critical sections have sufficient ductility to allow redistribution of actions to

occur as the ultimate load is approached (Park & Paulay, 1975:496). The behaviour at ultimate load depends on the deformation characteristics of the members, which for frames depend mainly on the moment-curvature relationship.

2.3.1. Moment-curvature relationship

A typical moment-curvature relationship for a conventionally reinforced concrete flexural member is presented in Figure 2.8. The curve follows a certain flexural stiffness up until first cracking of the concrete happens. After cracking occurs the flexural stiffness is reduced due to the loss of the concrete tensile resistance. When the section reaches the first yielding of the steel reinforcing in tension, it proceeds into the plastic zone.

As shown in Figure 2.8, the ultimate bending moment of the section is reached in the plastic zone, implying that the resistance is still increasing although the tension reinforcement has already yielded. The section will have failed when the tensile reinforcement has failed or when the concrete has crushed in the compression zone.

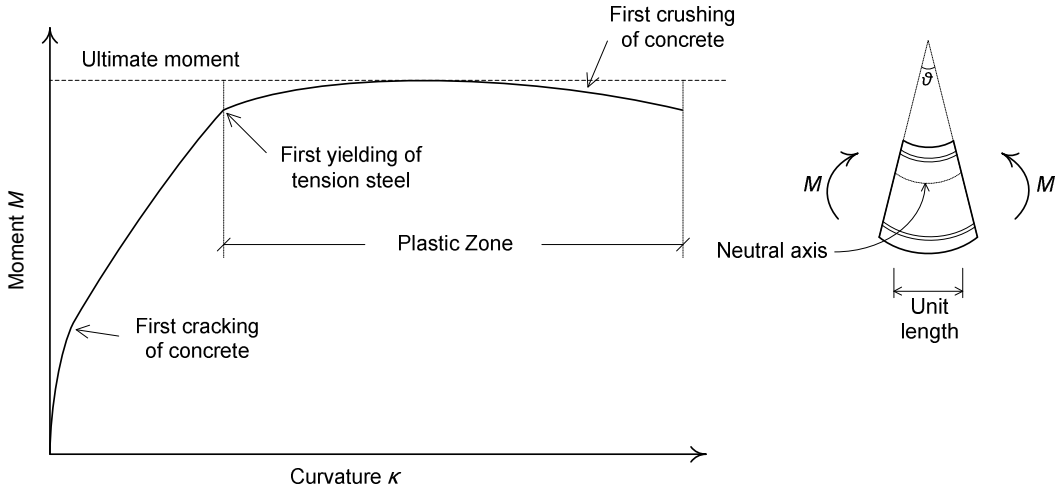

Figure 2.8 Typical moment-curvature relationship for a conventionally reinforced concrete flexural member (Park & Paulay, 1975:497).

2.3.2. Moment Redistribution Concept

Moment redistribution is possible in statically indeterminate structures, such as continuous beams or slabs. It is described as the transfer of moment between high moment regions, usually at the supports, to lower moment regions in the member while maintaining the overall structural resistance. This is due to the formation of plastic hinges at the zones where the yielding moment is reached.

As an example, a two-span continuous beam, having a uniform cross section as shown in Figure 2.9, is considered (Park & Paulay, 1975: 498). M'_u is the ultimate moment of resistance of the negative bending moment sections (hogging sections) and M_u the ultimate moment of resistance of the positive bending moment sections (sagging sections). It is assumed that the moment-curvature relationship for the sections is the idealised bilinear relationship for a ductile section shown in Figure 2.9 (b), with all sections having the same constant flexural rigidity up to the ultimate moment and the moment remaining constant at the ultimate value at higher curvatures.

At relative low loads the distribution of bending moment due to the two concentrated loads is in accordance with the elastic theory distribution as shown in Figure 2.9 (c). The self-weight of the beam is neglected in the calculation of the moment distribution. As the applied loads are increased further, the ultimate moment of resistance is reached at a critical section, for this scenario it would be over the centre support, before it is reached at the other sections. Then the moment at the centre support is M'_u, as in Figure 2.9 (d).

The extent to which further load can be carried by the beam depends on the capacity for plastic rotation at the centre support. If the section is brittle, the moment will decrease rapidly after reaching the maximum capacity (as in Figure 2.9 (d)), and the beam will fail suddenly without carrying any additional load. If the section is ductile, additional load can be carried because the plastic hinge at the centre support rotates while maintaining its moment of resistance constant at M'_u, and moment redistribution will occur until the maximum positive moment in the spans increases to M_u. At this instant the collapse mechanism in Figure 2.9 (e) is formed.

Figure 2.9 (f) traces the variation of bending moment at the critical sections with load on the beam, assuming that the plastic hinge develops at the centre support (this requires $M_u'/M_u < M'/M = 1.2$) (Park & Paulay, 1975: 496-502).

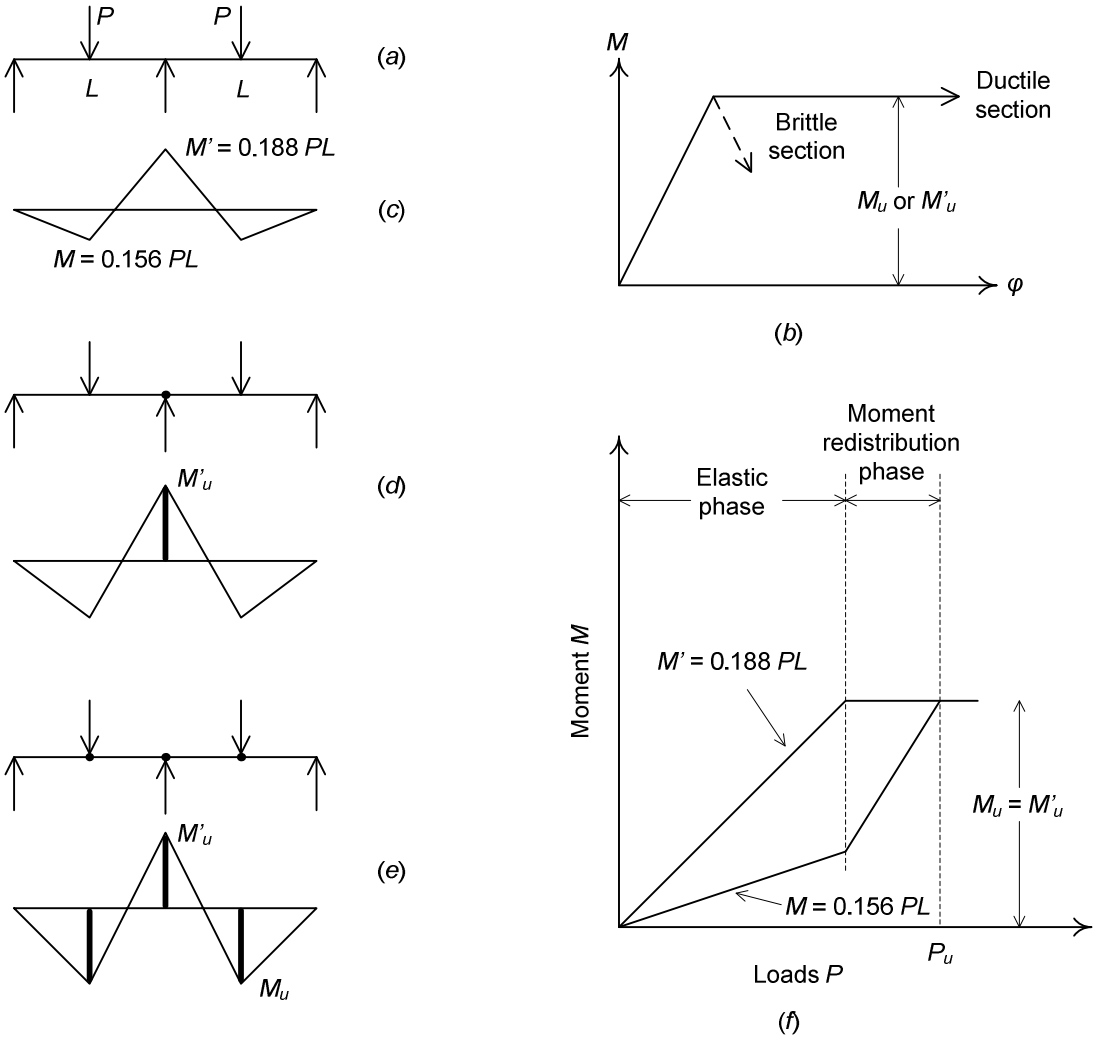

Figure 2.9 Moment redistribution and formation of a collapse mechanism for a continuous beam. (a) Beam. (b) Idealised moment-curvature relationship for the sections. (c) Elastic theory bending moment diagram. (d) At formation of first plastic hinge. (e) At formation of collapse mechanism. (f) Change of bending moment with load (Park & Paulay, 1975: 498).

2.3.3. Rotation capacity

According to Park and Paulay (1975:498-501) the rotation capacity at the centre support is derived as follows.

It is noted that all stage equilibrium requires that

$$M + \frac{M'}{2} = \frac{PL}{4} \tag{2.1}$$

$$\delta \geq k_6 \; P = \frac{4}{L}\left(M + \frac{M'}{2} \right) \tag{2.2}$$

And, if the moment at the centre support remains at M_u' until M_u develops at the midspan sections, we have

$$P_u = \frac{4}{L}\left(M_u + \frac{M_u'}{2} \right) \tag{2.3}$$

Therefore, if sufficient rotation capacity of the plastic hinges is available, the bending moment distribution at the ultimate load may be quite different from that calculated using elastic theory and depends on the ultimate moment resistance of the sections. In reinforced concrete structures, the ductility at the first plastic hinges formed may be insufficient to enable full redistribution of moments to take place with the ultimate moment at each critical section. Thus, if moment redistribution is to be relied on, the availability of sufficient ductility at the plastic hinges must be ensured.

As an example, the calculated required plastic rotation for the two-span continuous beam of Figure 2.9 for the case of the plastic hinge forming at the centre support is considered. The beam and the curvature diagrams of Figures 2.10 (a) and 2.10 (b) indicate the stage at which sufficient plastic rotation has occurred at the centre support, *B*, to enable the ultimate moment M_u to be just developed at midspan. Hence Figures 2.10 (a) and 2.10 (b) indicate the stage when P_u is just reached.

The plastic curvature is considered to occur over the equivalent plastic hinge length, l_p, each side of the critical section. The elastic curvature along the length of the member may be calculated from the distribution of bending moments and the assumed constant flexural rigidity, *EI*. The plastic rotation, ϑ_p, at the centre support, *B*, is described as the discontinuity of the slope between the ends of the adjacent members, and $\vartheta_p = 2\vartheta_B$ as indicated in Figure 2.10 (a).

ϑ_p is determined by considering the elastic deformations of the members supporting the loads P_u. First, the plastic hinge at *B* is replaced by a frictionless hinge as in Figure 2.10 (c). Then from the moment area theorem the rotation at *B* due to load P_u alone on one span is

$$\vartheta_B' = \frac{\left(M_u + 0.5 M_u' \right) L}{4EI} \tag{2.4}$$

The effect of the ultimate support moment, M_u', acting at the frictionless hinge, as in Figure 2.10 (d), can now be considered. The rotation at B due to M_u' alone is

$$\vartheta_B'' = \frac{M_u' L}{3EI} \tag{2.5}$$

$$\vartheta_B = \vartheta_B' - \vartheta_B'' = \frac{L}{4EI}\left(M_u - \frac{5}{6}M_u'\right) \tag{2.6}$$

$$\vartheta_p = 2\vartheta_B = \frac{L}{2EI}\left(M_u - \frac{5}{6}M_u'\right) \tag{2.7}$$

Equation 2.7 provides the rotation required at the plastic hinge at the centre support B for the case when $M_u > 5/6M_u'$. If $M_u = 5/6M_u'$ the required ϑ_p is zero, because of this the ratio of moments is given by elastic theory, and no bending moment redistribution is required. Also, if $M_u < 5/6M_u'$ the value given for ϑ_p is negative, in that case, the foregoing calculation does not apply, because the first plastic hinge forms at the load points at midspan and the required plastic rotation at those sections would have to be calculated.

In the example, when $M_u > 5/6M_u'$, redistribution of the bending moments can take place until the ultimate moment develops at each critical section if

$$\frac{L}{2EI}\left(M_u - \frac{5}{6}M_u'\right) \leq \left(\frac{\varepsilon_c}{c} - \frac{\varepsilon_{ce}}{d}\right)2L_p \tag{2.8}$$

with

ε_c the concrete strain at extreme compression fibre at the ultimate curvature

ε_{ce} the concrete strain at the extreme compression fibre when the yield curvature is reached

c the neutral axis depth at the ultimate moment

kd the neutral axis depth when the yield curvature is reached

L_p the equivalent plastic hinge length, each side of the critical section

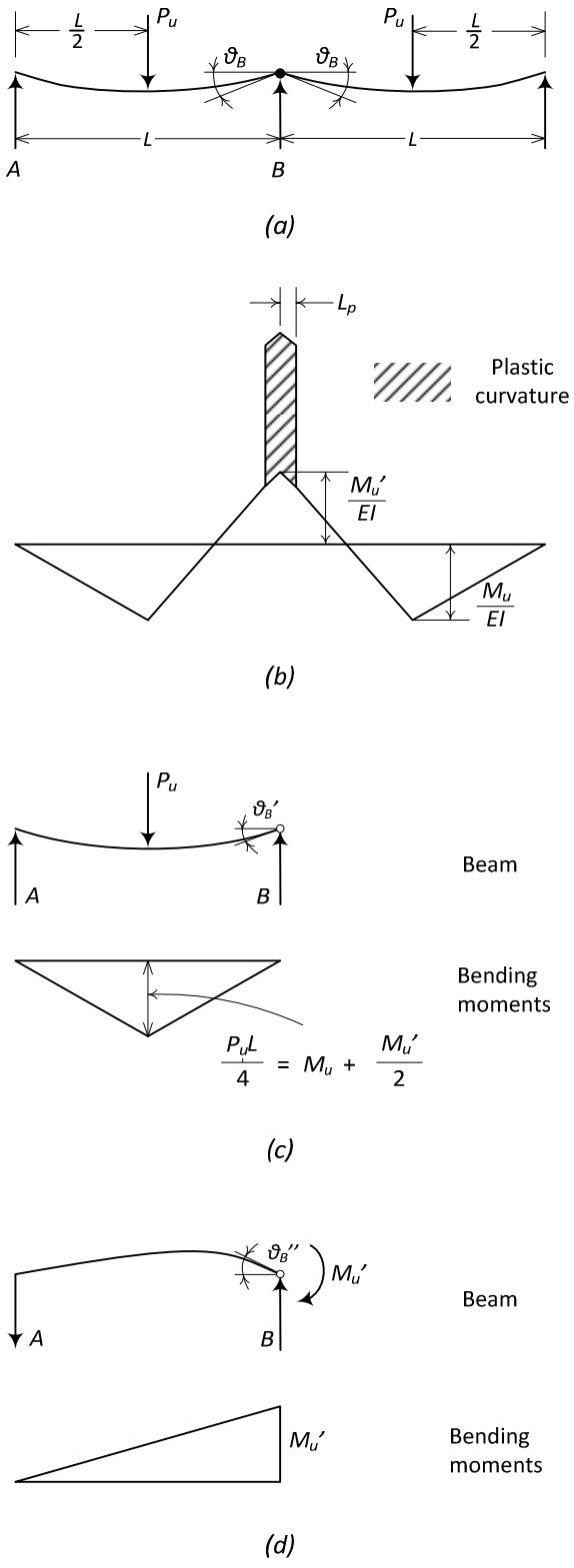

Figure 2.10 Calculation of plastic hinge rotation for beam of Figure 2.9. (a) Deflected shape when ultimate load is reached. (b) Idealised curvature distribution when ultimate load is reached. (c) P_u acting without M_u'. (d) M_u' acting without P_u (Park & Paulay, 1975: 500).

2.3.4. Plastic hinge length and rotation

In Figure 2.11 a reinforced concrete flexural member is considered, as proposed by Park and Paulay (1975:242-244), that has reached the ultimate curvature and bending moment at the critical section. End *A* of the member, for example, is the free end of a cantilever or a point of contraflexure, and end *B* is a column face. The distribution of curvature along the member is apparent. The region of inelastic curvature is spread over a length of beam where the bending moment exceeds the yield moment of the section.

The elastic contribution to the rotation over the full length of the member (the unshaded area of the curvature diagram of Figure 2.11 (c)) is given by

$$\vartheta = \int_A^B \kappa dx \tag{2.9}$$

$$\vartheta = \int_A^B \frac{M}{EI} dx \tag{2.10}$$

which is the application of the moment-area theorem.

The shaded area of Figure 2.11 (c) is the inelastic rotation that can occur at the "plastic hinge" in the vicinity of the critical section, thus representing the plastic rotation that occurs in addition to the elastic rotation at the ultimate stage of the member. The inelastic area at the ultimate stage can be replaced by an equivalent rectangle of height κ_u-κ_y and width L_p, having the same area as the actual inelastic curvature distribution. The width L_p, is the equivalent length of the plastic hinge over which the plastic curvature is considered to be constant. κ_y and κ_u represent the yield curvature and the ultimate curvature, respectively. Hence, the plastic hinge rotation to one side of the critical section may be written as

$$\vartheta_p = \left(\kappa_u - \kappa_y\right) L_p \tag{2.11}$$

Plastic hinge rotation for reinforced concrete structures has been studied by many authors, with each author deriving an expression to determine the plastic rotation with an accompanying plastic hinge length, e.g. Cohn (1964), Mattock (1964, 1983), Corley (1966), Baker and Amarakone (1964), Naaman et al. (1986), Riva and Cohn (1994). Although these numerous attempts have been made, it appears that none of the proposed formulations for ϑ_p can be considered completely satisfactory. Most of the formulations are based on tests of simply supported beams with point loads, in which

only a limited number of parameters concerning the plastic rotation capacity of a member is considered (Shakir & Rogowsky, 2000:1287).

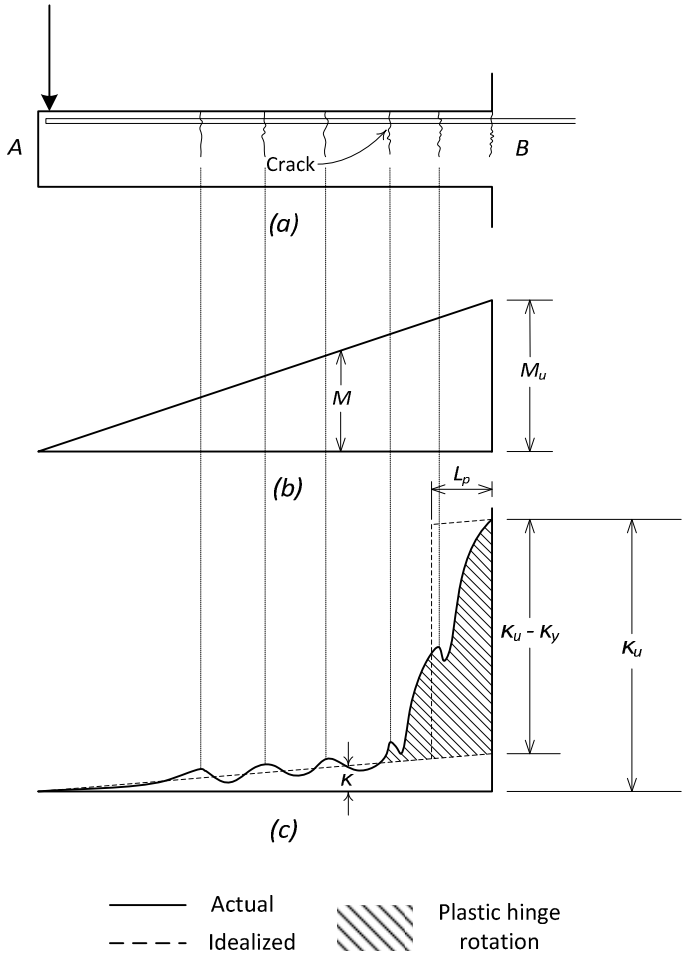

Figure 2.11 Curvature distribution along beam at ultimate moment. (a) Beam. (b) Bending moment diagram. (c) Curvature diagram (Park & Paulay, 1975: 243).

2.3.5. Ductility and Stiffness

Ductility is an important concept as it has a great influence on the rotation capacity of a structural member. The definitions of ductility and stiffness are illustrated in Figure 2.12 for materials, cross-sections and structural members. For simplicity the shape of the curves are chosen to be bi-linear, although in reality you would expect more curvilinear responses. The ability for a structural member to distribute bending moments depends on both the ductility and the stiffness (Oehlers, Griffith & Mohamed Ali, 2009).

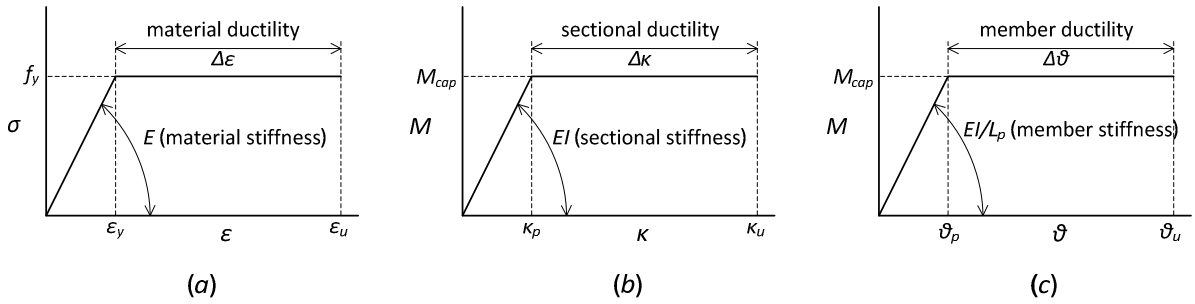

Figure 2.12 Stiffness and ductility behaviours; (a) material properties, (b) sectional properties, (c) member properties (Oehlers, Griffith & Mohamed Ali, 2009).

As shown in Figure 2.12 (a), the material ductility ($\Delta\varepsilon$) and Young's Modulus (E) are defined. There is a linear relation for the stress-strain behaviour up till the yield stress (f_y) is reached at the yield strain (ε_y). Afterwards, plastic deformation occurs over the ductile plateau ($\Delta\varepsilon$) until the failure deformation (ε_u) is reached.

Figure 2.12 (b) illustrates the sectional behaviour with the sectional ductility, in terms of curvature ($\Delta\kappa$), and the sectional stiffness, EI. The same is applicable as for the material, with the flexural rigidity, EI, decreasing while the sectional ductility is related to the change in curvature. The member behaviour, due to the rotation over a hinge length, L_p, with the member ductility ($\Delta\vartheta$) and member stiffness (EI/L_p) is shown in Figure 2.12 (c). The member rotational stiffness is EI/L_p and the member ductility ($\Delta\vartheta$) can be described as the change in rotation in the plastic zone (Oehlers, Griffith & Mohamed Ali, 2009).

2.3.6. Allowable Moment Redistribution

The design values implemented for the allowable amount of moment redistribution differ among various design codes. Design codes allow the moment redistribution to be measured relative to the designed neutral axis depth. Figure 2.13 provides an overview of the current design values for moment redistribution as applied in different codes.

According to the FIB Model Code (FIB, 2010) moments at the ultimate limit state (ULS) calculated using linear elastic analysis may be redistributed, provided that the resulting distribution of moments remains in equilibrium with the applied loads. Also, redistribution of bending moments without an explicit check on the rotation capacity is allowed for continuous beams or slabs which are

predominantly subjected to flexure and have a ratio of the lengths of adjacent spans in the range 0.5 to 2.0.

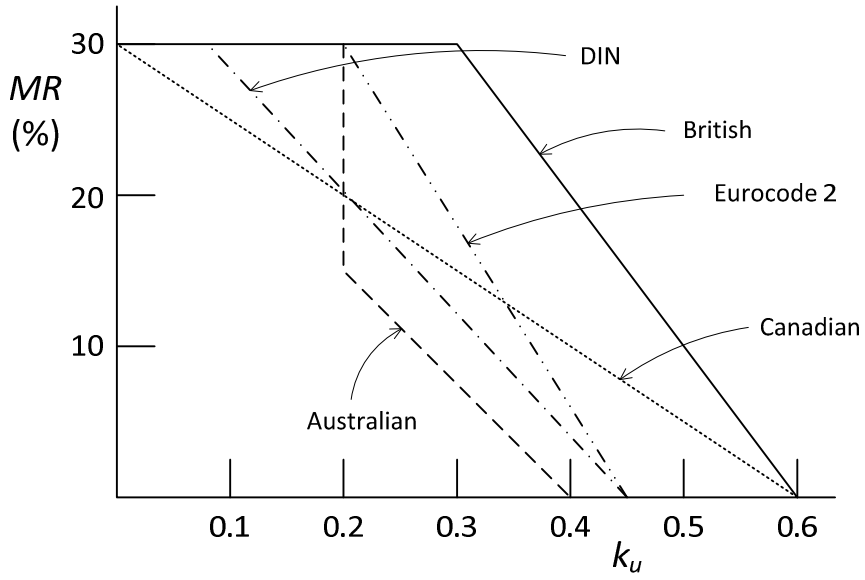

Figure 2.13 Prescribed moment redistribution according to neutral axis depth approach (Oehlers, et al, 2009:1539).

In this case the following relations should apply:

$$\delta \geq k_1 + k_2 . {}^{x_u}/_{d} \qquad \text{for } f_{ck} \leq 50\text{MPa} \qquad (2.12)$$

$$\delta \geq k_3 + k_4 . {}^{x_u}/_{d} \qquad \text{for } f_{ck} > 50\text{MPa} \qquad (2.13)$$

and

$$\delta \geq k_5 \qquad (2.14)$$

where Class B, Class C or Class D reinforcement is used, see subclause 5.2.5.4 of FIB Model Code (FIB, 2010).

$$\delta \geq k_6 \qquad (2.15)$$

where Class A reinforcement is used, see subclause 5.2.5.4 of FIB Model Code (FIB, 2010).

where:

δ is the ratio of the redistributed moment to the elastic bending moment

x_u is the depth of the neutral axis at the ULS after redistribution

d is the effective depth of the section

k_u neutral axis depth

$k_1 = 0.44$

$k_2 = 1.25(0.6 + 0.0014/\varepsilon_{cu2})$

$k_3 = 0.54$

$k_4 = 1.25(0.6 + 0.0014/\varepsilon_{cu2})$

$k_5 = 0.7$

$k_6 = 0.8$

ε_{cu2} = is ultimate strain according to subclause 7.2.3.1.1 of FIB Model Code

f_{ck} = characteristic value of cylinder compressive strength of concrete

In accordance with the current study it is decided to implement Equation 2.12, as the concrete cylinder strengths obtained in this study is below the indicated 50MPa characteristic value, and Equation 2.14, because it provides the upper bound value for the allowable moment redistribution. Therefore, the necessary ε_{cu2} value is equal to 0.0035, according to subclause 7.2.3.1.1 of the FIB Model Code (FIB, 2010). The resulting curve corresponds with that of the European specification with high ductility steel. Thus, a x_u/d value of 0.447 would produce zero allowable moment redistribution.

2.3.7. Crack band width

The crack band width (CBW) describes the average crack spacing of a flexural member. This characteristic has been previously researched by Broms (1965) and Rizk & Marzouk (2009). In their studies the crack spacing of reinforced concrete flexural members were predicted by taking certain influential factors into consideration.

The variables considered in the investigation by Rizk & Marzouk include the concrete cover, the slab thickness and the bar spacing for normal- and high-strength concrete. From their experimental tests it was concluded that an increase in the concrete cover resulted in an increased crack spacing. This is because the crack spacing (s) is inversely proportional to the effective reinforcement ratio, ρ_{eff}. Increasing the bottom cover increases the effective tension area of the concrete and decreases the effective reinforcement ratio, which results in larger crack spacing. Also increasing the tensile

reinforcement area decreases crack spacing and reduces crack width (because crack spacing is inversely proportional to the effective reinforcement ratio). Also, it was found that as the bar spacing is increased the crack spacing increased.

According to the findings of Broms (1965) the measured crack spacing observed at the level of the reinforcement of the flexural members can be described with a function of the concrete cover (t). This thickness has been measured from the centre of the reinforcing bar located closes to the side considered. According to the experimental results, the average crack spacing is determined with

$$s_{ave} = 2t \tag{2.16}$$

Thus, for SFRC flexural members the average crack spacing cannot be determined with the characteristics discussed above, as conventional steel is not used for this research. Therefore, four point bending tests have to be performed to measure the average crack spacing in the constant moment region or adequate assumptions have to be made.

2.4. Concluding Summary

The allowable amount of moment redistribution is important in cases where steel fibres are used in conjunction with conventional reinforcement, as the amount of moment redistribution could differ from that allowed for conventional reinforcement. In this chapter the factors influencing the structural behaviour is investigated, e.g. material properties, rotation capacity, ductility, plastic hinge length and crack spacing, which identifies the necessary testing to be performed in order to predict representative structural behaviour. These factors could also be used to classify the performance of each composite. From the knowledge obtained it is decided to obtain representative material properties, which would be used to derive the moment-curvature relationship for each composite. With these sectional behaviours computational analyses could be performed to establish the amount of moment redistribution for each SFRC member.

CHAPTER 3

CHARACTERISING MATERIAL PROPERTIES FOR MODELLING

In this chapter the method of obtaining the material properties for the SFRC is described, followed with the actual compressive and flexural results obtained from experimental tests. The inverse analysis procedure is discussed and accompanied with the tensile properties obtained from the finite element analysis. At the end of this chapter the properties required for the sectional analysis of Chapter 4 are presented.

3.1. Mix design and test setups

The aim was to design a self compacting concrete (SCC) mix for different percentage volume fibres without adjusting the value of too many constituents of the mix, so that the end results would be comparable in terms of the added amount of fibres.

3.1.1. Fibre characteristics

The fibres to be used were DRAMIX RC-80/60-CP hooked end steel fibres provided by BEKAERT.

According to BEKAERT this fibre type provides the highest performance in terms of ductility, energy absorption and crack control.

The fibres are stored in paper bags that are labelled with the distinctive marking shown in Figure 3.1. The most important characteristics for the fibres are provided in Table 3.1. Figure 3.2 provides an indication of the fibre geometry and how the fibres are bundled together with glue.

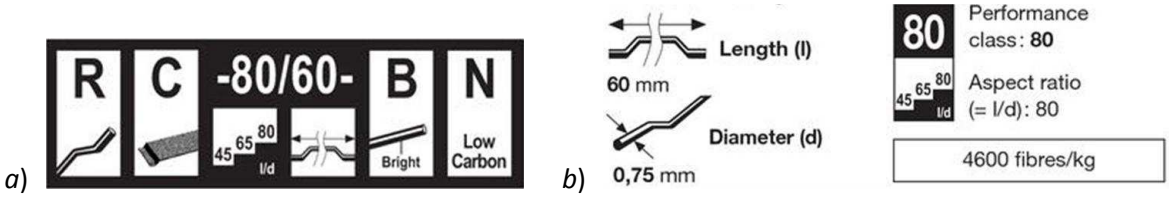

Figure 3.1 a) Label on packaging for steel fibres, b) Geometry of fibres (BEKAERT, 2004).

Table 3.1 Summary of fibre characteristics.

DESCRIPTION	
Label	RC-80/60-CP
Type	Hooked end
Glued	Yes
Coating	Galvanised

GEOMETRY	
Length [mm]	60
Diameter [mm]	0.75
Aspect ratio [*L/d*]	80

MATERIAL PROPERTIES	
Tensile strength [MPa]	1050
Young's Modulus [GPa]	210
Density [kg/m^3]	7850

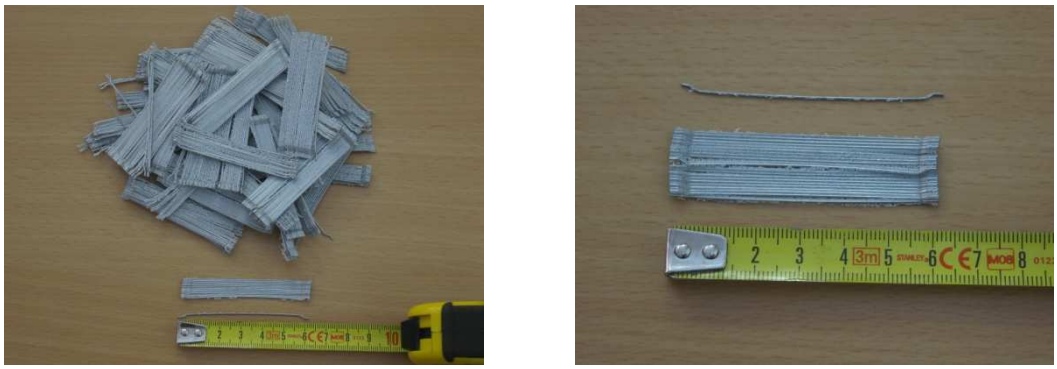

Figure 3.2 The RC-80/60-CP fibres used for this study.

3.1.2. Mix Design

As mentioned before the mixes are designed as self-compacting concrete, as it will ensure a better fibre distribution compared to that of a vibrated concrete. Trial mixes were made to create a mix characterised with a slump flow of more than 500mm and without segregation and fibre bundling. A mix was determined that is suitable for the range of 0.5% to 1.0% volume fibres with only the dosage of superplasticiser adjusted.

Due to small differences in the amount of the mix constituents it is only necessary to provide one mix design template (Table 3.2).

Table 3.2 Mix design template.

	% Fibres					
	0.5	**0.75**	**1.0**	**1.0**		
Material	**%**			**kg/m^3**	**RD**	**Vol. [litre]**
Cement				370	3.1	120.2
Fly ash				235	2.8	84.5
Stone				635	2.7	236.8
Sand				934	2.65	354.8
Water				190	1	191.3
Superplasticiser	0.4	0.45	0.5	3.025	1.2	2.5
Fibres	0.5	0.75	1	78.5	7.85	10
TOTAL				**2446**		**1000**

The combination of the used constituents provided a good self-compacting concrete with slump flows greater than 500mm and good cohesion between the coarse aggregate, cement paste and the fibres. It was decided that a water/binder ratio of 0.32 would be sufficient to provide a concrete strength of about 40MPa. The following constituents were used:

- Cement – A CEM I 42.5 cement, supplied by PPC, was used.
- Flyash – Durapozz, supplied by Ash Resources, was used to increase the binder content.
- Stone – 6mm crushed Graywacke stone was used.
- Sand – A natural sand, locally known as Malmesbury sand, was used.
- Superplasticiser – Premia 310, supplied by Chryso, was used to act as a water reducing agent.

The mixing procedure that provided the best concrete mixture is discussed next. Firstly, the dry constituents were added to the mixer and mixed for 1 minute. The water was then added slowly at a constant rate. To ensure decent mixture of all the constituents, part of the superplasticiser dosage (0.4%) was added to ensure enough fluidity for the complete mixture. The mixing is continued for another 2 minutes and followed with the gradual addition of the steel fibres. After all the fibres were added, the mixing was continued for another 6 minutes to ensure that the fibres were detached from one another and dispersed evenly throughout the concrete mixture. Finally the rest of the superplasticiser was added and mixed for another minute. To ensure the correct fluidity, a slump flow test was performed for every mix. If the required flow was not obtained additional superplasticiser was added, while ensuring that no segregation took place.

3.1.3. Compression test setup

In order to retrieve a representative compressive behaviour of the material, six cylinders were cast for each SFRC mix. The test specimen had a diameter of 150mm and a height of 250mm and was tested in a CONTEST Hydraulic Actuator machine. Usually the *L/d* ratio for cylinder specimens should be equal to two, but due to spacing constraints of the testing machine, it was inevitable to decrease the height of the specimens. The specimens were demoulded two days after casting and placed in curing baths that maintains a constant water temperature of 25°C. The specimens were removed on the testing day which was at an age of 28 days.

The applied load was measured with a 200ton HBM load cell that is placed on top of or beneath the specimen. The equivalent displacement was taken as the average value measured with two 50mm LVDTs (Linear Variable Displacement Transducers) that were fixed to the specimens with an aluminium frame at the mid section. The aluminium frame resulted in a gauge length of 133mm. All specimens were capped before testing using a paste consisting of cement and gypsum to ensure a uniform loading surface. The test setup can be seen in Figure 3.3.

The tests were force-controlled and conducted at a constant rate of 120kN/min. The following procedure was used:

- Firstly, the specimen was loaded up to 30% of the peak load and unloaded.
- Secondly, the previous procedure was repeated.
- Lastly, the specimen was loaded past the peak strength until half that of the peak load was reached.

- The reason for the loading and unloading is to achieve a good representation of the material stiffness (Young's Modulus), while the last step is performed to provide the ultimate strength and post-peak performance.
- The Young's Modulus is calculated as the slope of the stress-strain diagram between 10% and 30% of the peak strength.

a)  *b*) 

Figure 3.3 a) Capped specimen with LVDT frame attached and b) testing conducted in CONTEST with load cell at top of specimen.

3.1.4. Flexural test setup

The tensile response of a material can be evaluated using either a direct test or indirect test method. The uni-axial tensile response can be obtained with a direct test method such as the uni-axial tension test, but this is difficult to perform and therefore an indirect test method is typically used, such as the three point bending, four point bending or the wedge splitting test method. The only drawback of the indirect methods is that an inverse analysis needs to be performed to obtain the uni-axial tensile response. For simplicity and convenience it was decided to conduct three point bending tests (3PBT) on notched beams, as suggested in RILEM TC 162-TDF (2002), to evaluate the tensile behaviour.

RILEM TC 162-TDF (2003) proposes a design method based on a stress-strain approach, which implements the results obtained from the 3PBTs. The geometry of the beam recommended by RILEM TC 162-TDF (2003) is shown in Figure 3.4. The publication also suggests that the test is not intended for concrete with steel fibres longer than 60mm or for aggregate size larger than 32mm.

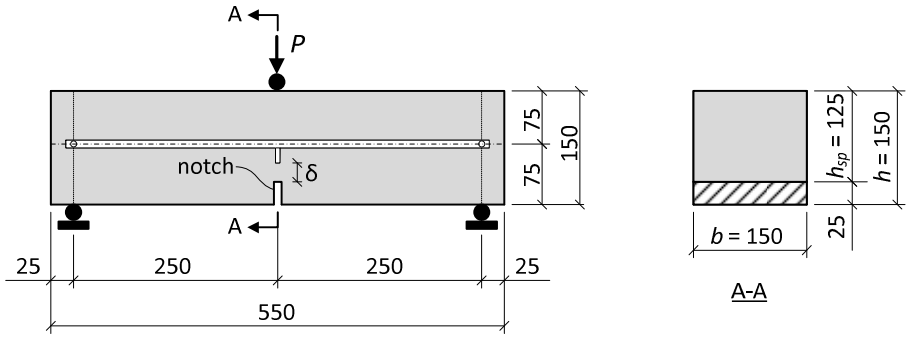

Figure 3.4 Test setup for the three-point bending test on notched beams according to RILEM TC 162-TDF (2002).

The beams were cast in 700mmx150mmx150mm steel moulds and were demoulded after 48 hours. The specimens were then placed in the curing baths at a constant temperature of 25°C. On the day of testing, 28 day strength, the specimens were notched using wet sawing. As prescribed by RILEM TC 162-TDF (2003), the notch had a depth of 25mm and a width that is not larger than 5mm.

The testing was conducted in a Zwick Z250 Universal Material Testing Machine, which has a compression and tensile capacity of 250kN. The test span length was 450mm. The necessary results include the force-deflection and force-CMOD (Crack Mouth Opening Displacement) responses. An aluminium frame was fitted to the specimens keeping four 10mm LVDTs in position to measure the vertical displacement of the beam next to the notch. At the tip of the notch a 10mm LVDT was fitted either side of the beam to measure the CMOD. The load was measured with the load cell of the Zwick Z250 testing machine. The test setup is shown in Figure 3.5.

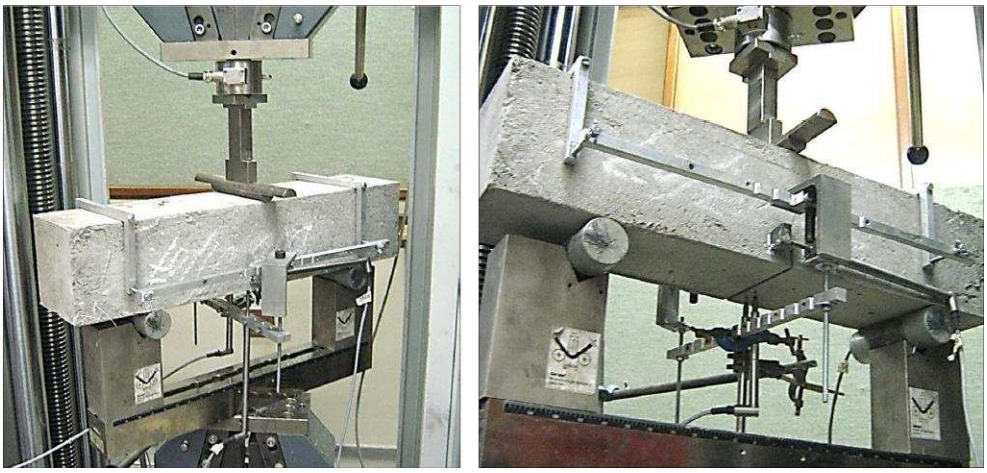

Figure 3.5 3PBT setup in Zwick Z250 Universal Material Testing Machine.

The test was performed using position control, with the Zwick's crosshead moving at a constant rate of 2mm/min. The steel fibres are activated once cracking commences and therefore the post-peak responses would provide a good indication of each SFRC member's performance. The test was stopped when the CMOD was around 10mm to ensure a well defined post-peak response.

3.2. Compressive characteristics

As previously mentioned, six cylinders of each SFRC member were tested to acquire a representative compressive material behaviour. The specimens were cast using two mixes per SFRC member, thus producing two batches.

The parameters utilised for the determination of the compressive characteristics is shown in Figure 3.6.

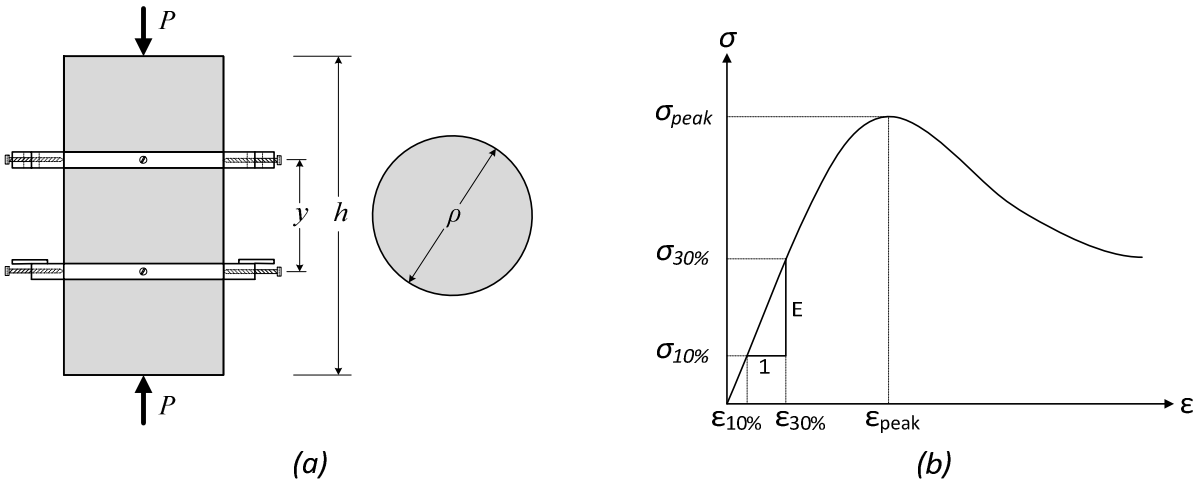

Figure 3.6 (a) Schematic representation of the fixed LVDT frame; (b) Illustration for E-modulus calculation.

3.2.1. Test Results

3.2.1.1. Compressive Stress-Strain Relations

The compressive stress-strain results for the specimens of each SFRC member are shown in Figure 3.7 and Figure 3.8.

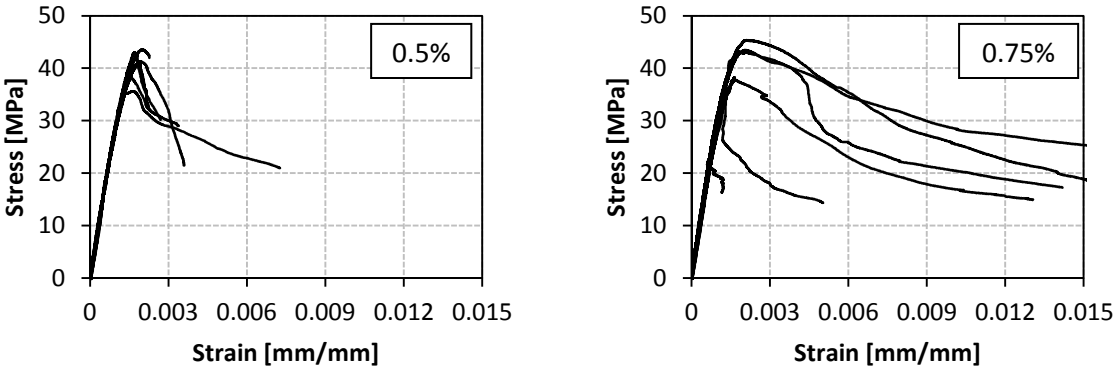

a) *b*)

Figure 3.7 Compressive stress-strain responses for a) 0.5% steel fibres and b) 0.75% steel fibres.

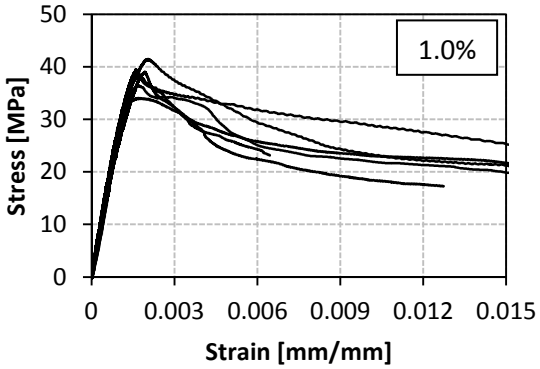

Figure 3.8 Compressive stress-strain responses for 1.0% fibres.

Table 3.3 summarises the compressive characteristics that are of most importance for the aim of this project. The shape of the curves also come into play and is discussed in the next section.

Table 3.3 Summary of compressive results.

	0.5% Fibres		0.75% Fibres		1.0% Fibres	
	AVE [MPa]	**COV [%]**	**AVE [MPa]**	**COV [%]**	**AVE [MPa]**	**COV [%]**
σ_{peak} **[MPa]**	40.4	7.4	41.8	7.4	38.1	6.8
ε_{peak}	0.00178	10.1	0.00185	10.5	0.00178	9.8
***E* [GPa]**	31.5	4.9	32.9	3.9	28.9	5.4

The crushing values of the cylinders are closely distributed for each SFRC member. The coefficient of variance (COV) for each mix is consistent at about 7% of the average value. There is also little difference in the average peak crushing values, σ_{peak}, among all three members with an average of 40.1 MPa. Nataraja (1999) and Fanella (1985) found that the strain values at the peak stresses

increase with an increase of the fibre content. This phenomenon was not observed with the test results, as the strain values at the peak load were relative constant with an average of 0.0018. The value of the Young's Modulus for each member is also closely distributed with an average of 31.1GPa.

The normalised stress-strain curves of typical representative compressive behaviours for all three members are illustrated in Figure 3.10. Nataraja *et al*. (1999) found that the toughness increased with a higher amount of fibres. The values of the toughness index for the 0.5% SFRC, 0.75% SFRC and 1.0% SFRC are 1.3, 4.0 and 6.3, respectively. These values were calculated according to the description provided in Section 2.1.3.2. From the results it is evident that the slope of the curve in the post-peak region decreases with an increase in amount of fibres, resulting in an increased ultimate strain value.

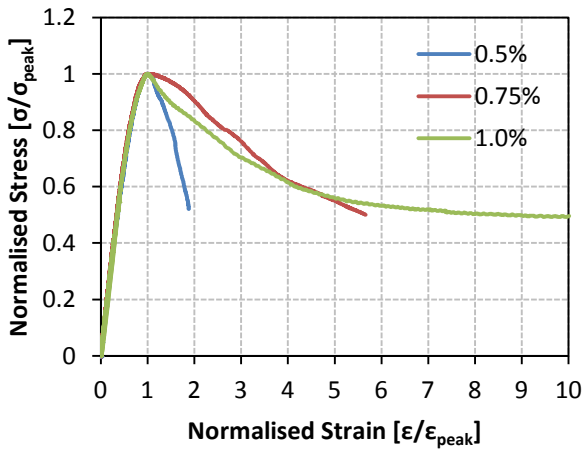

Figure 3.10 Normalised stress-strain graphs for all three SFRC members.

3.2.2. Model Parameters

The compressive model characteristics were derived using a best fit for each SFRC member. The derived compressive responses are illustrated in Figure 3.11. A summary of the model parameters at the peak stress value for each member is provided in Table 3.4. These curves will be utilised in the theoretical models that are discussed later in this report.

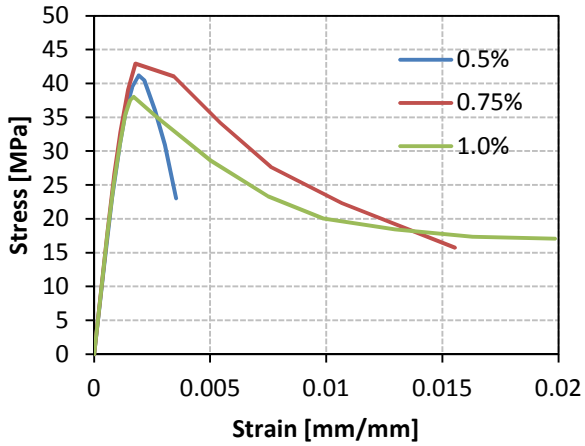

Figure 3.11 Final compressive response for each SFRC member.

Table 3.4 Summary of model parameters at the peak stress.

Fibre %	***σ_{peak} [MPa]***	***ε_{peak} [mm/mm]***	***E-Modulus [GPa]***
0.5	41.2	0.00216	30.1
0.75	42.9	0.00179	31.6
1	38.0	0.00170	31.2

3.3. Flexural characteristics

Just as for the compressive tests, a total of six specimens were produced from two batches for each SFRC mix. The force-displacement relations from the three point bending tests are illustrated in the next section.

3.3.1. Test Results

The increase in the flexural capacity is noticed when comparing the forces and displacements at the peak loads among the SFRC members (Figure 3.13). The post-peak behaviour has a major role in defining the material behaviour, with the shape of the curve having the largest influence. The first observation from the force-displacement curves is that all three members present deflection-softening behaviour. The second observation is that the peak load increased with larger fibre content, with the 1.0% SFRC having a peak load that is twice that of the 0.5% SFRC. The average peak

load values are 23.2kN, 40.5kN and 46.7kN for 0.5%, 0.75% and 1.0% SFRC, respectively. This increase in capacity is due to an increase in tensile reinforcement. As seen in Table 3.5, the average midspan displacement (Δ_{crack}) and CMOD at crack formation was about the same among all three members, but there was a slight increase in the average cracking force (P_{crack}) for an increased volume fibres.

Another result that indicates the improvement of the flexural capacity is the substantial increase of the crack width and midspan displacement at the peak load with an increase in the fibre content. The average values for the CMOD at the peak load is 0.7mm, 1.0mm and 1.15mm for the 0.5% SFRC, 0.75% SFRC and the 1.0% SFRC, respectively. An increase in volume fibres result in the absorption of more energy by the SFRC member during the crack initiating and crack developing phase, resulting in an increased crack width at the peak load. This is also found for the midspan displacement at the peak load, with the average values being 0.76mm, 1.09mm and 1.27mm for the 0.5% SFRC, 0.75% SFRC and 1.0% SFRC, respectively.

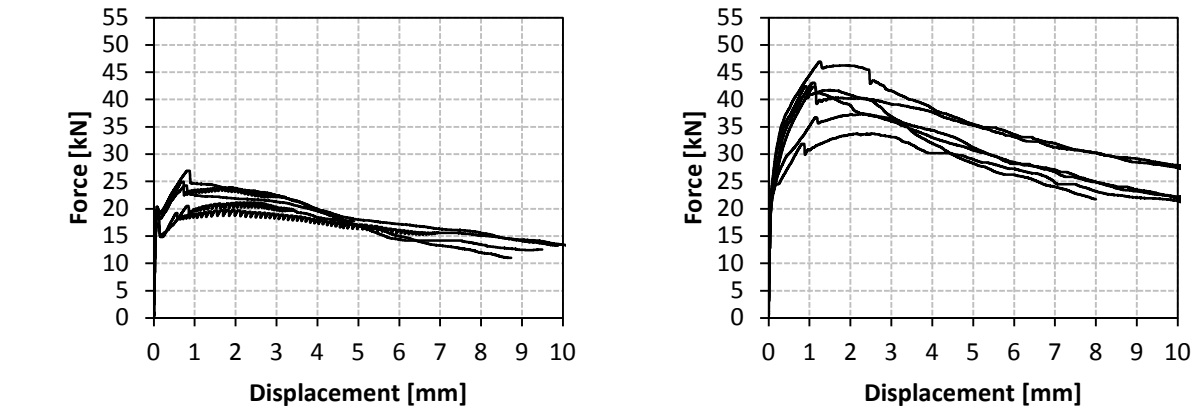

a) *b*)

Figure 3.12 Force-displacement responses for beams with a) 0.5% fibres and b) 0.75% fibres.

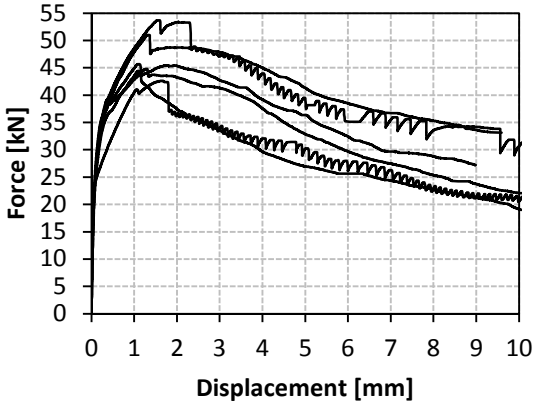

Figure 3.13 Force-displacement responses for beams with 1.0% fibres.

Table 3.5 Summary of flexural test results.

	0.5% Fibres		0.75% Fibres		1.0% Fibres	
	Average	**COV [%]**	**Average**	**COV [%]**	**Average**	**COV [%]**
P_{crack} [kN]	19.21	6.7	21.75	6.8	23.18	7.8
Δ_{crack} [mm]	0.09	15.7	0.06	12.0	0.07	12.0
$CMOD_{crack}$ [mm]	0.041	29.4	0.027	23.1	0.034	20.6
P_{peak} [kN]	23.15	14.1	40.50	13.2	46.69	9.9
Δ_{peak} [mm]	0.76	15.8	1.09	14.3	1.27	16.0
$CMOD_{peak}$ [mm]	0.696	15.6	0.999	12.1	1.148	12.2

In Figure 3.14 the representative flexural response for each SFRC member is shown. These force-displacement curves will be used as the parameters for the inverse analysis procedure that is discussed in the next section.

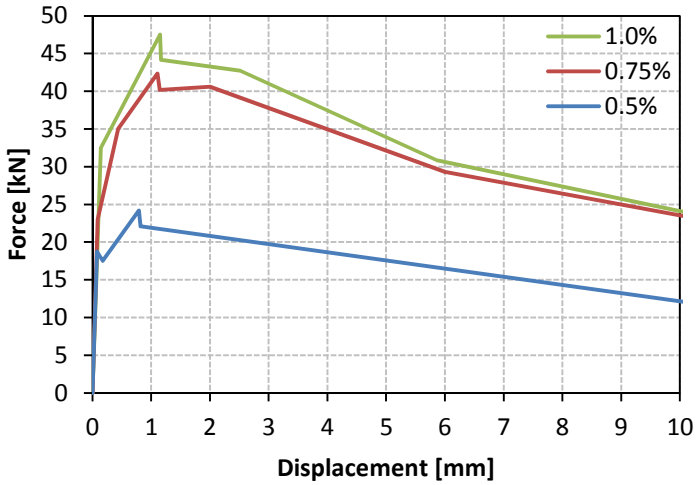

Figure 3.14 Representative flexural responses for all three SFRCs.

It was observed that crushing occurred in the compression zone of the specimens for the 0.75% SFRC and 1.0% SFRC. It is uncertain when the crushing occurred in the duration of the test, but it is valuable to know that an increase in the fibre content resulted in a compressive failure. This would explain why the relative small increase of the flexural capacity was found with the 1% volume fibres compared to the 0.75% volume fibres.

3.3.2. Crack band width and plastic hinge length

The crack band width (CBW) is the distance (*s*) between pure flexural cracks and can be measured by performing four point bending tests on flexural members. In this thesis it is used to calculate specific strain values utilised in the inverse analyses (Section 3.4) and the theoretical models (Chapter 4). As mentioned in the background study, theoretical models have been derived to calculate the plastic hinge length for reinforced concrete structures. No published results were found that correspond to these characteristics for fibre reinforced concretes and assumptions had to be made.

According to the FIB Model Code (FIB, 2010) the plastic rotation for conventionally reinforced concrete structures should be calculated across a distance of 1.2 times the height of the section, *h*. As Figure 3.15 illustrates, the rotation should be calculated over a distance that is 0.6*h* to each side of the critical section.

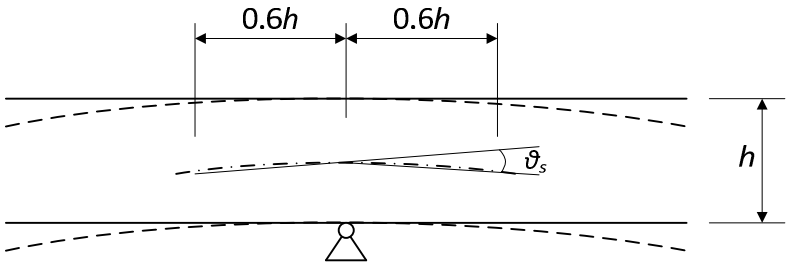

Figure 3.15 Plastic rotation ϑ_s of reinforced concrete sections for continuous beams and continuous one way spanning slabs (FIB Model Code (2), 2010: 13).

Taking these values into consideration it was decided to apply the assumptions proposed by Löfgren (2005), which considers the crack band width and the plastic hinge length to have a value of the half the specimen height, *h*.

3.4. Tensile characteristics

3.4.1. Inverse Analysis

As mentioned in the description of the flexural test setup, an inverse analysis is conducted with the results from the flexural tests to characterise the uni-axial tensile response. An Inverse Analysis consists of an iterative procedure which fits experimental data in order to obtain the parameters

that define an assumed shape for the constitutive diagram. A schematic diagram of the procedure is shown in Figure 3.16.

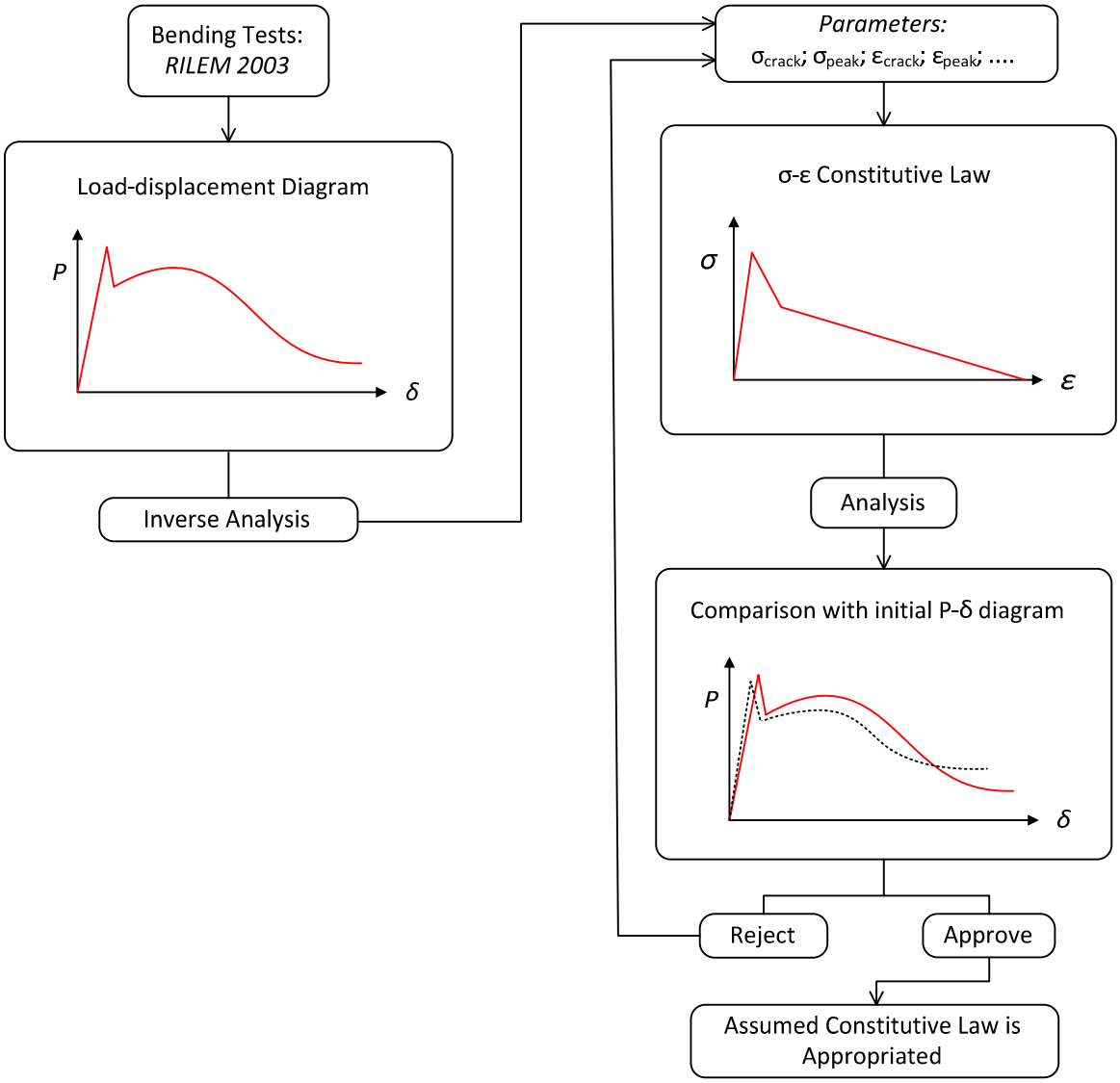

Figure 3.16 Schematic procedures associated with the Inverse Analysis.

The inverse analysis was performed by modelling the three point bending test with a tensile stress-strain response that is adjusted until the numerical load-displacement result concurs with that of the experimental results. This analysis was conducted using the finite element analysis software, TNO DIANA 9.3 (2008). The main objective was to determine the uni-axial tensile response with the assumed values for the crack band width and plastic hinge length.

3.4.2. Crack band width

The crack band width (*s*) affects the determination of the assumed tensile stress-strain response. The three point bending test is a statically determinate setup, with the beam requiring only a single hinge to develop for failure to commence. The beams are notched to ensure the position of crack formation. Referring to the load-displacement curves of Section 3.3, it was noticed that when cracking initiates the slope of the curve decreases, but the specimen's capacity was only reached when the crack has fully developed. After this point, the only further deformation occurring is crack widening. The only way to relate CMOD with a corresponding strain is by dividing the crack opening values with the crack band width. Before cracking occurs, the material remains elastic and the strain is calculated with

$$\varepsilon = \frac{\Delta x}{x} \tag{3.1}$$

with Δx the displacement measured over the gauge length, x. x is the distance over which the applicable deformation occurs. Theoretically, rigid body rotation occurs after the crack is fully developed, implying that the crack only widens. This implies that the gauge length across the crack (x) is equal to zero, which indicates an infinite strain. Recognising that a flexural crack should develop at an average spacing, s, it is assumed that the development of the crack is distributed across this distance, which theoretically enables the calculation of a pseudo strain value. This concept is shown in Figure 3.17, where the crack width (w) is converted to a corresponding strain value.

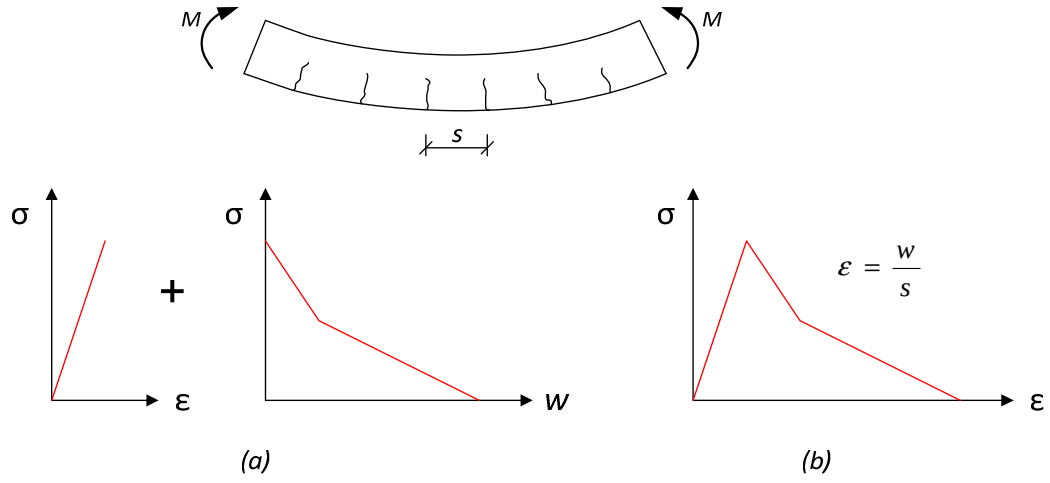

Figure 3.17 (a) Stress-crack width (σ-w) and (b) stress-strain (σ-ε) affiliation.

3.4.3. FEM Model

This section provides a full description of the model, including the necessary assumptions that had to be made. The aim was to create a model representative of the actual test to ensure the compatibility of the experimental and numerical results. A two-dimensional (2D) plane stress model was used.

3.4.3.1. Geometry

Due to certain constraints of the finite element procedure it was required to introduce small alterations to certain geometric aspects in order to produce a realistic representation. The beam is modelled to have a total length of 712.5mm with a cross-sectional dimension of 150mmx150mm. The span length was 462.5mm with the notch depth and notch width, 25mm and 12.5mm, respectively. A layout of the finite element model is shown in Figure 3.18.

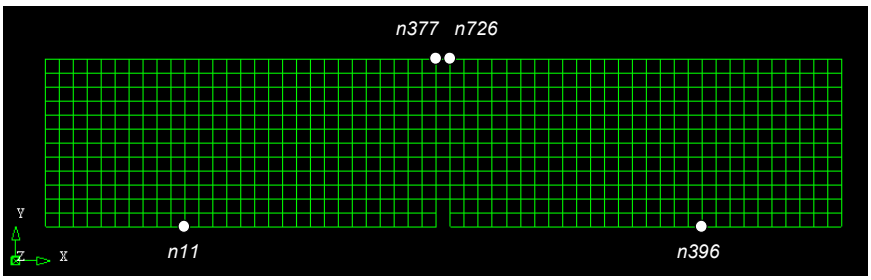

Figure 3.18 Layout of FE model.

3.4.3.2. Elements and Meshing

The beam is modelled with 2D plane stress elements. It is a four-node quadrilateral isoparametric plane stress element, which is based on linear interpolation and full Gauss integration. The element size is chosen to fit the geometry such that the boundary conditions could be applied at the correct positions. The computation time and accuracy of the results were also taken into consideration. Three element sizes were considered, 5mm, 12.5mm and 25mm square elements. Accurate results were obtained with the 5mm and 12.5mm elements, whilst the analysis procedure was prolonged with the 5mm elements (Figure 3.19). Considering the iterative procedure of the inverse analysis, it was decided to use the 12.5mm elements.

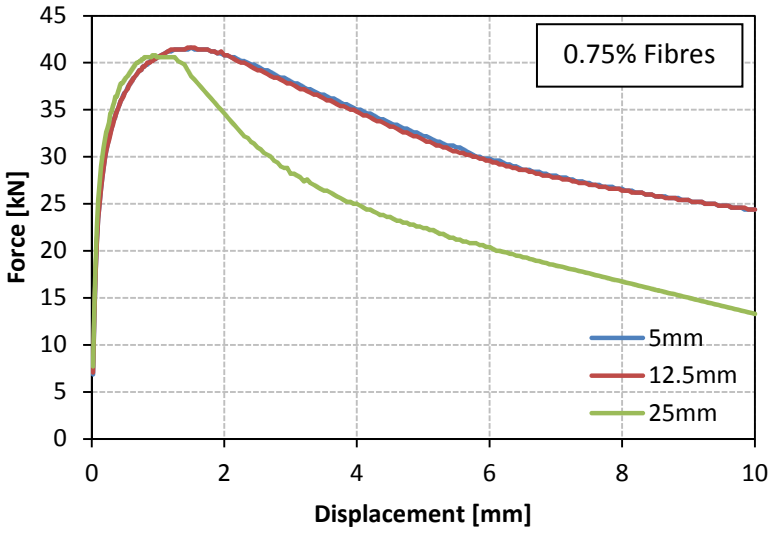

Figure 3.19 Comparison of load-displacement results obtained from different element sizes for the 0.75% SFRC mix.

3.4.3.3. Boundary Conditions

After meshing, the nodes that correspond with the bottom supports were constrained in the y-direction, allowing the beam to displace along the x-direction. At the top of the beam two nodes were constrained in the y-direction to represent the loading position for the displacement-controlled procedure.

3.4.3.4. Material Properties

An applicable material model was selected according to the following criteria.

- It should be compatible with plane stress elements.
- It should be able to describe the compressive and tensile material properties accurately.
- The compressive and tensile responses should be able to interact with one another.

The Total Strain Crack Model (TNO DIANA, 2008) meets the proposed criteria. The model is subdivided into a Fixed- and Rotating crack model. The Rotating crack model can be described as the coaxial stress-strain concept, in which the stress-strain relationships are evaluated in the principal directions of the strain vector. The Fixed crack model can be explained as a fixed stress strain

concept in which the stress-strain relationships are evaluated in a fixed coordinate system, which is fixed upon cracking (TNO DIANA, 2008). Both models were considered and it was found that the Rotating crack model acquired the convergence criteria faster in addition to conservative results.

The possible shape of the material response curves is shown in Figure 3.21 and Figure 3.22. The multi-linear approach provides the shape that ensures the best correlation with the actual material behaviour. For the compressive behaviour the results presented in Figure 3.10 were used as the input data, with the exception that the post-peak curve has a constant value at the peak strength. The size of the fracture zone influences the definition of the numerical post-peak response and is unknown in this case.

The multi-linear tensile response is adjusted until the numerical and actual load-displacement curves fit. The initial slope of the stress-strain relation until cracking is chosen to be the same as for the compressive behaviour. The pseudo strain value corresponds with the post-peak tensile response, as this region is equivalent to crack widening across a specific crack band width. According to DIANA the crack band width for the tensile material behaviour is considered to be the element size, as a crack can only develop in a single column of elements. The final point on the tensile stress-strain curve is chosen to be a zero stress, which corresponds with a CMOD of half the fibre length (shown in Figure 3.20). In this case the element size is 12.5mm and the assumed pullout length is 30mm, which corresponds with a pseudo strain of 2.4mm/mm. This pseudo strain value was calculated with $\varepsilon_{final} = \frac{CMOD}{CBW}$, with CBW equal to the default value according to DIANA.

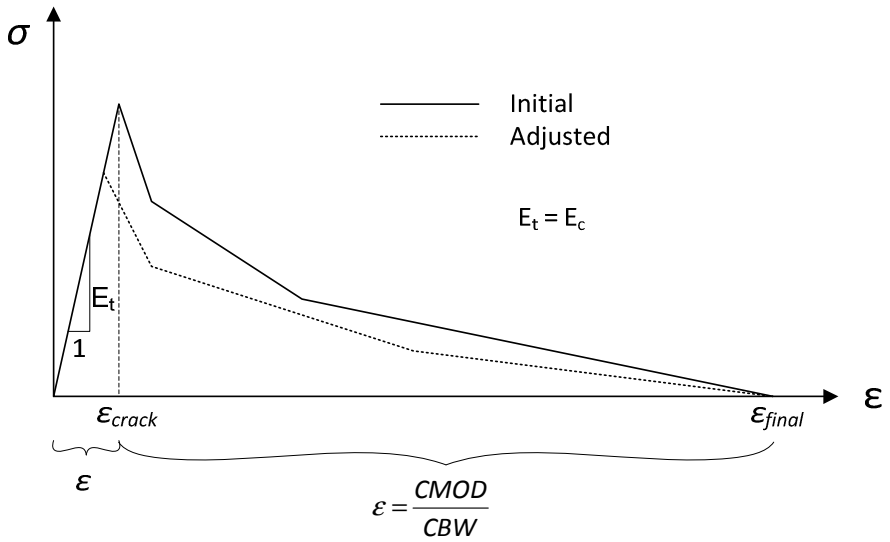

Figure 3.20 Tensile response calculation procedure.

Other factors such as the poisson ratio and the material density were taken to be 0.2 and 2400kg/m^3, respectively. It is important to note that the obtained post-peak uniaxial tensile response corresponds with a crack band width of the element size, which is 12.5mm. Thus, to obtain the real uniaxial tensile response it is necessary to convert the post-peak response with a more realistic crack band width, which corresponds with the actual structure. For this thesis the real crack band width is assumed to be half the section height, which is 62.5mm. Therefore, the real post-peak tensile response should be calculated by dividing the CMOD by the new crack band width.

DIANA assumes a default crack band width (h) that is related to the elements used. For linear two-dimensional elements this characteristic is $h = \sqrt{2A}$ and for higher order two-dimensional elements, $h = \sqrt{A}$, with A the total area of the element. Theoretically this characteristic is considered after the peak stress value has been reached on the either stress-strain diagram, as this corresponds with fracture.

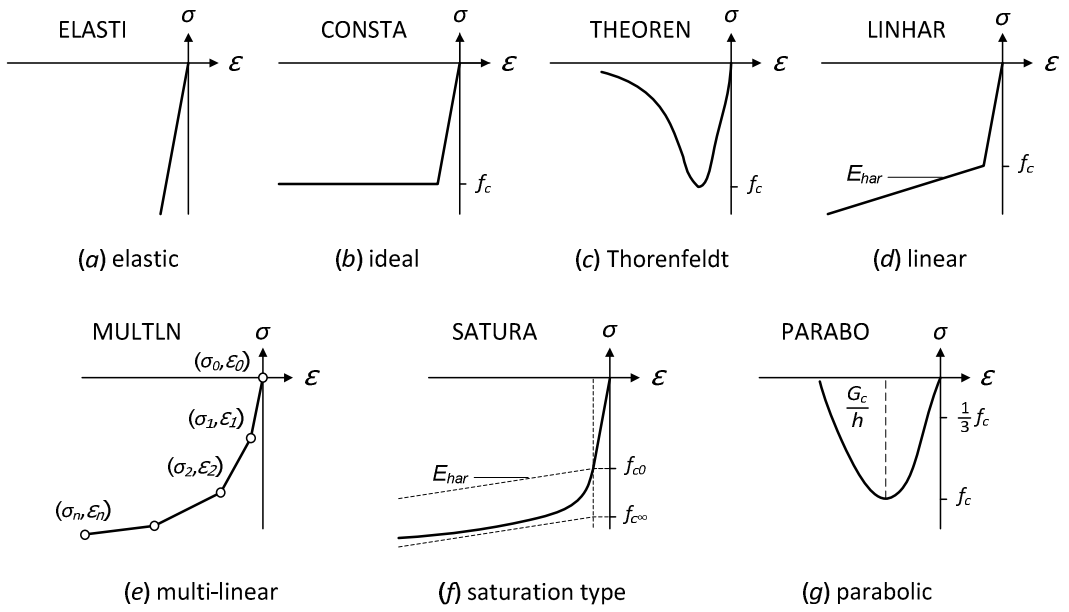

Figure 3.21 Predefined compression behaviour for Total Strain model (TNO DIANA, 2008).

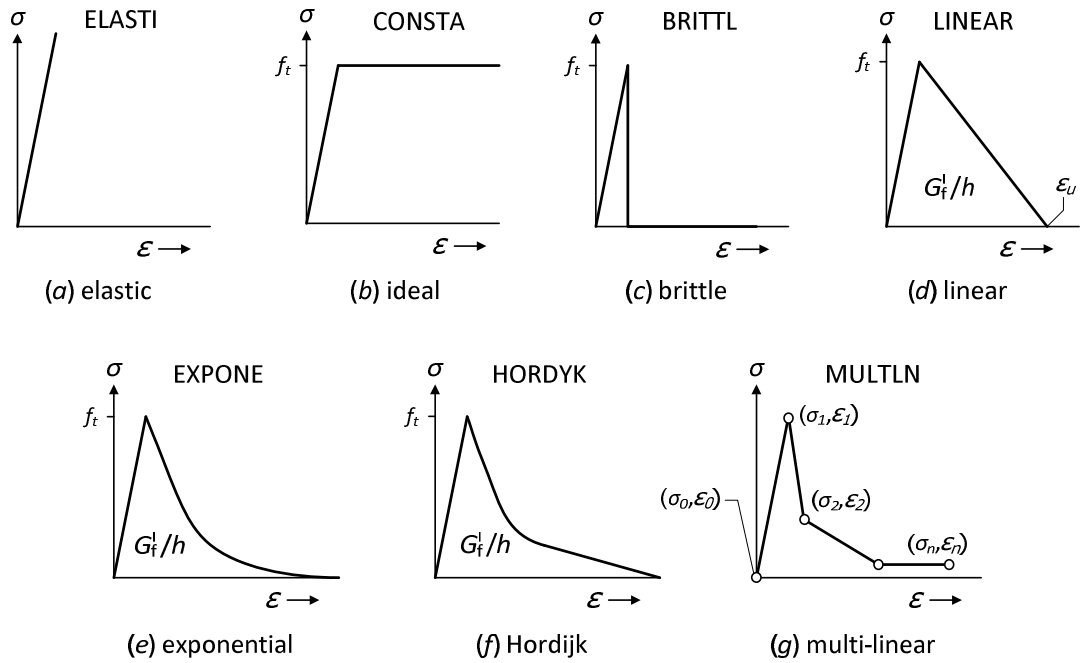

Figure 3.22 Predefined tension softening for Total Strain model (TNO DIANA, 2008).

3.4.3.5. Analysis Procedure

At the centre of the beam two nodes at the loading positions were prescribed to displace a total of 10mm downwards with a displacement-controlled procedure. This prescribed displacement was applied with small increments until a total displacement of 1mm had been reached and followed with larger load steps until the nodes have displaced 10mm.

The iteration procedure was executed with the Regular Newton-Raphson method. The method yielded a quadratic convergence characteristic, which enables the method to converge to the final solution within a few iterations.

3.4.3.6. Results

The following load-displacement results (Figure 3.23) correspond with the choice of the final tensile response (*Figure 3.24*).

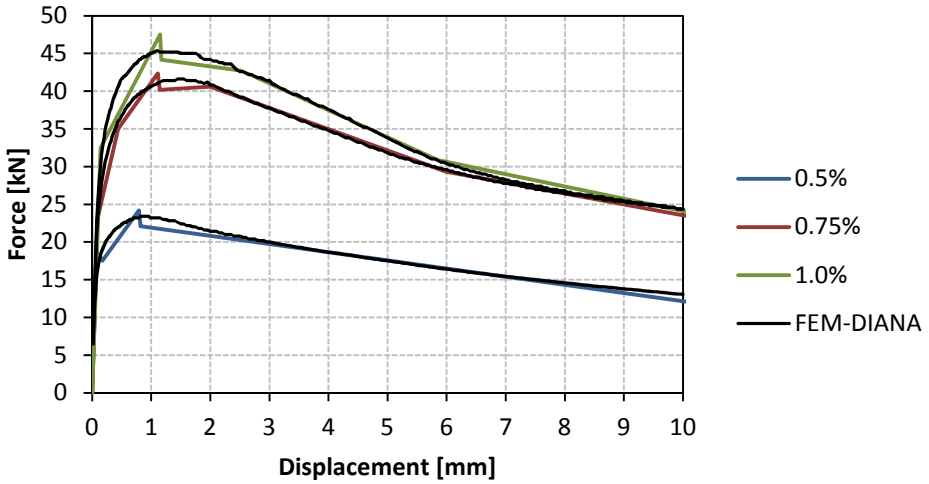

Figure 3.23 Comparison between DIANA and experimental force-displacement graphs.

The representative load-displacement (*P-δ*) curves served only as a guideline and it was not necessary to obtain a perfect fit. The numerical load-displacement response curves were obtained with the load calculated as the summation of the reaction forces at the supports, and the total displacement the average between the displacements of the nodes at the top. The displacement at the notch was also considered, as this corresponds with the measuring position in the actual test setup. The load-displacement results for both procedures were similar and it was decided to utilise the displacement at the loading position.

The criteria for the representative numerical load-displacement response were based on

- The shape of the curve
- The peak load value
- The initial slope of the curve

The proposed load-displacement curves correlated well with those predicted by DIANA (Figure 3.23). The peak load was modelled to correspond with the proposed peak displacement. The criteria for the shape of the curve prevented the possibility to fit the curve to the proposed peak load, but this induced a conservative approach. For the 0.5% SFRC member, the cracking force was slightly underestimated in order to fit the curve. This deviation would have a major effect on certain aspects, and is discussed at a later stage.

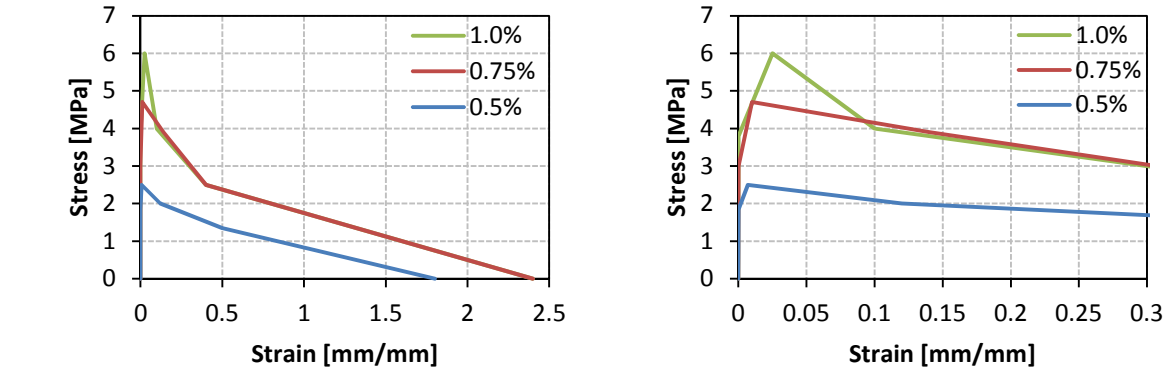

a) *b*)

Figure 3.24 Final Tensile response for DIANA; a) Full response, b) Partial response.

As shown in Figure 3.24, the increase in volume fibres induced an increase in the tensile resistance. The tensile curves were best represented with a multi-linear curve consisting of six data points. The material behaviour depicts a hardening effect subsequent to crack initiation. The increase in the cracking- and peak stresses (σ_{crack} and σ_{peak}), as well as its corresponding strain values (ε_{crack} and ε_{peak}), resulting from the addition of fibres, is indicated in Table 3.6. It is observed that the 0.75% and 1.0% SFRC members have similar tensile responses, except for the increased peak stress value and corresponding strain, for the latter. The shapes of the responses are similar with an exception of the hardening region of the 1.0% SFRC member, due to a much larger strain value at the peak stress.

Table 3.6 Tensile Characteristics.

Fibre %	σ_{crack} **[MPa]**	ε_{crack} **.10^{-3}[mm/mm]**	σ_{peak} **[MPa]**	ε_{peak} **[mm/mm]**
0.5%	1.85	0.0615	2.5	0.007
0.75%	3	0.0949	4.7	0.01
1.0%	3.8	0.1218	6	0.025

3.4.4. Model parameters

The tensile responses obtained in the previous section are related to the default crack band width assumed by the finite element software. The real uni-axial tensile behaviour is derived utilising the proposed actual crack band width. The height above the notch is considered to be the cracking surface resulting in the crack band width to be calculated as

$$s = \frac{h}{2} = \frac{125}{2} = 62.5mm$$

It was assumed that the CMOD increased after the peak stress has been reached, thus when the crack has fully developed. In this case the crack is forced to initiate at the notch, which is not always the case for real structures. The following procedure is performed:

- The theoretical CMOD is calculated with, $CMOD_{theor} = \varepsilon . s_{DIANA}$
- The theoretical strain applicable for the specimen is calculated with, $\varepsilon_{theor} = \frac{CMOD_{theor}}{s}$

The final result for the tensile behaviour relating to a physical specimen is shown in Figure 3.25.

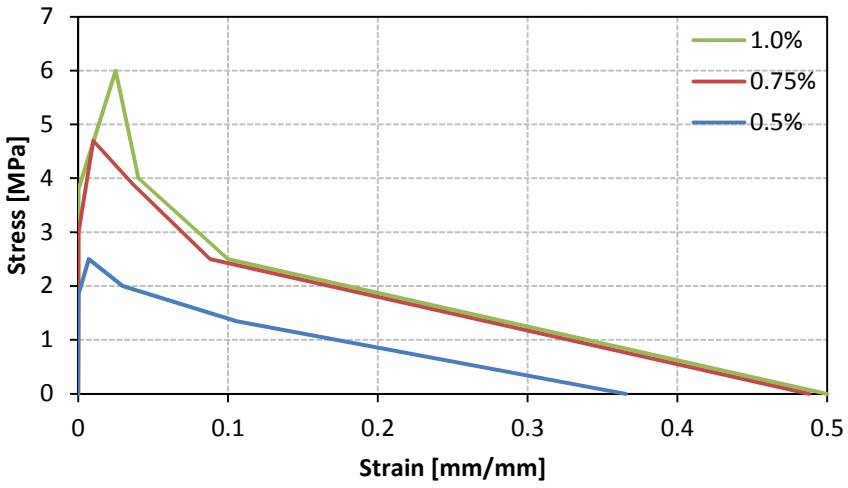

Figure 3.25 Final tensile response for each SFRC member.

3.5. Concluding remarks

From the experimental tests it was found that the SFRC members with different volume of fibres presented similar compressive characteristics in relation to the material stiffness and ultimate strength, but the toughness of the SFRC members increased with the increase of the volume of fibres. The final uniaxial tensile behaviours were determined with inverse analyses and the results indicated similar tensile response curves with increased tensile resistances for the SFRC members with larger volume fibres. The obtained uniaxial material behaviour is important in the next chapter where it is utilised in sectional analyses to provide representative moment-curvature responses.

CHAPTER 4

MODELLING MOMENT REDISTRIBUTION

Moment redistribution is a structural phenomenon which is dependent on the distribution of forces in a statically indeterminate structural member. The ability of a member to distribute forces depends on the flexural stiffness of the member and the rotation capacity at the plastic hinges. The flexural behaviour of a member can be derived via a sectional analysis, which provides a moment-curvature relationship for a cross-section.

In this chapter the flexural response of each SFRC type is evaluated by deriving the moment-curvature relations and developing a theoretical moment-rotation model that represents the rotational behaviour at the plastic hinges.

The background theory of a sectional analysis is provided to demonstrate the general concept of the moment-curvature relationship. This is followed with the approach developed to consider the material law. The derived moment-curvature relations form the basis of the theoretical models that follow, with the main objective the development of the moment-rotation model. The moment-curvature relations are implemented in finite element analyses of a representative statically indeterminate structure. The computational results are compared with the derived moment-rotation model and the possibility of moment redistribution is verified. Also the amount of moment redistribution is related to the rotational values at the hinges.

4.1. Section analysis model

4.1.1. Theory

As shown in Figure 4.1, it is assumed that Δx is infinitely small so that it is representative of a cross section. It is also assumed that a bending moment is applied at the ends of this infinitely small region without any externally applied axial force. Thus, this induces a curvature (κ) that is associated with that applied moment.

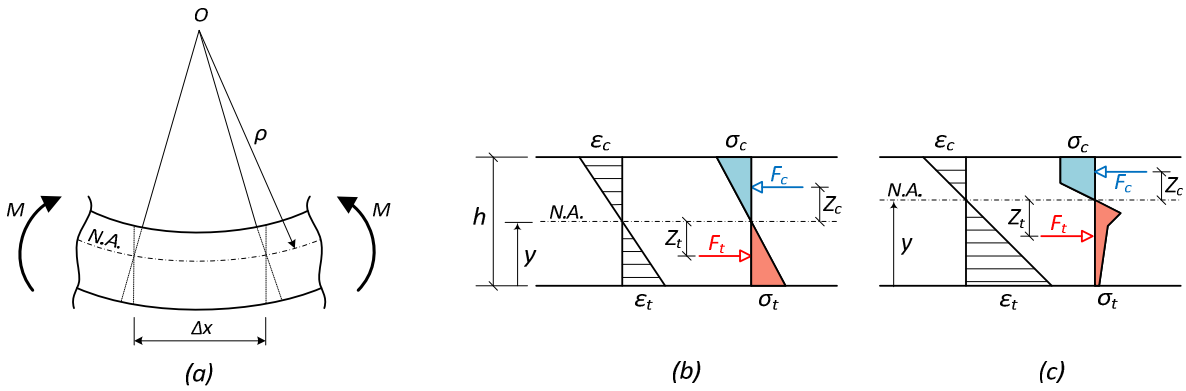

Figure 4.1 Schematic representation of internal stresses.

From first principles it is known that

$$\kappa = \frac{1}{\rho} \tag{4.1}$$

and

$$\varepsilon = \frac{-y}{\rho} = -\kappa y \tag{4.2}$$

This relation states that the strain at a certain point in the cross-section varies linearly with the distance from the neutral axis. This relation is derived for a cross section with the y-axis positively defined in the upward direction and the origin at the neutral axis (*NA*). From Equation 4.2 it is evident that the strain would yield a negative value at the top of the bending element, which is representative of a compression zone and vice versa.

The stress distribution across the section can be described by relating the material's stress-strain relation with the section height. The neutral axis defines the position of zero bending stress in the cross-section. The position of the neutral axis is calculated mathematically with an equilibrium equation of the internal forces in the x-direction.

$$F_t = \int \sigma_t dA_t \tag{4.3}$$

$$F_c = \int \sigma_c dA_c \tag{4.4}$$

$$\sum F_x = \sum F_t + \sum F_c = 0 \tag{4.5}$$

In the case of an elastic material, e.g. Figure 4.1 b), the tensile and compressive stress distributions are the same, resulting in a neutral axis that is positioned at the centre of the cross-section. In Figure 4.1 c) the stress distributions differ for tension and compression, which induces a shift in the neutral axis position. The bending moment (*M*) value which corresponds with the stress distribution due to the induced curvature is calculated as the summation of the forces in the x-direction multiplied with the applicable moment arms (*Z*) about the neutral axis.

$$M = \sum F_t Z_t + \sum F_c Z_c \tag{4.6}$$

From these calculations it is possible to relate the internal bending moment with the corresponding curvature, which produces a single point on the desired moment-curvature diagram. The total moment-curvature relation is determined with an iterative procedure, where the curvature is increased and the corresponding bending moment values calculated.

4.1.2. Numerical solving of section with a spreadsheet

The following assumptions were made to develop the required sectional analysis:

- The neutral axis depth is measured towards the extreme tensile fibre.
- The compression and tension regions are considered separately and the stress-strain behaviours for both are considered to be positive.
- The following units were utilised in this analysis; the distance in *m*, forces in *kN*, stresses in *MPa* and bending moment in *kNm.*
- The calculations are only applicable with rectangular cross-sections.

The sectional analysis procedure is as follows:

1. Prescribe the stress-strain relation for the uniaxial compressive and tensile behaviour.
2. Specify the desired curvature value.
    a. The material law is converted to a stress-section depth (σ-y) relationship.
    b. Internal forces are calculated.
3. Use a numerical solver to adjust the neutral axis depth (NAD) to ensure the equilibrium of the forces.
    a. The moment arms are calculated.
    b. The applicable bending moment is calculated.
4. Steps (2) through (3) are repeated until an adequate number of data points are available to provide a representative moment-curvature relationship.

4.1.3. Results

The resulting moment-curvature relationships provide an indication of the sectional ductility and it can be used to derive member ductility or be utilised as input for finite element analyses.

These responses were derived for a cross-sectional area with the width 250mmm and the height 125mm. The specimen is seen as part of a one way spanning slab. The height was chosen to be the same as that of the beams that were tested in the three point bending tests, to eliminate the possible 'size effect'.

The moment-curvature responses are compared with one another, as shown in Figure 4.2. The ultimate curvature is chosen to be 2 [1/m], as this produced an extensive post-peak response. The sectional analyses produced curves with similar shapes for the three SFRC types, with the magnitude of the bending capacity increasing with an increase in the volume fibres. It is also noticed that the curvature value at the peak bending moment increased with an increase in the volume fibres. For an increase in volume fibres the curves are also characterised with a more rapid decrease in the bending capacity at the post-peak region.

The most important moment-curvature characteristics are presented in Table 4.1. These values are used to compare the section ductility and section capacity among the different SFRC members.

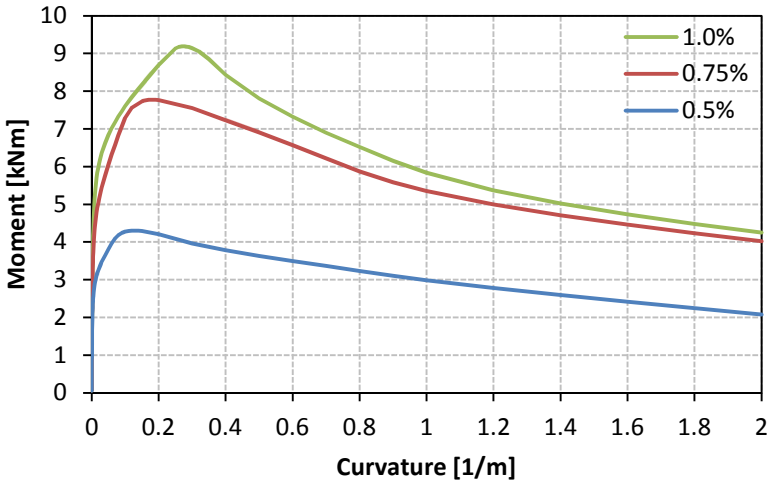

Figure 4.2 Theoretical derived moment-curvature relationships for the three SFRC mixes.

An indication of sectional improvement is calculated as ratios with the 0.5% SFRC characteristics utilised as the base values. The ratios were calculated for the characteristic moment values, M_{crack} and M_{peak}, as well as for the sectional ductility ($\Delta\kappa$). As shown in Table 4.1, the sectional characteristics due to the addition of fibres improved in the range of 58% to 75% for the 0.75% SFRC and 114% to 128% for the 1.0% SFRC members. The increase in the ductility is shown in Figure 4.3, with the $\Delta\kappa$ values normalised. This provides a better perspective on the improvement rate of the sectional characteristics in relation to the volume fibres used.

The following equations were used to calculate the ratios:

Moment ratios:

$$Ratio = \frac{M_i}{M_{0.5\%}} \tag{4.7}$$

Sectional ductility:

$$\Delta\kappa = \left(\kappa_{peak} - \kappa_{crack}\right) \tag{4.8}$$

Sectional ductility ratio:

$$Ratio = \frac{\Delta\kappa_i}{\Delta\kappa_{0.5\%}} \tag{4.9}$$

Table 4.1 Theoretical moment-curvature characteristics.

	CRACKING			ULTIMATE			DUCTILITY
Fibre %	M_{crack} [kNm]	κ_{crack} [1/m]	$M_i/M_{0.5\%}$	M_{peak} [kNm]	κ_{peak} [1/m]	$M_i/M_{0.5\%}$	$\Delta\kappa_i/\Delta\kappa_{0.5\%}$
0.5	1.1	0.0009	*1.0*	4.3	0.12	*1.0*	*1.0*
0.75	1.93	0.0015	*1.75*	7.77	0.19	*1.81*	*1.58*
1.0	2.41	0.0019	*2.19*	9.19	0.274	*2.14*	*2.28*

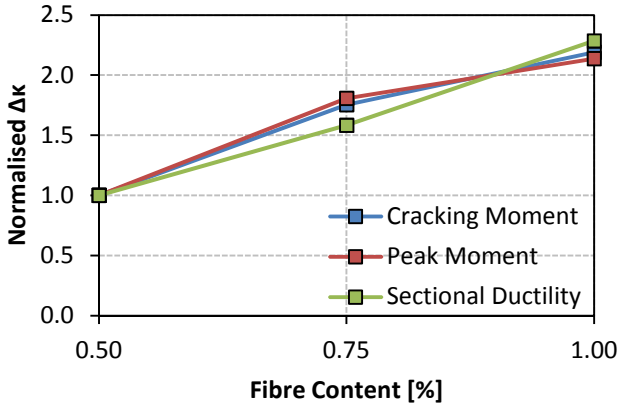

Figure 4.3 Comparison of sectional ductility normalised to 0.5% SFRC.

Figure 4.4 presents the development of the neutral axis depth with increasing curvature. The results indicate a decrease in the ultimate NAD with an increase in volume fibres. This is ascribed to the smaller crack development rate with an increase in volume fibres. This was also observed with the three point bending tests, where the crack path became crooked due to larger fibre content, opposed to a straight crack.

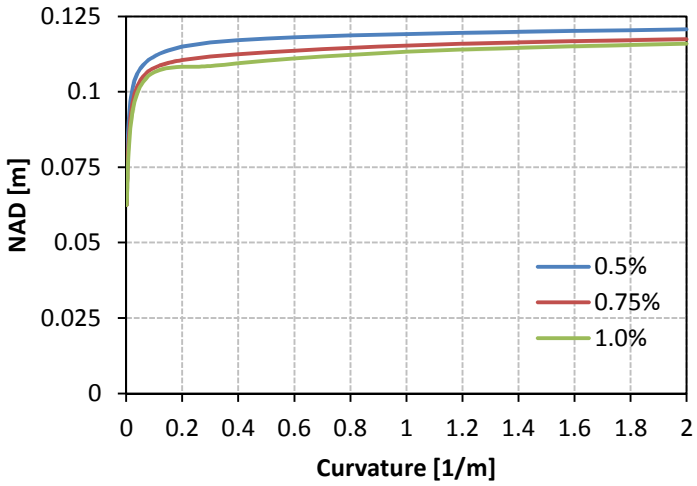

Figure 4.4 Theoretical NAD-curvature relationships.

4.2. Moment-rotation model

The moment-rotation behaviour describes the structural behaviour of a flexural member in the process of hinge development. It provides an indication of the bending capacity and member ductility. The derivation of an accurate moment-rotation model is deemed difficult due to specific assumptions made to approximate real structural behaviour, e.g. crack formation, hinge lengths, etc. Therefore, the method discussed in Section 2.3.4 is deemed incompatible with the available information. The approach is simplified to a 'Rigid Body' rotation model, with the proposed concept shown in Figure 4.5.

It is uncertain how many cracks would develop in the plastic hinge, but a universal comparison method is developed by assuming that a single crack develops in the plastic hinge region, which induces the rotation of two 'rigid bodies' about the plane of the crack. For this model, the material characteristics is utilised in accordance with previously obtained moment-curvature data to predict the crack mouth opening displacement of a single crack, which is implemented to simulate rigid body rotation. Therefore the proposed moment-rotation model predicts the structural behaviour in relation to only the material characteristics. This allowed for the comparison of the member ductility among the different mixes based on only the different material characteristics.

4.2.1. Rigid body rotation model

As mentioned, this is a simplified approach implementing specific assumptions, which are listed below.

- A single crack forms in the plastic hinge region.
- The plastic rotation (ϑ_p) has the value of the rotation about the plane of the crack to one side of the crack.
- The crack band width (s) is equal to half the section height for all three composites.
- The plastic hinge length (L_p) is equal to half the section height.

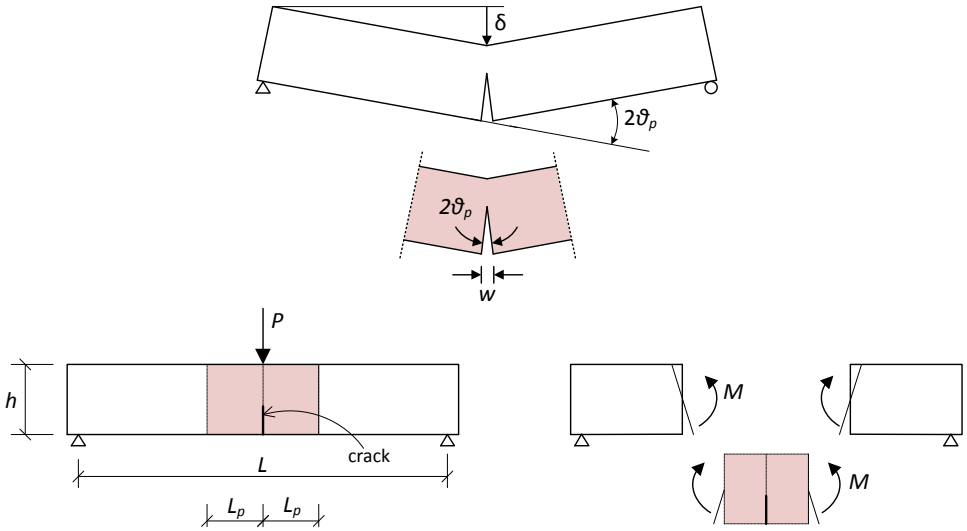

Figure 4.5 'Rigid body' rotation concept

4.2.1.1. Procedure

In Figure 4.6 a tensile material law is shown, which illustrates how to calculate the CMOD for the development of a single crack. Plastic rotation is initiated when the material has reached the elastic limit, thus when the cracking strain is reached. Due to the formation of a single crack, an increase in the tensile strain would induce the increase in the CMOD. The resulting CMOD is calculated by multiplying the strain in the post-peak region (ε_{crack}) with the assumed crack band width (CBW).

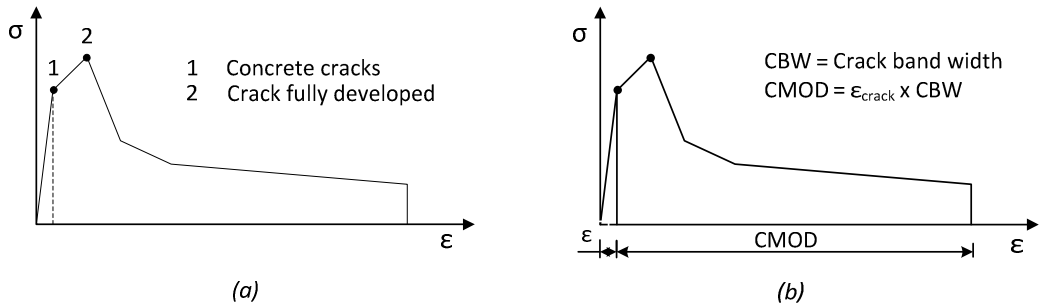

Figure 4.6 Schematic illustration of calculation procedure for CMOD.

In the inverse analysis procedure the CMOD was determined with the difference between the peak strain value and the ultimate strain value. This differs from the concept implemented for the moment-rotation procedure. For the inverse analysis procedure the CMOD was considered to increase only after the peak stress has been reached, which implies that the hardening behaviour could cause multiple cracking to occur. In the case of the moment-rotation model it is assumed that

a single crack is developed, which implies that the CMOD of the single crack increases after the cracking strain has been reached.

A schematic representation of the 'rigid body' rotation model is shown in Figure 4.7. It represents the plastic hinge region of a flexural member with the two bodies rotating about the centre of the crack. The moment-rotation results are derived from the tensile stress distribution across the crack plane. The plastic hinge rotational values were calculated with half the CMOD at the extreme tensile fibre relative to the neutral axis depth. The possibility of compression failure was also considered with the identification of a compression wedge where crushing is applicable.

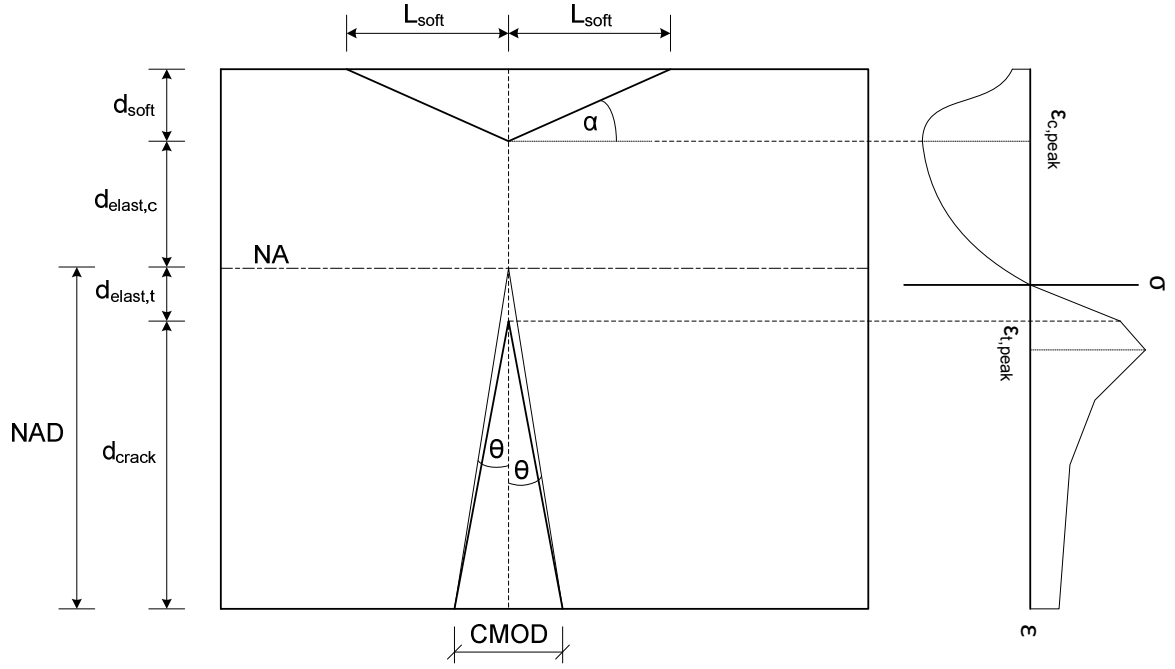

Figure 4.7 Schematic presentation of the parameters in the rotation mechanism.

The parameters were calculated as follows:

The bending moments (M) and corresponding neutral axis depths were calculated during the sectional analysis. $d_{elast,t}$ is the depth of the elastic region in the tensile zone and is calculated with

$$d_{elast,t} = NAD, \qquad \text{if} \quad NAD < y_{t1} \tag{4.10}$$

$$d_{elast,t} = y_{t1}, \qquad \text{if} \quad NAD > y_{t1} \tag{4.11}$$

d_{crack} is the depth over which the crack is developed and is determined with

$$d_{crack} = NAD - d_{elast,t} \tag{4.12}$$

The derivation of ε_{crack}, the strain value used to calculate the theoretical CMOD, is shown in Figure 4.8. This value corresponds with the strain developed across d_{crack} and is derived as follows:

$$\varepsilon_{crack} = \varepsilon_{end} - \varepsilon_{t1} \tag{4.13}$$

and with the application of a linear relationship

$$\varepsilon_{end} = \frac{\varepsilon_{t1}.NAD}{d_{elast,t}} \tag{4.14}$$

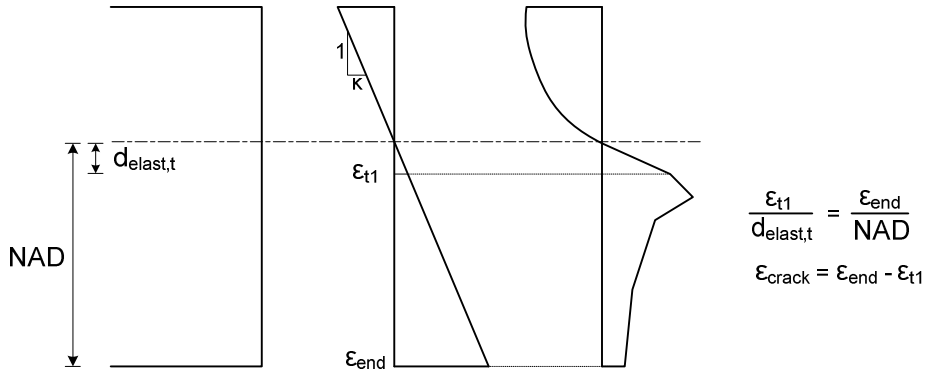

Figure 4.8 Derivation of ε_{crack}.

which results in

$$\varepsilon_{crack} = \varepsilon_{t1}\left(\frac{NAD}{d_{elast,t}} - 1\right) \tag{4.15}$$

with ε_{end} representing the strain at the ultimate tensile surface and ε_{t1}, the cracking strain.

With these calculations the theoretical CMOD is calculated with

$$CMOD = \varepsilon_{crack}.CBW \tag{4.16}$$

The theoretical 'rigid body' rotation to one side of the crack plane is calculated with

$$\vartheta_p = \arctan\left(\frac{CMOD}{2.NAD}\right) \tag{4.17}$$

As mentioned before, the development of the crushing behaviour, if any at all, was also considered to provide the idea of what would happen in the compression region in the plastic hinge zone.

For the compressive region the following parameters were adjudicated:

$d_{elast,c}$ is the depth of the pre-peak compressive region. This is the depth where crushing has not yet occurred and is calculated as follows:

$$d_{elast,c} = h - NAD, \qquad \text{if } (h - NAD) < y_{c2} \tag{4.18}$$

$$d_{elast,c} = y_{c2}, \qquad \text{if } (h - NAD) > y_{c2} \tag{4.19}$$

with

y_{c2} representing the depth that corresponds with the concrete crushing on the compressive σ-y curve.

d_{crush} is the depth in the compressive zone that is susceptible to crushing and is calculated with

$$d_{crush} = h - NAD - d_{elast,c} \tag{4.20}$$

To provide a visual representation of the crushing zone, the assumption was made that the crushing region is described with a compression wedge, with the width of the wedge governed by an angle, α. This width could be seen as the compressive softening length (L_{soft}).

$$L_{soft} = \frac{d_{crush}}{\tan(\alpha)} \tag{4.21}$$

4.2.2. Moment-rotation results

The obtained moment-rotation results are presented in Figure 4.9. The first characteristic that is observed is that the shapes of the curves are similar to that of the moment-curvature relations. This was expected due to the definition of rotation according to the moment-area theorem,

$$\vartheta = \int_0^{L_p} \frac{M}{EI} dx \tag{4.22}$$

The magnitude of the bending moments was already discussed in the findings of the moment-curvature relations. In Figure 4.9 it is seen that the plastic rotation capacity has increased with an increase in the volume fibres. As a measure to define this, member ductility ($\Delta\vartheta$) was prescribed to be the amount of plastic rotation experienced at the peak bending moment. These values are presented in Table 4.2 with a ratio calculated, using the 0.5% SFRC result as the base value. The

member ductility has increased 1.5 times and 2.28 times, for the 0.75% SFRC and 1.0% SFRC member, respectively, compared to that of the 0.5% SFRC member's rotation capability.

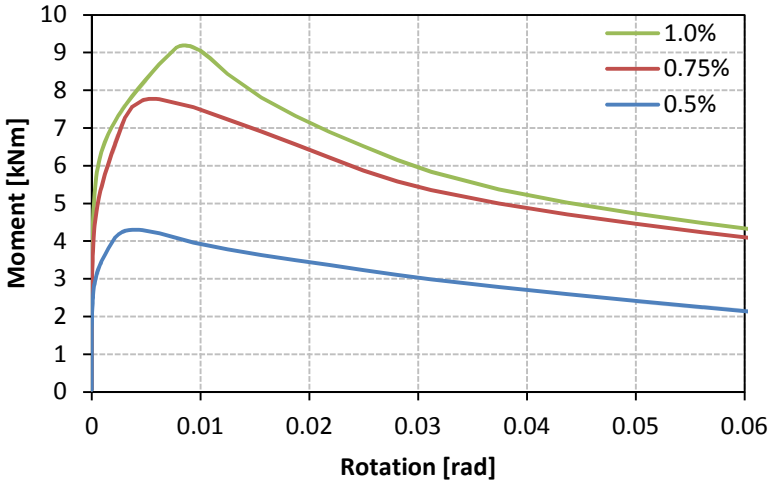

Figure 4.9 Theoretical moment-rotation responses for all three SFRC mixes.

Table 4.2 Theoretical rotation characteristics.

	MEMBER DUCTILITY		COMPRESSION SOFTENING		
Fibre %	Δθ [rad]	$\Delta\theta_i/\Delta\theta_{0.5\%}$	θ_{crush} [rad]	$\theta_{crush,peak}$ [rad]	$L_{soft,max}$ [m]
0.5	0.0037	1	0.0047	0.0281	0.008
0.75	0.0056	1.50	0.0031	0.0187	0.018
1.0	0.0085	2.28	0.0025	0.0125	0.024

A graphical representation of the calculated member ductility ratio for all three SFRC members is shown in Figure 4.10. The theoretical member ductility ($\Delta\vartheta$) had increased almost linearly, just as for the sectional ductility ($\Delta\kappa$).

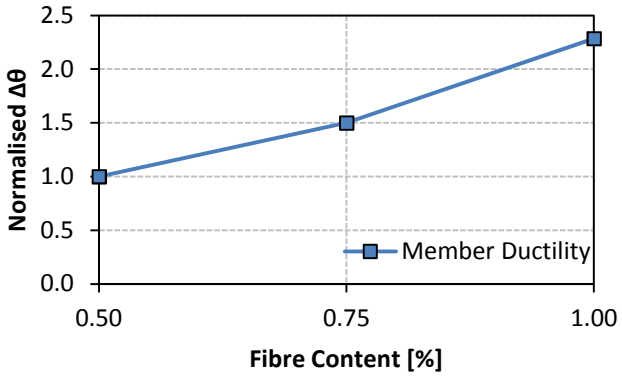

Figure 4.10 Comparison of member ductility normalised to 0.5% SFRC.

4.3. Moment redistribution

So far the theoretical behaviour for a cross-section (M-κ) and for a plastic hinge (M-ϑ) has been determined. The following task is to derive the amount of moment redistribution (MR) and relate this value with the corresponding rotational behaviour. As mentioned, moment redistribution can only occur in statically indeterminate structures. A structure's ability to redistribute bending moments is related to the structure's ability to rotate at the critical sections. Factors that could influence the rotational behaviour include the structure's geometry, such as the section height and the L/d ratio, while the loading type, e.g. a point load or a distributed load, could also have a major influence. The governing factor that influences the moment redistribution behaviour is the moment-curvature relation.

To provide an indication of the amount of moment redistribution it is required to create a finite element model of a statically indeterminate structure that implements the derived moment-curvature relationships. To validate the numerical approximations, it is also required to investigate the proposed structural behaviour with experimental testing. Thus, the finite element model should represent a structure that could be simulated in the laboratory with the equipment available.

4.3.1. Statically indeterminate structure

For simplicity it was decided to model a two span continuous one-way spanning slab. The slab is loaded with a point load at both midspans. This is representative of the structure that is schematically shown in Figure 2.9. From the literature review it was found that researchers, such as Scott & Whittle (2005), Oehlers (2006), Aiello & Ombres (2011) and Oehlers, *et al* (2004), utilised reinforced two-span continuous beams to determine the amount of moment redistribution. In their case studies they also used point loads at the midspans to apply the loads.

4.3.2. Expected results

The fibre reinforced concrete is considered homogenous throughout the whole structure. This implies that the moment-curvature relationship would be the same for any section throughout the structure.

The expected failure process is summarised as follows.

- The first plastic hinge would develop at the centre support due to the concentration of a larger bending moment.
- Once the hinge is formed at this position, the bending moment could increase or decrease in accordance with the moment-curvature relationship, but simultaneously the bending moments at the midspan would increase at a faster rate until their ultimate bending capacity is reached.
- The failure of the structure occurs when the plastic hinges are developed at both the centre support and the midspans, forming a 'mechanism'.

4.3.3. Moment Redistribution calculation

Theoretically moment redistribution occurs when the structure's response deviate from that of an elastic response, which implies that moment redistribution initiates after cracking occurred. The amount of moment redistribution is seen to be proportional to the difference between the failure bending moment (M_u) and the elastic bending moment (M_e).

According to researchers such as Oehlers, *et al* (2004), Liu, *et al* (2006) and Barros & Dalfré (2009) the equation used for the calculation of the amount of moment redistribution is

$$MR = (1-\delta).100 \tag{4.23}$$

with

$$\delta = \frac{M_{red}}{M_{elast}} \tag{4.24}$$

with

δ Relation between redistributed bending moment and elastic bending moment

M_{red} The value of the redistributed bending moment at the centre support

M_{elast} The value of the elastic bending moment at the centre support

4.4. Computational modelling of moment redistribution

The following sections describe the development of a finite element model of the statically indeterminate structure mentioned in the previous section. A two-span continuous slab was modelled using the finite element analysis software, ABAQUS. The aim was to predict the amount of moment redistribution experienced and to derive a moment redistribution-plastic rotation (MR-ϑ_p) behaviour.

4.4.1. Geometry

The layout of the modelled structure is shown in Figure 4.11. The slab dimensions were chosen to be the following:

- Span length (L): 1450mm
- Slab width (b): 250mm
- Slab height (h): 125mm

The total length of the slab is 3100mm with a span length to height (L/h) ratio of 11.6. The specimen height was chosen to be the same as for the three point bending specimens to eliminate the 'size effect' across the section height. The section height to width (h/b) ratio is equal to 2.

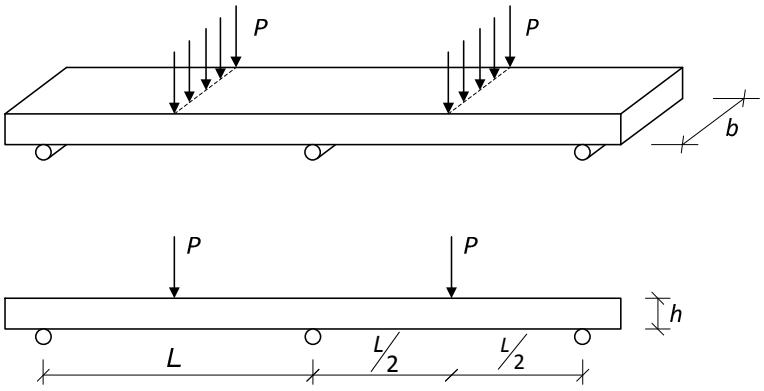

Figure 4.11 Layout of modelled structure.

4.4.2. Elements and Meshing

For this analysis it was decided to use beam elements. Specifically, B21 beam elements were implemented, having two nodes and six degrees of freedom (Figure 4.12). According to the description provided by ABAQUS, the elements are 2 dimensional with linear interpolation of the characteristics conducted between the two nodes. The principal motive for the use of these elements is that it is able to implement a non-linear moment-curvature relationship.

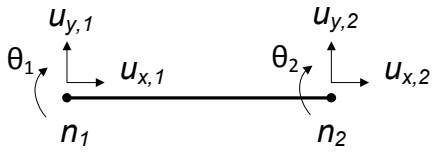

Figure 4.12 Beam element degrees of freedom (ABAQUS, 2010).

The element size was chosen to be 12.5mm in length, as this element size contributed to a smooth curvature response. The element size also contributed to the generation of nodes at the positions to apply the boundary conditions.

4.4.3. Boundary Conditions

The boundary conditions were defined to induce symmetrical structural behaviour, as seen in Figure 4.13. The displacement at the node representing the centre support is constrained in the x- and y-direction to ensure the stability of the structure. The side supports were only constrained in the y-direction to allow for the horizontal movement of the member. These nodes were also defined to rotate freely. The nodes at the midspans were used to define the prescribed displacements.

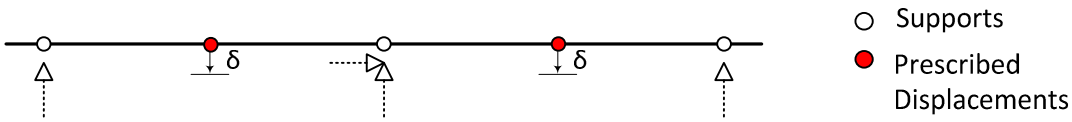

Figure 4.13 Layout of model indicating position of boundary conditions.

4.4.4. Material Properties

The possible moment-curvature relationship as prescribed by ABAQUS is shown in Figure 4.14.

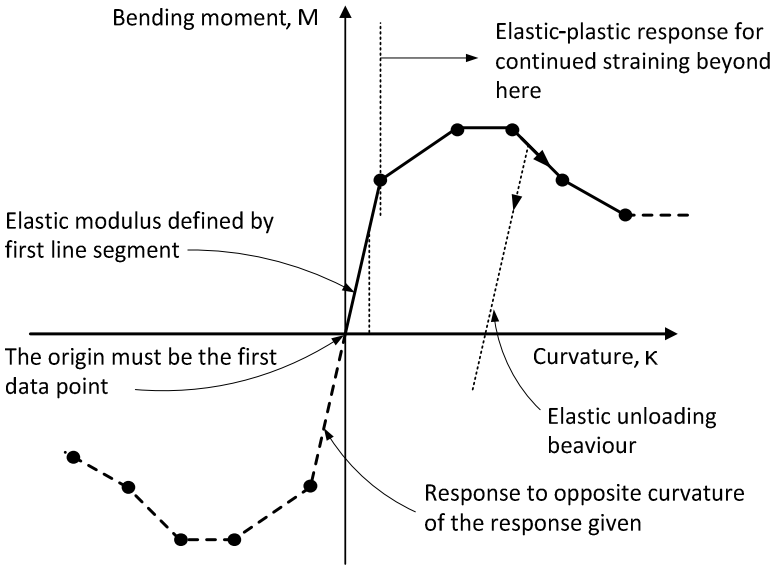

Figure 4.14 Example of inelastic nonlinear beam section behaviour definition (ABAQUS, 2010).

For the description of the material behaviour, it is required to provide the moment-curvature and axial force-axial strain relationships. The axial force-axial strain relationship was considered to represent a very stiff member. It was necessary to derive an adjusted moment-curvature relationship for each SFRC member due to the influence of the element size on the plastic hinge length. A seen in Figure 4.15, the inverse analysis provided the uniaxial tensile response for a concrete beam in three-point bending with a CBW of 12.5mm, which is the element size. Thus, the real moment-curvature relation corresponding to the real crack band width of the concrete member is related by utilising an appropriate CBW, $h/2$. In the case of the 5PBT, the material property provided for the beam elements are the representative moment-curvature relationships. As shown in Figure 4.15, yielding occurs first at the centre support by implementing a weaker element at that position, which induces a plastic hinge length that corresponds with that element size. For this research the plastic hinge length is assumed to be the same as the CBW and it is therefore necessary to derive the moment-curvature relation according to the numerical plastic hinge length by adjusting the uniaxial tensile response to correspond with this numerical plastic hinge length, $h/2$. This adjusted uniaxial tensile response is used in conjunction with the compressive behaviour in the sectional analysis to derive the numerical moment-curvature relation.

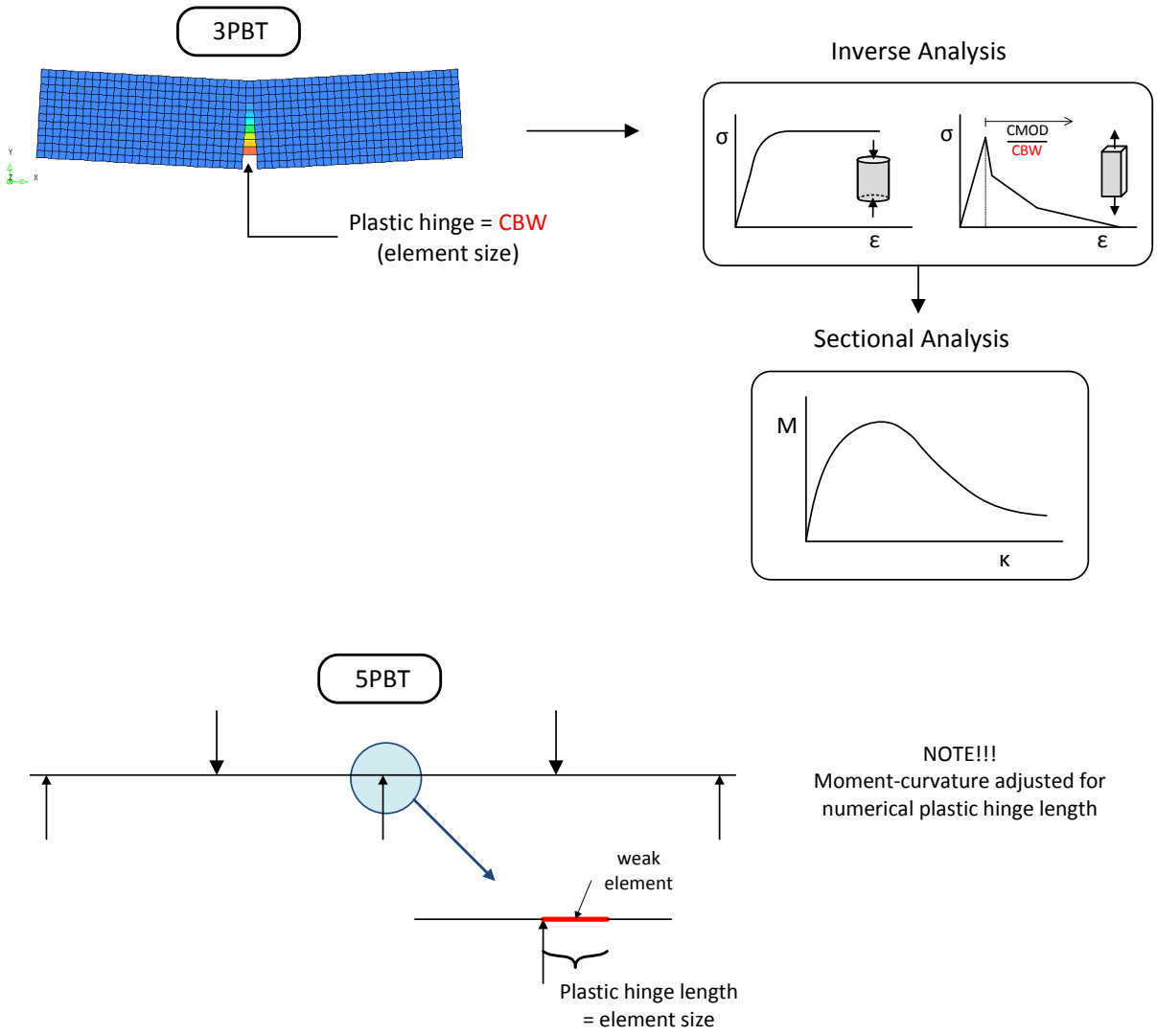

Figure 4.15 Interpretation of correct moment-curvature relation for modelling.

The tensile material behaviour was adjusted for a CBW of 12.5mm and implemented in the sectional analysis procedure to derive the applicable moment-curvature results. To ensure clarity for this procedure the following relations are provided:

$$\kappa = \frac{\varepsilon}{y} \tag{4.25}$$

and

$$\varepsilon = CMOD.CBW \tag{4.26}$$

The curvature is directly proportional to the strain value, which in turn is considered to be directly proportional to the crack band width (*CBW*) in the post-peak region of the tensile material behaviour.

The material properties were defined as a number of data points which represents a multi-linear relationship, as shown in Figure 4.14. The adjusted moment-curvature relationships for all three SFRC members are presented in Figure 4.16. It is noticed that the peak bending moments are slightly larger than that predicted for the real structural behaviour in Chapter 3, which is ascribed to the influence of the adjusted tensile behaviour.

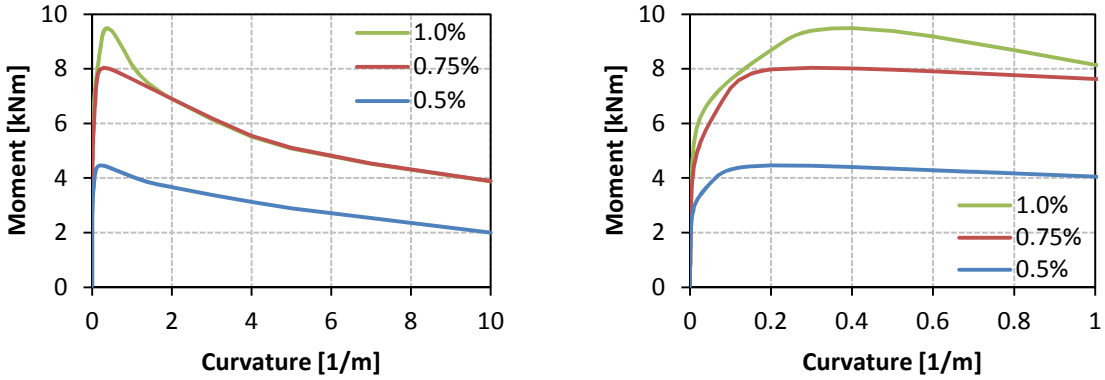

a) *b*)

Figure 4.16 Adjusted moment-curvature results for beam elements; a) Full response, b) Partial response.

4.4.5. Analysis Procedure

A displacement controlled procedure was performed. The nodes at the midspans were prescribed with a vertical displacement of 20mm. This prescribed displacement was applied in increments of 0.01mm. The first crack was expected at the centre support, thus one of the elements at this position was provided with a 1% weaker material property to ensure the crack position. The necessary results are the bending moment distribution, curvature distribution, the reaction forces and the corresponding displacements and rotations.

4.4.6. Results

4.4.6.1. ABAQUS output

The results obtained from the analyses are shown in Figures 4.17 through 4.20. Certain aspects of the results for all three SFRC members are similar, thus to avoid repetition only the results for the 0.5% SFRC are illustrated. If desired, the reader could examine the other results in Appendix B.

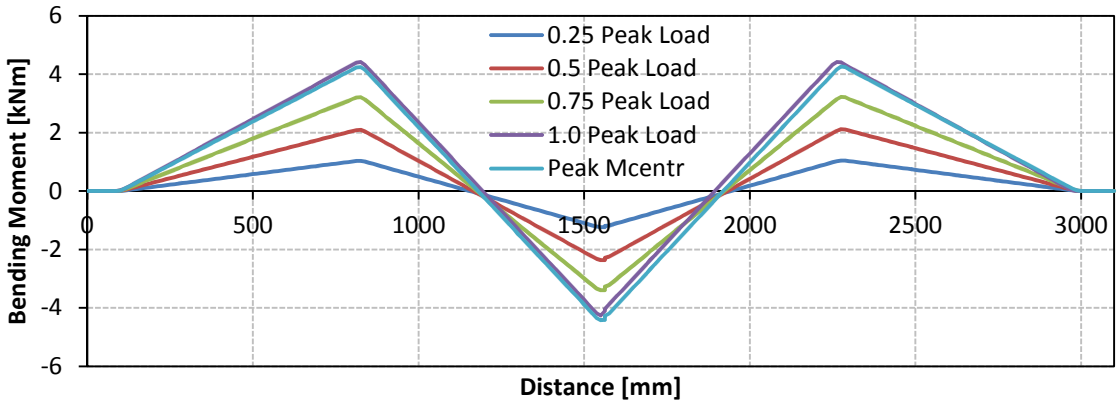

Figure 4.17 Bending moment distribution with increase in load for 0.5% fibre volume.

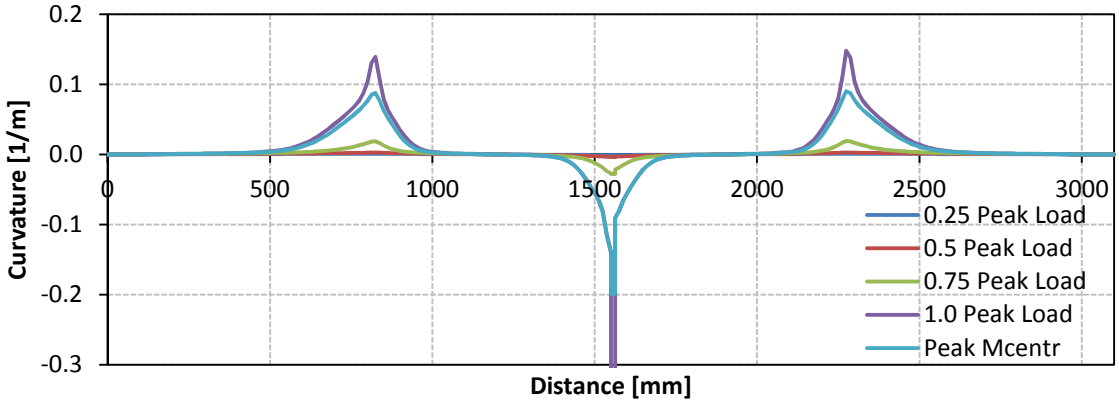

Figure 4.18 Curvature distribution with increase in load for 0.5% fibre volume.

Figures 4.17 and 4.18 provide an indication of the development of the bending moments and corresponding curvatures in the structural member with the increase in the applied load. As expected, the magnitude of the bending moment at the centre support is greater than that of the midspans at relative low loads. As the load increases the magnitude of the midspan bending moment increases until failure has occurred. Structural failure is considered to have occurred when the maximum load has been exceeded. In all three analyses failure occurred after the peak bending moment ($M_{ctr\ sup,Peak}$)has been reached at the centre support. It is seen in Figure 4.18 that the curvature at the centre support has increased into the post-peak moment-curvature region, thus inducing a greater increase in curvature at the midspans due to the sudden decrease in structural stiffness. Referring to the bending moment distributions in Figure 4.17, it is noticed that there is only a small increase in the structural capacity subsequent to the attainment of the peak moment at the centre support.

The development of the bending moments at the critical sections with the increase in load till failure is shown in Figure 4.19. To improve the interpretation of this graph, the bending moments according

to the linear-elastic material law are added. Once the linear material behaviour is exceeded and moment redistribution is in effect, the bending moment development decreases at the centre support with an accompanying increase in the development at the midspans. It should be noted that the load curves shown in Figure 4.18 represent the load applied on one span.

The comparison between the theoretical moment-rotation behaviour for the 0.5% SFRC and that obtained from the numerical analysis is also shown in Figure 4.19. The plastic hinge taken into consideration is at the centre support and theoretically the bending moment should be negative. In order to simplify the comparison procedure, the bending moment value was considered to be positive. The shape of the curves correlates well, with a slight deviation of the rotational value at the peak bending moment. The peak moment of the numerical analysis is also larger than that predicted by the moment-rotation model due to the influence of the adjusted moment-curvature responses.

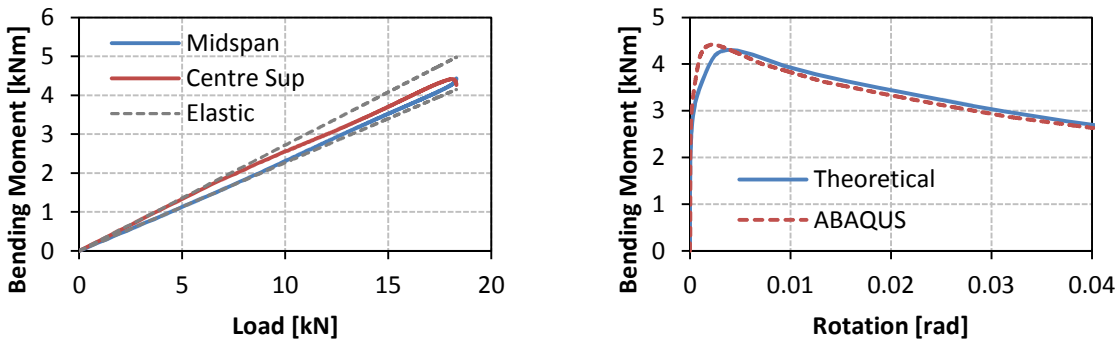

a) *b*)

Figure 4.19 0.5% Fibre Volume. a) Relation between the bending moment development and the load applied; b) Comparison between moment rotation output at the centre support and its theoretical approximation.

In Figure 4.20 the moment-rotation behaviour for the 0.75% and 1.0% SFRCs are compared with their corresponding theoretical predictions. Just as for the 0.5% SFRC, the numerical and predicted shape of the curves are closely correlated, with a numerical peak moment that is slightly higher than predicted with the moment-rotation model. It is noticed that the deviation of the rotational value at the peak bending moment increased with an increase in the fibre volume.

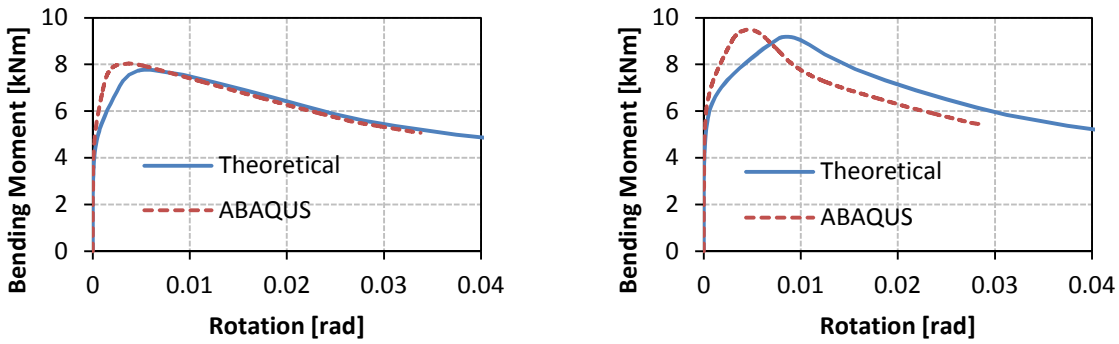

a) *b*)

Figure 4.20 0.5% Fibre Volume. Comparison between moment-rotation output at the centre support and its theoretical approximation for; a) 0.75% fibre volume and b) 1.0% fibre volume.

The rotational values of the plastic hinges at the instance the centre support has reached its maximum bending moment (ϑ_{max}) and at failure (ϑ_{fail}) are presented in Table 4.3. The ratio between the rotation at failure and at the maximum bending moment for the centre support provides an indication of the increase in the rotational capacity. For the 0.5% and 0.75% SFRC members the rotation has increased by 111% and 62%, respectively, with the 1.0% SFRC member indicating no increase in the rotational capacity after the maximum bending moment has been reached. These unexpected results could be adjudicated to the influence of the rapid decrease in the bending capacity in post-peak region of the derived moment-curvature relations (Figure 4.16).

Table 4.3 Numerical rotation characteristics.

	CENTRE SUPPORT			MIDSPANS		
% Fibres	ϑ_{max} [rad.10^{-3}]	ϑ_{fail} [rad.10^{-3}]	$\vartheta_{fail}/\vartheta_{max}$	ϑ_{max} [rad.10^{-3}]	ϑ_{fail} [rad.10^{-3}]	$\vartheta_{fail}/\vartheta_{max}$
0.5	2.119	4.471	*2.11*	1.092	1.732	*1.59*
0.75	3.755	6.094	*1.62*	1.778	2.682	*1.51*
1.0	4.982	4.994	*1.0*	2.987	2.989	*1.0*

The rotational values for the midspan hinges are also included in Table 4.3 to indicate how critical sections influence each other. The rotational capacity for the 0.5% and 0.75% SFRCs has increased between 50% and 60% from the instance the maximum moment has been reached at the centre support until failure, with the 1.0% SFRC member indicating no further rotational development. These low values are adjudicated to the decrease in the structural integrity of the member due to the decrease in the resistance at the centre support. Thus, after the peak moment has been reached

at the centre support the indeterminate structure reacts as two simply supported structures, which provides less resistance.

The member ductility ratios, as prescribed in Section 4.2.2, are also calculated with the numerical results.

$$Ductility\ Ratio = \frac{\vartheta_{max,i}}{\vartheta_{max,0.5\%}} \tag{4.27}$$

Just as for the theoretical approximations, the magnitude of this characteristic increased with an increase in volume fibres, with the 0.5%, 0.75% and 1.0% SFRCs presenting numerical ductility ratios of 1, 1.77 and 2.35, respectively.

The structural characteristics necessary to derive the amount of moment redistribution for each member is presented in Table 4.4. The amount of moment redistribution was calculated to be 14.48%, 13.05% and 9.47% for the 0.5%, 0.75% and 1.0% SFRCs, respectively.

Table 4.4 Calculation of moment redistribution.

	AT FAILURE			ELASTIC LAW		MOMENT REDISTRIBUTION	
Fibres [%]	P_{max} [kN]	M_{midsp} [kNm]	M_{centr} [kNm]	$M_{e,midsp}$ [kNm]	$M_{e,centr}$ [kNm]	δ [-]	*MR* [%]
0.5	18.31	4.44	4.26	4.15	4.98	0.855	14.48
0.75	33.21	7.95	7.85	7.52	9.03	0.869	13.05
1.0	38.55	9.10	9.49	8.73	10.48	0.905	9.47

Thus, a decrease in the amount of moment redistribution is obtained with an increase in the fibre volume, which is attributed to the more rapid decrease of the post-peak bending capacity. The final amount of moment redistribution depends on the ability of the first plastic hinge to maintain adequate resistance whilst enabling the midspan hinges to develop to their maximum capacity. To achieve larger moment redistribution it would be beneficial to have a moment-curvature relation with a post-peak behaviour which invokes the development of the hinge whilst retaining the necessary structural resistance.

4.4.6.2. Moment redistribution-plastic rotation predictions

The amount of moment redistribution related to both the applied load at each midspan and the amount of plastic rotation of the plastic hinge at the centre support is shown in Figure 4.21. Both these graphs are plotted until failure has occurred. It is noticed that the shapes of the curves for all three members are similar.

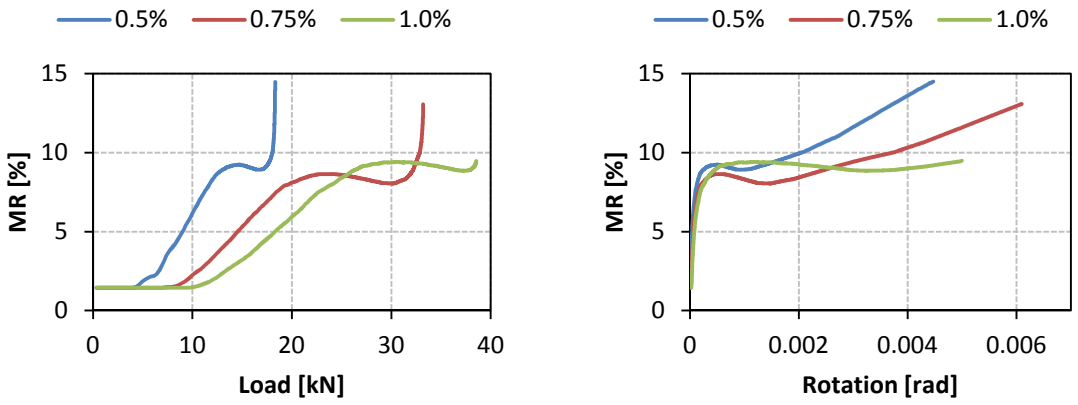

a) *b*)

Figure 4.21 a) MR vs applied load; b) MR vs plastic rotation.

As seen in Figure 4.21 a), the moment redistribution value is constant at 1.436% until cracking is initiated, then further moment redistribution is developed. After cracking commences at the centre support, the moment redistribution increases at a constant rate, gradually plateaus and increases at a rapid rate until failure commences. This behaviour is recognised for all three SFRCs, with a difference in the rate of moment redistribution development and the size of the midpoint plateau region. It is noticed that the moment redistribution is developing at a decreased rate for the members with an increase in the fibre volume. The size of the plateau region also increased with an increase in the fibre content. A possible reason for change in the moment redistribution development rate is the redistribution of the forces, with the maximum load always subjected to the part of the structure which has the greater stiffness (or structural integrity).

The numerical moment redistribution-plastic rotation relationships are shown in Figure 4.21 b). It is concluded that the composites with the lesser fibre content experience a larger amount of moment redistribution, but the rotation capacity is limited. The reason for the lower rotational capacity for a lesser amount of fibres is due to the lower tensile resistance in the plastic region. Thus, the crack develops at a faster rate which induces a greater developing ratio between the rotation at the section and the amount of forces redistributed.

4.5. Concluding remarks

In this chapter the theory for providing the theoretical moment-curvature and moment-rotation behaviour of a flexural member were discussed, followed with the results obtained. It was found that the SFRC member's bending capacity increased with an increase in the amount of fibres utilised. The moment-rotation results yielded an increase in the member ductility with the rotational value at the peak load increasing with the use of larger volumes of fibres.

The results obtained from the computational analyses correlate well with the theoretical predictions, as the shapes of the curves were similar with minor discrepancies obtained in the rotational values at the peak moment values. Further, it is noticed that the structural behaviour is similar for all three composites, when referring to the moment-load graphs. Failure occurred when the maximum capacity was reached at the midpsans after the plastic hinge has been formed at the centre support.

The moment redistribution-plastic rotation relations illustrated that the 0.5% SFRC member experienced the highest amount of moment redistribution at failure, with this amount decreasing with the increase in the amount of fibres used. It was also noticed that the member rotation at failure was larger for an increased amount of fibres. Thus, a SFRC member with an increased amount of fibres was able to rotate more at the critical sections, but experienced a lower amount of moment redistribution. This phenomenon was ascribed to the shape of the post-peak moment-curvature curves with the bending capacity decreasing more rapidly with an increased fibre volume, resulting in a more rapid loss of capacity at a specific critical section.

CHAPTER 5

MODEL VERIFICATION

In this chapter the experimental statically indeterminate tests are described and the obtained results are compared with the theoretical predictions in order to validate the theoretical models. Due to irregular results the test procedure is validated with extra computational analyses and conclusions made in terms of the validity of the assumed moment redistribution model.

5.1. Statically indeterminate tests

5.1.1. Aim

The aim of these tests is to experimentally determine the amount of moment redistribution experienced and the corresponding rotational capacity at the plastic hinges of the SFRC flexural members. A total of nine specimens were tested with three specimens per SFRC mix.

5.1.2. Test setup

5.1.2.1. Specimen

The specimens had the dimensions of 3100x250x125mm (*L*x*b*x*h*) and represent a strip of a one-way spanning continuous slab. The specimens were cast in wooden moulds that were lined with water resistant paint (Figure 5.1). The specimens were demoulded after two days and cured using wet blankets for a further 14 days. The following 12 days the specimens were left unsealed in laboratory conditions. With each slab specimen two cylinders were cast to obtain the compressive strength of the specific SFRC mix. All specimens were tested on the 28 day strength. The specimens were defined with letters A, B and C, for the 0.5%, 0.75% and 1.0% SFRC members, respectively, which is followed by the specimen number, e.g. specimen A1 is the first specimen for the 0.5% SFRC mixture.

Figure 5.1 Wooden moulds used for the casting process.

5.1.2.2. Experimental setup

The test setup was designed to represent a structure in five point bending. A schematic of the test setup is provided in Figure 5.2.

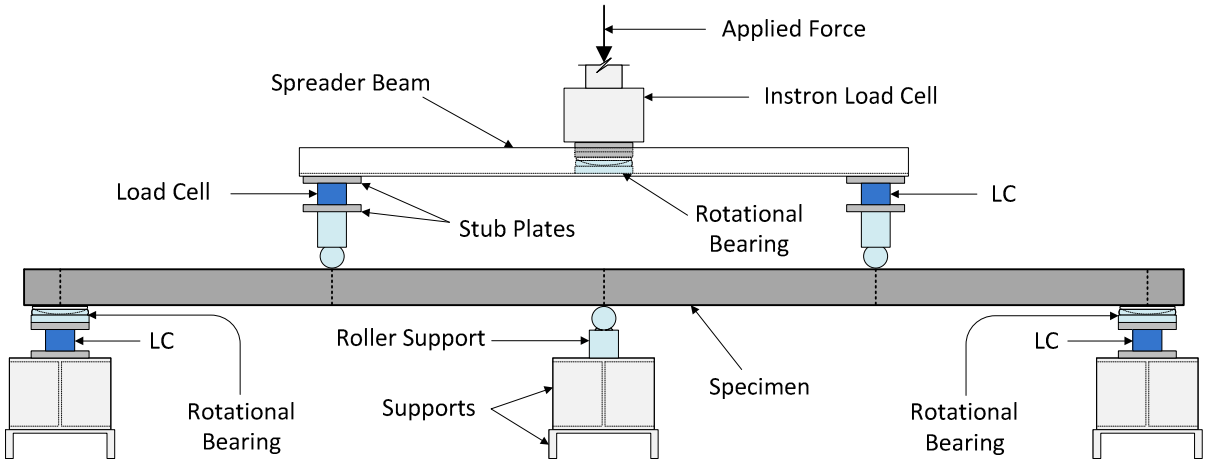

Figure 5.2 Schematic of five point bending test setup.

Force Distribution Measurement

The specimens were simply supported with roller supports. The end supports and load points were fitted with load cells to measure the reaction forces. Each load cell had an ultimate capacity of 50kN. An Instron Hydraulic Actuator with a capacity of 500kN was used to apply the force on a spreader beam, which is free to rotate at the loading point. The end supports were also fitted with rotational bearings to allow the free rotation of the specimen ends. The point loads and the centre support were provided with roller supports to prevent any applied moments. The placement of the load cells enabled the calculation of the complete force distribution across the specimen length with the measured reaction forces.

Rotation Measurement

LVDTs were glued to the top and bottom of the specimen at each section where the plastic hinges were expected to develop (Figure 5.3), i.e. at the loading points and centre support. A gauge length of twice the assumed plastic hinge length was considered in order to measure the curvature and rotation of the plastic hinges so that it could be compared with the calculated values. LVDTs were also placed at the loading points to provide an approximation of the vertical displacement at each

midspan. The actual test setup is shown in Figure 5.4 which illustrates the positions of the defined measuring equipment.

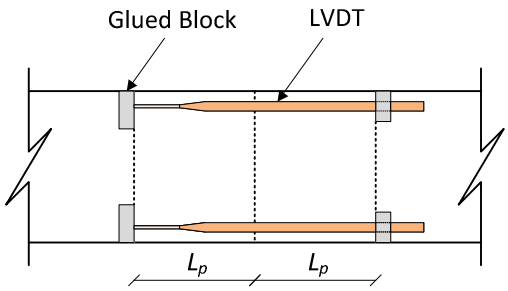

Figure 5.3 Schematic of the LVDT setup at the plastic hinges on a side view of the specimen.

Figure 5.4 Actual test setup.

5.1.2.3. Surface deformation system

In addition, the ARAMIS was utilised to measure the displacement of the slab face at the centre support, where the first plastic hinge was expected to develop. The ARAMIS system is a non-contact optical 3D digital deformation measuring device (Figure 5.5). It consists of hardware components, such as a high performance PC system, a sensor that contains two cameras, a sensor controller for power supply and to control the image recording and a tripod to ensure stability to the sensor. The image recording and analyses were performed with the ARAMIS v6.1 software.

Figure 5.5 ARAMIS optical 3D deformation measuring device.

The software could implement a frame rate up to 12 images per second, but a frame rate of 1 image per second was considered to be sufficient for this test procedure. The measured surface is coated with a white base colour and a stochastic sprinkle pattern, provided with black aerosol paint, as seen in Figure 5.6. This stochastic pattern provides identifiable object characteristics that are used to determine the deformation across the measured surface.

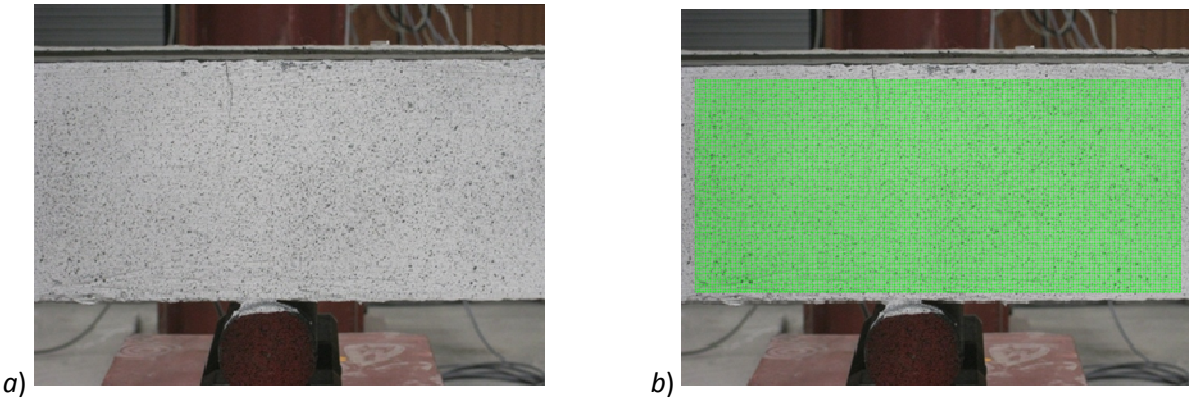

Figure 5.6 a) Stochastic sprinkle pattern provided on the specimen surface and b) An example of the masked area.

At the start of the analysis procedure the required surface area to analyse is identified by providing a mask on the measured surface. The mask is designated by a green rectangular shape on the surface, as seen in Figure 5.6 b), and corresponds with the contour defined area shown in Figures 5.7 and 5.8.

A mask area of 700mmx125mm was considered sufficient. During an analysis the deformation of to the object characteristics is calculated in relation to the reference stage. During testing the stochastic pattern sometimes failed due to large cracks developing that made it impossible for the ARAMIS software to calculate any deformations. In the contour results these regions are illustrated by the white regions.

The software allows various methods to export the history of the deformed data points of each stage. To calculate the rotation of the measured area three horizontal section lines were constructed across the length of the measured area. As seen in Figure 5.7, each section line consists of numerous data points, of which the displacement history is exported. With these results the rotational values of the measured area were calculated for each stage.

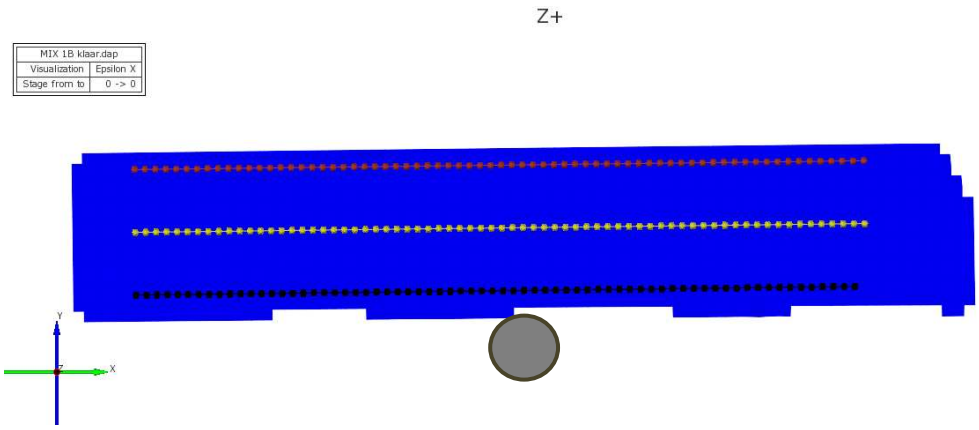

Figure 5.7 Definition of three section lines on the slab surface.

It is possible to visually present the crack formation process with the presentation of the strain results in the x-direction. A representation of this characteristic is shown in Figure 5.8. This is used to distinguish among the plastic hinge behaviours of the different SFRCs.

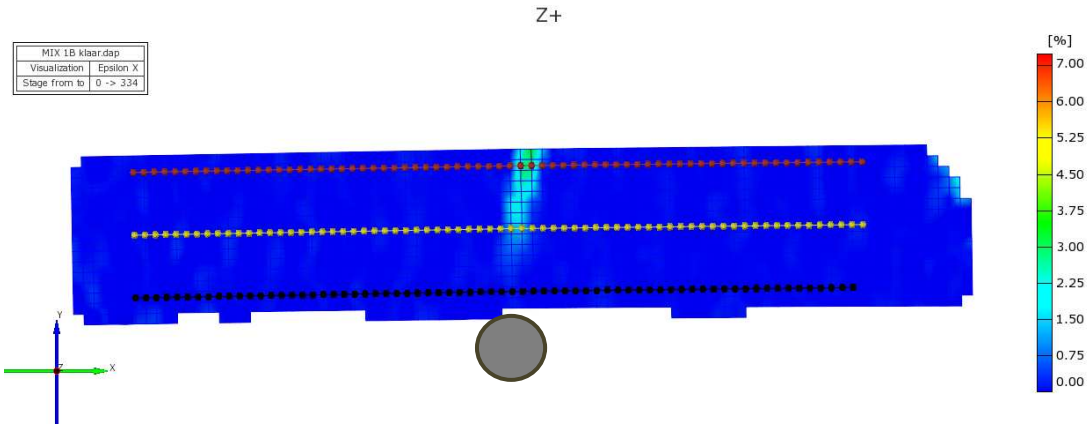

Figure 5.8 Measured strain in the x-direction.

5.1.2.4. Test Procedure

The test was performed using displacement control with the Instron applying a displacement at a rate of 2mm/min. This rate was selected to ensure that structural failure commenced before the image limit of the ARAMIS system was reached. The test procedure was ended when the load has decreased sufficiently after the peak value has been reached. The measurements were collected using the CATMAN V4.5 software package with the use of HBM Spider8 electronic measurement devices. The sample rate for the LVDTs, the loadcells and the Instron measurements were 25Hz to ensure enough data points. The sample rate for the ARAMIS system was 1 photo per second to simplify the synchronisation procedure between the CATMAN data and the ARAMIS data.

5.1.3. Calculations

5.1.3.1. Bending moments across specimen length

The bending moments were calculated with the measured reaction forces at the end supports and the loading points (Figure 5.9). It was not necessary to use the reaction force at the centre support to derive equations for the bending moment calculation. The moment values were derived using elastic theory and the superposition characteristic.

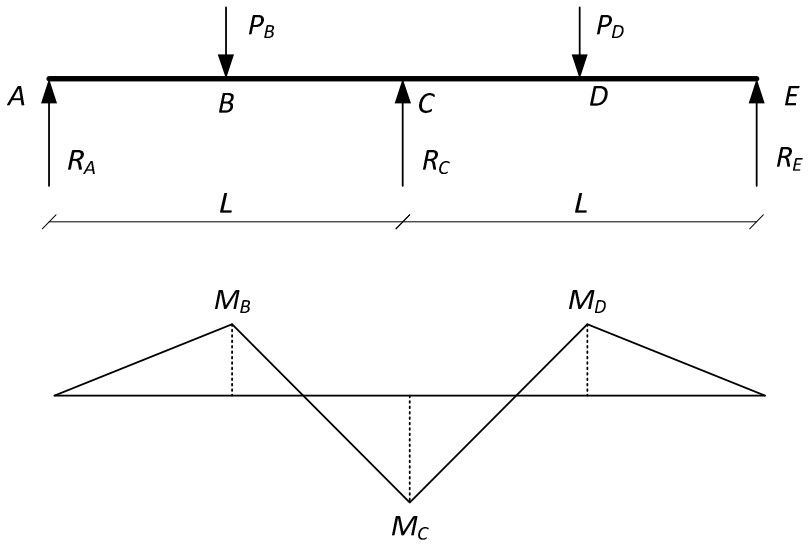

Figure 5.9 Measured forces and resulting bending moment diagram.

The following equations were derived:

$$M_B = R_A . L/2 \tag{5.1}$$

$$M_C = \frac{1}{2}\left[\left(R_A.L - P_B.L/2\right) + \left(R_E.L - P_D.L/2\right)\right] \tag{5.2}$$

$$M_D = R_E . L/2 \tag{5.3}$$

Note that the bending moment value at the centre support was taken to be the average of the calculated value of the two spans due to some minor differences in the reaction values at the end supports and at the loading positions.

5.1.3.2. Curvatures and rotations

The LVDTs only provide displacement measurements, but it is sufficient for the calculation of the rotation and curvature at the plastic hinges. Due to the implementation of the glued blocks, the LVDTs were attached to the specimen face at a distance of 20mm from the top and bottom surface, as shown in Figure 5.10. The distance between the LVDTs, *j*, was calculated as *h*-2*a*. As seen in Figure 5.10, there are two cases to be considered to evaluate the measurements due to the development of the crack in the tensile region. The tensile region is considered to be at the bottom and the compressive region at the top, which corresponds with a sagging flexural member. For Case 1 the tensile crack has not developed beyond the top LVDT's centreline and includes the uncracked section, while for Case 2 the tensile crack has developed beyond the top LVDT's centreline.

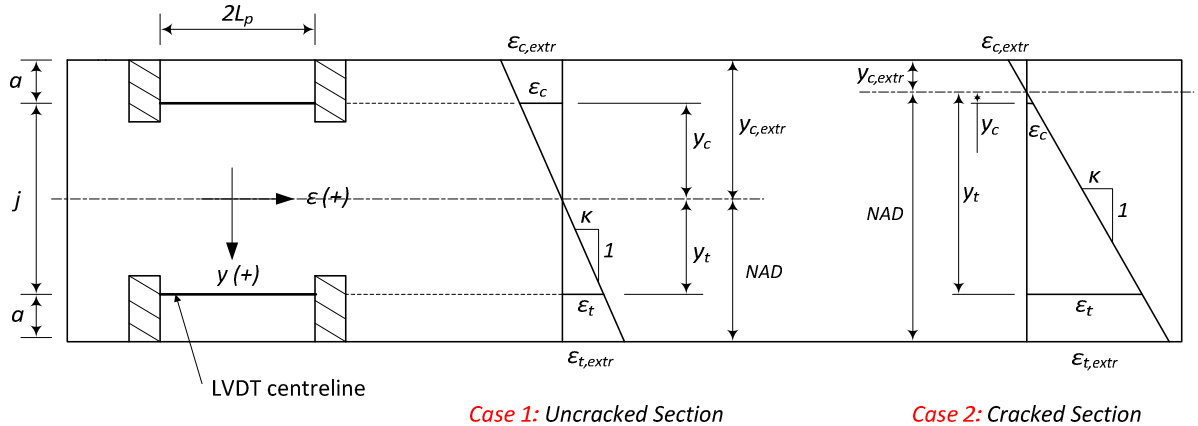

Figure 5.10 Schematic of the definition for the terminology used for derivation of curvatures.

In a hogging region the bending moment and curvature is negative, e.g. at the centre support, opposed to a sagging region where it is positive. Thus, to simplify the comparison between the experimental and the theoretical moment-curvature results, the curvature and bending moment at the centre support was also considered to be positive.

The following parameter values were utilised for the calculations:

- L = 1.45m
- h = 0.125m
- a = 0.02m
- j = 0.085m
- L_p = 0.0625m
- CBW = 0.0625m
- $\varepsilon_{t,crack}(0.5\%)$ = 61.52E-06
- $\varepsilon_{t,crack}(0.75\%)$ = 94.95E-06
- $\varepsilon_{t,crack}(1.0\%)$ = 121.8E-06

As the first step, the strain values corresponding to the LVDT displacements were calculated. For the purpose of this derivation the two strain values were defined as ε_t and ε_c, with the LVDT in the tensile region providing the results for ε_t and the other LVDT for ε_c. The procedure was developed to be compatible with both cases and the equations are as follows:

$$\varepsilon_t = \frac{\Delta x_{tens}}{2L_p} \tag{5.4}$$

$$\varepsilon_c = \frac{\Delta x_{comp}}{2L_p} \tag{5.5}$$

with

Δx_{tens} the displacement measured by the LVDT in the tensile region, and

Δx_{comp} the displacement measured by the LVDT in the compressive region.

The following calculations were also performed:

1. The *curvature* (κ) that corresponds with a section in the plastic hinge area:

$$\kappa = \frac{\varepsilon_t - \varepsilon_c}{j} \tag{5.6}$$

2. The *distance* (y_t) from the neutral axis to the LVDT in the tensile region:

$$y_t = \frac{\varepsilon_t}{\kappa} \tag{5.7}$$

3. The *neutral axis depth (NAD)*:

$$NAD = y_t + a \tag{5.8}$$

4. The *distance* ($y_{c,extr}$) from the neutral axis to the ultimate compression surface:

$$y_{c,extr} = NAD - h \tag{5.9}$$

5. The *deformation* at the ultimate tension surface ($\varepsilon_{t,extr}$):

$$\varepsilon_{t,extr} = \kappa.NAD \tag{5.10}$$

6. The *deformation* at the ultimate compression surface ($\varepsilon_{c,extr}$):

$$\varepsilon_{c,extr} = \kappa.y_{c,extr} \tag{5.11}$$

7. The *crack mouth opening displacement* for a single crack in the plastic hinge area:

$$CMOD = \left(\varepsilon_{t,extr} - \varepsilon_{t,crack}\right).CBW \tag{5.12}$$

with

$\varepsilon_{t,crack}$ representing the theoretical cracking strain value as calculated with the sectional analyses and CMOD prescribing the approximated crack mouth opening displacement for a single plastic hinge length.

8. The *rigid body rotation* (ϑ) value:

$$\vartheta = \arctan\left(\frac{CMOD}{NAD}\right) \tag{5.13}$$

with

ϑ approximating the rigid body rotation to one side of the crack, assuming that the rotation is distributed symmetrically about the loaded position.

5.1.4. Test results

As mentioned earlier, the focus of the experimental tests was to validate the theoretical moment redistribution-plastic rotation model and also to obtain insight on the mechanism of moment redistribution in a statically indeterminate structure. Thus, all of the theoretical models and experimental results is compared. Due to the similarity of the results, all of the results for each specimen are not presented in this chapter, but all of the results are presented in Appendix C.

5.1.4.1. Failure mode

All the test specimens failed similarly with failure commencing in one span, as seen in Figure 5.11. The displacement increased at each midspan in accordance to the force applied until the ultimate resistance for the weaker span is reached. Afterwards the crack develops at the weaker span while the opposite span relaxes.

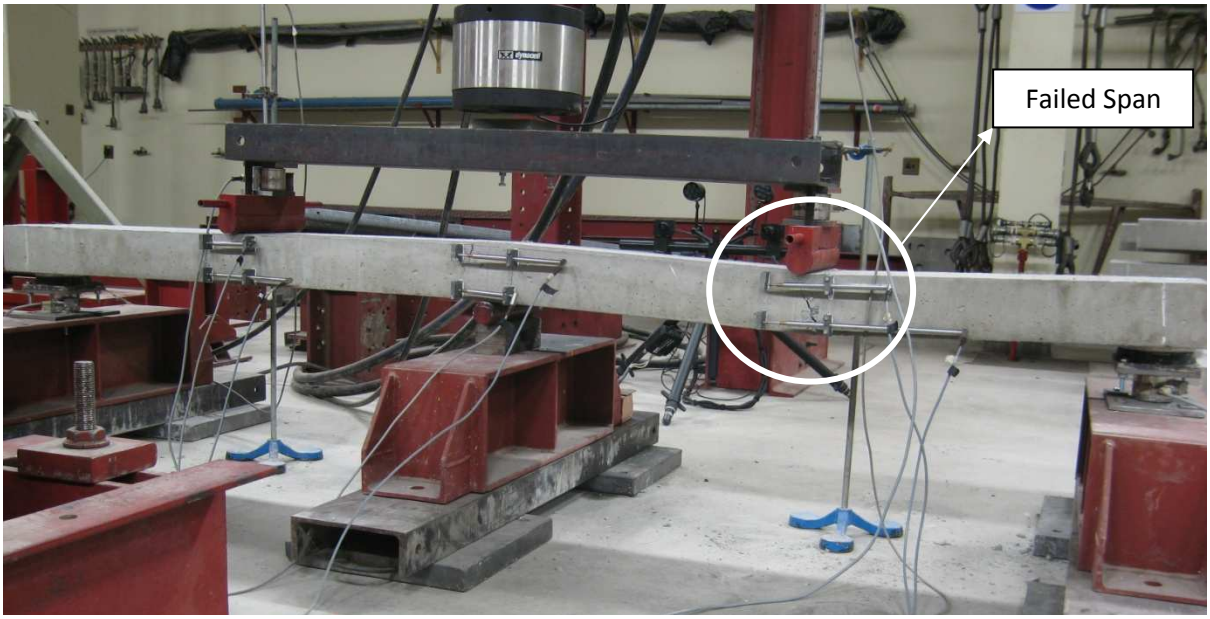

Figure 5.11 Typical failure mode of the test specimens.

5.1.4.2. Overview

To prevent any confusion concerning the presented results, the results for a representative specimen is discussed prior to the presentation of the general results. The results obtained for specimen A1 is shown in Figures 5.12 to 5.15. Note that, as mentioned before, the centre support and midspan moments are all shown as positive.

The experimental results are presented in conjunction with theoretical moment-curvature, NAD-curvature and moment-rotation results for comparison purposes. The results for the bending moment distribution at 50% of the peak load, 75% of the peak load and at the peak load is presented in Figure 5.12 to provide insight on the structural behaviour until failure. The overall structural behaviour is better interpreted when referring to the bending moment-load curve for the critical sections, also shown in Figure 5.12. This figure describes the bending moment distribution value of the critical sections at any stage of the test until failure. It is utilised to compare the bending moment relation between the midspans and the centre support.

In Figure 5.13 the experimental moment–curvature results are compared with the theoretical predictions. It should be noted that these results are only used to validate the derived moment-curvature relationship. On these moment-curvature curves three different loading stages are marked which correspond with the appropriate bending moment distribution in Figure 5.12. This provides insight on how the structural behaviour is associated with the increase in the curvature at the plastic hinges.

The comparison between the experimental and theoretical NAD-curvature results is shown in Figure 5.14. The comparison between the experimental moment-rotation results for the three critical sections and the results obtained from the Rigid-body rotation model is shown in Figure 5.15. The motive for using the Rigid-body rotation results for comparison purposes is that the experimental rotations were calculated similarly to the derivation of the theoretical model by utilising the displacements recorded with the LVDTs and assuming that a single crack developed in the measured plastic hinge area. It was not possible to utilise the ARAMIS system for this specimen at the time the testing was conducted, but the ARAMIS results for the rotational behaviour at the centre support are included for the rest of the specimens.

Although the figures include the results of all three critical sections, it should be noted that the aim was to validate the moment redistribution-plastic rotation behaviour at the centre support. Due to

unforeseen circumstances it was not possible to plot this result from load initiation until failure commenced, but the issue is addressed at a later stage.

5.1.5. General results

Due to the large amount of results, it was decided to only present the results of the centre support, as this is the critical section which defines the rotational capability during the moment redistribution process. The bending moment distributions across the specimen length were excluded as the moment-load graphs sufficiently describe the structural behaviour. Although the other results are not presented here it also contributes towards the conclusions made from the results.

The average cylinder compressive strengths for the mixes were 48.6MPa, 52.1MPa and 56.4MPa for the 0.5% SFRC, 0.75% SFRC and the 1.0% SFRC, respectively. Thus, the obtained ultimate strengths are larger than that of the specimens utilised in the three point bending tests, which was 40MPa. It is also noticed that an increase in fibre content resulted in an increased crushing value. This differs from the compressive behaviour obtained in Chapter 3, where the crushing values were similar.

In Figures 5.16 to 5.23 the measured moment-load, moment-curvature and moment-rotation relations are presented for each specimen. Also, a summary of the test results and the preliminary moment redistribution results are presented in Table 5.1 and Table 5.2, respectively.

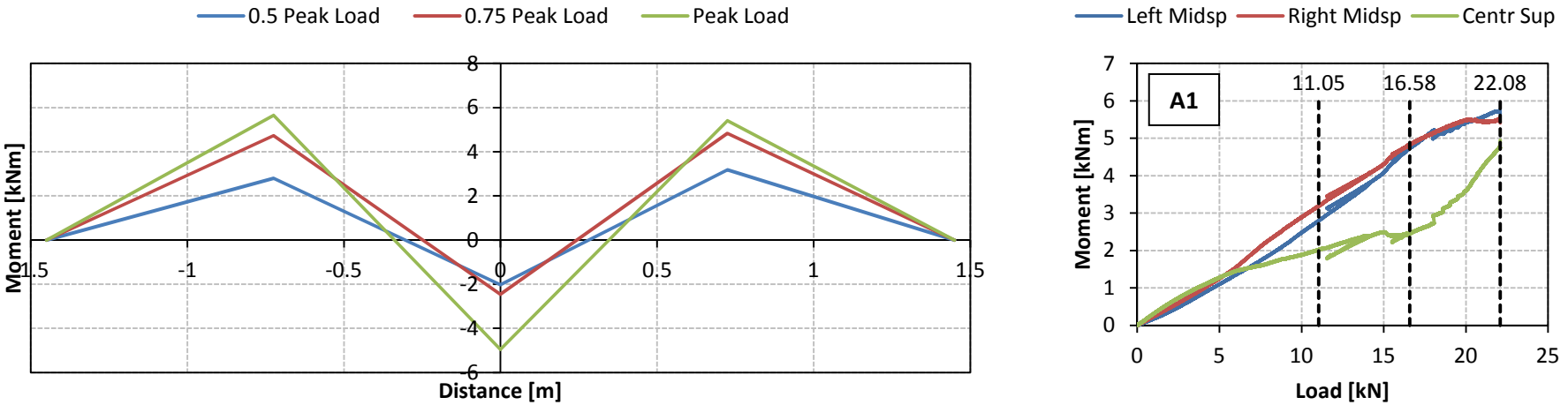

a) *b*)

Figure 5.12 Specimen A1. a) Bending moment distribution; b) Bending moment vs Load for the critical sections.

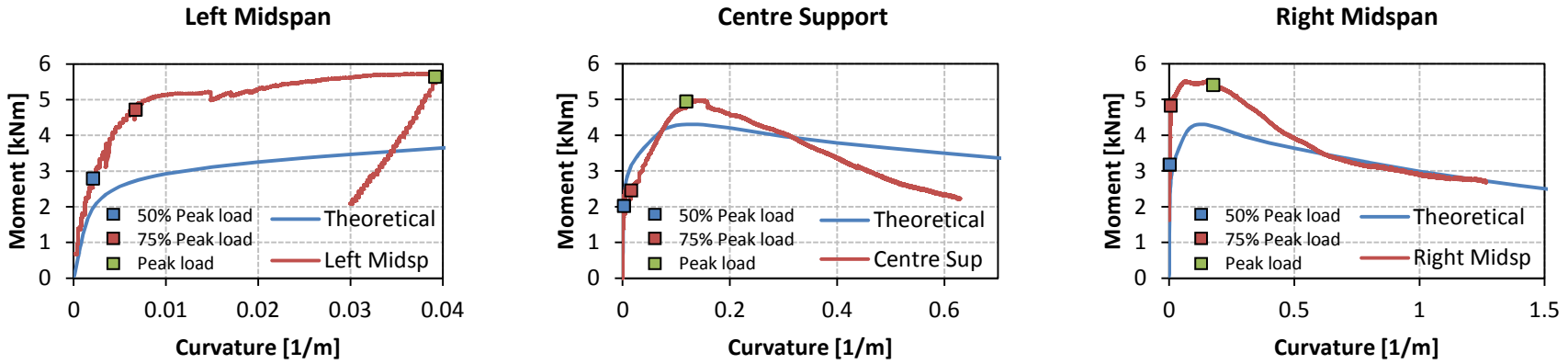

a) *b*) *c*)

Figure 5.13 Specimen A1. Experimental moment-curvature results for a) Left midspan, b) Centre support, c) Right midspan.

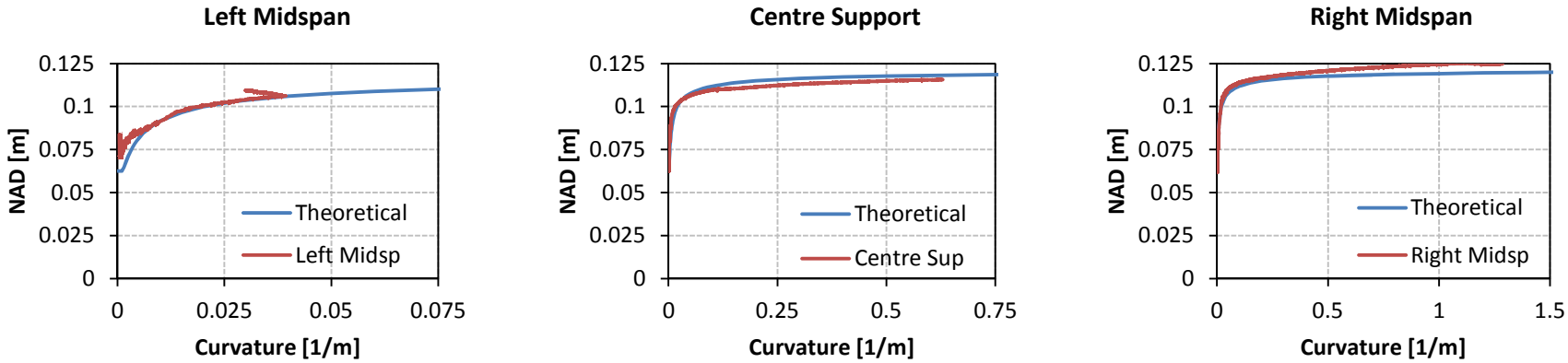

a) *b*) *c*)

Figure 5.14 Specimen A1. Experimental NAD-curvature results for a) Left midspan, b) Centre support, c) Right midspan.

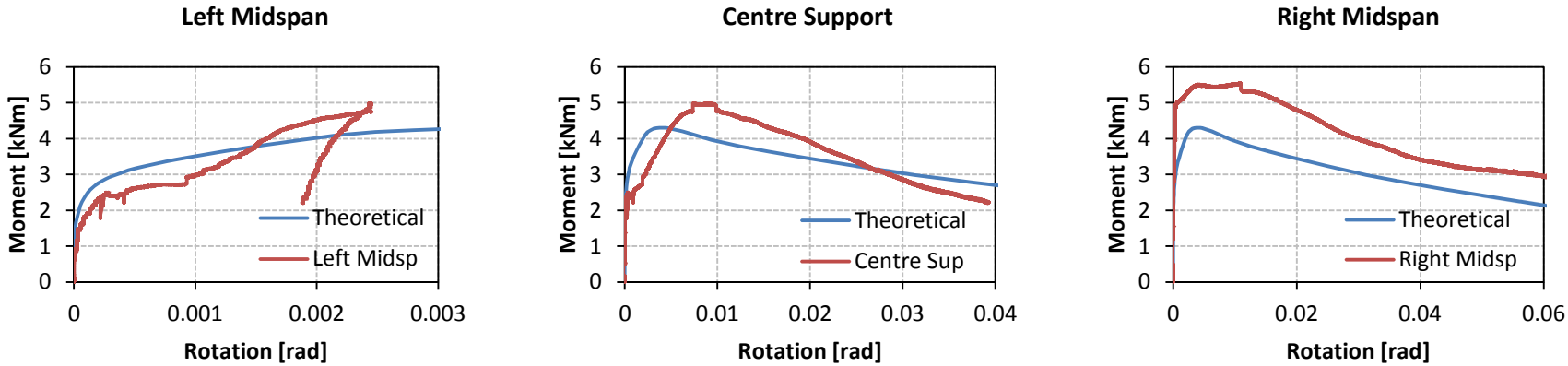

a) *b*) *c*)

Figure 5.15 Specimen A1. Experimental moment-rotation results for a) Left midspan, b) Centre support, c) Right midspan.

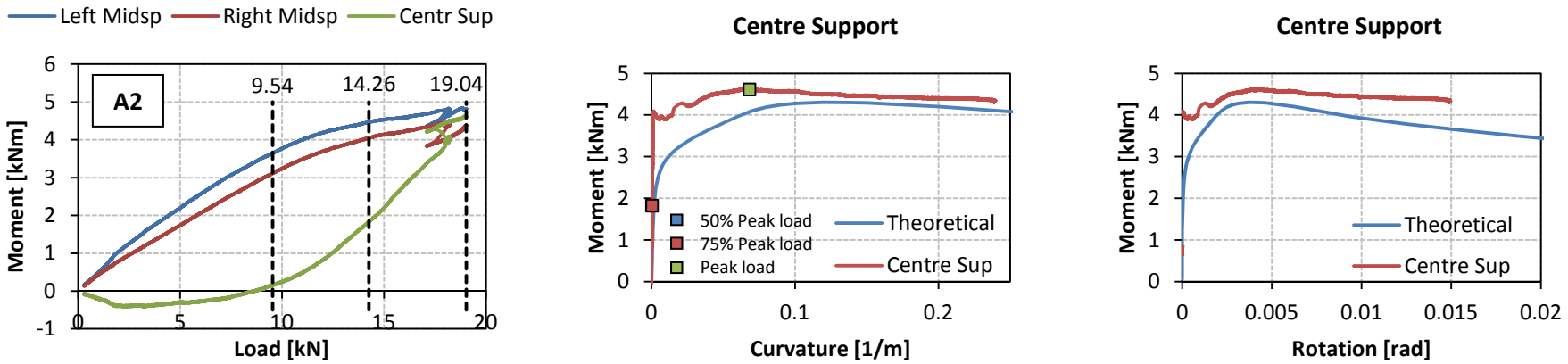

a) *b*) *c*)

Figure 5.16 Specimen A2 – a) Experimental moment-load relation at critical sections, b) Experimental moment-curvature result at centre support and c) Experimental moment-rotation result at centre support.

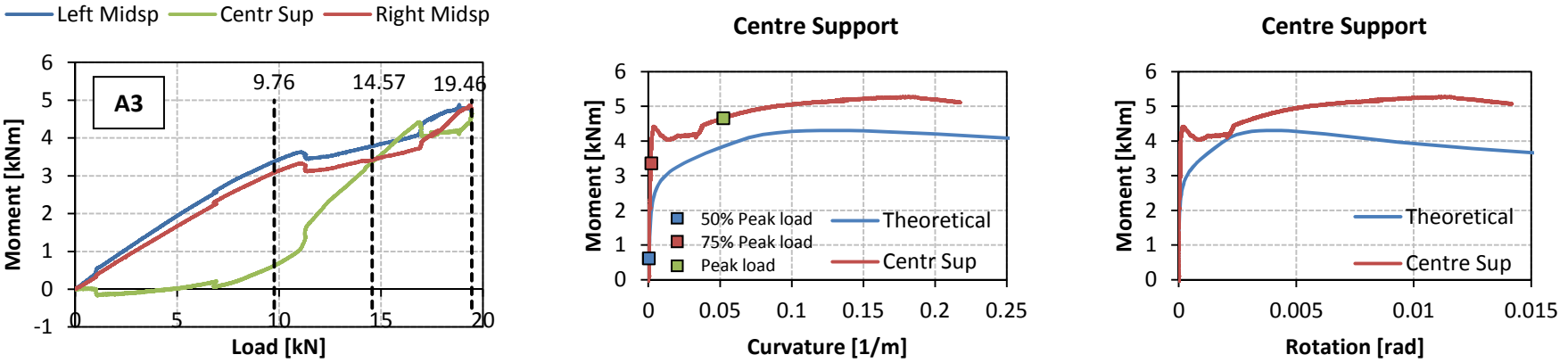

a) *b*) *c*)

Figure 5.17 Specimen A3 – a) Experimental moment-load relation at critical sections, b) Experimental moment-curvature result at centre support and c) Experimental moment-rotation result at centre support.

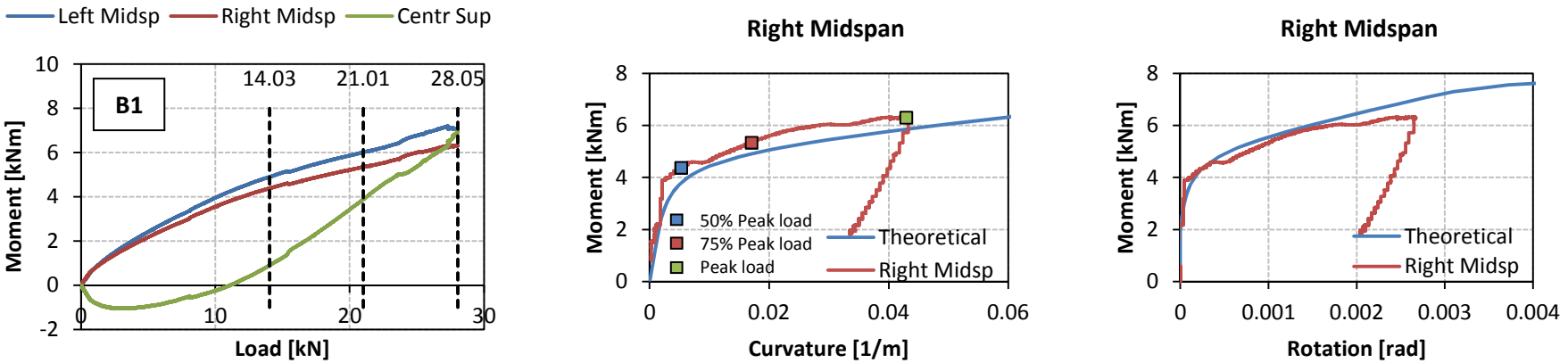

a) *b*) *c*)

Figure 5.18 *Specimen B1 – a) Experimental moment-load relation at critical sections, b) Experimental moment-curvature result at right midspan and c) Experimental moment-rotation result at right midspan.*

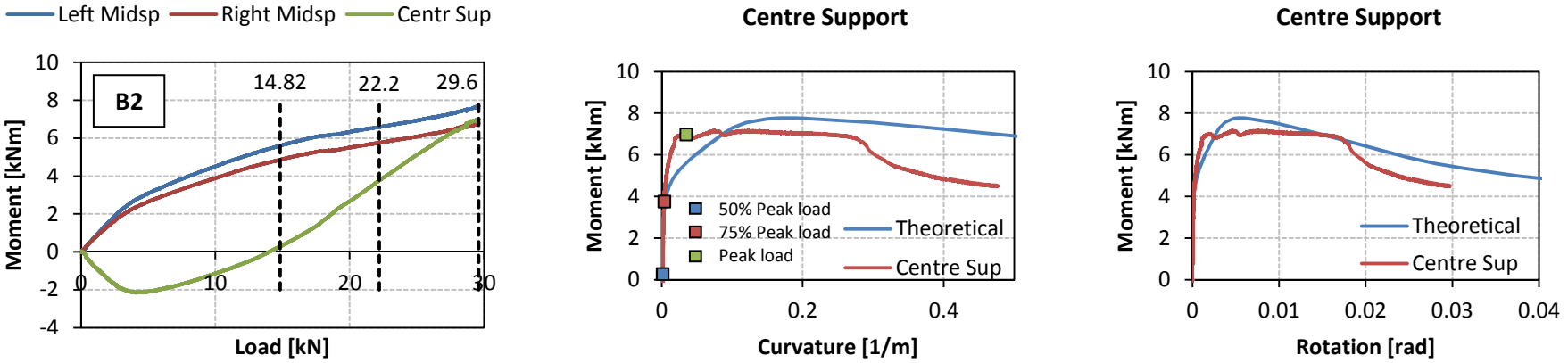

a) *b*) *c*)

Figure 5.19 *Specimen B2 – a) Experimental moment-load relation at critical sections, b) Experimental moment-curvature result at centre support and c) Experimental moment-rotation result at centre support.*

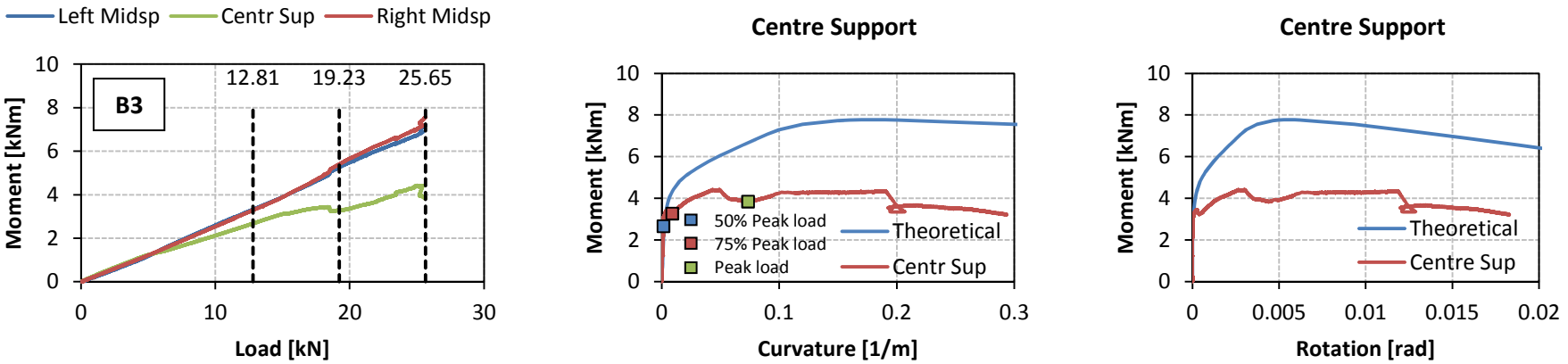

a) *b*) *c*)

Figure 5.20 Specimen B3 – a) Experimental moment-load relation at critical sections, b) Experimental moment-curvature result at centre support and c) Experimental moment-rotation result at centre support.

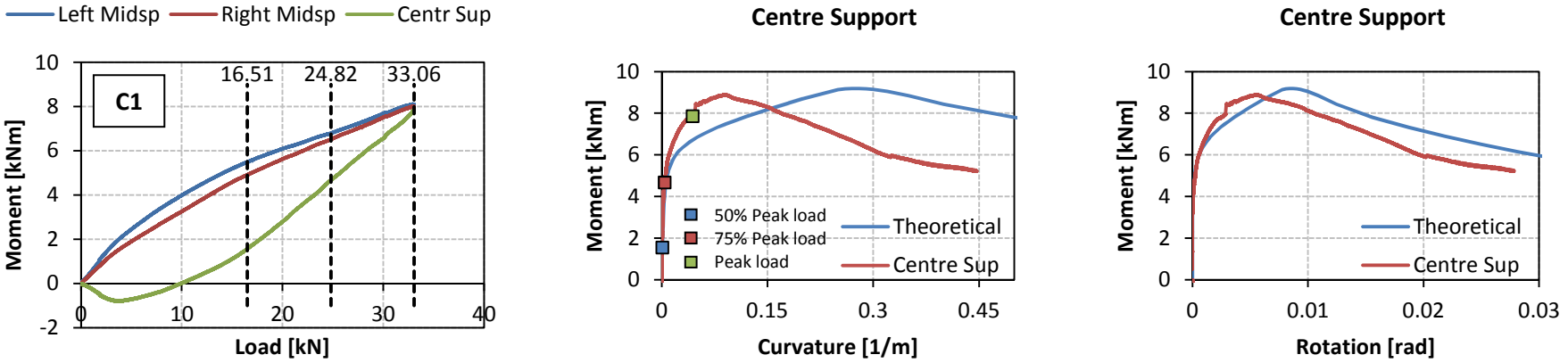

a) *b*) *c*)

Figure 5.21 Specimen C1 – a) Experimental moment-load relation at critical sections, b) Experimental moment-curvature result at centre support and c) Experimental moment-rotation result at centre support.

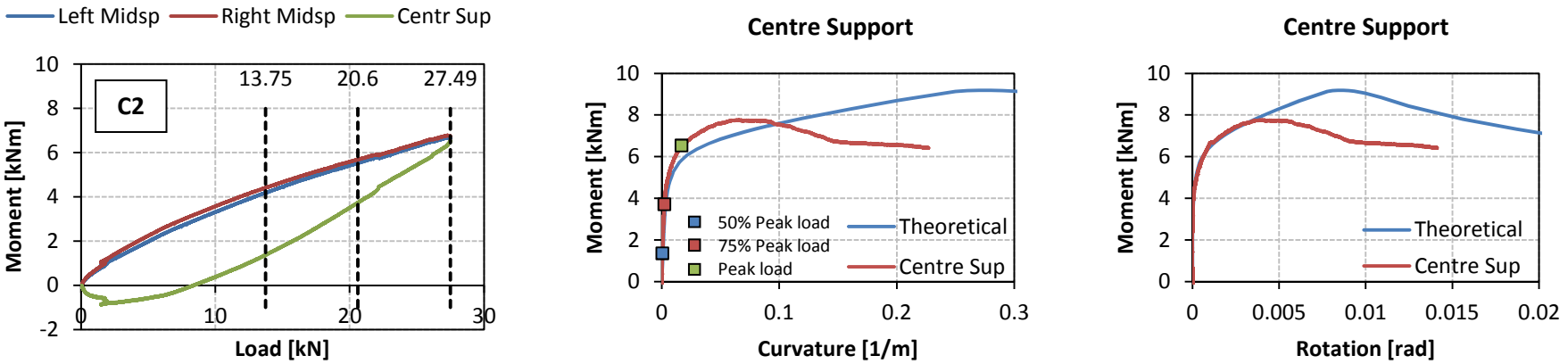

a) *b*) *c*)

Figure 5.22 Specimen C2 – a) Experimental moment-load relation at critical sections, b) Experimental moment-curvature result at centre support and c) Experimental moment-rotation result at centre support.

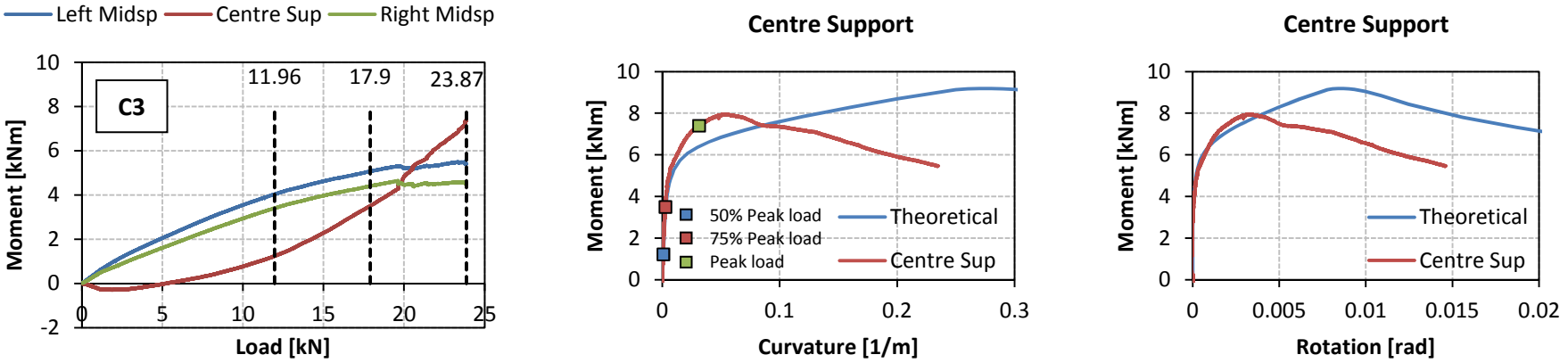

a) *b*) *c*)

Figure 5.23 Specimen C3 – a) Experimental moment-load relation at critical sections, b) Experimental moment-curvature result at centre support and c) Experimental moment-rotation result at centre support.

Table 5.1 Summary of test results for the critical sections at failure.

		LEFT MIDSPAN				CENTRE SUPPORT				RIGHT MIDSPAN			
Specimen	P_{fail} [kN]	M_{fail} [kNm]	κ_{fail} [1/m]	ϑ_{fail} [rad]	NAD_{fail} [m]	M_{fail} [kNm]	κ_{fail} [1/m]	ϑ_{fail} [rad]	NAD_{fail} [m]	M_{fail} [kNm]	κ_{fail} [1/m]	ϑ_{fail} [rad]	NAD_{fail} [m]
A1	22.08	5.65	0.039	0.00245	0.106	-4.95	-0.118	0.00735	0.110	5.41	0.176	0.01094	0.116
A2	19.04	4.81	0.005	0.00026	-	-4.62	-0.068	0.00423	0.107	4.38	0.127	0.00791	0.119
A3	19.46	4.69	0.176	0.01097	0.121	-4.66	-0.052	0.00325	-	4.76	0.078	0.00487	-
B1	28.05	7.07	-	-	-	-6.96	-	-	-	6.31	0.043	0.00263	0.106
B2	29.60	7.69	0.002	-	-	-6.98	-0.035	0.00211	0.100	6.79	0.065	0.00401	0.112
B3	25.65	7.19	0.022	0.00129	0.102	-3.86	-0.073	0.00453	0.103	7.54	0.072	0.00445	0.112
C1	33.06	8.10	0.032	0.00191	0.098	-7.86	-0.044	0.00265	0.106	8.01	0.106	0.00655	0.111
C2	27.49	6.65	0.023	0.00134	0.100	-6.55	-0.017	0.00096	0.091	6.73	0.656	0.04092	0.105
C3	23.87	5.39	-	-	-	-7.41	-0.031	0.00188	0.101	4.51	-	-	-

Table 5.2 Summary of moment redistribution results.

	FAILURE			ELASTIC	MOMENT REDISTRIBUTION	
Specimen	P_{fail} *[kN]*	M_{centr} *[kNm]*	ϑ_{centr} *[rad]*	$M_{e,centr}$ *[kNm]*	δ *[-]*	*MR [%]*
A1	22.08	-4.95	0.00735	-6.00	0.824	17.6
A2	19.04	-4.62	0.00423	-5.18	0.893	10.7
A3	19.46	-4.66	0.00325	-5.29	0.881	11.9
B1	28.05	-6.96	-	-7.63	0.913	8.7
B2	29.60	-6.98	0.00211	-8.05	0.868	13.2
B3	25.65	-3.86	0.00453	-6.97	0.553	44.7
C1	33.06	-7.86	0.00265	-8.99	0.875	12.5
C2	27.49	-6.55	0.00096	-7.47	0.876	12.4
C3	23.87	-7.41	0.00188	-6.49	1.141	-14.1

*The shaded results are that of outliers in terms of moment redistribution calculations.

5.1.6. Discussion of results

5.1.6.1. Moment-load graphs

At first glance the structural behaviour differs from what was expected theoretically. From Table 5.1 it is concluded that the structural capacity is similar for the specimens of the same mixture, with the deviation in the peak load more pronounced for the specimens with 1.0% volume fibres.

0.5% SFRC specimens

Specimen A1 correlates well with the expected behaviour at first, which implies that the bending moment at the centre support is greater than that of the midspans. At about a load of 5kN the moment development decreases at the centre support with the midspan moments increasing at an increased rate and at about 18kN the moment at the centre support develops faster in relation to that of the midspans until failure commences. This graph is important as it indicates the process of how the moment development is shifted about the length of the specimen, which implies the occurrence of moment redistribution. Thus, the bending moments are redistributed towards the stiffer regions as cracks develop at the critical sections.

Specimens A2 and A3 on the other hand indicate different structural behaviour compared to the first specimen and the theoretical results. At the beginning of the test the bending moment at the centre support is positive, which is the opposite of the expected negative bending moment. The rate of the moment development at the centre support is much lower in relation to that of the midspans. As the test continues there is a point where the resistance at the midspans is less contributing, thus inducing the redistribution of the forces towards the centre support (stiffer region), which causes an increase in the development of the bending moment at the centre support until failure occurs.

The different structural behaviour recorded for specimen A2 and A3 is ascribed to the occurrence of the end supports carrying a larger load during the start phase of the test and as the test continues the influence of the centre support become more pronounced as it provides greater resistance with time. The most probable explanation for such behaviour would be an error in the test setup, with the centre support not fully supporting the contributing weight, as modelled in the numerical analysis, due to the geometrical alignment. This could most probably be due to either a small gap

between the support and the specimen and/or due to a difference in the stiffness of the centre support in relation to the end supports.

0.75% SFRC specimens

Specimens B1 and B2 present similar structural behaviour as described for specimens A2 and A3. After studying the pictures provided by the ARAMIS system and from the reaction force calculations it was concluded that there was a 1-2mm gap between specimen B2 and the centre support at the start of the test procedure. This implies that the specimen was in four point bending before the beam was supported by the centre support.

Specimen B3 presents similar structural behaviour as specimen A1, with the centre support bending moment initially developing at a higher rate, which diminishes with time and with failure occurring when the maximum resistance has been reached for the midspans.

1.0% SFRC specimens

All three specimens conform to the behaviour described for specimens A2 and A3. Although the shapes are similar, there is a major difference in the values of the peak load. This difference could be due to weak points at structurally critical positions. The result for specimen C3 indicates that the capacity at the midspans is less than at the centre support, which could be attributed to different volumes of fibres at these sections.

5.1.6.2. Moment curvature results

It is useful to examine the moment-curvature results in conjunction with the moment-load results as it provides a better understanding of the structural integrity at the critical sections for the duration of the test procedure. From the results shown in Figure 5.13 it is evident that failure occurs when the maximum capacity has been reached at both the critical sections of a single midspan and at the centre support.

0.5% SFRC specimens

It is evident that the theoretical moment-curvature results under predict the real sectional behaviour of all three specimens at all the measured critical sections, as seen in Figures 5.13, 5.16 and 5.17. During the inverse analysis procedure it was noticed that the cracking load was under predicted to enable the theoretical force-displacement curve to fit the experimental results. It is found that the shapes of the experimental and theoretical curves are similar and that the curvatures at the peak moments correspond well, which implies that the theoretical approximation could be acceptable.

0.75% SFRC specimens

The magnitude of the ultimate bending capacity according to the experimental tests is in the vicinity of the theoretically determined capacity. The shapes of the curves correlate well, but the theoretical derivation overestimates the curvatures at the peak moments. Due to certain complications the moment-curvature relation could not be calculated for the failing critical sections of specimen B1. The behaviour determined at the centre support of specimen B3 presented irregular results. The capacity calculated at this section was only half of the sectional capacity at the midspans, which invoked a large moment redistribution value, as seen in Table 5.2.

1.0% SFRC specimens

The comparison between the experimental and the theoretical results are similar to that discussed for the 0.75% SFRC members. The shape of the experimental curves and the magnitude of the bending capacity correspond well with that derived theoretically. As mentioned for the 0.75% SFRC specimens, it was found that the curvature at the peak moment was over predicted with the theoretical model.

5.1.6.3. Moment rotation results

The results obtained for this characteristic provides an indication of the actual rotation behaviour of the plastic hinges.

0.5% SFRC specimens

The shapes of the experimental curves correspond well with that of the theoretical results, although the centre support of specimen A3 produced a curve that deviates from the other obtained results. The theoretical estimation also under predicts the rotational value at the ultimate capacity, which concurs with a larger rotational ductility.

0.75% SFRC specimens

The shape of the experimental curves also corresponds well with that of the theoretical derivation. The theoretical approximation overestimated the experimental rotational value at the peak moment, which concurs with a smaller rotational ductility.

1.0% SFRC specimens

The overall shape of the theoretical curves corresponds well with that of the experimentally obtained results. As for the 0.75% SFRC members the theoretical model also over estimates the rotational value at the peak moment, which concurs with a smaller rotational ductility.

5.1.6.4. Moment redistribution results

The amount of moment redistribution calculated at the point of failure is shown in Table 5.2. These are preliminary results and the moment redistribution percentages calculated could be incorrect depending on certain factors, which are discussed next.

From the moment-load graphs, it was determined that most of the specimens indicated a structural behaviour that deviates from the expected results, possibly due to a setup error, as explained. The experimental moment redistribution-plastic rotation relation could not be determined due to the incorrect structural behaviour, which induced irregular moment redistribution results.

The results indicated that the moment redistribution value was large at the start of the test and gradually decreased until failure commenced. The amount of moment redistribution is directly proportional to the ratio between the elastic and actual bending moment. Thus, as the bending moment at the centre support develops at a later stage, the moment redistribution was calculated to be larger than expected.

There are two exceptions to the possible error in the test setup, namely specimens A1 and B3. Both these specimens' moment-load responses indicate that the forces were initially distributed correctly as determined with the elastic law. Both their moment-redistribution calculations is considered to be legitimate, although there is a concern with specimen B3's measured moment-curvature response at the centre support. Only half the capacity has been reached in relation to that of the other critical sections, which justifies the large moment redistribution value shown in Table 5.2.

The rotational values of the plastic hinge at the centre support (Table 5.2) suggest that its magnitude decreases with an increase in the volume fibres used. With an increased fibre content the CMOD decreases, but more cracks may develop, as discussed in Section 5.1.7. Thus, smaller rotations are calculated which could be ascribed to the loss of deformation measurements corresponding with the cracks that develop outside the LVDT measuring range.

5.1.6.5. Concluding remarks

The influence of the possible errors in the test setup is a major concern as it complicates the procedure to verify the moment redistribution-plastic rotation behaviour. With the moment-curvature and moment-rotation theoretical derivations the major uncertainty is the crack band width. With the five point bending tests it was discovered that the crack band width differs among the different SFRCs. With an adjustment of this characteristic more promising theoretical results could be derived.

The overall shapes of the theoretical results are representative of the experimental results, although the values of the peak characteristics differ. These differences could be ascribed to the actual

difference in the crack band widths. To verify the cause of the irregular moment-load relations, it is required to validate the test setup by performing computational analyses with the predicted setup errors taken into account. If these finite element models accurately predict the experimental results obtained, the numerical moment redistribution-plastic rotation model is considered to be valid.

5.1.7. ARAMIS results

The ARAMIS system enabled the calculation of the rotation experienced by the total hinge at the centre support utilising the capability to measure an area larger than the gauge length of the LVDTs. The larger measuring area enabled the identification of the positions of the all the cracks that developed in the plastic hinge region.

5.1.7.1. Moment-rotation responses

The moment-rotation responses obtained with the ARAMIS are compared to that obtained with the LVDTs and the theoretical predictions, as shown in Figures 5.24 to 5.26. It was found that the ARAMIS and LVDT results are similar, which indicates that the LVDTs provided a good approximation of the real behaviour at the hinges. It is noticed that the ARAMIS results simulate slightly larger rotational values in relation to the LVDT responses, which is ascribed to the rotations occurring outside the scope of the LVDT measuring range.

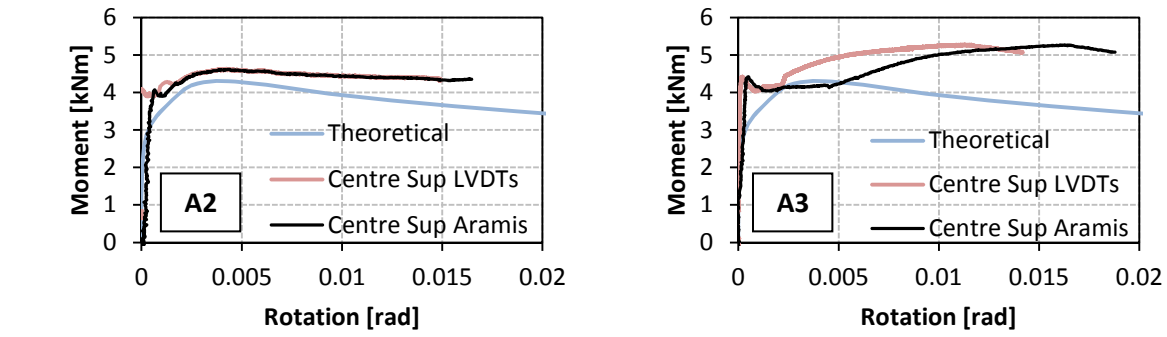

a) *b*)

Figure 5.24 ARAMIS. a) Moment rotation for A2; b) Moment-rotation for A3.

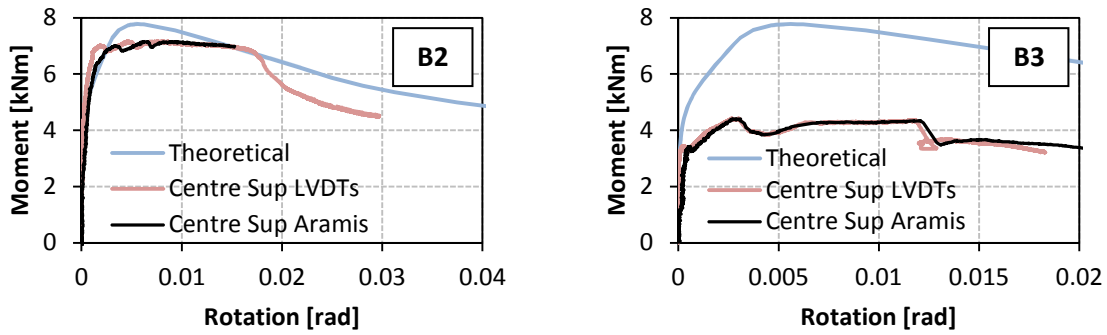

a) *b*)

Figure 5.25 ARAMIS. a) Moment-rotation for B2; b) Moment-rotation for B3.

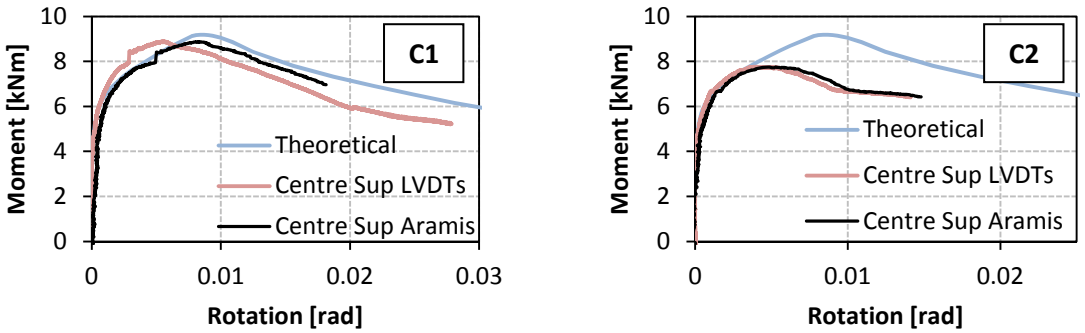

a) *b*)

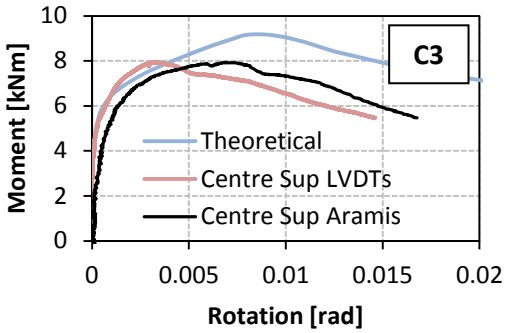

c)

Figure 5.26 ARAMIS. a) Moment-rotation for C1; b) Moment-rotation for C2; c) Moment-rotation for C3.

5.1.7.2. Plastic hinge responses

In the following results the formation of the plastic hinge at the centre support is investigated, with the focus on crack development. The results shown in Figures 5.27 to 5.34 are the strain and

displacement measurements in the x-direction, with the former providing a visual representation of the crack development and the latter indicating the part of the member that rotates about the major crack. It should be noted that the ARAMIS measured the displacements of the surface on the opposite side of the specimen where the LVDTs were implemented. Thus, the crack development could differ from that obtained on the LVDT surface.

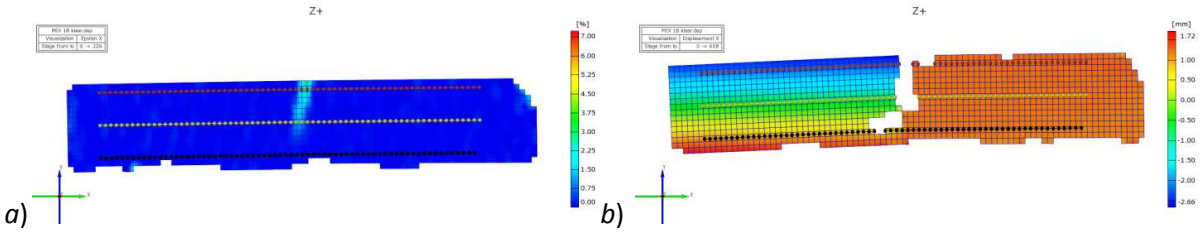

Figure 5.27 Specimen A2. a) Strain in X-direction; b) Displacement in X-direction.

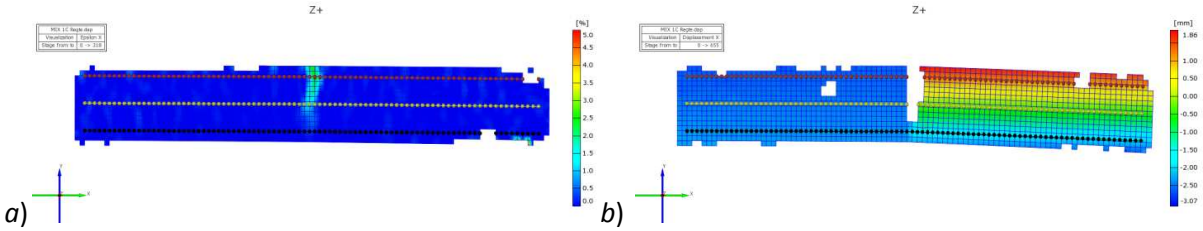

Figure 5.28 Specimen A3. a) Strain in X-direction; b) Displacement in X-direction.

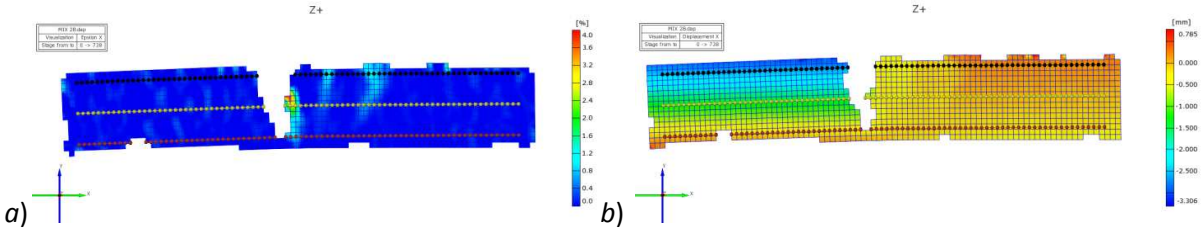

Figure 5.29 Specimen B2. a) Strain in X-direction; b) Displacement in X-direction.

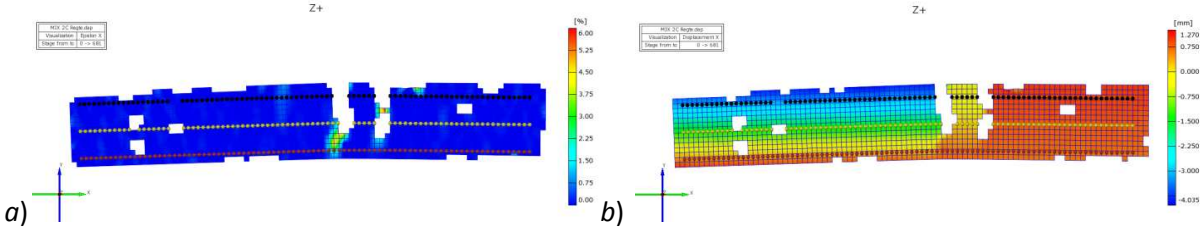

Figure 5.30 Specimen B3. a) Strain in X-direction; b) Displacement in X-direction.

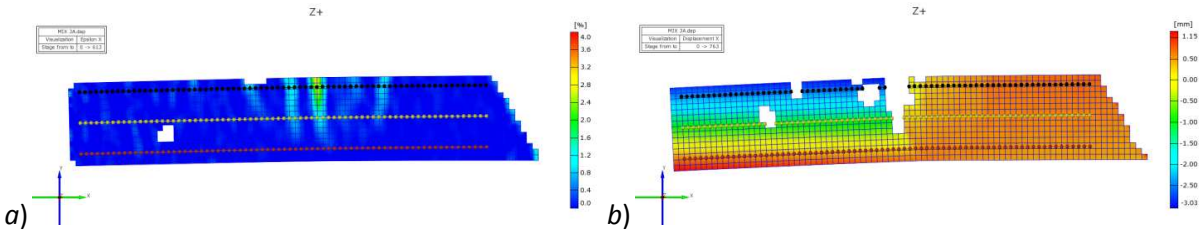

Figure 5.31 Specimen C1. a) Strain in X-direction; b) Displacement in X-direction.

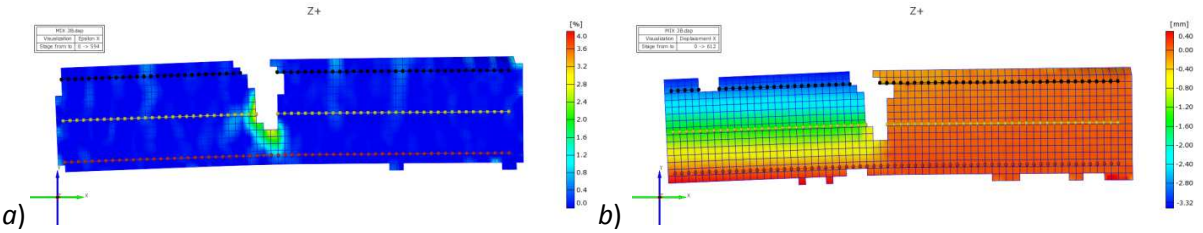

Figure 5.32 Specimen C2. a) Strain in X-direction; b) Displacement in X-direction.

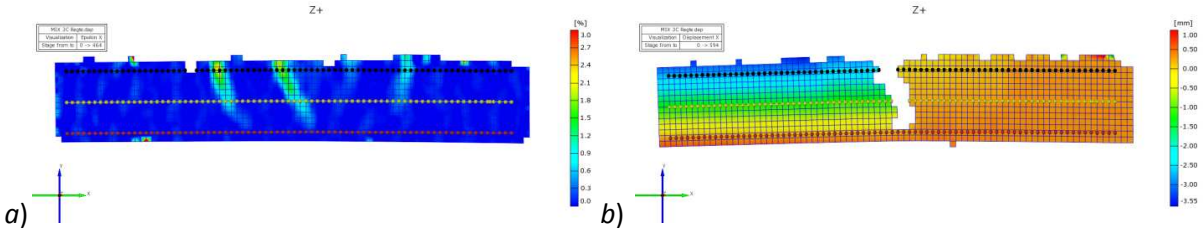

Figure 5.33 Specimen C3. a) Strain in X-direction; b) Displacement in X-direction.

The total hinge length increased with an increased volume of fibres, which is ascribed to the development of a larger number of cracks. The specimens indicate flexural hardening behaviour at the centre support due to multiple crack formation. The results presented in Table 5.3 were calculated from the ARAMIS data with the exception (indicated with an asterisk) of specimen B1, which was determined with measurement on the actual specimen. The 0.5% SFRC specimens only developed a single crack at the plastic hinge, thus the theoretical values implemented in the derivation of the moment-rotation model is shown (shaded results).

From the results presented in Table 5.3 it is derived that the average crack spacing increased with an increase in the volume fibres, which was not expected. With a larger fibre volume it is expected to obtain a larger amount of cracks that are spaced closer together. This assumption is based on the development of pure flexural cracks, but at the centre support the shear behaviour has a major

effect on the crack orientation. Shear behaviour is characterised by the formation of diagonal cracks, which are seen in Figures 5.29 to 5.33.

Table 5.3 Summary of crack development results at centre support plastic hinge.

Specimen	*# Cracks*	*Total hinge length [mm]*	*Average crack spacing [mm]*
A1	1	62.5	62.5
A2	1	62.5	62.5
A3	1	62.5	62.5
B1	3	220*	110*
B2	3	135	67.5
B3	3	145	72.5
C1	5	180	45.0
C2	4	263	87.7
C3	4	245	81.7

5.1.7.3. Concluding remarks

The ARAMIS system provided valuable data about the behaviour of the plastic hinge. The device is useful in determining other characteristics such as the development of the neutral axis in the plastic hinge, but this requires intensive calculation methods that are time consuming. The moment-rotation results are similar to that obtained with the LVDT measurements. It was found that the plastic hinge length increased with an increase in the fibre volume, with an increase in the amount of cracks developed. Also, it is evident that the crack band width differs among the SFRC members. The ARAMIS also aided in the approximation of the vertical displacement of the specimen, if any, at the centre support. These results were applied in the validation of the test setup procedure that is discussed in the following section.

5.2. Validation of test

The purpose of this section is to justify the irregular results obtained from the five point bending tests with the intention to validate the theoretical models used to predict the structural behaviour. The task is performed by modelling the proposed setup errors in finite element analysis software and comparing the numerical results with that obtained from the experimental tests. After studying the images of the centre support, taken by the ARAMIS, two setup errors were considered. Namely

CASE I, which implies that there is a small gap between the test specimen and the centre support at the start of test and CASE II, which implies that the stiffness of the centre support is less than that of the end supports.

5.2.1. *CASE I* – Gap between specimen and centre support

The reference image taken before testing is conducted indicated that certain specimens were not in contact with the centre support when testing initiated. I was possible to determine the size of this gap with measuring software. A contact analysis procedure is performed with the centre support situated a small distance below the end supports. Thus, the centre support provides resistance when the specimen comes in contact with it. It was possible to perform this analysis with the same model as used in Section 4.4, with some adjustments made.

5.2.1.1. Geometry

The layout of the model is shown in Figure 5.34. The layout is exactly the same as discussed in Section 4.4, but with a few additions to invoke the contact process.

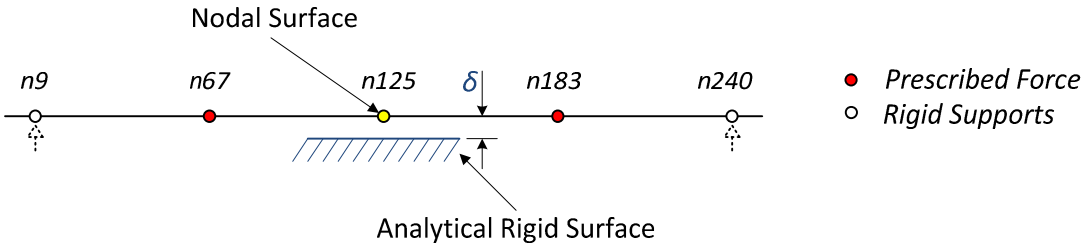

Figure 5.34 Schematic representation of model implemented (CASE I).

5.2.1.2. Elements and meshing

The same beam elements are used as for the previous model with the element size remaining 12.5mm. To perform a contact analysis two surfaces had to be constructed. A *master surface* was

created beneath the expected position of contact, while a *slave surface* was created on the specimen to represent the contact point.

The master surface provides a rigid support and is located a distance, δ, beneath the centre of the beam model, which physically represents the gap between the specimen and the centre support. This distance is calculated by implementing the reference image into measuring software.

5.2.1.3. Boundary conditions

As seen in Figure 5.34, the end supports are constrained in the y-direction, thus producing rigid roller supports. The analytical rigid surface provides a contact surface which is constrained in all directions.

5.2.1.4. Material properties

The material properties of all the beam elements are the same as presented in Section 4.4. To consider that first cracking initiates at a midspan, it was decided to weaken the moment-curvature relation of an element at the right midspan with 1%.

5.2.1.5. Analysis procedure

To correctly simulate the test procedure, a force-controlled analysis procedure was conducted, with the force applied at each midspan. The ultimate force was prescribed to be just larger than the expected capacity of the test specimen. To retrieve the post-peak behaviour it was necessary to utilise an arc-length method.

To ensure the compatibility of the numerical results with the experimental results, representative specimens (A2, B2 and C1) were selected and the numerical analyses were conducted with a δ-value that provided similar results. The shapes of the numerical and experimental moment-load curves were compared to validate the results. The δ-value for specimens A2, B2 and C1 were 0.3mm, 1.7mm and 0.7mm, respectively.

5.2.1.6. Results

Deformed shape

The general deformed shape is presented in Figure 5.35, with the results scaled using a factor of 2. It should be noted that the numerical failure shape is similar to the results obtained from all of the experimental tests. Due to similarity, the deformed shape is only illustrated for the 0.5% SFRC member, but the deformed shapes for the other mixes are presented in Appendix C.

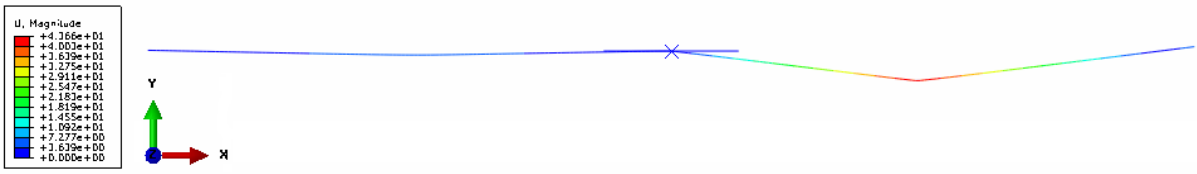

Figure 5.35 Vertical displacement presented on deflected shape for 0.5% SFRC composite (CASE I).

Moment-load results

The numerical moment-load results for all three specimens are presented in Figures 5.36 to 5.38. In these figures the bending moment is considered to have the opposite sign convention for comparison purposes.

The similarity between the numerically predicted and the experimental results is more prominent for specimens B2 and C1. For specimen B2 the numerical results accurately predicted the experimental results, as the shapes of the curves are similar up to failure. It is concluded that the cause of the irregular results obtained for this specimen was greatly due to the influence of the gap between the specimen and the centre support.

For specimen C1 the numerical slope of the curves before contact is initiated differs from that obtained from the experimental test, with the experimental bending moment developing at a lower rate. In contrast, the shape of the curves after contact is similar.

For specimen A2 the influence of the gap is not as major as for the other specimens. It was concluded that there was a gap of about 0.3mm, which is a fraction of the magnitude predicted for

the other specimens. The difference in the shapes of the curves is more pronounced for this specimen. From the results it could be interpreted that the minor influences that caused the deviation of the resulting shapes for specimen C1 have a greater contribution in influencing this specimen's structural behaviour. Stated otherwise, the actual gap small enough that the influence that it would have is minor in relation to other external factors that could be responsible for the irregular results.

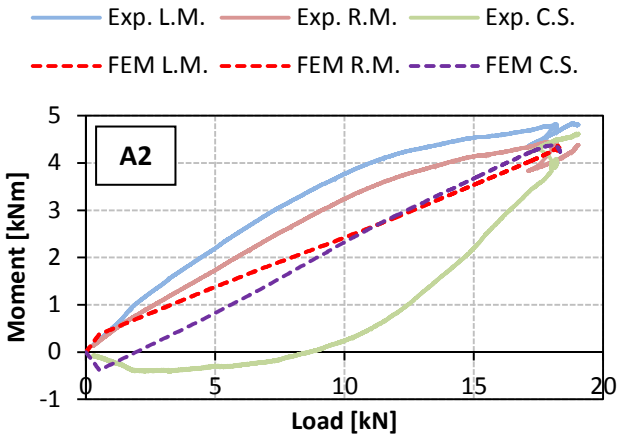

Figure 5.36 Comparison of moment-load curves for specimen A2.

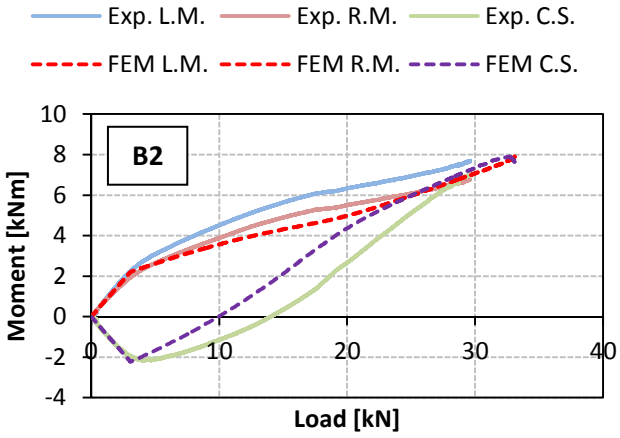

Figure 5.37 Comparison of moment-load curves for specimen B2.

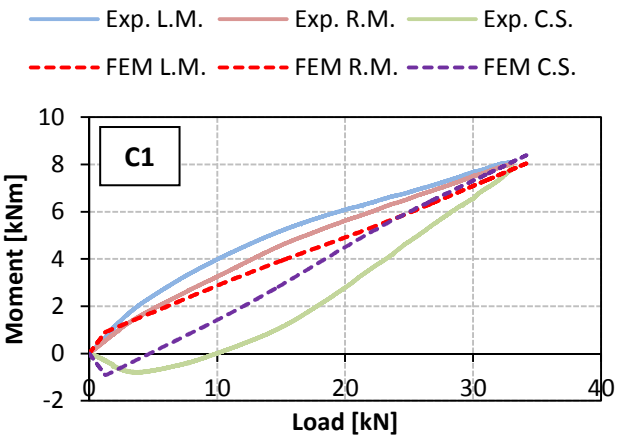

Figure 5.38 Comparison of moment-load curves for specimen C1.

From the obtained numerical results it is concluded that the gap between the test specimen and the centre support was a contributing factor in the measurement of the irregular results. With "irregular results" it is meant that the expected results were not obtained.

5.2.2. *CASE II* – Centre support having lower stiffness in relation to end supports

The centre support differed from the end supports in the test setup, which could have influenced the results of a statically indeterminate test. From the images taken during the test procedure it was noticed that the centre support displaced a distance downwards until failure commenced. It was required to validate if a possible difference in the relation between the stiffness of these supports could have influenced the structure's behaviour as such that it contributed to the experimental results obtained.

5.2.2.1. Geometry

Geometrically the model remains the same as for Case I, with the only adjustments the elements used at the centre support and specific boundary conditions. A layout of the model is shown in Figure 5.39.

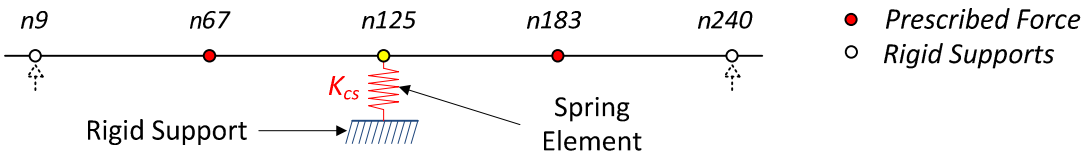

Figure 5.39 Schematic representation of model implemented (CASE II).

5.2.2.2. Elements and meshing

As for the previous models, B21 beam elements were used to represent the slab specimen with an element size of 12.5mm. A linear spring element was used to simulate a support with a specific stiffness, K_{cs}, at the position of the centre support. The spring acts in the direction of the axis it is specified in, which is vertically.

5.2.2.3. Boundary conditions

As for the previous case, the end supports were constrained in the y-direction to simulate the effect of rigid roller supports. The spring element was defined with two nodes, with the bottom node constrained in both the x- and y-directions and the top node attached to the beam elements at the position of the centre support.

5.2.2.4. Material properties

The material properties for the beam elements are defined exactly as for the previous case, where the moment-curvature input was defined. Also, the weaker element was placed at the same position as before. The stiffness (K_{cs}) of the spring element at the centre support is representative of the axial stiffness, which is provided with the value of the force per relative displacement (N/mm). This value was approximated with the following equation

$$P = K_{cs}.\Delta_v \tag{5.14}$$

with the displacement (Δ_v) and force (P) known at any time during the test procedure. It was found that a value of 10000N/mm resulted in a representative structural behaviour.

5.2.2.5. Analysis procedure

The procedure was the same as for Case I, with a force-controlled procedure implemented at the midspan nodes. The representative specimens for this case were specimens A2, B1 and C1.

5.2.2.6. Results

Deformed shape

As for the previous case, the deformed shapes among the SFRC members were similar and the deformed shape for the 0.5% SFRC member is shown in Figure 5.40, with the other specimens' results presented in Appendix C.

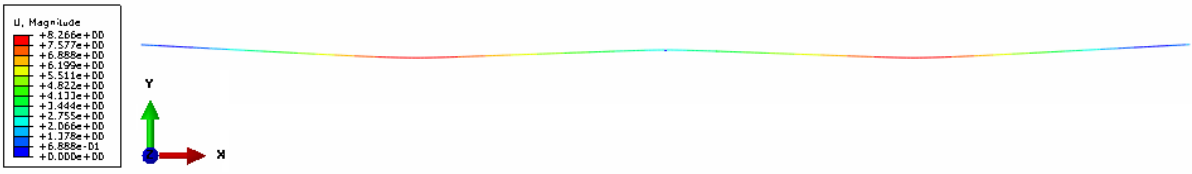

Figure 5.40 Vertical displacement presented on deflected shape for 0.5% SFRC composite (CASE II).

Moment-load results

The numerical moment-load results for all three specimens are presented in Figures 5.41 to 5.43. In the previous case study it was determined that a gap between the test specimens and the centre support caused the specimen to follow four point bending characteristics before contact is made. Thus, the structure is only influenced by the support after contact has initiated. The shape of the curves after contact is initiated correlates well with the experimental results of all three specimens, with the shift in the results justified by the influence of the gap at the support.

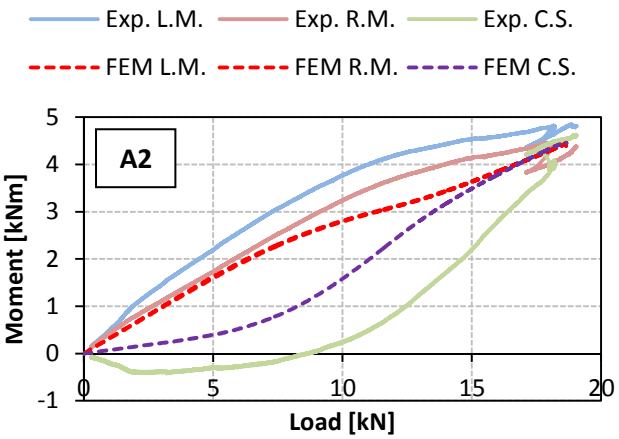

Figure 5.41 Comparison of moment-load curves for specimen A2.

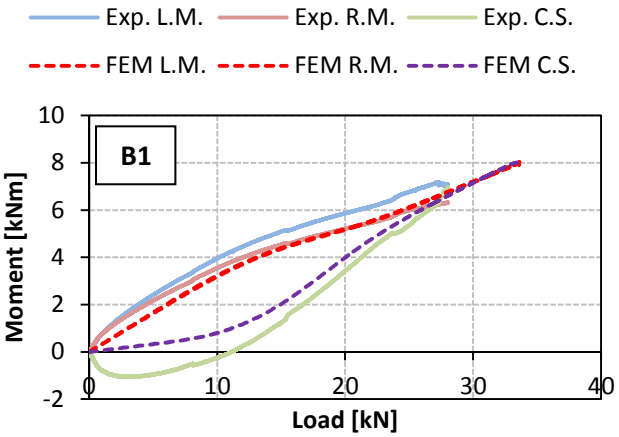

Figure 5.42 Comparison of moment-load curves for specimen B1.

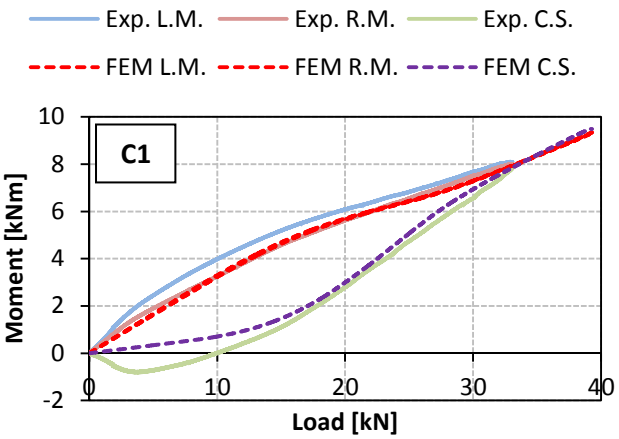

Figure 5.43 Comparison of moment-load curves for specimen C1.

5.2.3. Concluding summary

Subsequent to the comparative study between the experimental and numerical results, it is concluded that both setup errors were present, which resulted in the unexpected results. The contribution of either setup error differed for all of the specimens. When the gap between the centre support and the test specimen was large, its influence was more prominent in relation to the effect that the lower stiffness of the support would have. On the other hand, when the gap was relative small (specimen A2), the support stiffness has a larger influence, as seen in the comparison between the moment-load curves after contact has been initiated.

5.3. Validation of moment redistribution model

In the previous section the possible setup errors were investigated via finite element analyses. It was found that the structural behaviour due to the possible errors was correctly predicted with the finite element model. Together with the similarities between the theoretical and experimental member characteristics, the moment redistribution-plastic rotation responses derived in Section 4.4 is considered valid for the structure modelled in the finite element software.

The experimental moment redistribution values, which could not be correctly interpreted before, is now predicted with the assumed moment redistribution-plastic rotation model, by utilising the rotational values measured at the centre support. A possible range for the moment redistribution value is provided for each SFRC member, by investigating the differences between the theoretical and experimental pre-peak and post-peak moment-curvature responses.

5.3.1. Approximated results

The derived moment redistribution results for each specimen are presented in Table 5.4. The values were derived by implementing the calculated rotational values of the centre support at failure. These rotational values represent under predicted values for the rotational capacity at the centre support due to the influence of the setup errors, thus ensuring conservative moment redistribution results.

Table 5.4 Final moment redistribution values for all specimens.

Specimen	*Centre support rotation [rad]*	*MR [%] from tests*	Numerical MR values [%]
A1	0.00735	> or < 14	14.5
A2	0.00423	14	
A3	0.00325	12	
B1	-	-	13.1
B2	0.00211	8.5	
B3	0.00453	11	
C1	0.00265	9	9.5
C2	0.00096	9.4	
C3	0.00188	9.3	

5.3.2. Discussion

5.3.2.1. 0.5% SFRC

The post-peak moment-curvature values of specimen A1 decrease at a faster rate than predicted theoretically, thus the critical section's ability to maintain its capacity is over predicted. Thus, the moment redistribution value is expected to be less than that predicted by the model. On the other hand, the experimental rotational result is outside the scope of the predicted model, which implies a greater redistribution amount than the ultimate value shown in the model. Considering both these factors, the moment redistribution could be beneath or above the predicted moment redistribution value.

The moment-curvature relationships obtained with specimens A2 and A3 are similar to the theoretical responses, which imply that the moment redistribution values indicated in Table 5.4 is realistic.

5.3.2.2. 0.75% SFRC

No rotational values were recorded for the centre support of specimen B1. The post-peak moment-curvature slopes obtained for specimens B2 and B3 are similar to the theoretical predictions, which imply that the approximated amount of moment redistribution is realistic.

5.3.2.3. 1.0% SFRC

All of the specimens' post-peak moment-curvature slopes are similar to that of the theoretical predictions. Thus, the approximated moment redistribution values are considered to be realistic.

5.3.3. Conclusion

The approximated moment redistribution values are considered to be conservative as it is derived from the theoretical model using the rotational values obtained from the experimental tests, with the rotation at the centre support being under developed due to the errors in the setup. From the predicted moment redistribution values, it was found that the amount of moment redistribution at failure decreased with an increase in the volume fibres. The moment redistribution values ranges between 12% and 14% for the 0.5% SFRC members, between 8.5% and 11% for the 0.75% SFRC members and between 9% and 9.4% for the 1.0% SFRC members.

5.4. Summary

All the specimens failed with a critical section developing at the centre support and at the weaker midspan. The LVDTs provided accurate results, as the measured moment-rotation results were similar to that obtained with the ARAMIS.

With the measured moment-curvature and moment-rotation responses it was found that the bending capacity of the 0.5% SFRC members was under predicted. In the case of the 0.75% and 1.0% SFRC members, the capacity was slightly over estimated. The overall shapes of the curves were similar for all three composites. The rotational values at the peak bending moments correlated well with that predicted theoretically, except for that of the 1.0% SFRCs, where the theoretical rotational value was over estimated for all three specimens.

Certain complications with the setup directly affected the moment redistribution calculation. Due to undesirable structural behaviour, the first critical section did not develop at the centre support, but rather at the weaker midspan. This allowed for the incorrect representation of the moment redistribution calculation procedure. The setup errors were validated with finite element analyses

and it was concluded that the possible setup errors is either a gap between the specimen and the centre support or that the stiffness of the centre support is less than that of the end supports, or a combination of both.

These finite element models accurately predicted the structural behaviour, thus the theoretical moment redistribution-plastic rotation behaviour was considered to be valid. The validated model was utilised on the specimens in to determine the amount of moment redistribution experienced. It was found that the amount of moment redistribution at failure decreased with an increase in the volume fibres, with the moment redistribution values ranging between 12% and 14% for the 0.5% SFRC members, between 8.5% and 11% for the 0.75% SFRC members and between 9% and 9.4% for the 1.0% SFRC members. The rotational values at the instance of structural failure at the centre support also decreased with an increase in the volume fibres.

The theoretical moment redistribution-plastic rotation prediction is applicable for the assumed structure and developed until theoretical failure has occurred. From these predictions it is evident that about 9% moment redistribution is obtained for all three SFRCs until a plastic rotation value of $0.6x10^{-3}$rad is reached. With these numerical relationships it was concluded that the rotational values at failure increased with an increase in the fibre volume, with the exception of the 1.0% SFRC mix. It was also concluded that the amount of moment redistribution was directly affected by the shape of the moment-curvature relationship and specifically the angle of the post-peak slope, with a less steep slope providing greater structural integrity during plastic hinge formation.

CHAPTER 6

PARAMETER STUDY

The theoretical models derived in Chapter 4 were completed by assuming certain values for certain material characteristics that were unknown at the time. The key characteristic that featured in most of the models was the *crack band width* of each SFRC member. The aim of this chapter was to study the influence of this assumed value on the theoretical models by conducting a sensitivity analysis.

It was assumed that the crack band width had a value of half the section height, as proposed by Löfgren (2005). The sensitivity analysis was performed with viable crack band width values, to enable comparison with the experimental test results. With the ARAMIS measurements it was concluded that the crack spacing for all the flexural members range between 45mm and 110mm. Thus, four crack band width values were implemented, namely 31.25mm, 62.5mm, 93.75mm and 125mm, which correspond with $h/4$, $h/2$, $3h/4$ and h, with h the section height.

The theoretical models that are investigated are the moment-curvature and moment-rotation behaviours for all three SFRCs.

6.1. General overview

The importance of the crack band width in the derivation process of the theoretical models is highlighted in Figure 6.1. The stress-strain relation obtained from the inverse analysis is modified to fit the real structural behaviour by considering the assumed crack band width for the structure. With this modified stress-strain relationship it was capable to derive the theoretical moment-curvature relation. The assumed crack band width is utilised once more in the derivation of the moment-rotation behaviour, with the rigid-body rotation model. Thus, the magnitude of the assumed crack band width is a defining factor in the derivation process of the material and structural behaviour.

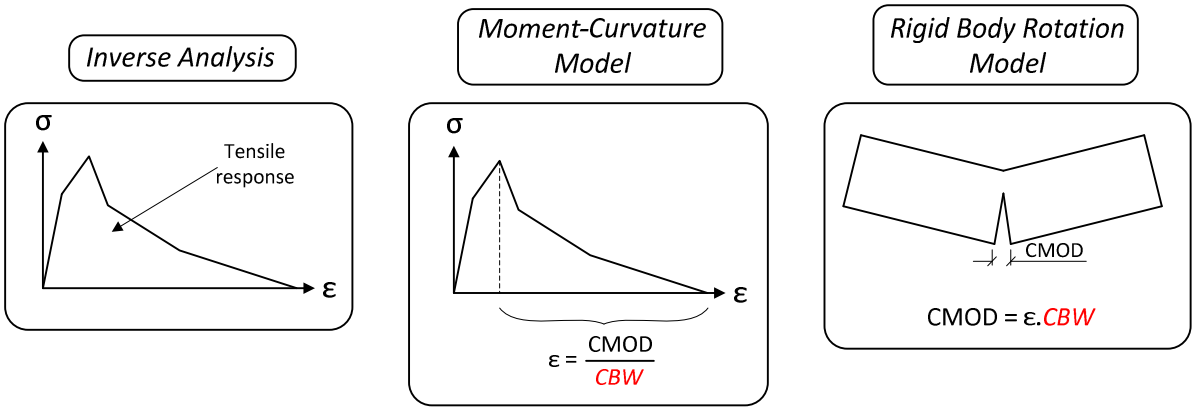

Figure 6.1 Diagram demonstrating the importance of the assumed CBW.

6.2. Results

In this section the theoretical results of the sensitivity analysis are compared with the experimental results obtained. The similarities and differences are discussed with the aim to prescribe a possible range for the real crack band width for each SFRC mix. It should be noted that only the shape of the curves are compared, as the difference in the magnitude of the peak values has been justified in the previous chapter.

6.2.1. Results of 0.5% SFRC

A seen in Figure 6.2, the crack band width only affects the post-peak region of the moment-curvature relation, with the post-peak angle of declination decreasing with a lower crack band width value. On the contrary, the pre-peak moment-rotation behaviour is influenced, as seen in Figure 6.2. The rotational value at the peak moment decreases with a decrease in the crack band width value, which induces a greater angle of inclination towards the peak moment value. Also, the peak moment values decrease slightly with an increase in the crack band width value.

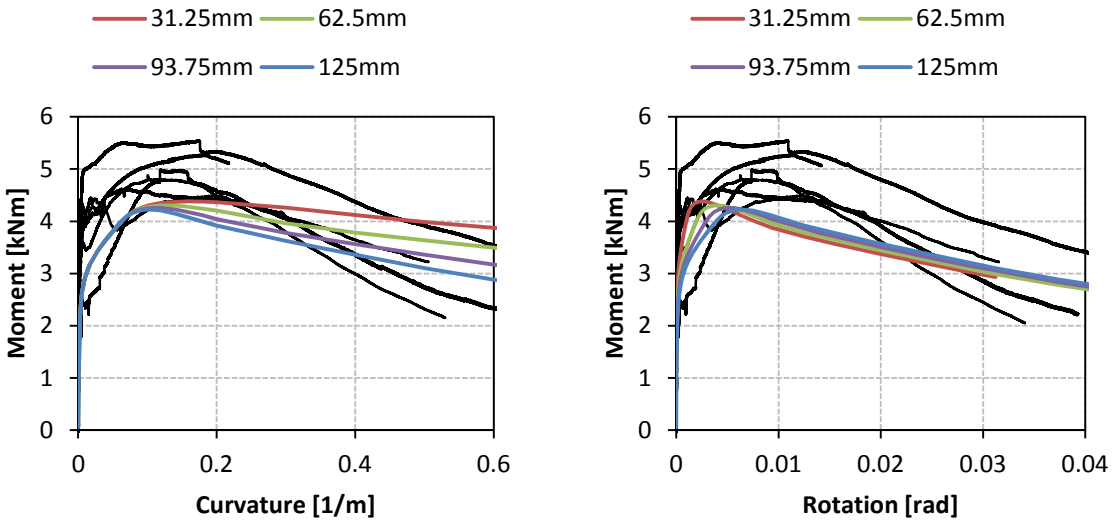

a) *b*)

Figure 6.2 0.5% SFRC. a) Moment-curvature responses; b) Moment-rotation responses.

It is seen that a CBW greater than 125mm would produce a post-peak angle of declination that corresponds with the experimental results. It was previously discussed that the theoretical approximations under predict the capacity of the structure and it is noticed that the shape of the pre-peak inclination of the moment-rotation response for a crack band width of 125mm correspond well with the experimental results. Thus the crack band width range for the 0.5% SFRC mix is prescribed to be larger than 125mm.

6.2.2. Results of 0.75% SFRC

The same differences in the shape of the theoretical curves as discussed for the previous SFRC mix are applicable. According to the obtained results there is a larger difference in the magnitude of the rotational values at the peak moments and for the post-peak angle of declination of the moment-curvature relation, as seen in Figure 6.3.

The theoretical post-peak behaviour that corresponds best with the experimental results is the curve provided with a crack band width of 93.75mm. As shown in the moment-rotation responses, the crack band width value that produces a curve with the most similar pre-peak angle of inclination and rotational value at the peak moment when compared to the experimental results ranges from 62.5mm to 93.75mm. It is concluded that the representative crack band width value for the 0.75% SFRC members ranges from 62.5mm to 93.75mm.

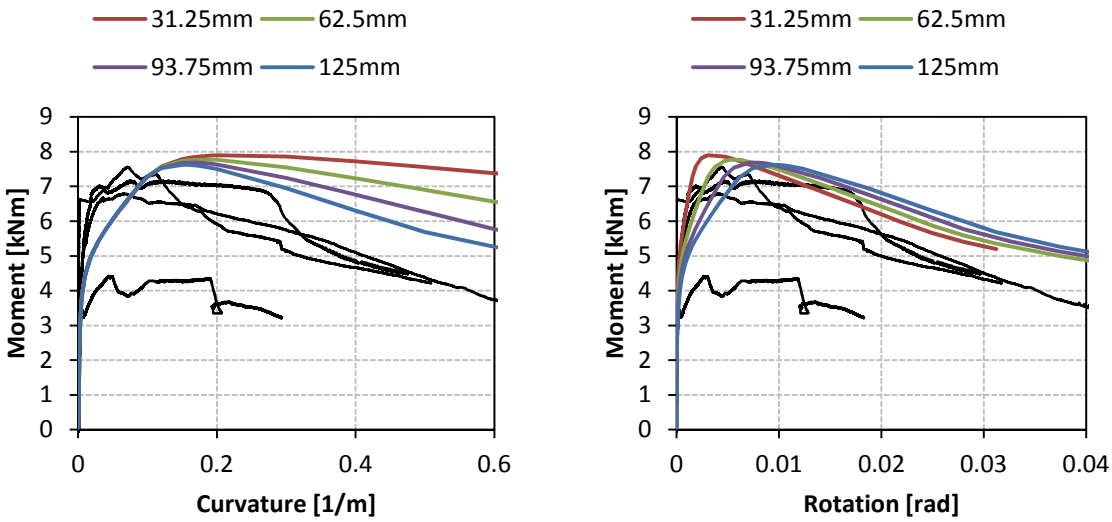

a) *b*)

Figure 6.3 0.75% SFRC. a) Moment-curvature responses; b) Moment-rotation responses.

6.2.3. Results of 1.0% SFRC

The same differences are encountered for the theoretical results as for the previous SFRC members, with the shift of the rotational values at the peak bending moments even more pronounced, as seen in Figure 6.4.

As seen in Figure 6.4, it is evident that the post-peak moment curvature behaviours produced by crack band width values, 31.25mm and 62.5mm, are representative of the experimental results obtained. Considering the shape of the pre-peak angle of inclination and the rotational value at the peak moment shown in Figure 6.4, it is concluded that the best fit curve is produced with a crack and width of 31.25mm. It is concluded that the representative crack band width value for the 1.0% SFRC members ranges from 31.25mm to 62.5mm.

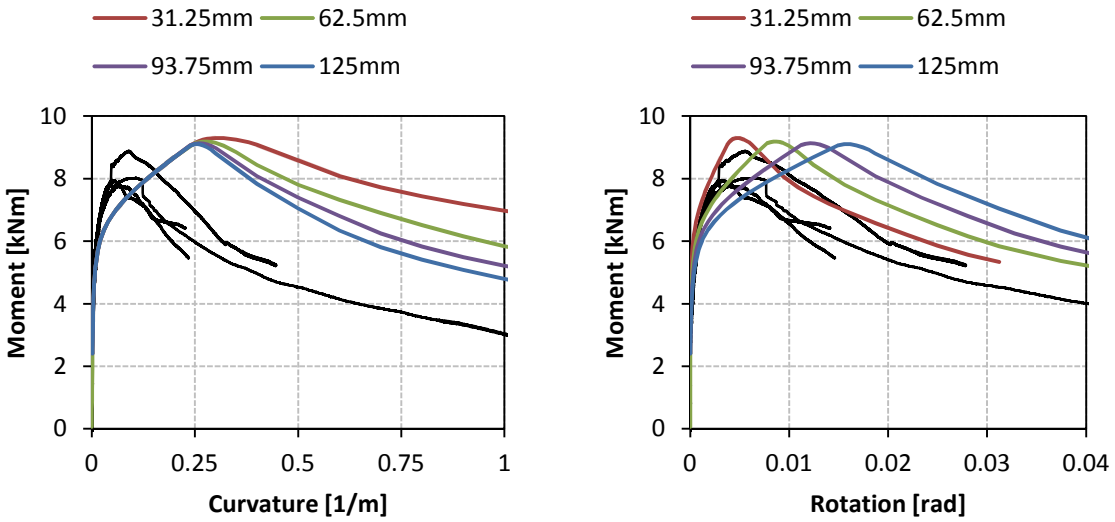

a) *b*)

Figure 6.4 1.0% SFRC. a) Moment-curvature responses; b) Moment-rotation responses.

6.3. Summary of results

The theoretical values of the characteristics at the peak bending moments are shown in Table 6.1. An indication of the sensitivity of the crack band width values in respect with the peak moments and the corresponding values are presented in Figure 6.5. A ratio is calculated between these predicted theoretical values and that obtained using the crack band width implemented in Chapter 4, *62.5mm*.

Table 6.1 Summary of characteristic values at the peak moment.

	0.5% SFRC			0.75% SFRC			1.0% SFRC		
CBW [mm]	M_{peak} *[kN]*	κ_{peak} *[1/m]*	ϑ_{peak} *[rad]*	M_{peak} *[kN]*	κ_{peak} *[1/m]*	ϑ_{peak} *[rad]*	M_{peak} *[kN]*	κ_{peak} *[1/m]*	ϑ_{peak} *[rad]*
31.25	4.381	0.16	0.00249	7.897	0.2	0.00311	9.302	0.3	0.00467
62.5	4.302	0.12	0.00373	7.774	0.18	0.00560	9.187	0.274	0.00853
93.75	4.257	0.11	0.00513	7.688	0.16	0.00746	9.135	0.26	0.01213
125	4.224	0.1	0.00622	7.626	0.15	0.00932	9.101	0.25	0.01555

A greater difference in the ratio shown in Figure 6.5 indicate that the characteristic is more sensitive towards the assumed crack band width, which is the case for the rotations corresponding with the peak bending moments. The curvature values at the peak moments are also influenced, but to a lesser extent. It is noticed that the change in the crack band width has an inverse effect on the two mentioned characteristics. Thus, an increase in the crack band width results in a larger rotational value, but smaller curvature value at the peak moment position, and vice versa. The peak moment values also decrease with an increase in the crack band width, but to such small extent that it is considered negligible.

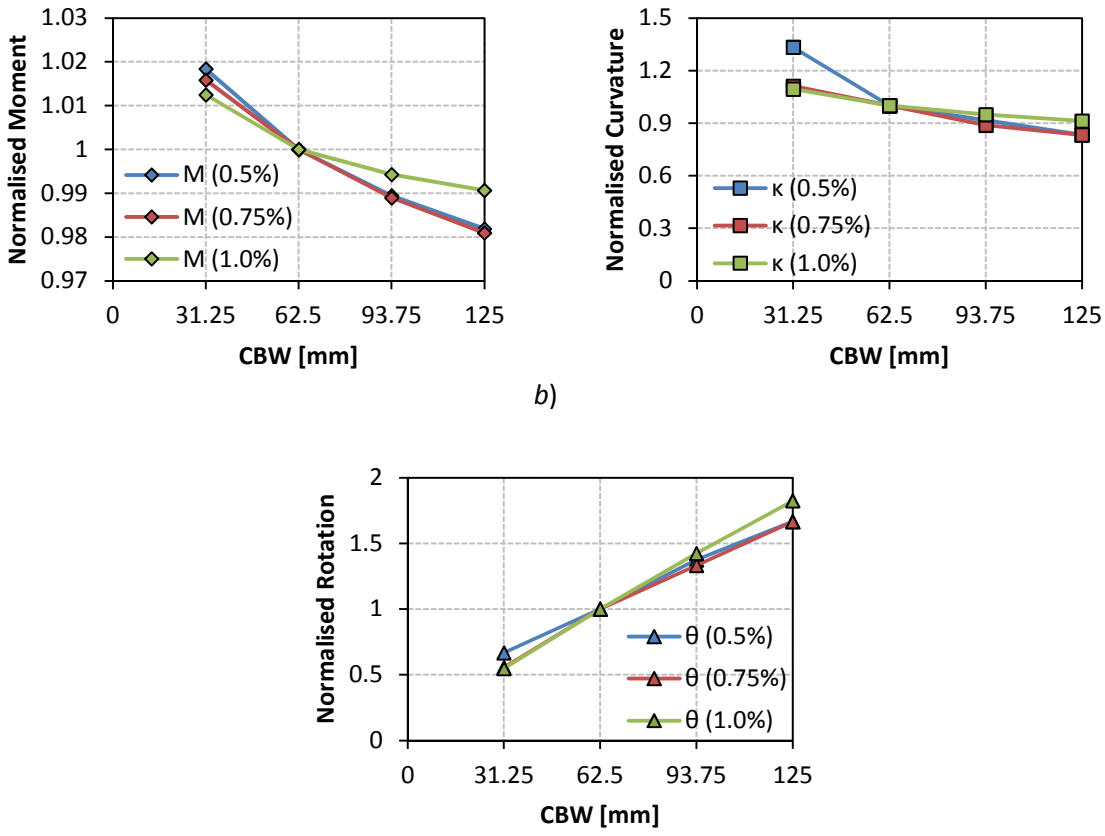

a) *b*)

c)

Figure 6.5 Comparison between the characteristic values determined for different CBWs and normalised to a CBW of 62.5mm.

6.4. Concluding Summary

It is concluded that the representative crack band width values for the 0.5% SFRC members are larger than 125mm, and ranges from 62.5mm to 93.75mm for the 0.75% SFRC members, while it ranges from 31.25mm to 62.5mm for the 1.0% SFRC members.

It should be noted that the rotational models are based on a constant plastic hinge length for all three SFRC mixes. It was found that the size of the real crack band width decreased with an increase of the amount of fibres. With the obtained ARAMIS measurements the average crack band width increased with an increase in volume fibres. Thus, the average crack spacing was not the deciding factor in the structural behaviour, but actually the size of the plastic hinge length.

There are two ways to consider the behaviour at the plastic hinge. Firstly, considering the same plastic hinge length for all three SFRCs implies that more cracks need to develop in the prescribed hinge length for the structure to absorb more energy with the pull-out action of the fibres. This corresponds with the crack band width calculations as determined with this sensitivity analysis. Secondly, with the crack distances for all three SFRC members relatively in the same range, more cracks have to develop to absorb more energy. This would produce an increase in the total plastic hinge length, which was obtained with the experimental results.

Although the sensitivity analysis provided an estimation of the crack band width range, realistic results can only be obtained by measuring the spacing of flexural cracks, e.g. by conducting four point bending tests on the SFRC specimens.

CHAPTER 7

CONCLUSIONS AND FUTURE PROSPECTS

7.1. Conclusions

The main objective of this research project was to provide insight on the moment redistribution behaviour of steel fibre reinforced concrete members and to determine if the allowable moment redistribution value prescribed in design codes for conventionally reinforced concrete could be implemented for design of SFRC structures. Also, the rotation capacity of a structural SFRC member at its plastic hinges was investigated in conjunction with the moment redistribution development.

The following conclusions can be made:

- From the inverse analyses it was concluded that the uniaxial tensile resistance increased from 2.5MPa to 6.0MPa with an increase of the fibre content from 0.5% to 1.0%.

- With the moment-curvature and moment-rotation responses it was found that the bending capacity, section ductility and member ductility increased with an increase in the volume of fibres. The bending capacity increased from 4.3kNm to 9.2kNm with an increase in the fibre content from 0.5% to 1.0%.

- From the finite element analyses it was concluded that the amount of moment redistribution decreased from 14.5% to 9.5% with an increase in the fibre content from 0.5% to 1.0%.

- It was also concluded that the amount of moment redistribution is greatly affected by the post-peak moment-curvature behaviour. A post-peak curve with a smaller angle of declination would produce structural behaviour at the plastic hinges that upholds the bending capacity more efficiently with an increase in the curvature, which allows for greater moment redistribution capability.

- It was found that the numerical moment redistribution predictions were accurate, as finite element analyses accurately predicted the irregular structural behaviour that occurred. Also the experimental moment-curvature and moment-rotation behaviour correlated well with the theoretical predictions.

- It is concluded that the amount of moment redistribution available for these composites are much less than the ultimate value of 30% currently prescribed in design codes for conventionally reinforced structures. Thus, it is not recommended to utilise the prescribed values in current design codes for the design of steel fibre reinforced concrete structures.

- With a parameter study it was concluded that the crack band width decreased with an increase in the volume of fibres for a constant plastic hinge length. The concluded crack band width ranges are larger than 125mm for the 0.5% SFRCs, between 62.5mm and 93.75mm for the 0.75% SFRCs and between 31.25mm and 62.5mm for the 1.0% SFRCs.

7.2. Future Developments

The research conducted in this study was the first attempt to quantify the objective proposed, thus many improvements can be made in future developments. The following future developments could provide a greater understanding of the moment redistribution behaviour.

- To consider the correct value for the crack band width, it is necessary to perform four point bending tests which allow the measurement of the spacing of the flexural cracks.

- To ensure greater representative material properties, it is recommended that the experimental tests are performed with a larger number of specimens, as imperfections could influence the results obtained.

- The effect of shear was only included in the inverse analysis, with the results used to derive a pure flexural structural behaviour, the moment-curvature relationship. The effect of shear was not in the scope of this study, but could it be an influencing factor in the behaviour at the plastic hinges where the shearing force has a significant value, e.g. how it affects the plastic hinge length, crack spacing, crack orientation, etc.

- The moment redistribution-plastic rotation model was only derived with respect to a specific statically indeterminate structure. The effect of important characteristics, such as the span length, cross sectional dimensions, different load applications, etc. should be investigated to determine the influence on the proposed model. Also, the effect that different statically indeterminate structures, e.g. a greater number of span lengths or a two way spanning slab structure, have on the proposed model, could be investigated.

- To obtain a direct relation with the standards prescribed in the design codes, it is necessary to derive the amount of moment redistribution in relation with the neutral axis depth.

- Considering the difficulties experienced with the statically indeterminate tests, it should be taken into consideration that the supports have a major effect on the force distribution. It is recommended to ensure an aligned support system and that the specimens are cast perfectly straight.

- The ARAMIS provided accurate results at the centre support and it would be beneficial to provide such a system at all the critical sections in the structure to fully understand the structural behaviour.

- The research was only conducted with 0.5%, 0.75% and 1.0% fibre volume with RC-80/60-CP steel fibres. Similar research could be conducted with other volumes of fibres and different fibre types, which could contribute to the development of a diagram that provides the SFRC's capacity and its ability to redistribute bending moments.

CHAPTER 8

BIBLIOGRAPHY

ABAQUS. 2010. Online Documentation, V6.1. SIMULIA.

ACI Committee 318. 2008. *Building code and commentary*. ACI 318-08/318R-08. Farmington Hills. American Concrete Institute.

ACI Committee 544. 1996. *Design considerations for steel fiber reinforced concrete*. ACI 544.4R-88. Farmington Hills. American Concrete Institute.

Aiello, M.A. & Ombres, L. 2011. Moment redistribution in continuous fiber-reinforced polymer-strengthened reinforced concrete beams. ACI Structural Journal. 108 (2): 158-166.

ARAMIS V6.1. 2007. User Information – Hardware. GOM Optical Measuring Techniques.

Baker, A.L.L. & Amarakone, A.M.N. 1964. Inelastic hyperstatic frame analysis. *Proceedings of the International Symposium on Flexural Mechanics of Reinforced Concrete.* 85-142.

Barros, J.A.O. & Dalfré, G. 2009. Numerical simulation of continuous RC Slabs strengthened using NSM technique. Concrete Repair, Rehabilitation and Retrofitting II. 1081-1088.

BEKAERT. 2004. *Dramix Steel fibres for concrete reinforcement* [Online]. Available: http://www.bekaert.com/en/Functional/Search/Site%20Search.aspx?searchCategory=site&searchTerm=steel+fibres [2011, December 12].

Brandt, A.M. 2008. Fibre reinforced cement-based (FRC) composites after over 40 years of development in building and civil engineering. *Composite Structures*. 86:3-9.

Broms, B.B. 1965. Crack width and crack spacing in reinforced concrete members. *Journal of the American Concrete Institute*. 62: 1237-1256.

BS EN 1992-1-1:2004. Eurocode 2: Design of concrete structures. Part 1-1: General rules and rules for buildings. Brussels. European Committee for Standardization: 2004.

Carreira, D.J. & Chu, K.H. 1985. Stress-strain relationship for plain concrete in compression. *ACI Journal*. 82(6):797-804.

Cohn, M.Z. 1964. Rotation compatibility in the limit design of reinforced concrete continuous beams. *Proceedings of the International Symposium on Flexural Mechanics of Reinforced Concrete*. 359-381.

Corley, G.W. 1966. Rotational capacity of reinforced concrete beams. *ASCE Journal of the Structural Division*. 92(5):121-146.

Di Prisco, M., Felicetti, R. & Plizzari, G. 2004. Fibre reinforced concrete*. RILEM Proceedings of the 6th RILEM Symposium (BEFIB2004)*.

Di Prisco, M., Plizzari, G & Vandewalle, L. 2009. Fibre reinforced concrete: new design perspectives. *Materials and Structures*. 42: 1261-1281.

Ezeldin, A.S. & Balaguru, P.N. 1992. Normal and high strength fiber reinforced concrete under compression. *Journal of Materials in Civil Engineering*. 4(4): 415-427.

Fanella, D.A. & Naaman, A.E. 1985. Stress-strain properties of fiber reinforced mortar in compression. *ACI Journal*, 82(4): 475-483.

FIB. 2010. *Model Code 2010*. Laussanne, Switzerland.

Hibbeler, R.C. 2005. *Mechanics of materials, Sixth Edition*. Singapore. Prentice-Hall, Inc.

Jansson, A. 2008. *Design methods for fibre-reinforced concrete: a state-of-the-art review*. PhD Thesis. Göteborg, Sweden. Chalmers University of Technology.

König, G. & Kützing, L. 1999. Modelling the increase of ductility of HPC under compressive forces, a fracture mechanical approach, in *Proceedings of the 3rd International RILEM Workshop 'High performance Fibre Reinforced Cementitious Composites (HPFRCC 3)*. Mainz: 251-260.

Liu, I.S.T., Oehlers, D.J. & Seracino, R. 2006. Moment redistribution in FRP and steel-plated reinforced concrete beams. Journal of composites for construction. 10 (2): 115-124.

Löfgren, I. 2005. *Fibre-reinforced Concrete for Industrial Construction – a fracture mechanics approach to material testing and structural analysis*. PhD Thesis. Göteborg, Sweden. Chalmers University of Technology.

Mattock, A.H. 1964. Rotational capacity of hinging regions in reinforced concrete beams. *Proceedings of the International Symposium on Flexural Mechanics of Reinforced Concrete*. 143-182.

Mattock, A.H. 1983. Secondary moments and moment redistribution in ACI 318-77 code. *Proceedings of the the International Symposium on Nonlinearity and Continuity in Prestressed Concrete*. 3:27-48.

Naaman, A.E. et al. 1986. Analysis of ductility in partially prestressed concreteconcrete flexural members. *Prestressed Concrete Journal*. 31(3):64-87.

Naaman, A.E. & Reinhardt, H.W. 2006. Proposed classification of HPFRC composites based on their tensile response. *Materials and Structures*. 39:547-555.

Nataraja, M.C., Dhang, N. & Gupta, A.P. 1999. Stress-strain curves for steel-fiber reinforced concrete under compression. *Cement and Concrete Composites*. 21: 383-390.

Oehlers, D.J., Ju, G., Liu, I.S.T. & Seracino, R. 2004. Moment redistribution in continuous plated RC flexural members. Part 1: neutral axis depth approach and tests. Engineering structures. 26: 2197-2207.

Oehlers, D.J. 2006. Ductility of FRP plated flexural members. Cement & Concrete Composites. 28: 898-905.

Oehlers, D.J., Griffith, M.C. & Mohamed Ali, M.S. 2009. Ductility components and limits of FRP-plated structures. *Construction and Building Materials*. 23: 1538-43.

Park, R. & Paulay, T. 1975. *Reinforced Concrete Structures*. Canada: John Wiley & Sons.

RILEM TC 162-TDF. 2002. Test and design methods for steel fibre reinforced concrete-Bending Test. *Materials and Structures*. 35:579-582.

RILEM TC 162-TDF. 2003. Test and design methods for steel fibre reinforced concrete: σ-ε Method. *Materials and Structures*. 36: 560-567.

Riva, P. & Cohn, M.Z. 1994. Rotation capacity of structural concrete members. *Magazine of Concrete Research*. 46(168):223-234.

Rizk, E & Marzouk, H. 2010. A new formula to calculate crack spacing for concrete plates. *ACI Structural Journal*. 107 (1): 43-52.

Schumacher, P. 2006. Rotation capacity of self-compacting steel fiber reinforced concrete. PhD Thesis. Netherlands. Delft Technical University.

Scott, R.H. & Whittle, R.T. 2005. Moment redistribution effects in beams. Magazine of concrete research. 57 (1): 9-20.

Shakir, A. & Rogowsky, D.M. 2000. Evaluation of ductility and allowable moment redistribution in reinforced concrete structures. *Can. J. Civ. Eng*. 27:1286-1299.

TNO DIANA. 2008. DIANA Finite Element Analysis User's Manual, release notes 9.3. TNO Building and Construction Research. 2008.

Vandewalle, L. *et al*. 2003. RILEM TC162-TDF – 'Test and design methods for steel fibre reinforced concrete': σ-ε Design Method. Materials and Structures. 36: 560-567.

Appendix A

CHARACTERISING MATERIAL PROPERTIES FOR MODELLING

This appendix presents the obtained test results and input characteristics that were excluded in the thesis, but could be utilised for further study.

A.1. Mix designs

Table A.1 Mix design for 0.5% fibres.

Material	%	kg/m^3	RD	Vol. [litre]
Cement (CEM I)		370	3.1	120.8
Fly Ash		235	2.8	84.9
Stone 6 mm		635	2.7	238.0
Sand (Malmesbury)		934	2.65	356.7
Water		190	1	192.3
SP (Premia 310)	0.45	2.72	1.2	2.3
Fibres	0.5	39.25	7.85	5.0
TOTAL		2406		1000

Table A.2 Mix design for 0.75% fibres.

Material	%	kg/m^3	RD	Vol. [litre]
Cement (CEM I)		370	3.1	120.5
Fly Ash		235	2.8	84.7
Stone 6 mm		635	2.7	237.4
Sand (Malmesbury)		934	2.65	355.7
Water		190	1	191.7
SP (Premia 310)	0.5	3.03	1.2	2.5
Fibres	0.75	58.88	7.85	7.5
TOTAL		2426		1000

A.2. Compressive characteristics

Table A.3 Summary of compressive results.

0.5% SFRC	σ_{peak} ***[MPa]***	ε_{peak}	***E [GPa]***
1	43.5	0.00201	30.2
2	41.1	0.00188	29.1
3	42.9	0.00169	32.5
4	41.2	0.00192	31.7
5	38.2	0.00156	32.6
6	35.6	0.00162	33.1
AVERAGE	**40.4**	**0.00178**	**31.5**
COV	**7.4**	**10.1**	**4.9**

0.75% SFRC	σ_{peak} ***[MPa]***	ε_{peak}	***E [GPa]***
1	43.1	0.00183	33.6
2	45.3	0.00210	34.8
3	43.4	0.00207	31.1
4	37.7	0.00169	32.3
5	38.2	0.00163	33.5
6	43.0	0.00177	32.4
AVERAGE	**41.8**	**0.00185**	**32.9**
COV	**7.4**	**10.5**	**3.9**

1.0% SFRC	σ_{peak} ***[MPa]***	ε_{peak}	***E [GPa]***
1	41.5	0.00205	27.4
2	38.2	0.00168	31.0
3	36.4	0.00170	27.7
4	39.4	0.00161	29.7
5	39.0	0.00194	27.5
6	34.0	0.00168	30.2
AVERAGE	**38.1**	**0.00178**	**28.9**
COV	**6.8**	**9.8**	**5.4**

A.3. Flexural characteristics

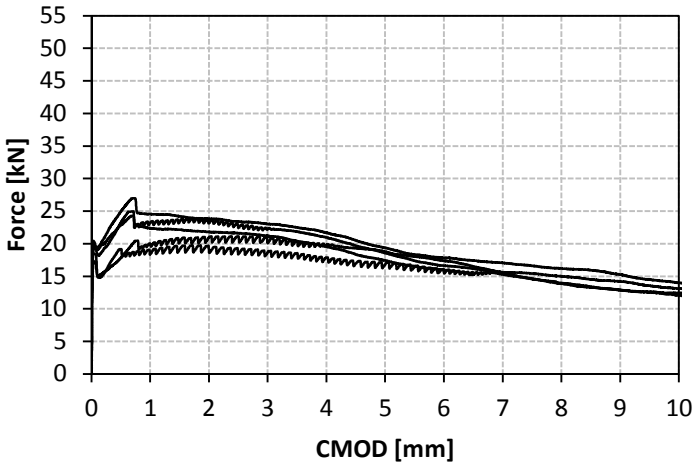

Figure A.1 Force-CMOD responses for beams with 0.5% fibres.

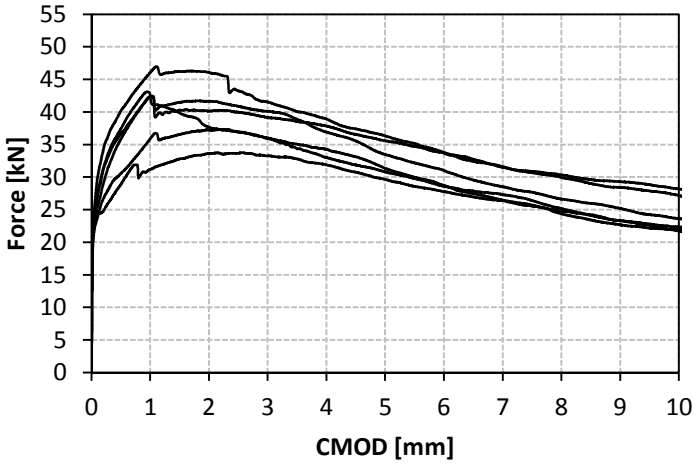

Figure A.2 Force-CMOD responses for beams with 0.75% fibres.

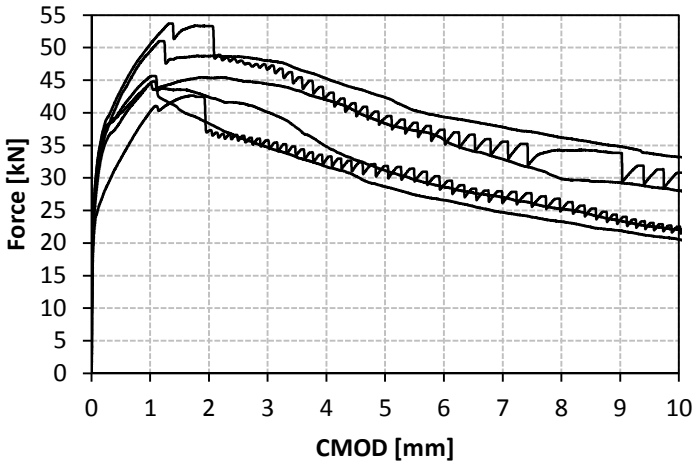

Figure A.3 Force-CMOD responses for beams with 1.0% fibres.

Table A.4 Summary of flexural test results.

0.5% SFRC	P_{crack} [kN]	Δ_{crack} [mm]	$CMOD_{crack}$ [mm]	P_{peak} [kN]	Δ_{peak} [mm]	$CMOD_{peak}$ [mm]
1	19.93	0.10	0.059	24.28	0.80	0.719
2	17.31	0.08	0.036	20.48	0.85	0.791
3	19.91	0.10	0.049	26.95	0.87	0.746
4	20.41	0.08	0.035	24.94	0.73	0.716
5	18.51	0.07	0.029	19.1	0.57	0.510
AVERAGE	**19.21**	**0.09**	**0.041**	**23.15**	**0.76**	**0.696**
COV	**6.7**	**15.7**	**29.4**	**14.1**	**15.8**	**15.6**

0.75% SFRC	P_{crack} [kN]	Δ_{crack} [mm]	$CMOD_{crack}$ [mm]	P_{peak} [kN]	Δ_{peak} [mm]	$CMOD_{peak}$ [mm]
1	23.58	0.07	0.035	42.39	0.92	1.045
2	23.36	0.08	0.034	46.9	1.27	1.100
3	19.82	0.05	0.019	36.62	1.18	1.104
4	21.01	0.06	0.025	42.97	1.13	0.964
5	21.77	0.07	0.027	42.25	1.15	1.000
6	20.97	0.06	0.023	31.84	0.87	0.780
AVERAGE	**21.75**	**0.06**	**0.027**	**40.50**	**1.09**	**0.999**
COV	**6.8**	**12.0**	**23.1**	**13.2**	**14.3**	**12.1**

1.0% SFRC	P_{crack} [kN]	Δ_{crack} [mm]	$CMOD_{crack}$ [mm]	P_{peak} [kN]	Δ_{peak} [mm]	$CMOD_{peak}$ [mm]
1	25	0.09	0.042	44.73	1.31	1.058
2	24.86	0.08	0.038	45.56	1.14	1.091
3	23	0.07	0.041	50.88	1.36	1.237
4	20.04	0.06	0.029	44.39	1.11	1.007
5	22.62	0.07	0.025	41.01	1.07	1.110
6	23.56	0.07	0.033	53.59	1.61	1.388
AVERAGE	**23.18**	**0.07**	**0.034**	**46.69**	**1.27**	**1.148**
COV	**7.8**	**12.0**	**20.6**	**9.9**	**16.0**	**12.2**

Table A.5 Force-displacement data for representative curves.

0.5% Fibres	
Force [kN]	**Displacement [mm]**
0	0
18.75	0.0765
17.5	0.177
24.17	0.79
22.08	0.82
11.46	10.65

0.75% Fibres	
Force [kN]	**Displacement [mm]**
0	0
23	0.088
35	0.44
42.33	1.11
40.17	1.147
40.6	2
29.3	6
22.67	10.62

1.0% Fibres	
Force [kN]	**Displacement [mm]**
0	0
32.5	0.145
47.5	1.15
44.17	1.17
42.71	2.52
30.83	5.87
22.92	10.74

A.4. FEM Model

A.4.1. Material properties

Table A.6 Compressive input values.

0.5% Fibres	
Stress [MPa]	**Strain [mm/mm]**
0	0
13	0.00043
23.1	0.00077
31.15	0.00112
36.21	0.00139
39.5	0.00165
41.2	0.00192

0.75% Fibres	
Stress [MPa]	**Strain [mm/mm]**
0	0
17.82	0.00056
26.66	0.00087
32.86	0.00113
39.11	0.00147
42.92	0.00179

1.0% Fibres	
Stress [MPa]	**Strain [mm/mm]**
0	0
18.07	0.00058
25.096	0.00085
30.915	0.00111
35.38	0.00134
37.48	0.00155
38	0.00170

Table A.7 Tensile model parameters for each SFRC member.

	0.5% Fibres		0.75% Fibres		1.0% Fibres	
i	σ_i	ε_i	σ_i	ε_i	σ_i	ε_i
crack	1.85	6.15E-05	3	9.49E-05	3.8	0.000122
peak	2.5	0.007	4.7	0.01	6	0.025
3	2	0.0296	3.9	0.036	4	0.04
4	1.35	0.1056	2.5	0.088	2.5	0.1
5	0	0.3656	0	0.488	0	0.5

A.5. DIANA Data Files

In this appendix examples of the *.dat* and *.com* files are presented for that of the 0.5% SFRC model.

A.5.1. *.dat* File

```
FEMGEN MODEL     :
BEAM_12_5VS_5MM_CRK
ANALYSIS TYPE     : Structural 2D
'UNITS'
LENGTH   MM
TIME     SEC
TEMPER   KELVIN
FORCE    N
'COORDINATES' DI=2
   1     0.000000E+00    0.000000E+00
   2     1.250000E+01    0.000000E+00
   3     2.500000E+01    0.000000E+00
   4     3.750000E+01    0.000000E+00
   5     5.000000E+01    0.000000E+00
...
...
...
 752     6.875000E+02    1.500000E+02
 753     7.000000E+02    1.500000E+02
 754     7.125000E+02    1.500000E+02
'ELEMENTS'
CONNECTIVITY
   1 Q8MEM  1 2 31 30
   2 Q8MEM  2 3 32 31
   3 Q8MEM  3 4 33 32
...
...
...
 680 Q8MEM  290 639 668 319
 681 Q8MEM  319 668 697 348
 682 Q8MEM  348 697 726 377
:
MATERIALS
:FRC
/ 1-682 / 1
:
GEOMETRY
: FRC
/ 1-682 / 1
:
:
'MATERIALS'
:FRC
  1  DENSIT 2400.0E-9
     TOTCRK ROTATE
     POISON 0.2
     YOUNG 32.0E+03
     COMSTR 38.0
     COMCRV MULTLN
     COMPAR 0 0
          -13.0 -0.000432331
          -23.1 -0.000774436
          -31.15 -0.001116541
          -36.21 -0.001387218
          -39.5 -0.001646617
          -41.2 -0.0019173
     TENCRV MULTLN
     TENPAR 0 0
          1.85 0.0000615240
          2.5 0.007
          2.0 0.12
          1.35 0.5
          0. 1.8
:
'GEOMETRY'
:FRC
   1  THICK  150.0
:
'GROUPS'
ELEMEN
   1 FRC / 1-682 /
:
'SUPPORTS'
:Left Support
   / 11 /  TR 2
:Right Support
  / 396 /  TR 2
:Displacement Control
  / 377 726 / TR 2
:
'LOADS'
CASE 1
DEFORM
 / 377 726 /  TR 2 -1.
'DIRECTIONS'
```

```
   1   1.000000E+00   0.000000E+00
0.000000E+00
   2   0.000000E+00   1.000000E+00
0.000000E+00
   3   0.000000E+00   0.000000E+00
1.000000E+00
'END'
```

A.5.2. *.com* File

```
*FILOS
 INITIA
*INPUT
*LINSTA
 BEGIN OUTPUT
  FILE "beam_12_5"
  TEXT "beam_12_5"
  DISPLA
  FORCE
  STRAIN
  STRAIN TOTAL GREEN PRINCI
  STRESS total cauchy global intpnt
  STRESS TOTAL CAUCHY PRINCI
  stress total cauchy princi intpnt
  FORCE REACTI
  FORCE EXTERN
  force residu
 END OUTPUT
*NONLIN
 BEGIN EXECUT
  BEGIN ITERAT
   METHOD NEWTON REGULA
   LINESE
   BEGIN CONVER
    DISPLA OFF
    ENERGY
:    TOLCON 0.0001
    FORCE OFF
    SIMULT
   END CONVER
   contin
   MAXITE 500
  END ITERAT
  BEGIN LOAD
   LOADNR 1
   STEPS EXPLIC SIZES 0.02 (50) 0.05 (180)
  END LOAD
 END EXECUT
 BEGIN OUTPUT TABULAR
 STRESS TOTAL CAUCHY LOCAL XX INTPNT
 STRAIN TOTAL GREEN LOCAL XX INTPNT
 END OUTPUT
 BEGIN OUTPUT FEMVIEW BINARY
  FILE "beam_12_5"
  DISPLA
  FORCE EXTERN
  FORCE REACTI
  STRAIN total green local intpnt
  STRAIN total green PRINCI intpnt
  STRESS total cauchy local intpnt
  STRESS total cauchy PRINCI intpnt
  STRESS PRINCI
 END OUTPUT
*End
```

APPENDIX B

MODELLING MOMENT REDISTRIBUTION

In this appendix the procedure for calculating the moment-curvature responses is presented. Also, the omitted ABAQUS results are shown to enable the reader to compare the results if desired.

B.1. Implemented sectional analysis procedure

B.1.1. Input Data

Dimensions:

The dimensions are denoted with *b* and *h*, which represents the width and height of the cross section, respectively.

Material Behaviour:

The material behaviour that was obtained in Chapter 3 serves as the basis for this sectional analysis. To ensure the versatility of the developed Excel datasheet, the analysis was enabled to be conducted with any material behaviour. Provision is made for a total of five 7^{th} degree polynomial equations to

depict the compressive stress-strain relation, with each equation's range also defined (as shown in Figure B.1 (a)). Per illustration, assume the following compressive stress-strain relation;

$$\sigma_{ci}(\varepsilon) = 2\varepsilon^2 + 3\varepsilon + 1, \qquad \text{with} \qquad \varepsilon_{c(i-1)} \le \varepsilon < \varepsilon_{ci} \tag{B.1}$$

The tensile behaviour is described with series of data points which depict a multi-linear tensile response (as shown in Figure B.1 (b)). A possibility of five data points is prescribed, excluding the origin.

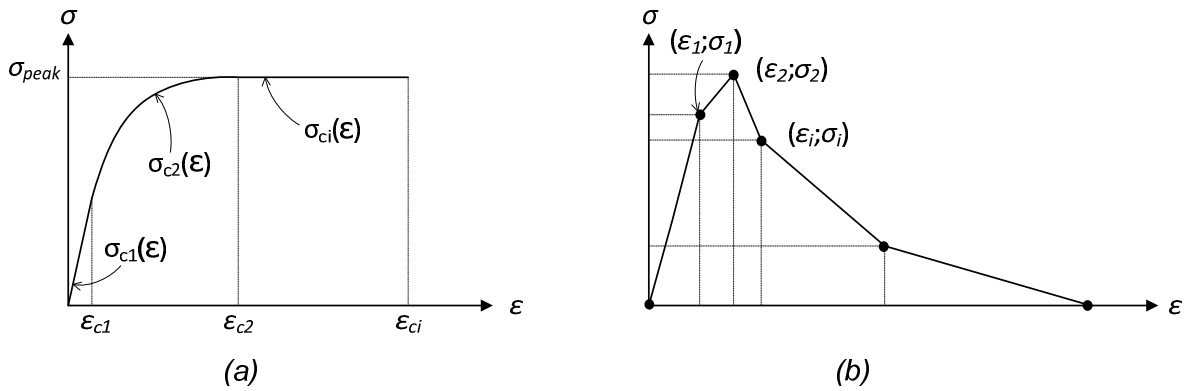

Figure B.1 Specification of material behaviour; (a) in Compression, and (b) in Tension.

B.1.2. Transformation process

The stress-strain relation can be altered in various fashions to be used in further calculations. With the use of Equation B.2 the stress-strain relations is converted to stress-section height (σ-y) relationships to enable the visual presentation of the stress distribution across the section (Figure B.2)

$$\varepsilon = \kappa y \qquad \text{and} \qquad y = \frac{\varepsilon}{\kappa} \tag{B.2}$$

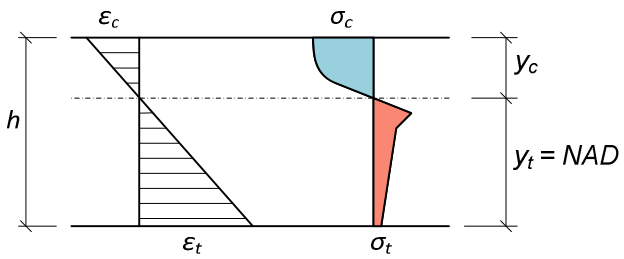

Figure B.2 Stress distributions related to position across the cross-section.

Per illustration, the compressive behaviour is altered as follows

$$\sigma_{ci}(y) = 2(\kappa y)^2 + 3(\kappa y) + 1 \tag{B.3}$$

$$\sigma_{ci}(y) = \left(2\kappa^2\right) y^2 (3\kappa) y + 1, \qquad \text{with} \quad y_{c(i-1)} \le y < y_{ci} \tag{B.4}$$

with κ (curvature)constant for each iteration.

As mentioned earlier, the tensile behaviour is not specified in an equation form, but as data points that are linearly connected. Thus, these data points are transformed to depict the shape of the stress-section height (σ-y) curve, as follows:

Firstly, the y-values for the corresponding strain values are calculated,

$$y_{ti} = \frac{\varepsilon_{ti}}{\kappa} \tag{B.5}$$

This is followed by the derivation of the series of linear equations that describe the multi-linear tensile curve (Figure B.3).

$$\sigma_{ti}(y) = m_{ti}(y) + c_{ti}, \qquad \text{for} \quad y_{t(i-1)} \le y_t < y_{ti} \tag{B.6}$$

with

$$m_{ti} = \frac{\sigma_{ti} - \sigma_{t(i-1)}}{y_{ti} - y_{t(i-1)}} \tag{B.7}$$

and

$$c_{ti} = \sigma_{ti(i-1)} - m_{ti} y_{ti(i-1)} \tag{B.8}$$

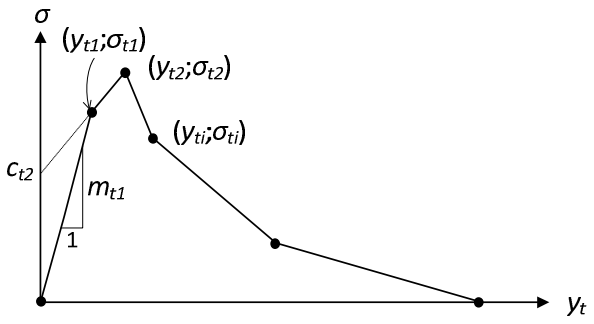

Figure B.3 Schematic illustration of generated stress relation.

B.1.3. Internal Forces

For a specific curvature the stress distribution across the section is determined with the application of the equilibrium equation, Equation 4.5, which results in the necessary shift in the neutral axis depth. The cross section was subdivided according to the stress distribution and the corresponding internal forces were calculated and summated to obtain the total tensile and compressive forces, as shown in Figure B.4.

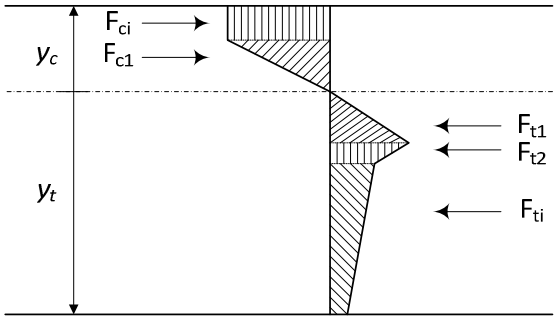

Figure B.4 Schematic representation of internal forces.

Neutral axis depth:

The calculation of the NAD depends on the necessary shift (δ) that allows force-equilibrium to be achieved.

Tension Zone:

$$y_t = NAD = \frac{h}{2} + \delta \tag{B.9}$$

$$\sum F_t = \sum F_{ti} \tag{B.10}$$

with i = 1, 2, 3, ...n

$$F_{ti} = \int_{y_{t(i-1)}}^{y_t} \sigma_{ti}(y) b dy, \qquad \text{if } y_t < y_{ti} \tag{B.11}$$

$$F_{ti} = \int_{y_{t(i-1)}}^{y_{ti}} \sigma_{ti}(y) b dy, \qquad \text{if } y_t > y_{ti} \tag{B.12}$$

Compression Zone:

$$y_c = h - y_t \tag{B.13}$$

$$\sum F_c = \sum F_{ci} \tag{B.14}$$

with i = 1, 2, 3, ...*n*

$$F_{ci} = \int_{y_{c(i-1)}}^{y_c} \sigma_{ci}(y) b dy, \qquad \text{if } y_c < y_{ci} \tag{B.15}$$

$$F_{ci} = \int_{y_{c(i-1)}}^{y_{ci}} \sigma_{ci}(y) b dy, \qquad \text{if } y_c > y_{ci} \tag{B.16}$$

B.1.4. Moment Arms

The calculated neutral axis depth allows for the calculation of the moment arms of the stress distributions that correspond with the force values determined in the previous section. To be able to calculate the moment arm for any shape of stress distribution, it is required to perform a similar calculation as shown in Figure B.5 (a).

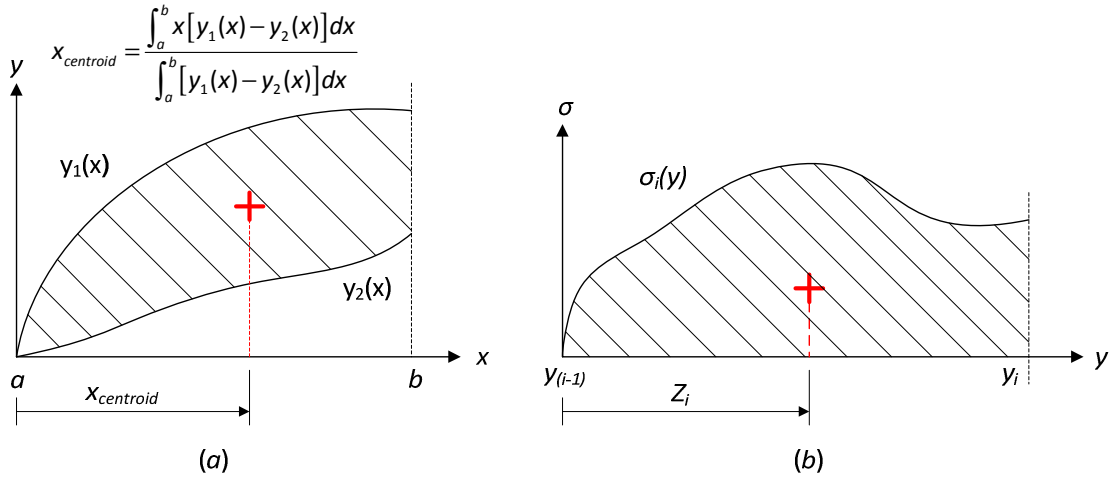

Figure B.5 (a) Calculation of the centroid of a random area, (b) Schematic of centroid calculation for current application.

The equation was modified to calculate the moment arm of any stress distribution as shown in Figure B.5 (b). The calculations required are:

$$Z_i = \frac{\int_{y_{(i-1)}}^{y} y.\sigma_i(y)dy}{\int_{y_{(i-1)}}^{y} \sigma_i(y)dy}, \qquad \text{for} \quad y < y_i \tag{B.17}$$

$$Z_i = \frac{\int_{y_{(i-1)}}^{y_i} y.\sigma_i(y)dy}{\int_{y_{(i-1)}}^{y_i} \sigma_i(y)dy}, \qquad \text{for} \quad y > y_i \tag{B.18}$$

B.1.5. Bending Moments

This is the final step of the calculation procedure. The calculated forces are multiplied with their corresponding moment arms and summated to yield the internal bending moment value at the section for the specified curvature.

$$M_i = \sum F_{ti}.Z_{ti} + \sum F_{ci}.Z_{ci} \tag{B.19}$$

B.2. Moment-curvature calculation Excel Spreadsheet

B.3. ABAQUS Results

B.3.1. 0.5% SFRCC Results

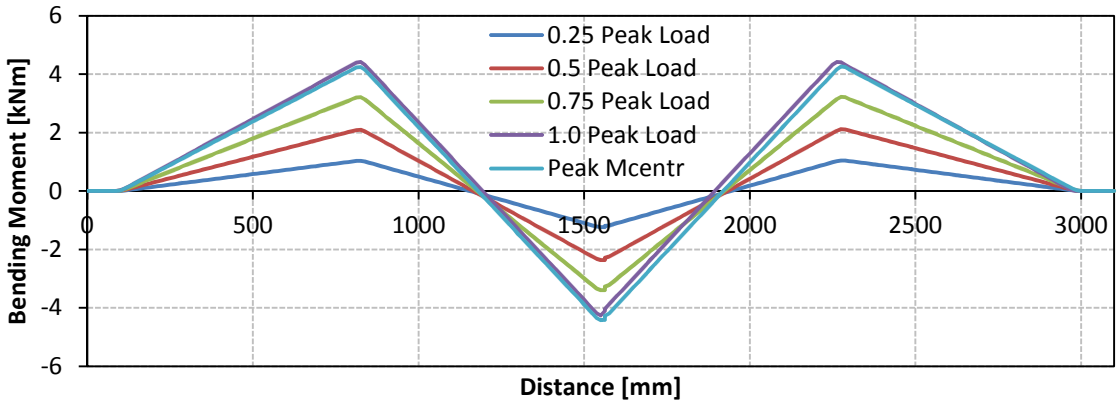

Figure B.1 Bending moment distribution with increase in load for 0.5% fibre volume.

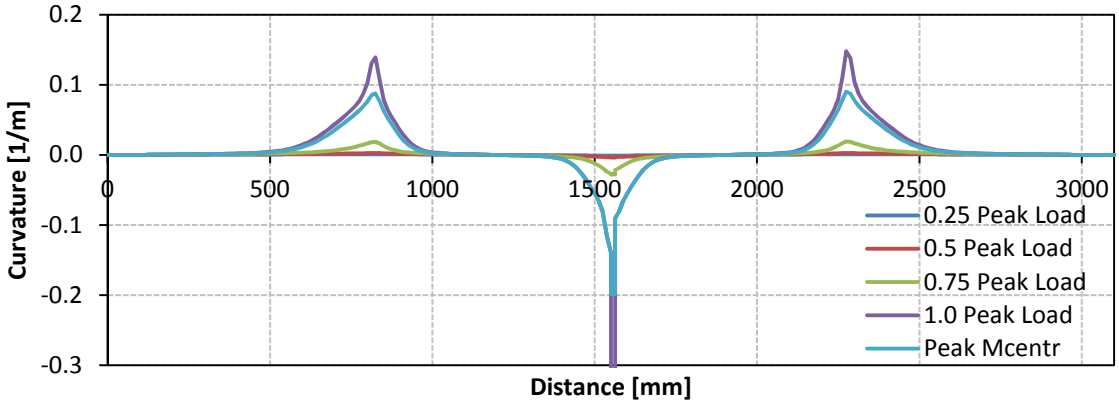

Figure B.2 Curvature distribution with increase in load for 0.5% fibre volume.

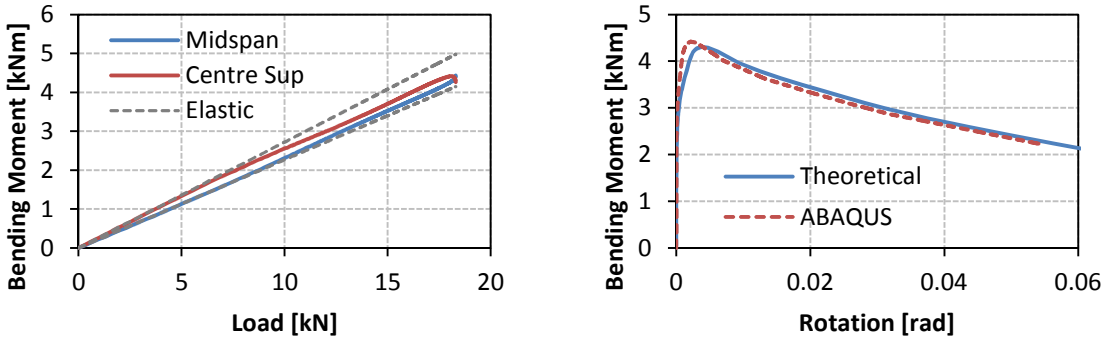

a) *b*)

Figure B.3 0.5% Fibre volume. a) Relation between bending moment and load applied at midspan and the centre support; b) Comparison between moment rotation output at the centre support and theoretical approximation.

B.3.2. 0.75% SFRCC Results

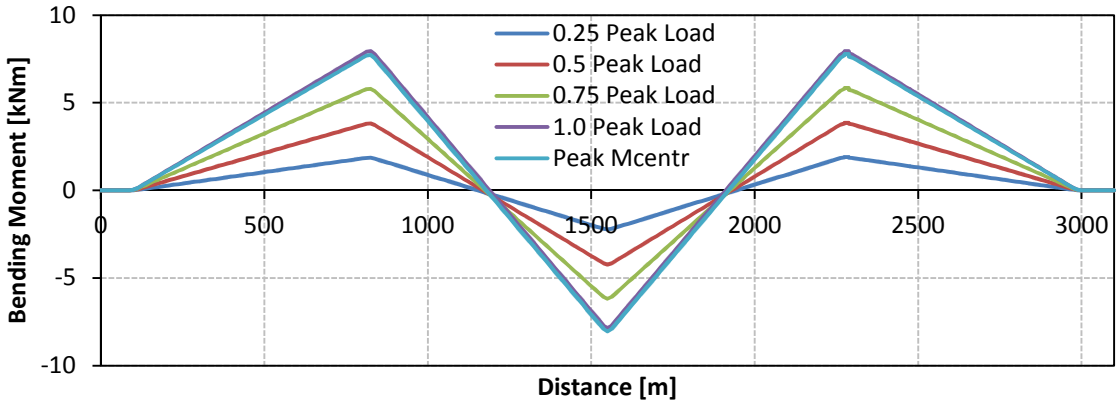

Figure B.4 Bending moment distribution with increase in load for 0.75% fibre volume.

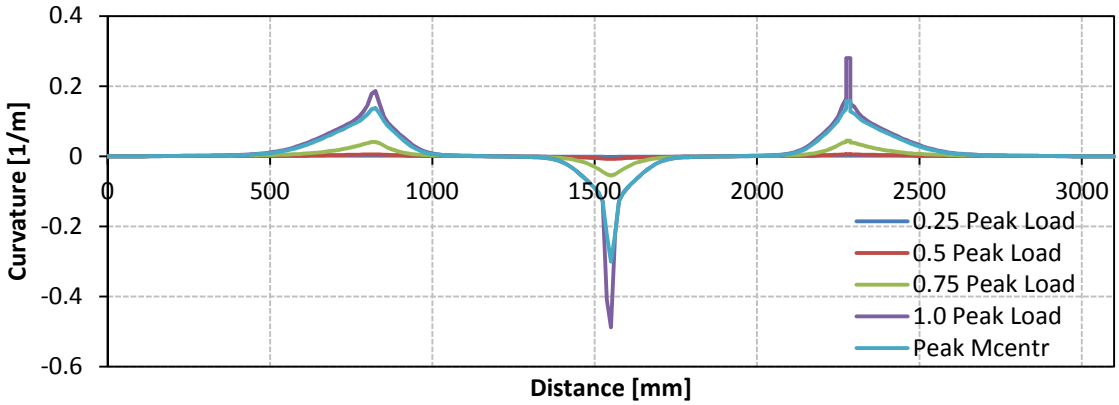

Figure B.5 Curvature distribution with increase in load for 0.75% fibre volume.

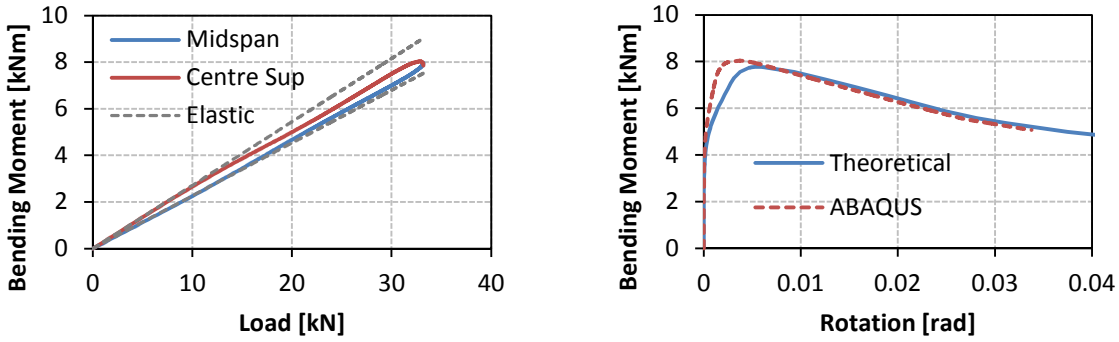

a) *b*)

Figure B.6 0.75% Fibre volume. a) Relation between bending moment and load applied at midspan and the centre support; b) Comparison between moment rotation output at the centre support and theoretical approximation.

B.3.3. 1.0% SFRCC Results

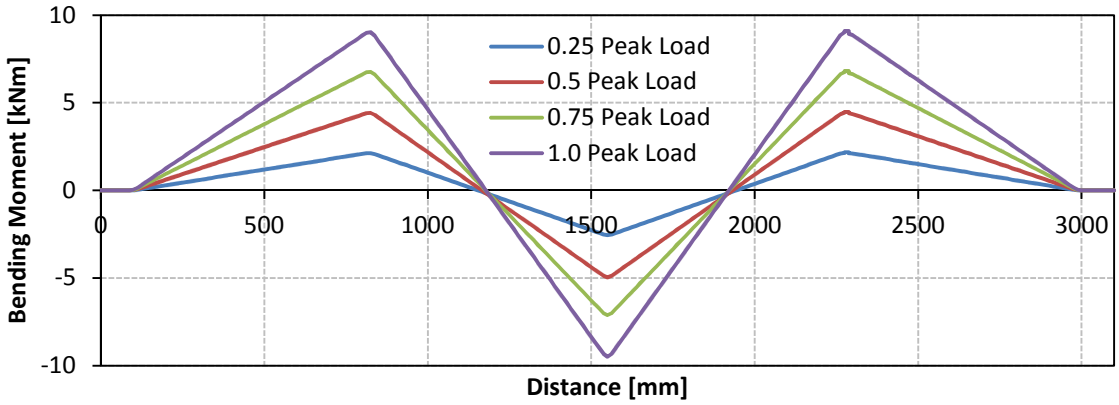

Figure B.7 Bending moment distribution with increase in load for 1.0% fibre volume.

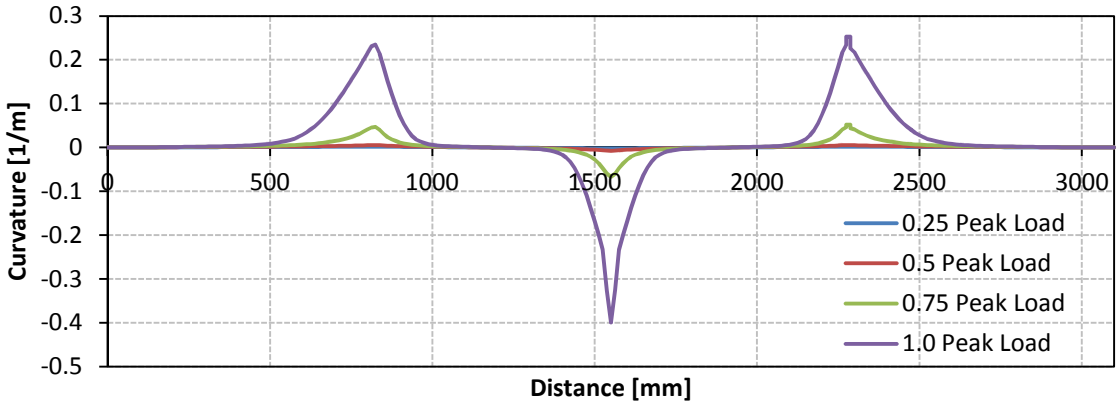

Figure B.8 Curvature distribution with increase in load for 1.0% fibre volume.

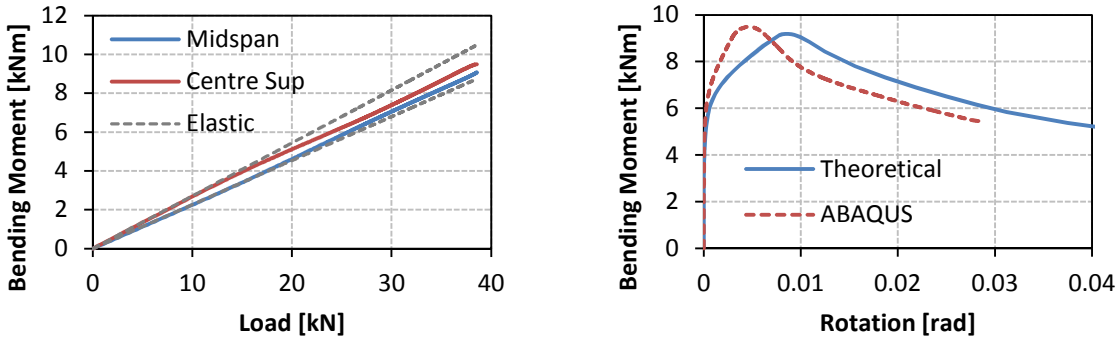

a) *b*)

Figure B.9 1.0% Fibre volume. a) Relation between bending moment and load applied at midspan and the centre support; b) Comparison between moment rotation output at the centre support and theoretical approximation.

B.4. ABAQUS data file

B.4.1. *.inp* File

```
*HEADING
INELASTIC NONLINEAR BEAM GENERAL
SECTION DYNAMICS
*NODE
1,
*NODE,NSET=N11
249,3100.
*NGEN
1,249
*ELEMENT,TYPE=B21
1,1,2
*ELGEN,ELSET=EALL
1,248,1,1
*BEAM GENERAL SECTION,DENSITY=2400.E-
09,
SECTION=NONLINEAR GENERAL,ELSET=EALL
31250., 40690104.2, 0., 162760416.7,
112000000.
0.,0.,-1.
*AXIAL
0., 0.
18.E+08, 0.0065
24.E+08, 0.073
12.5E+08, 0.1
*M1
0., 0.
1.101E+06, 0.0009E-03
1.663E+06, 0.0015E-03
2.106E+06, 0.0025E-03
2.346E+06, 0.0035E-03
2.504E+06, 0.0045E-03
2.667E+06, 0.006E-03
2.815E+06, 0.008E-03
2.923E+06, 0.01E-03
3.173E+06, 0.017E-03
3.365E+06, 0.025E-03
3.466E+06, 0.03E-03
3.807E+06, 0.05E-03
3.960E+06, 0.06E-03
4.098E+06, 0.07E-03
4.195E+06, 0.08E-03
4.263E+06, 0.09E-03
4.313E+06, 0.1E-03
4.351E+06, 0.11E-03
4.380E+06, 0.12E-03
4.419E+06, 0.14E-03
4.433E+06, 0.15E-03
4.463E+06, 0.2E-03
4.447E+06, 0.3E-03
4.401E+06, 0.4E-03
4.347E+06, 0.5E-03
4.290E+06, 0.6E-03
4.231E+06, 0.7E-03
4.171E+06, 0.8E-03
4.111E+06, 0.9E-03
4.050E+06, 1.0E-03
3.660E+06, 2.0E-03
3.388E+06, 3.0E-03
3.132E+06, 4.0E-03
2.896E+06, 5.0E-03
2.006E+06, 10.0E-03
*BOUNDARY
9, 2, 2
125, 1 ,1
125, 2, 2
241, 2, 2
**
** STEP: loading
**
*Step, name=loading, inc=5000
*Static, Direct
0.0005, 1.0,
**
** BOUNDARY CONDITION - DISPL CONTR
**
*BOUNDARY
67, 2, 2, -15.
183, 2, 2, -15.
**
** OUTPUT REQUESTS
*RESTART, WRITE, FREQUENCY=0
**
** FIELD OUTPUT
*OUTPUT, FIELD
*NODE OUTPUT
CF, RF, U, UR
*ELEMENT OUTPUT, DIRECTIONS=YES
SE, SF
**
** HISTORY OUTPUT
*OUTPUT, HISTORY, VARIABLE=PRESELECT
*END STEP
```

APPENDIX C

MODEL VERIFICATION

In this appendix all the experimental results for the statically indeterminate tests are presented. Also, the failure modes and input data are shown for that of the finite element models that were implemented in the test validation procedure.

C.1. Statically indeterminate test results

C.1.1. Specimen A1

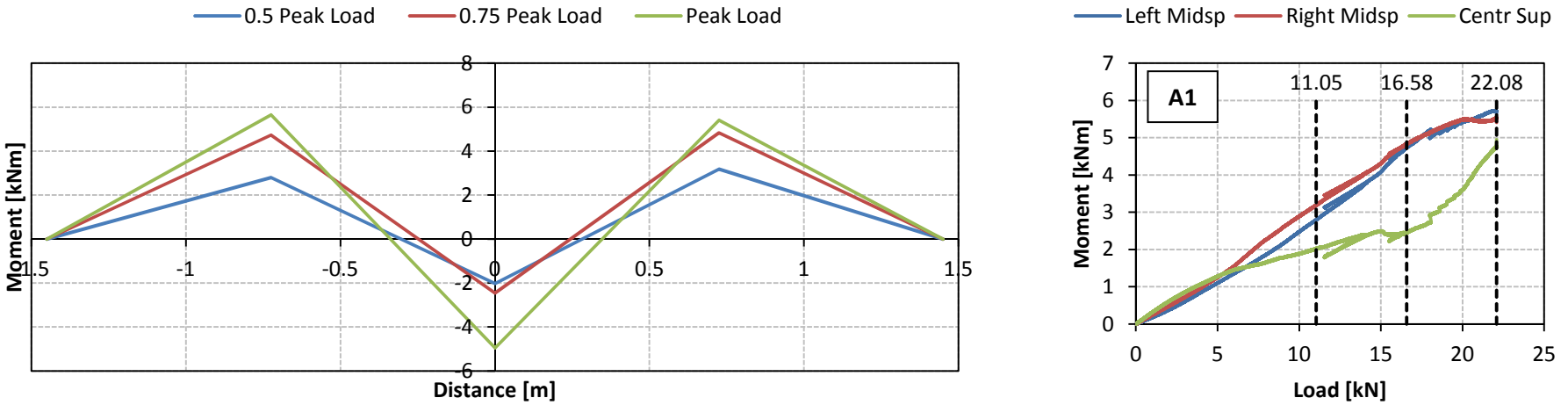

a) *b*)

Figure C.1 a) Bending moment distribution; b) Moment vs Load for the critical sections.

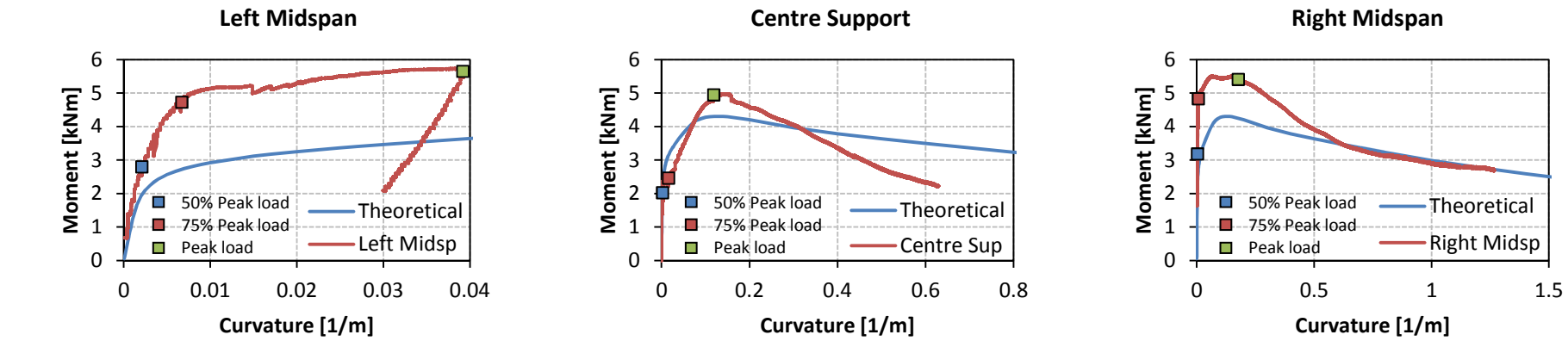

a) *b*) *c*)

Figure C.2 Experimental moment-curvature results for a) Left midspan, b) Centre support, c) Right midspan.

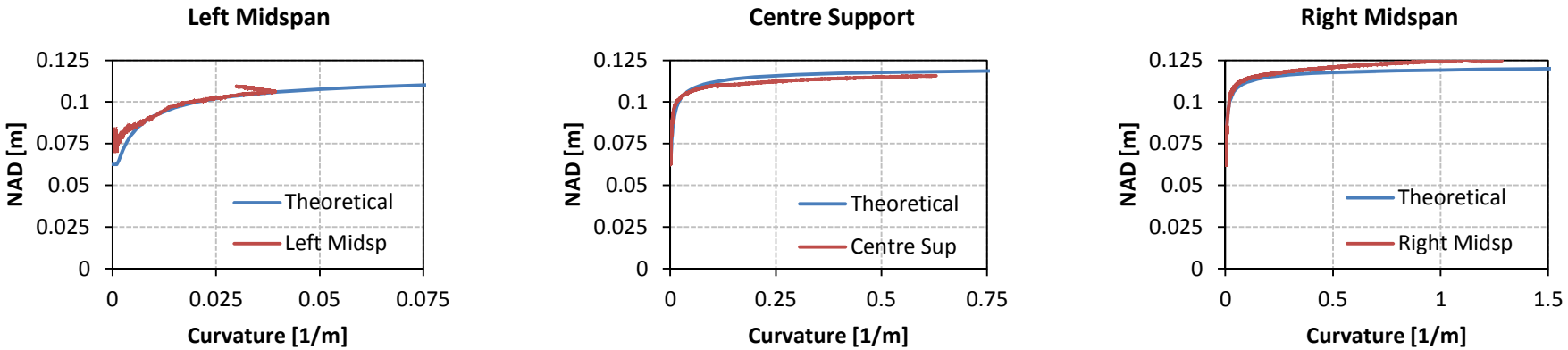

a) *b*) *c*)

Figure C.3 Experimental NAD-curvature results for a) Left midspan, b) Centre support, c) Right midspan.

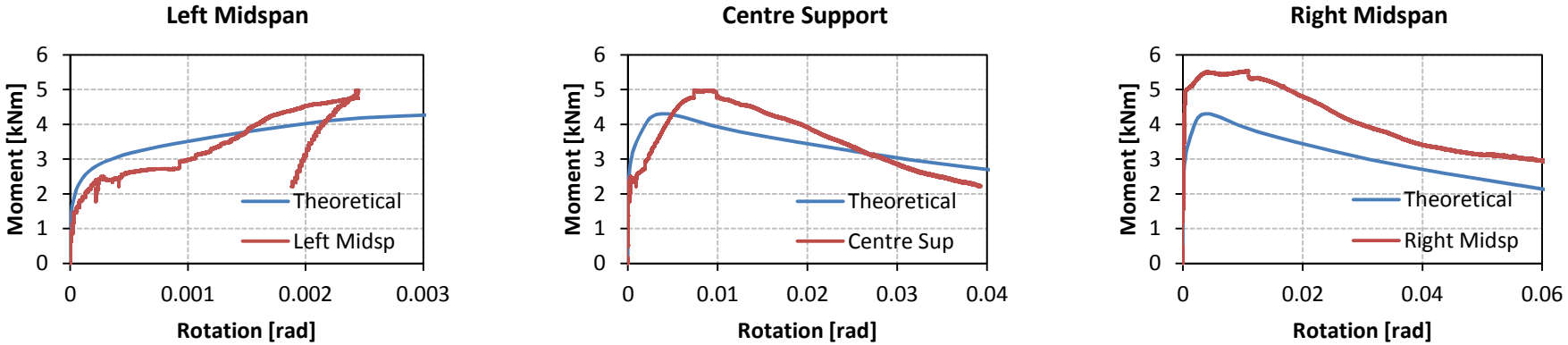

a) *b*) *c*)

Figure C.4 Experimental moment-rotation results for a) Left midspan, b) Centre support, c) Right midspan.

C.1.2. Specimen A2

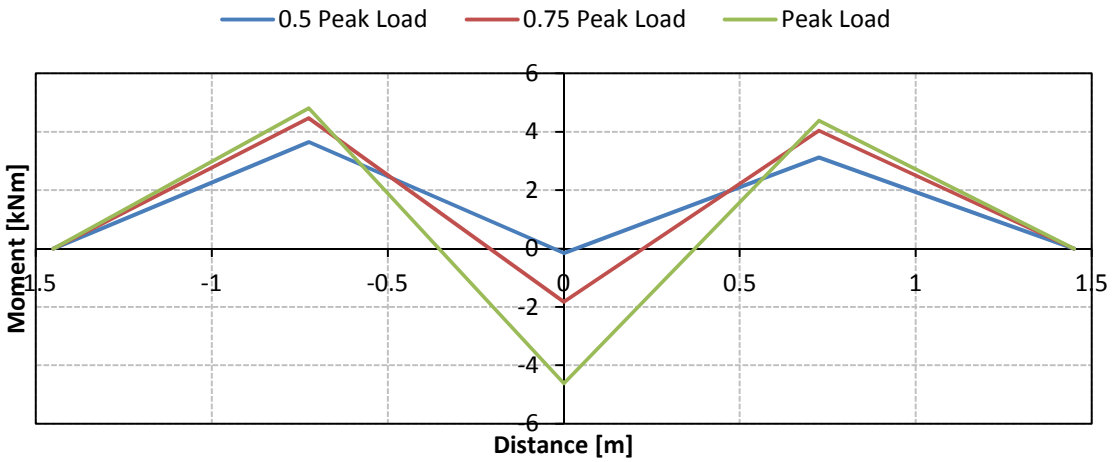

a)

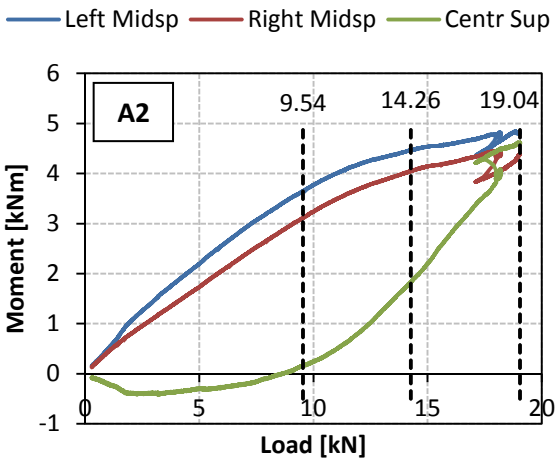

b)

Figure C.5 a) Bending moment distribution; b) Moment vs Load for the critical sections.

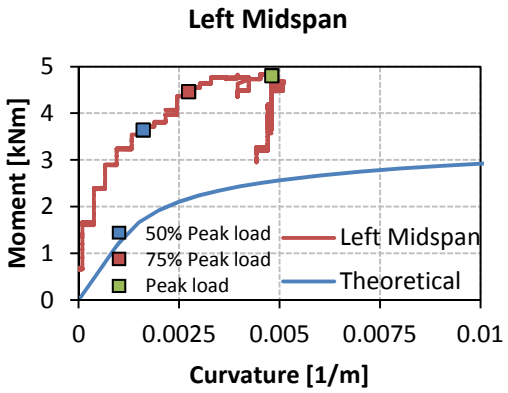

a)

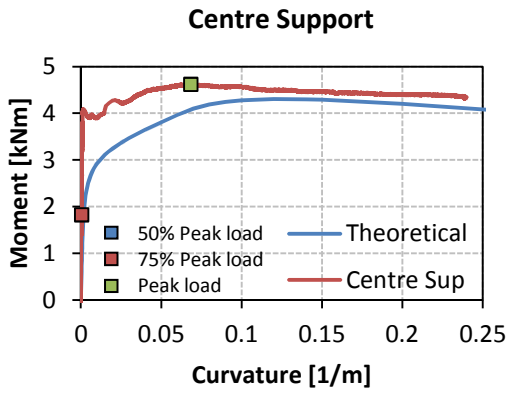

b)

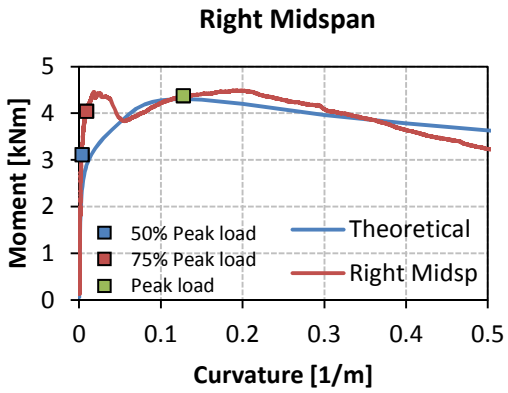

c)

Figure C.6 Experimental moment-curvature results for a) Left midspan, b) Centre support, c) Right midspan.

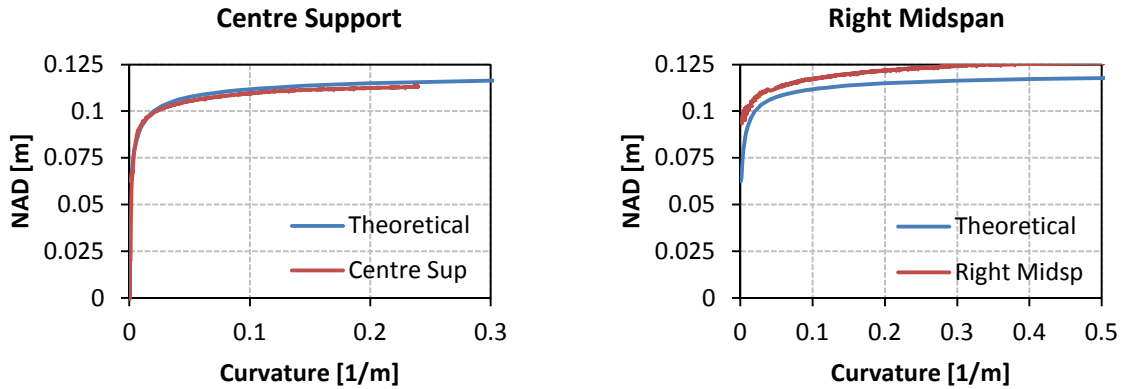

a) *b*)

Figure C.7 Experimental NAD-curvature results for a) Centre support, b) Right midspan.

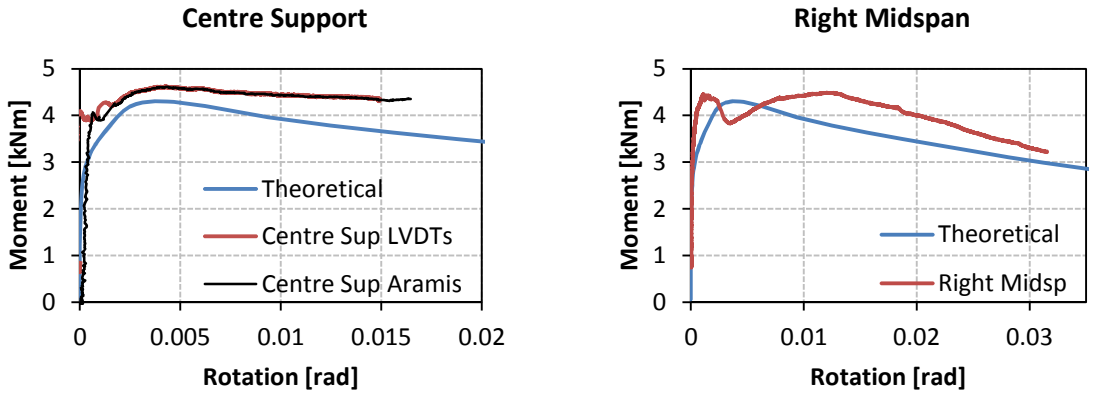

a) *b*)

Figure C.8 Experimental moment-rotation results for a) Centre support, b) Right midspan.

C.1.3. Specimen A3

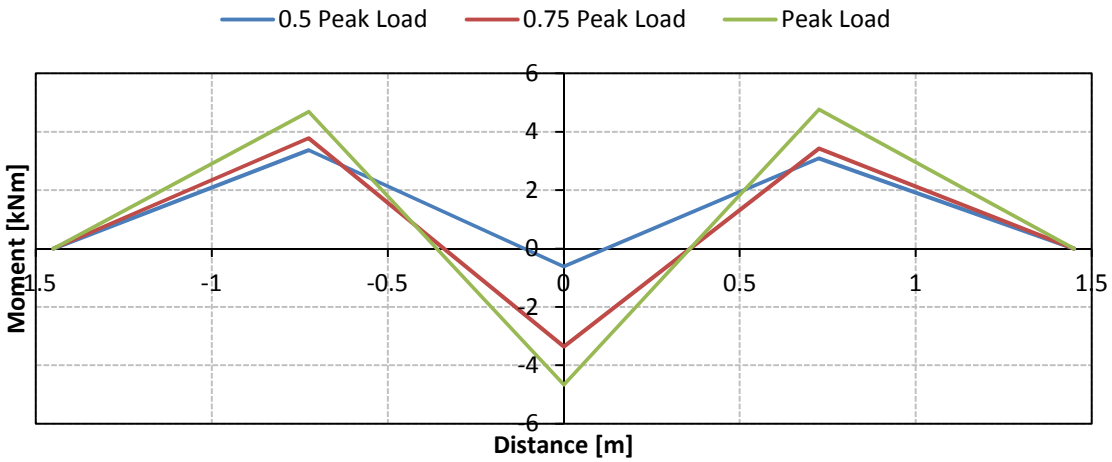

a)

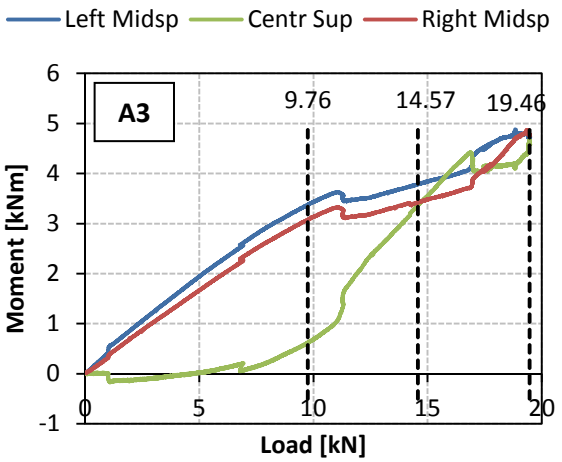

b)

Figure C.9 a) Bending moment distribution; b) Moment vs Load for the critical sections.

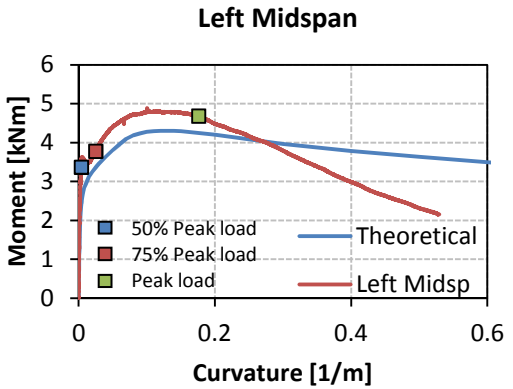

a)

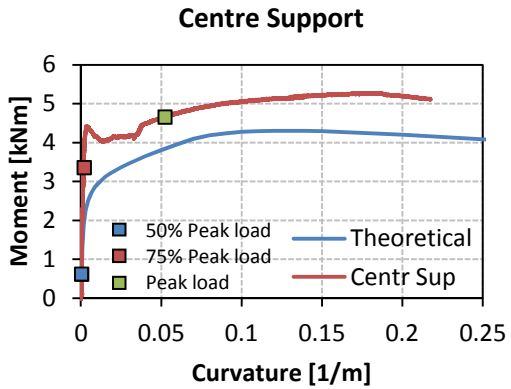

b)

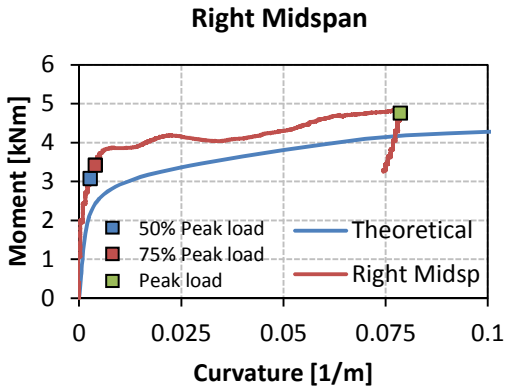

c)

Figure C.10 Experimental moment-curvature results for a) Left midspan, b) Centre support, c) Right midspan.

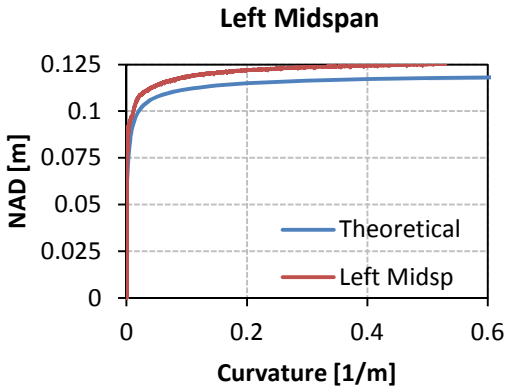

Figure C.11 Experimental NAD-curvature results for the left midspan.

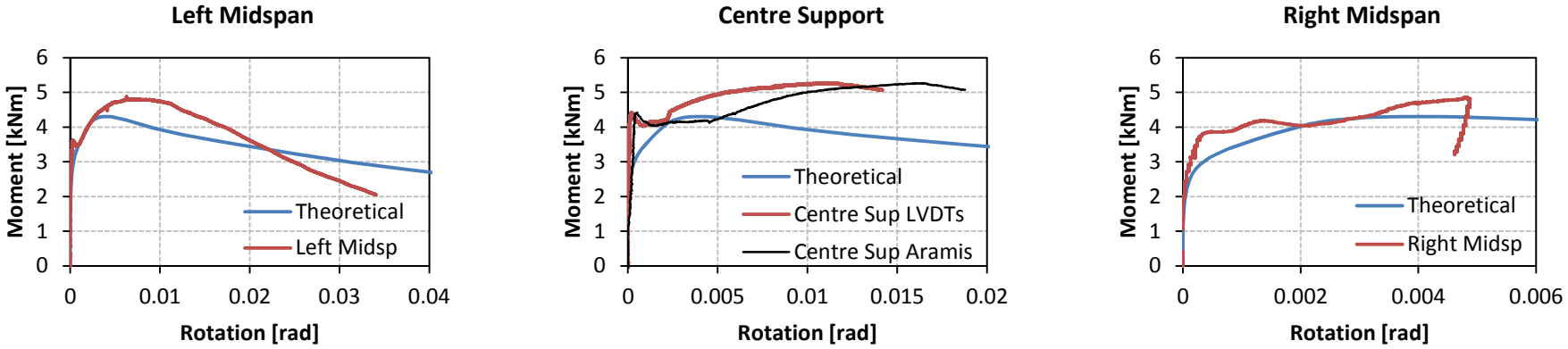

a) *b*) *c*)

Figure C.12 Experimental moment-rotation results for a) Left midspan, b) Centre support, c) Right midspan.

C.1.4. Specimen B1

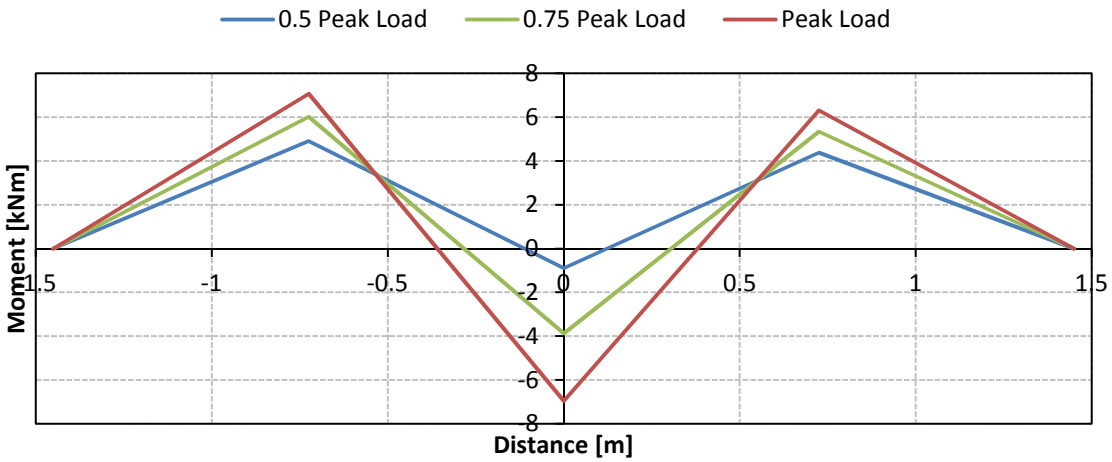

a)

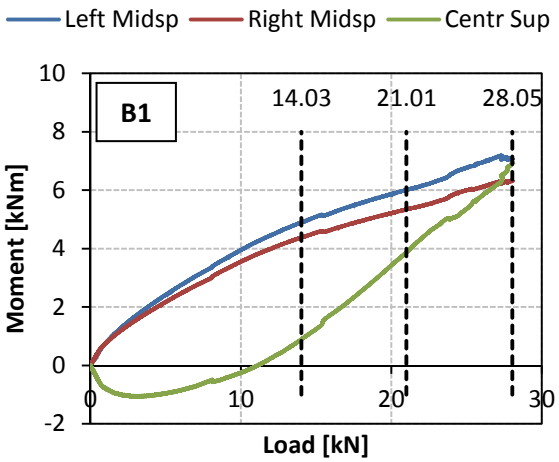

b)

Figure C.13 a) Bending moment distribution; b) Moment vs Load for the critical sections.

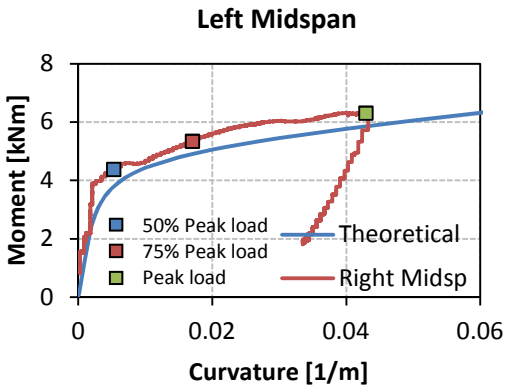

a)

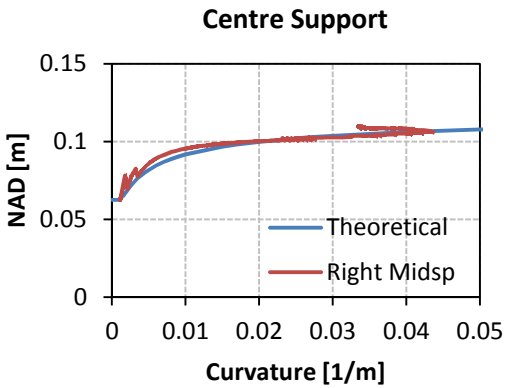

b)

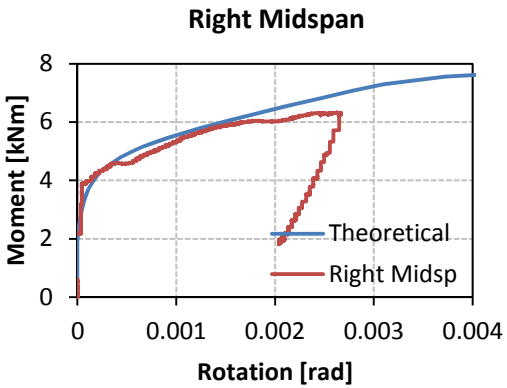

c)

Figure C.14 Experimental results for right midspan. a) Moment-curvature results; b) NAD-curvature results; c) Moment-rotation results.

C.1.5. Specimen B2

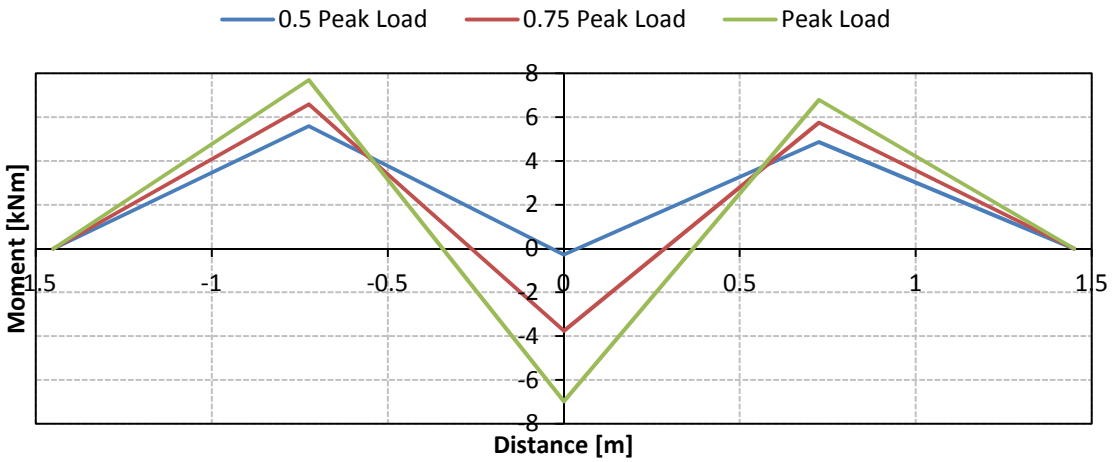

a)

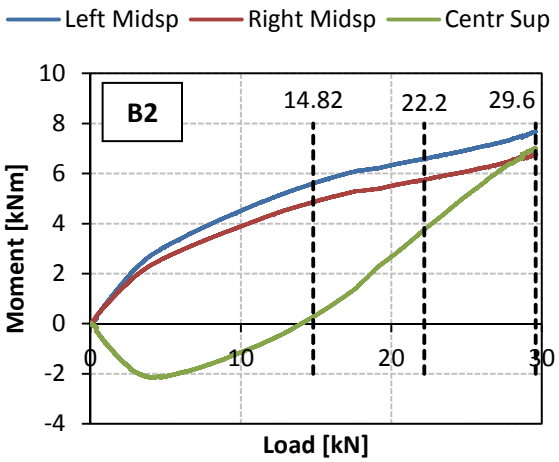

b)

Figure C.15 a) Bending moment distribution; b) Moment vs Load for the critical sections.

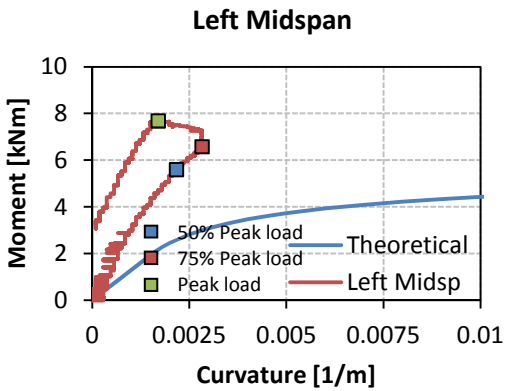

a)

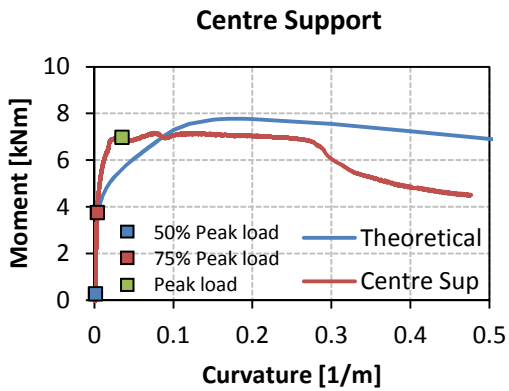

b)

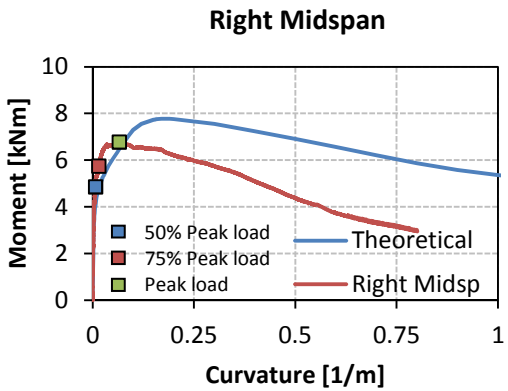

c)

Figure C.16 Experimental moment-curvature results for a) Left midspan, b) Centre support, c) Right midspan.

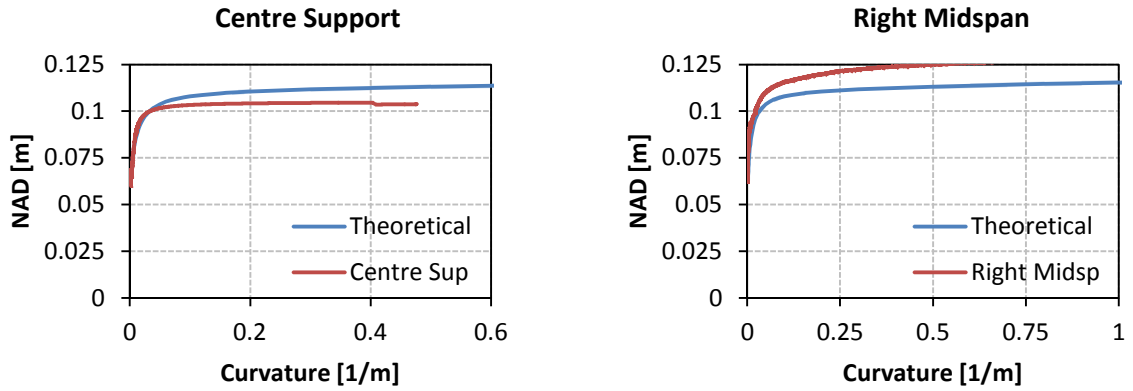

a) *b*)

Figure C.17 Experimental NAD-curvature results for a) Centre support, b) Right midspan.

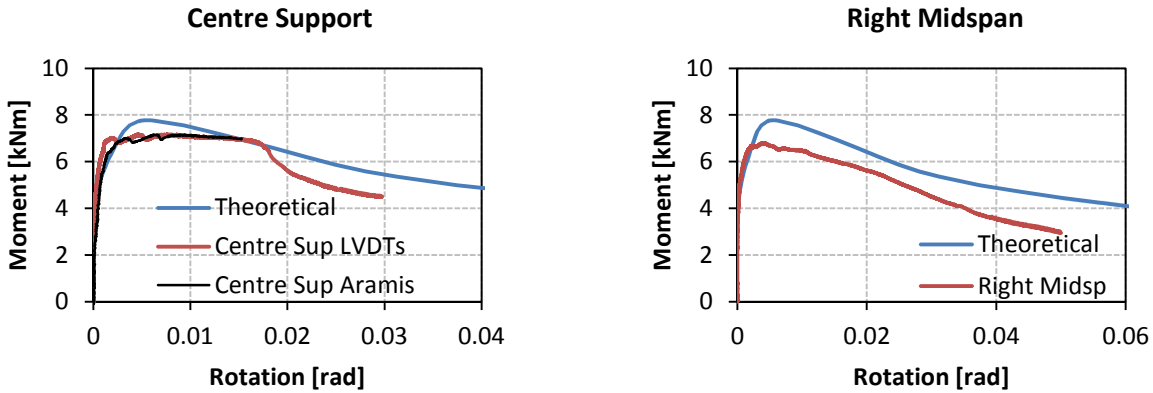

a) *b*)

Figure C.18 Experimental moment-rotation results for a) Centre support, b) Right midspan.

C.1.6. Specimen B3

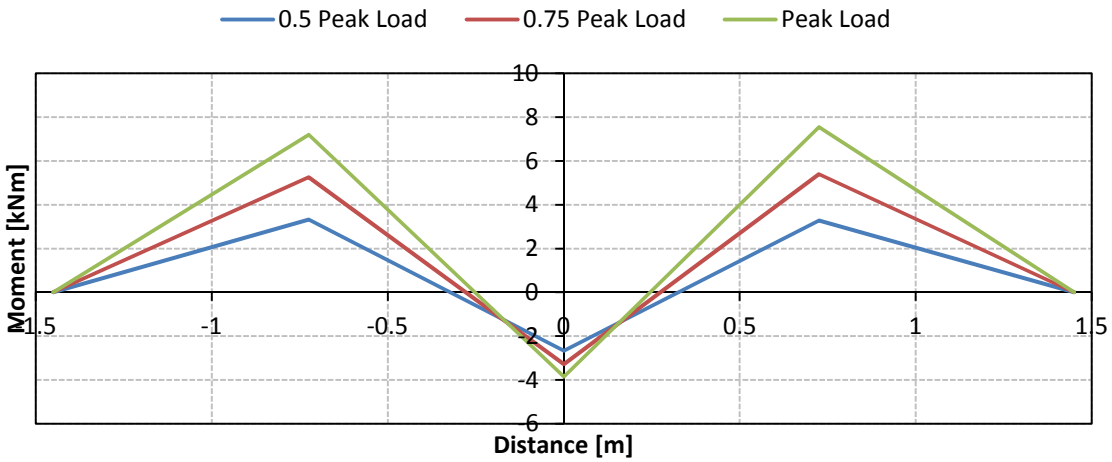

a)

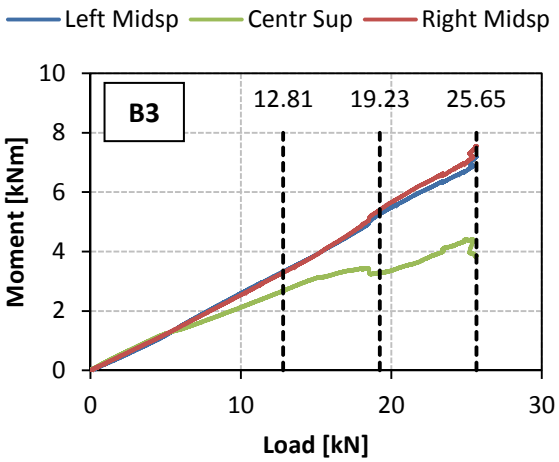

b)

Figure C.19 a) Bending moment distribution; b) Moment vs Load for the critical sections.

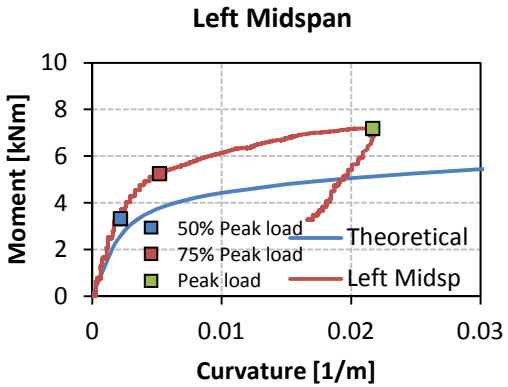

a)

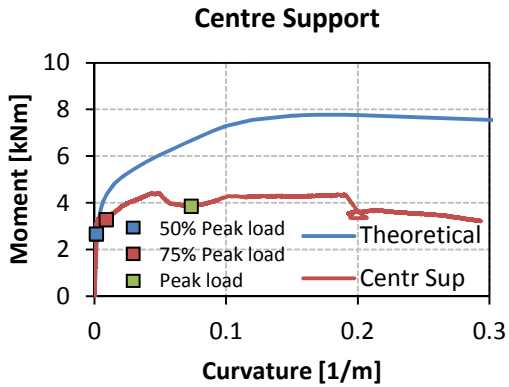

b)

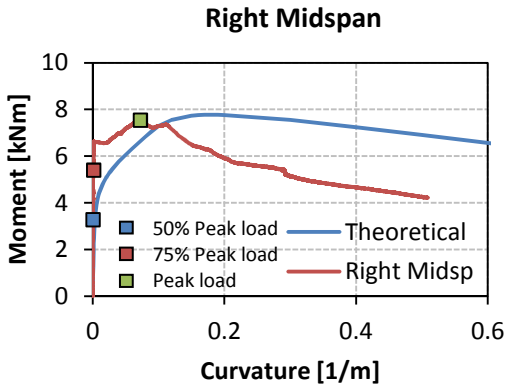

c)

Figure C.20 Experimental moment-curvature results for a) Left midspan, b) Centre support, c) Right midspan.

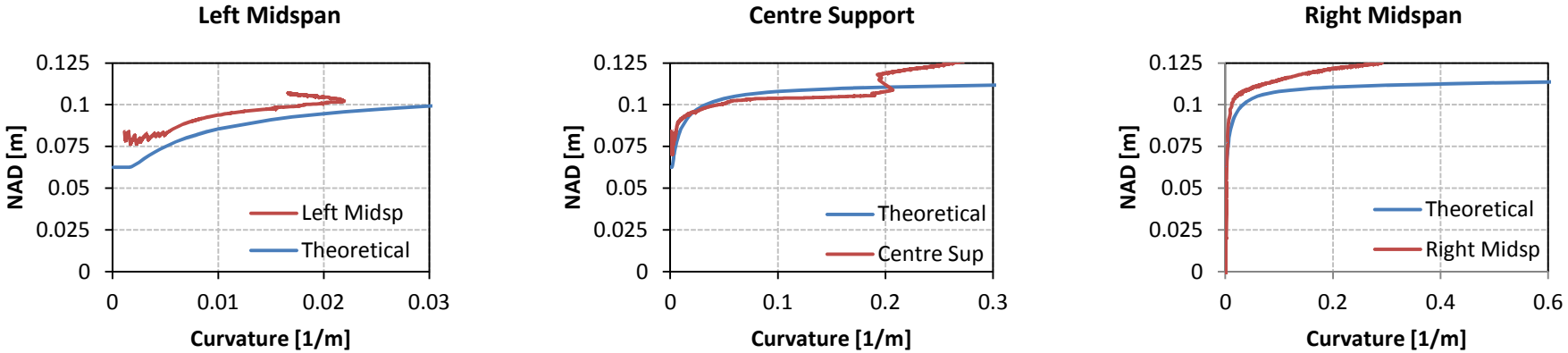

a) *b*) *c*)

Figure C.21 Experimental NAD-curvature results for a) Left midspan, b) Centre support, c) Right midspan.

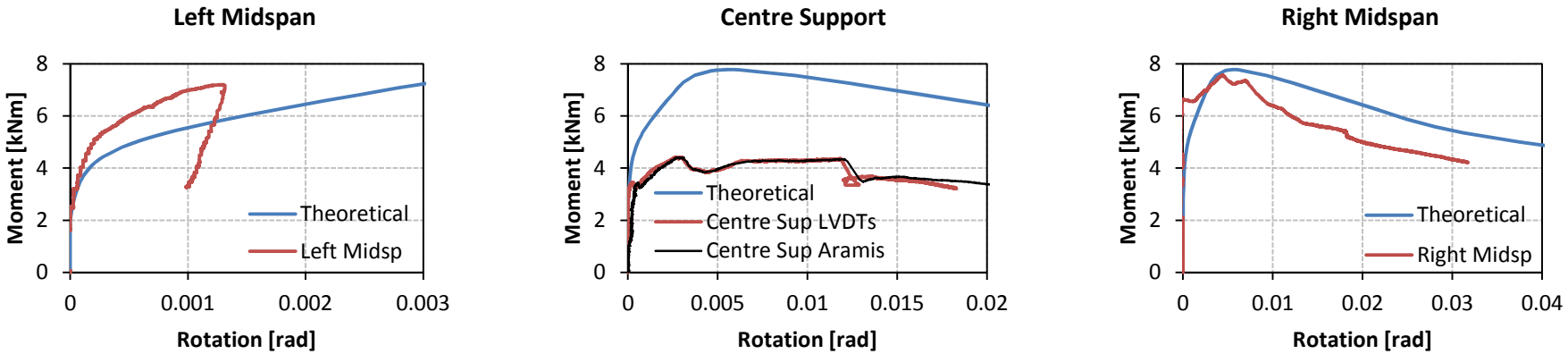

a) *b*) *c*)

Figure C.22 Experimental moment-rotation results for a) Left midspan, b) Centre support, c) Right midspan.

C.1.7. Specimen C1

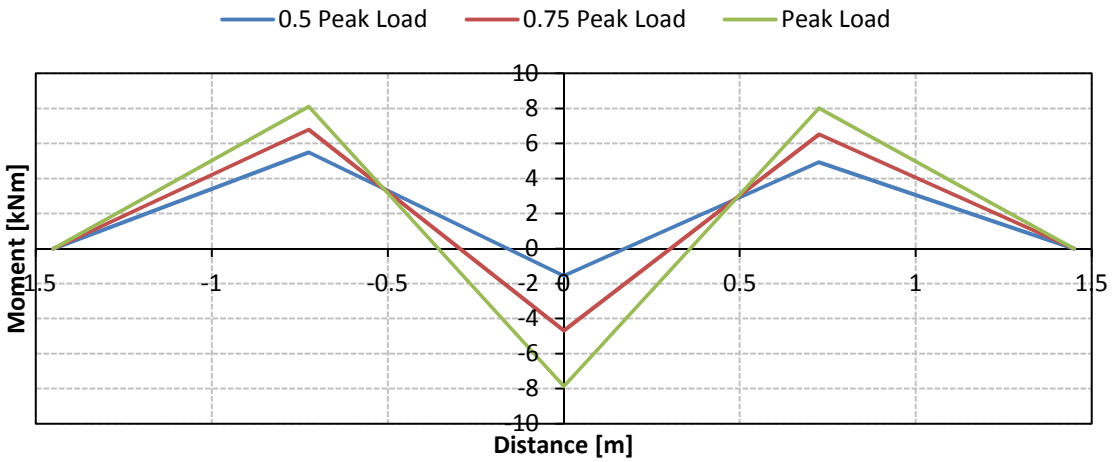

a)

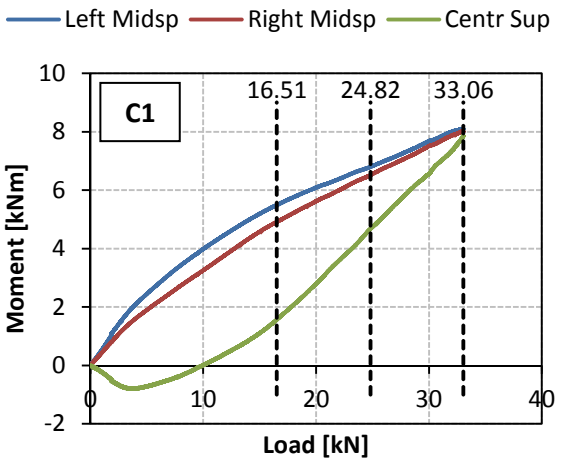

b)

Figure C.23 a) Bending moment distribution; b) Moment vs Load for the critical sections.

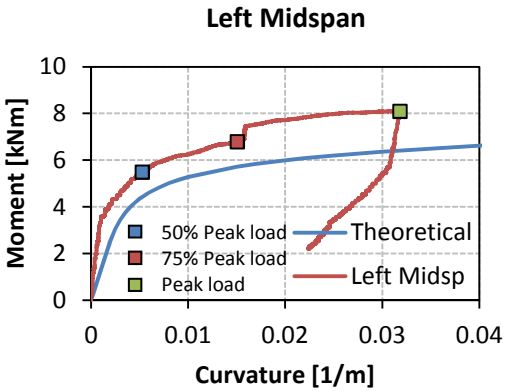

a)

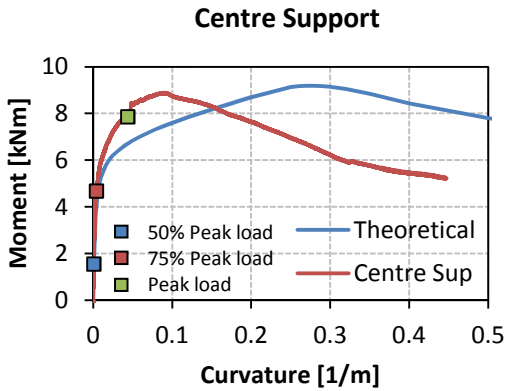

b)

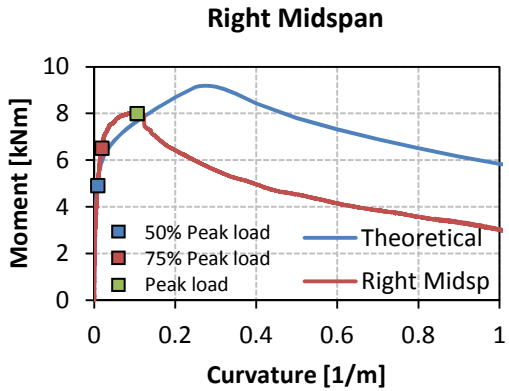

c)

Figure C.24 Experimental moment-curvature results for a) Left midspan, b) Centre support, c) Right midspan.

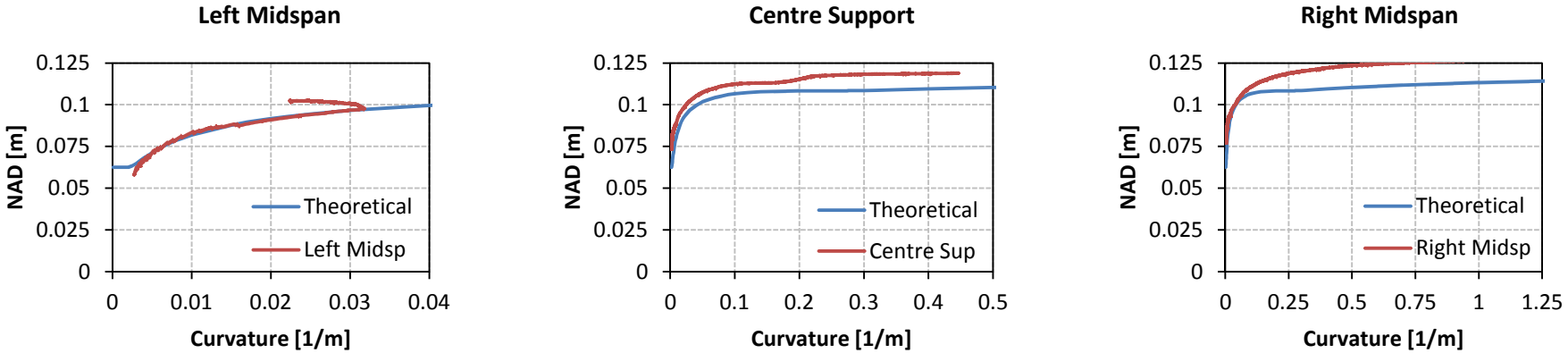

a) *b*) *c*)

Figure C.25 Experimental NAD-curvature results for a) Left midspan, b) Centre support, c) Right midspan.

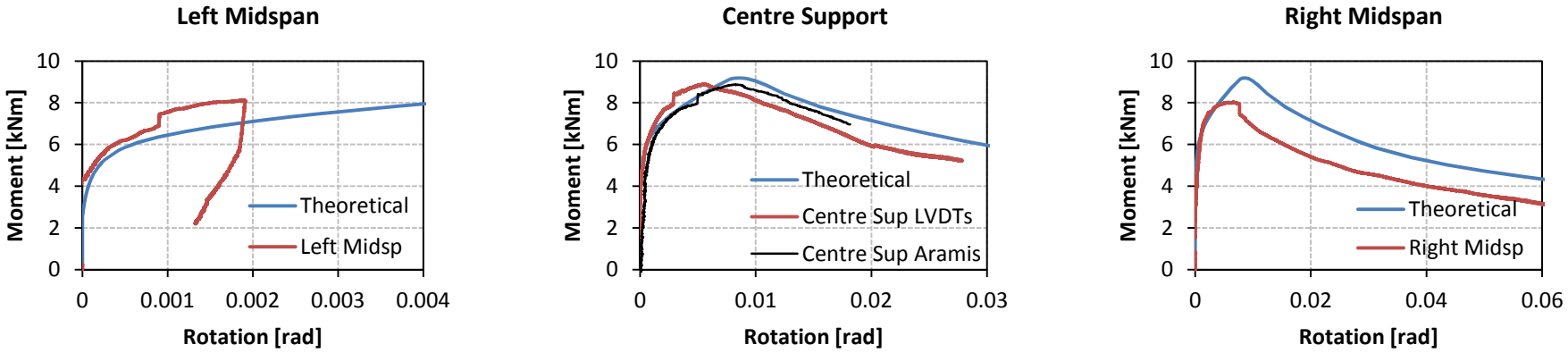

a) *b*) *c*)

Figure C.26 Experimental moment-rotation results for a) Left midspan, b) Centre support, c) Right midspan.

C.1.8. Specimen C2

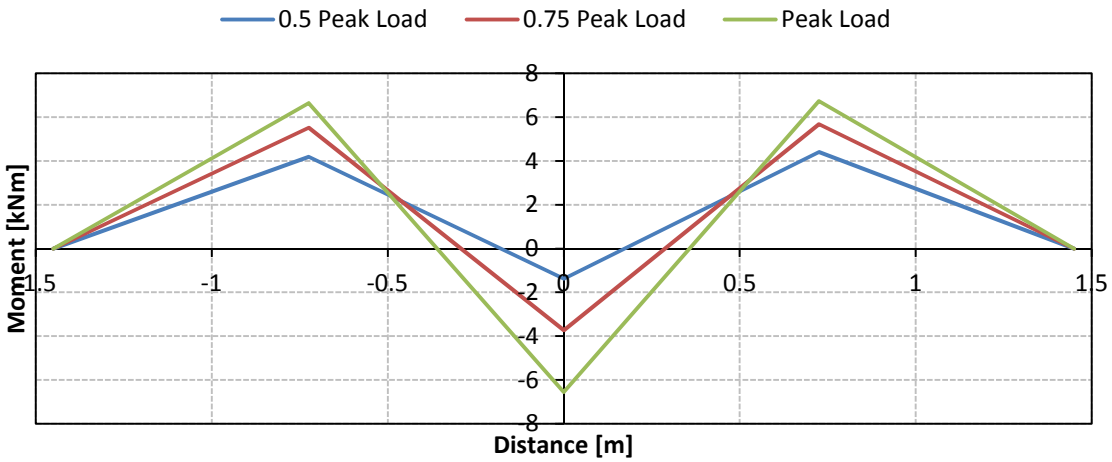

a)

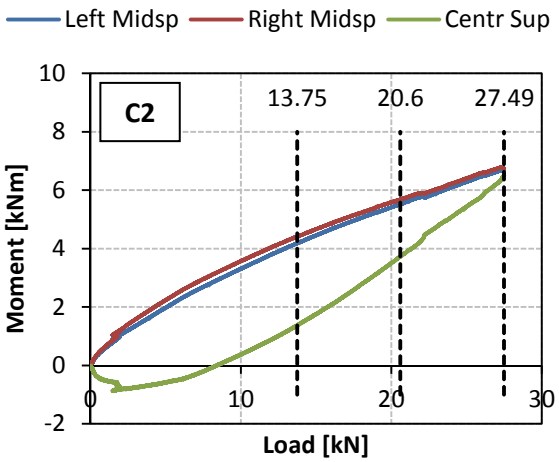

b)

Figure C.27 a) Bending moment distribution; b) Moment vs Load for the critical sections.

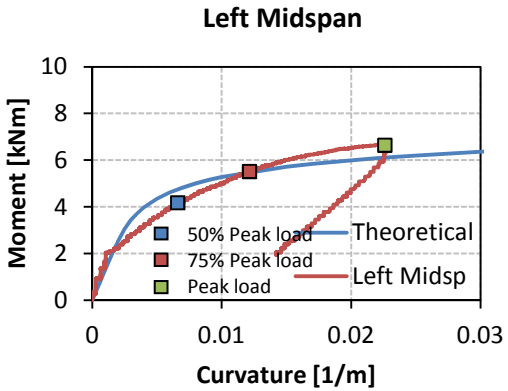

a)

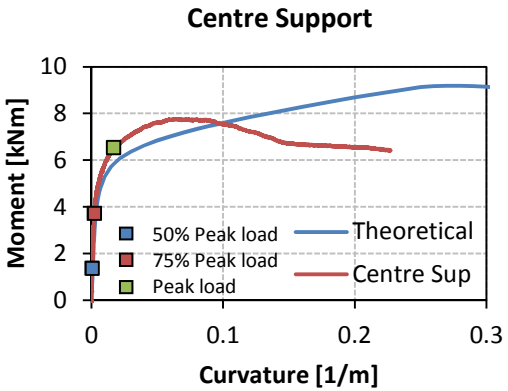

b)

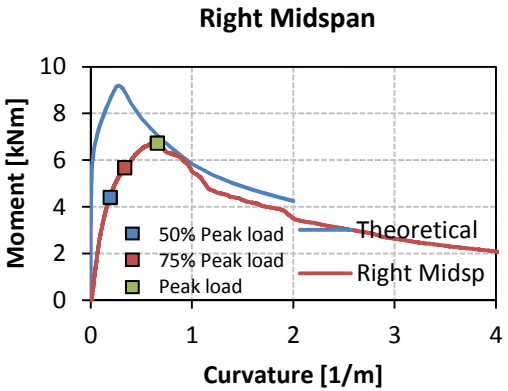

c)

Figure C.28 Experimental moment-curvature results for a) Left midspan, b) Centre support, c) Right midspan.

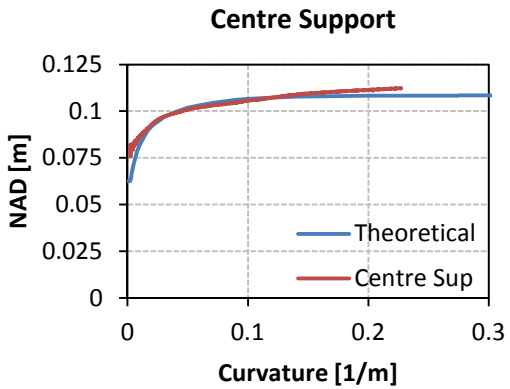

Figure C.29 Experimental NAD-curvature results for the centre support.

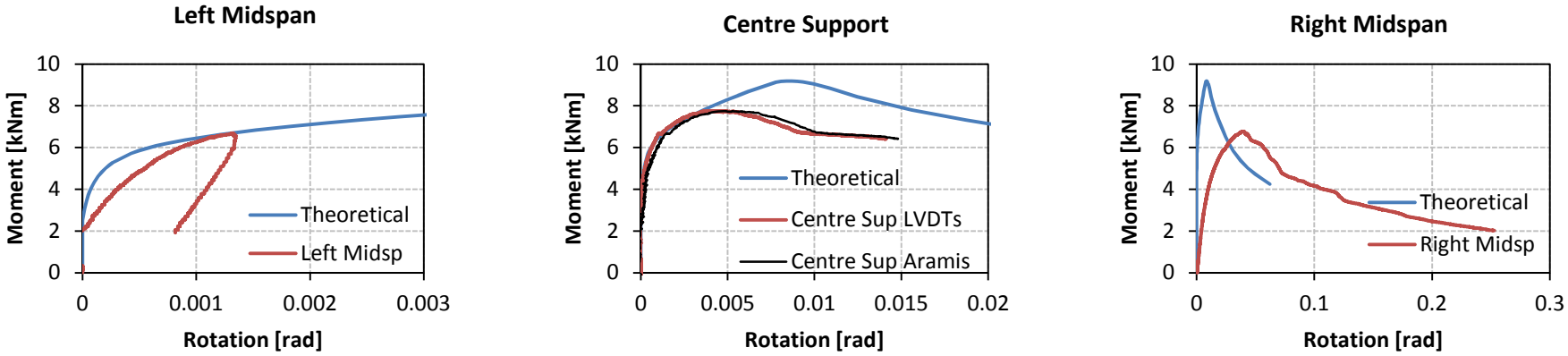

a) *b*) *c*)

Figure C.30 Experimental moment-rotation results for a) Left midspan, b) Centre support, c) Right midspan.

C.1.9. Specimen C3

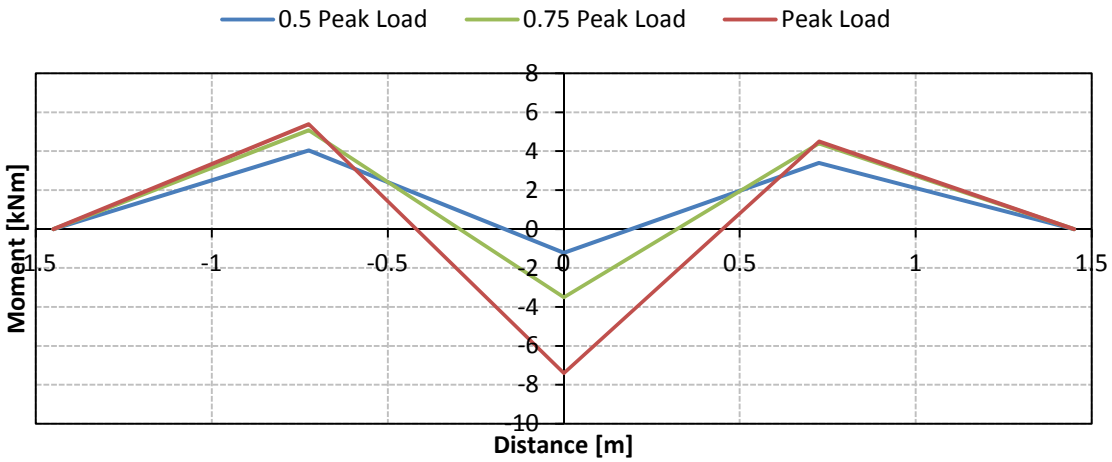

a)

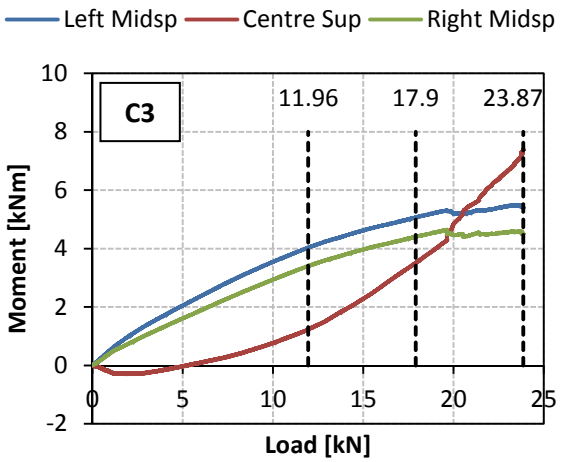

b)

Figure C.31 a) Bending moment distribution; b) Moment vs Load for the critical sections.

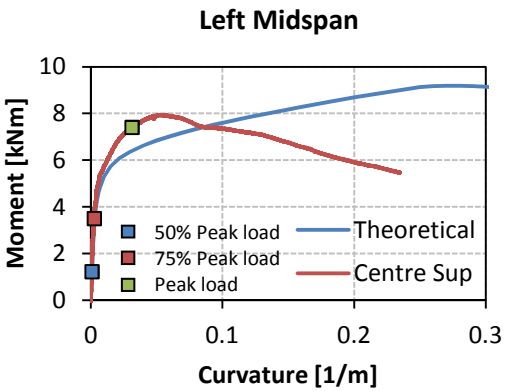

a)

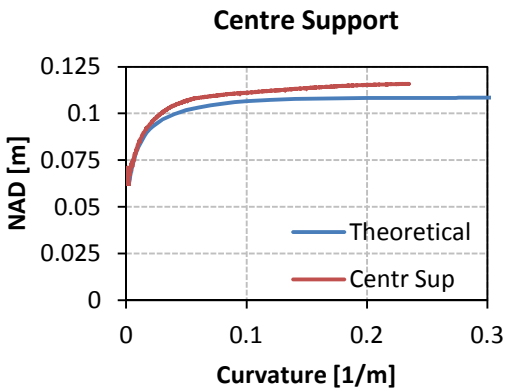

b)

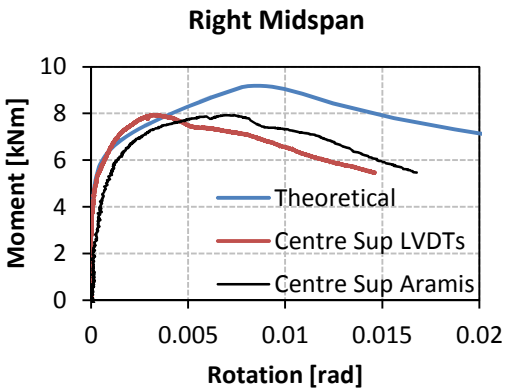

c)

Figure C.32 Experimental results for centre support. a) Moment-curvature results; b) NAD-curvature results; c) Moment-rotation results.

C.2. Finite Element Models

C.2.1. *CASE I* – Gap between specimen and centre support

C.2.1.1. Failure Modes

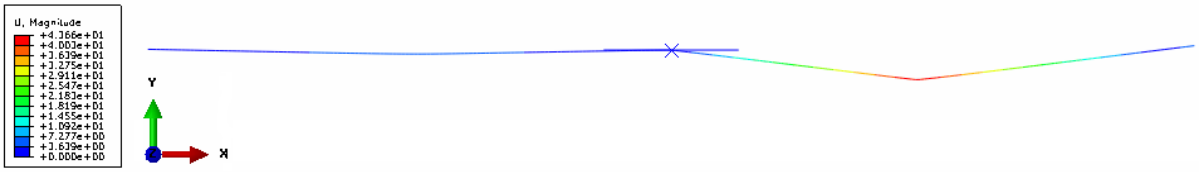

Figure C.33 Vertical displacement presented on deflected shape for 0.5% SFRC member.

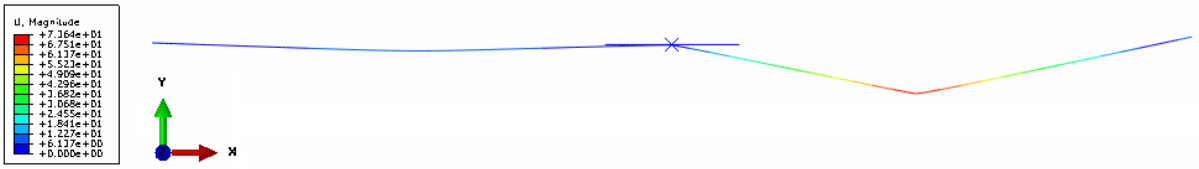

Figure C.34 Vertical displacement presented on deflected shape for 0.75% SFRC member.

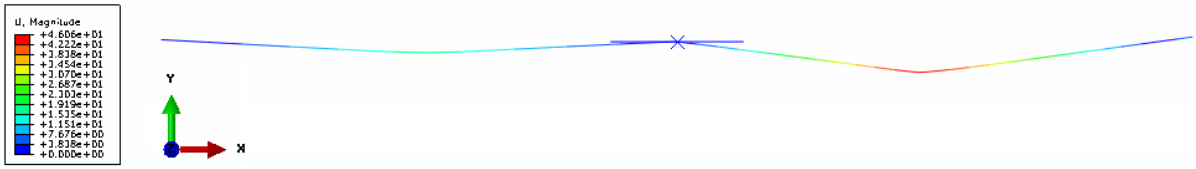

Figure C.35 Vertical displacement presented on deflected shape for 1.0% SFRC member.

C.2.1.2. ABAQUS *.inp* File

```
*Heading
** Job name: Feas-Job Model name: 5pbt_1b
** Generated by: Abaqus/CAE 6.11-1
*Preprint, echo=NO, model=NO, history=NO,
contact=NO
**
** PARTS
**
*Part, name=PART-1
*Node
     1,          0.,          0.
     2,        12.5,          0.
...
...
249,       3100.,          0.
   250,       1350.,         -0.3
   252,       1750.,         -0.3
*Element, type=B23
 1,  1,  2
 2,  2,  3
...
...
247, 247, 248
248, 248, 249
*Elset, elset=EALL, generate
  1,  248,    1
*Elset, elset=_PickedSet3, internal, generate
  1,  182,    1
*Elset, elset=_PickedSet4
  183
*Elset, elset=_PickedSet5, internal, generate
  184, 248, 1
*ELSET, ELSET=NormalEl
_PickedSet3, _PickedSet5
**
*BEAM GENERAL
SECTION,ELSET=NormalEl,DENSITY=2400.E-09,
SECTION=NONLINEAR GENERAL
31250., 40690104.2, 0., 162760416.7,
112000000.
0.,0.,-1.
*AXIAL
0., 0.
18.E+08, 0.0065
24.E+08, 0.073
12.5E+08, 0.1
*M1
0., 0.
1.101E+06, 0.0009E-03
1.663E+06, 0.0015E-03
...
...
2.896E+06, 5.0E-03
2.006E+06, 10.0E-03
**
**
**WEAK ELEMENT
**
*BEAM GENERAL
SECTION,ELSET=_PickedSet4,DENSITY=2400.E-
09,
SECTION=NONLINEAR GENERAL
31250., 40690104.2, 0., 162760416.7,
112000000.
0.,0.,-1.
*AXIAL
0., 0.
18.E+08, 0.0065
24.E+08, 0.073
12.5E+08, 0.1
*M1
0., 0.
1.08999E+06, 0.000891E-03
1.64637E+06, 0.001485E-03
...
...
2.86704E+06, 4.95E-03
1.98594E+06, 9.9E-03
*End Part
**
*Part, name=RIGID_SURF
*End Part
**
**
** ASSEMBLY
**
*Assembly, name=Assembly
**
*Instance, name=RIGID_SURF-1,
part=RIGID_SURF
*Node
     1,       1550.,        -0.3,          0.
*Nset, nset=RIGID_SURF-1-RefPt_, internal
1,
*Surface, type=SEGMENTS,
name=RigidSurface_, internal
```

```
START,       1350.,        -0.3
 LINE,       1750.,        -0.3
*Rigid Body, ref node=RIGID_SURF-1-RefPt_,
analytical surface=RigidSurface_
*End Instance
**
*Instance, name=PART-1-1, part=PART-1
*End Instance
**
*Nset, nset=_PickedSet17, internal,
instance=RIGID_SURF-1
 1,
*Nset, nset=N11, instance=PART-1-1
 249,
*Nset, nset=N12, instance=PART-1-1
 252,
*Nset, nset=SLAB_SURF, instance=PART-1-1
 125,
*Nset, nset=_M13, internal, instance=PART-1-
1
  9, 241
*Nset, nset=_M14, internal, instance=PART-1-
1
 67, 183
*Nset, nset=_PickedSet16, internal,
instance=PART-1-1
 9,
*Surface, type=NODE,
name=SLAB_SURF_CNS_, internal
SLAB_SURF, 1.
*End Assembly
** INTERACTION PROPERTIES
**
*Surface Interaction, name=SURFINTERACT
1.,
**
** BOUNDARY CONDITIONS
**
** Name: Disp-BC-1 Type:
Displacement/Rotation
*Boundary
_M13, 2, 2
** Name: End-X Type: Displacement/Rotation
*Boundary
_PickedSet16, 1, 1
** Name: Ref Type: Displacement/Rotation
*Boundary
_PickedSet17, 1, 1
_PickedSet17, 2, 2
_PickedSet17, 6, 6
**
** INTERACTIONS
**
** Interaction: SURFINTERACT-1
*Contact Pair, interaction=SURFINTERACT,
type=SURFACE TO SURFACE
SLAB_SURF_CNS_, RIGID_SURF-
1.RigidSurface_
**
**
** STEP: loading
**
*Step, name=loading,  inc=5000
*Static,Riks,Direct
0.0005, 1.0,
**
** NAME: FORCE-CONTROLLED
*CLOAD
_M14,2,-19000
**
** OUTPUT REQUESTS
**
*Restart, write, frequency=0
**
** FIELD OUTPUT: F-Output-1
**
*Output, field
*Node Output
CF, RF, U, UR
**
** FIELD OUTPUT: F-Output-2
**
*Element Output, directions=YES
SE, SF
**
** HISTORY OUTPUT: H-Output-1
**
*Output, history, variable=PRESELECT
*End Step
```

C.2.2. *CASE II* – Centre support having lower stiffness in relation to end supports

C.2.2.1. Failure Modes

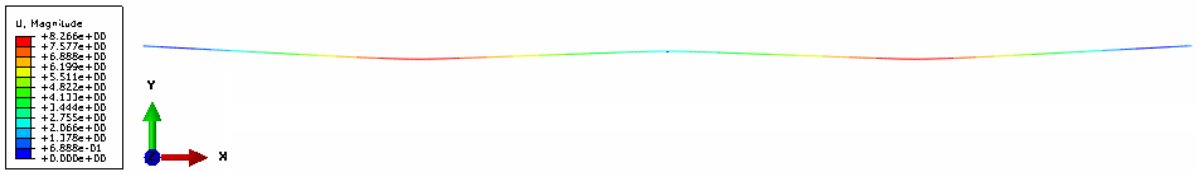

Figure C.36 Vertical displacement presented on deflected shape for 0.5% SFRC member.

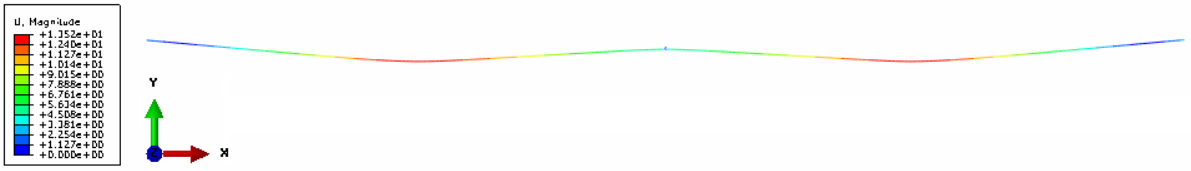

Figure C.37 Vertical displacement presented on deflected shape for 0.75% SFRC member.

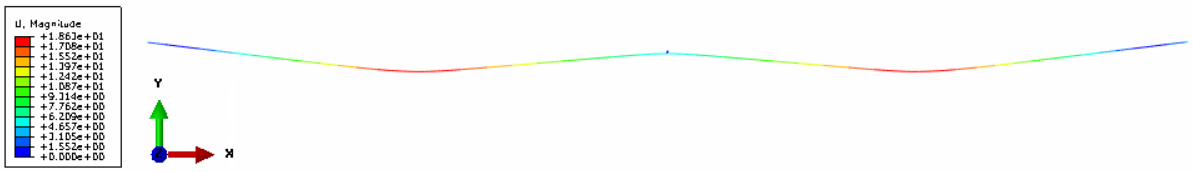

Figure C.38 Vertical displacement presented on deflected shape for 1.0% SFRC member.

C.2.2.2. ABAQUS *.inp* File

```
*HEADING
INELASTIC NONLINEAR BEAM GENERAL
SECTION DYNAMICS
*NODE
1,
*NODE,NSET=N11
249,3100.
*NGEN
1,249
*NSET, nset=loadPoints
67,183
*NODE
250, 1550., -12.5
*ELEMENT,TYPE=B21
1,1,2
*ELGEN, ELSET=EALL
1,248,1,1
**ELSET,ELSET=EALL, generate
**1,248,1
*ELSET, elset=left_full, generate
1, 182, 1
*ELSET, elset=weak
```

```
183
*ELSET, elset=right_full, generate
184, 248, 1
*ELSET, ELSET=full
left_full, right_full
**
*ELEMENT, TYPE=SPRINGA
249, 250, 125
*ELSET, Elset=spring
249
**
*SPRING, ELSET=spring

10000.
**
*BEAM GENERAL SECTION,DENSITY=2400.E-
09,
SECTION=NONLINEAR GENERAL,ELSET=full
31250., 40690104.2, 0., 162760416.7,
112000000.
0.,0.,-1.
*AXIAL
0., 0.
18.E+08, 0.0065
24.E+08, 0.073
12.5E+08, 0.1
*M1
0., 0.
1.101E+06, 0.0009E-03
1.663E+06, 0.0015E-03
...
...
3.132E+06, 4.0E-03
2.896E+06, 5.0E-03
2.006E+06, 10.0E-03
*M2
0, 0
1, 1
*TORQUE
0, 0
1, 1
**
**WEAK ELEMENT
**
*BEAM GENERAL
SECTION,ELSET=weak,DENSITY=2400.E-09,
SECTION=NONLINEAR GENERAL
31250., 40690104.2, 0., 162760416.7,
112000000.
0.,0.,-1.
*AXIAL
0., 0.
18.E+08, 0.0065
24.E+08, 0.073
12.5E+08, 0.1
*M1
0., 0.
1.08999E+06, 0.000891E-03
1.64637E+06, 0.001485E-03
...
...
3.10068E+06, 3.96E-03
2.86704E+06, 4.95E-03
1.98594E+06, 9.9E-03
*M2
0, 0
1, 1
*TORQUE
0, 0
1, 1
*BOUNDARY
9, 2, 2
250, 1, 1
250, 2, 2
240, 2, 2
**---------------------------------
** STEP: loading
**
*Step, name=loading, inc=10000
*Static, Direct
0.0002, 1.0
** LOADS
*CLOAD
loadPoints, 2, -20000
** OUTPUT REQUESTS
*RESTART, WRITE, FREQUENCY=0
**
** FIELD OUTPUT
*OUTPUT, FIELD
*NODE OUTPUT
CF, RF, U, UR
*ELEMENT OUTPUT, DIRECTIONS=YES
SE, SF
**
** HISTORY OUTPUT
*OUTPUT, HISTORY, VARIABLE=PRESELECT
*END STEP
```

INPUT INPUT INPUT INPUT INPUT

Choose

UNITS: m, kN, MPa

b (width)	0.25	m
h (height)	0.125	m
E	30	GPa

Material behaviour:

COMPRESSION: # Pieces 3

	$\sigma_{c1}(\varepsilon)$	$\sigma_{c2}(\varepsilon)$	$\sigma_{c3}(\varepsilon)$
ε^7			
ε^6			
ε^5			
ε^4			
ε^3		-2614603100.0	
ε^2		-40998.7	
ε	30069.6	31266.1	
c			41.4

Range

ε_0	ε_{c1}	ε_{c2}	ε_{c3}
0	0.000660	0.001940	0.30

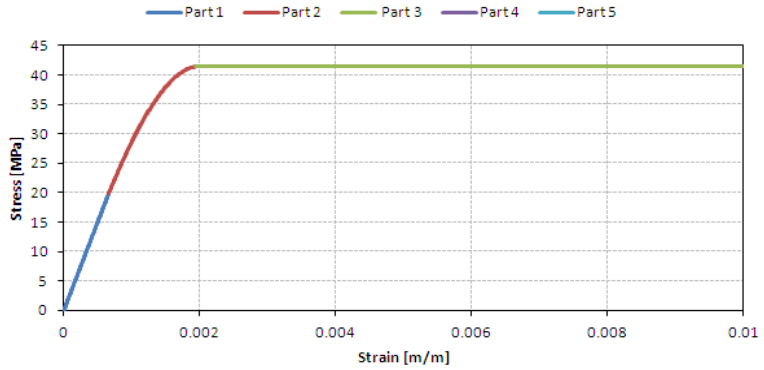

TENSION: # Points 5

Point 0	σ_{t0}	0	MPa	ε_{t0}	0
Point 1	σ_{t1}	1.85	MPa	ε_{t1}	6.1524E-05
Point 2	σ_{t2}	2.5	MPa	ε_{t2}	0.007
Point 3	σ_{t3}	2	MPa	ε_{t3}	0.0296
Point 4	σ_{t4}	1.35	MPa	ε_{t4}	0.1056
Point 5	σ_{t5}	0	MPa	ε_{t5}	0.3656

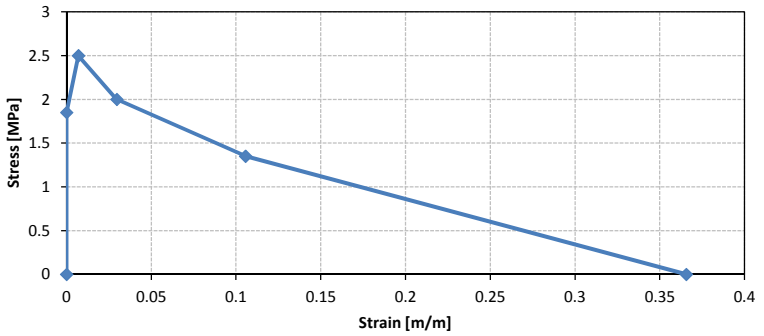

EBS TO Y EBS TO Y EBS TO Y EBS TO

Vary curvature: Kappa 0.11 [1/ρ]

COMPRESSION: # Pieces 3

	$\sigma_{c1}(y)$	$\sigma_{c2}(y)$	$\sigma_{c3}(y)$
y^7	0	0	0
y^6	0	0	0
y^5	0	0	0
y^4	0	0	0
y^3	0	-3480036.7	0
y^2	0	-496.1	0
y	3307.7	3439.3	0
c	0	0	41.4

Range

y_0	y_{c1}	y_{c2}	y_{c3}
0	0.006	0.018	2.727

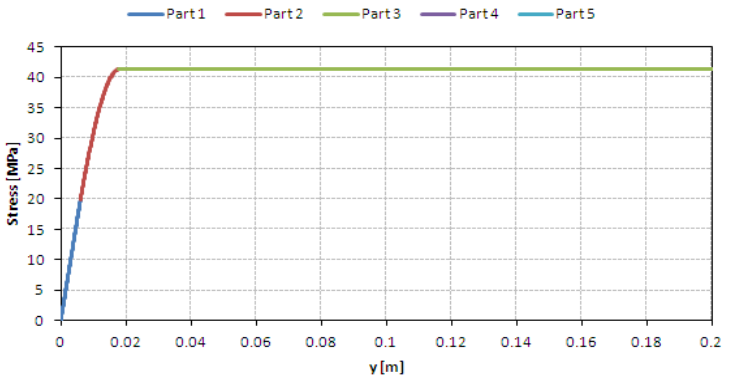

TENSION: # Points 5

Point 0	σ_{t0}	0	MPa	y_{t0}	0 m
Point 1	σ_{t1}	1.85	MPa	y_{t1}	0.001 m
Point 2	σ_{t2}	2.5	MPa	y_{t2}	0.064 m
Point 3	σ_{t3}	2	MPa	y_{t3}	0.269 m
Point 4	σ_{t4}	1.35	MPa	y_{t4}	0.960 m
Point 5	σ_{t5}	0	MPa	y_{t5}	3.324 m

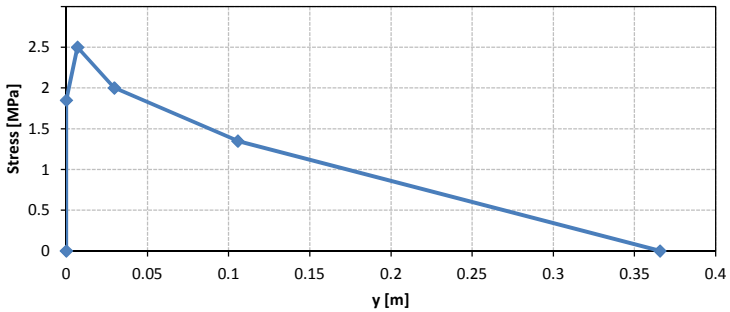

EBS TO Y EBS TO Y EBS TO Y EBS TO Y EBS TO Y EB

Tension relationship can be benaderd as multi-linear equations

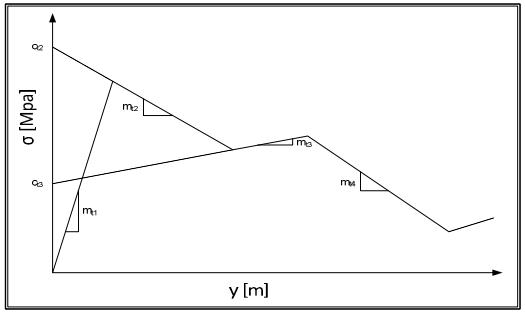

If $y_{t0} \le y_t < y_{t1}$

$$m_{t1} = \frac{\sigma_{t1}}{y_{t1}} = 3307.65$$

If $y_{t1} \le y_t < y_{t2}$

$$m_{t2} = \frac{\sigma_{t2} - \sigma_{t1}}{y_{t2} - y_{t1}} = 10.30$$

$$c_{t2} = \sigma_{t1} - m_{t2} y_{t1} = 1.84$$

If $y_{t2} \le y_t < y_{t3}$

$$m_{t3} = \frac{\sigma_{t3} - \sigma_{t2}}{y_{t3} - y_{t2}} = -2.43$$

$$c_{t3} = \sigma_{t2} - m_{t3} y_{t2} = 2.65$$

If $y_{t3} \le y_t < y_{t4}$

$$m_{t4} = \frac{\sigma_{t4} - \sigma_{t3}}{y_{t4} - y_{t3}} = -0.94$$

$$c_{t4} = \sigma_{t3} - m_{t4} y_{t3} = 2.25$$

If $y_{t4} \le y_t < y_{t5}$

$$m_{t5} = \frac{\sigma_{t5} - \sigma_{t4}}{y_{t5} - y_{t4}} = -0.57$$

$$c_{t5} = \sigma_{t4} - m_{t5} y_{t4} = 1.90$$

TENSION: # Pieces 5

	$\sigma_{t1}(y)$	$\sigma_{t2}(y)$	$\sigma_{t3}(y)$	$\sigma_{t4}(y)$	$\sigma_{t5}(y)$
y	3307.65	10.30	-2.43	-0.94	-0.57
c	0.00	1.84	2.65	2.25	1.90

FORCES FORCES FORCES FORCES FORCES

FORCES: $F = \int \sigma(y) b dy$

TENSION INTEGRALS

	$\int \sigma_{t1}(y)dy$	$\int \sigma_{t2}(y)dy$	$\int \sigma_{t3}(y)dy$	$\int \sigma_{t4}(y)dy$	$\int \sigma_{t5}(y)dy$
y^2	1653.83	5.15	-1.22	-0.47	-0.29
y	0.00	1.84	2.65	2.25	1.90

5

COMPRESSION INTEGRALS

	$\int \sigma_{c1}(y)dy$	$\int \sigma_{c2}(y)dy$	$\int \sigma_{c3}(y)dy$	$\int \sigma_{c4}(y)dy$	$\int \sigma_{c5}(y)dy$
y^8	0	0	0	0	0
y^7	0	0	0		
y^6	0	0	0		
y^5	0	0	0		
y^4	0	-870009.2	0		
y^3	0	-165.4	0		
y^2	1653.8	1719.6	0		
y	0	0	41.4		

3

TENSION FORCES:

If $y_{t0} \le y_t < y_{t1}$ y = 0.112 m

$F_{t1} = \int_0^{y} \sigma_{t1}(y) b dy$ = 5206.34 kN

If $y_{t1} \le y_t < y_{t2}$

$F_{t1} = \int_0^{y_{t1}} \sigma_{t1}(y) b dy$ = 0.13 kN

$F_{t2} = \int_{y_{t1}}^{y} \sigma_{t2}(y) b dy$ = 67.70 kN

COMPRESSION FORCES:

If $y_{c0} \le y_c < y_{c1}$ $y_c = h - y$ = 0.013 m

$F_{c1} = \int_0^{h-y} \sigma_{c1}(y) b dy$ = 67.58 kN

If $y_{c1} \le y_c < y_{c2}$

$F_{c1} = \int_0^{y_{c1}} \sigma_{c1}(y) b dy$ = 14.86 kN

$F_{c2} = \int_{y_{c1}}^{y_c} \sigma_{c2}(y) b dy$ = 49.21 kN

FORCES FORCES FORCES FORCES

If $y_{t2} \le y_t < y_{t3}$

$$F_{t1} = \int_0^{y_{t1}} \sigma_{t1}(y) b\,dy = 0.13 \text{ kN}$$

$$F_{t2} = \int_{y_{t1}}^{y_{t2}} \sigma_{t2}(y) b\,dy = 34.30 \text{ kN}$$

$$F_{t3} = \int_{y_{t2}}^{y} \sigma_{t3}(y) b\,dy = 29.64 \text{ kN}$$

If $y_{t3} \le y_t < y_{t4}$

$$F_{t1} = \int_0^{y_{t1}} \sigma_{t1}(y) b\,dy = 0.13 \text{ kN}$$

$$F_{t2} = \int_{y_{t1}}^{y_{t2}} \sigma_{t2}(y) b\,dy = 34.30 \text{ kN}$$

$$F_{t3} = \int_{y_{t2}}^{y_{t3}} \sigma_{t3}(y) b\,dy = 115.57 \text{ kN}$$

$$F_{t4} = \int_{y_{t3}}^{y} \sigma_{t4}(y) b\,dy = -81.33 \text{ kN}$$

If $y_{t3} \le y_t < y_{t4}$

$$F_{t1} = \int_0^{y_{t1}} \sigma_{t1}(y) b\,dy = 0.13 \text{ kN}$$

$$F_{t2} = \int_{y_{t1}}^{y_{t2}} \sigma_{t2}(y) b\,dy = 34.30 \text{ kN}$$

$$F_{t3} = \int_{y_{t2}}^{y_{t3}} \sigma_{t3}(y) b\,dy = 115.57 \text{ kN}$$

$$F_{t4} = \int_{y_{t3}}^{y_{t4}} \sigma_{t4}(y) b\,dy = 289.32 \text{ kN}$$

$$F_{t5} = \int_{y_{t4}}^{y} \sigma_{t5}(y) b\,dy = -337.44 \text{ kN}$$

If $y_{c2} \le y_c < y_{c3}$

$$F_{c1} = \int_0^{y_{c1}} \sigma_{c1}(y) b\,dy = 14.86 \text{ kN}$$

$$F_{c2} = \int_{y_{c1}}^{y_{c2}} \sigma_{c2}(y) b\,dy = 97.27 \text{ kN}$$

$$F_{c3} = \int_{y_{c2}}^{y_c} \sigma_{c3}(y) b\,dy = -50.21 \text{ kN}$$

If $y_{c3} \le y_c < y_{c4}$

$$F_{c1} = \int_0^{y_{c1}} \sigma_{c1}(y) b\,dy = 14.86 \text{ kN}$$

$$F_{c2} = \int_{y_{c1}}^{y_{c2}} \sigma_{c2}(y) b\,dy = 97.27 \text{ kN}$$

$$F_{c3} = \int_{y_{c2}}^{y_{c3}} \sigma_{c3}(y) b\,dy = 28052.52 \text{ kN}$$

$$F_{c4} = \int_{y_{c3}}^{y_c} \sigma_{c4}(y) b\,dy = 0.00 \text{ kN}$$

If $y_{c4} \le y_c < y_{c5}$

$$F_{c1} = \int_0^{y_{c1}} \sigma_{c1}(y) b\,dy = 14.86 \text{ kN}$$

$$F_{c2} = \int_{y_{c1}}^{y_{c2}} \sigma_{c2}(y) b\,dy = 97.27 \text{ kN}$$

$$F_{c3} = \int_{y_{c2}}^{y_{c3}} \sigma_{c3}(y) b\,dy = 28052.52 \text{ kN}$$

$$F_{c4} = \int_{y_{c3}}^{y_{c4}} \sigma_{c4}(y) b\,dy = 0.00 \text{ kN}$$

$$F_{c5} = \int_{y_{c4}}^{y_c} \sigma_{c5}(y) b\,dy = 0.00 \text{ kN}$$

MOMENT ARMS MOMENT ARMS MOMENT ARMS

MOMENT ARMS:

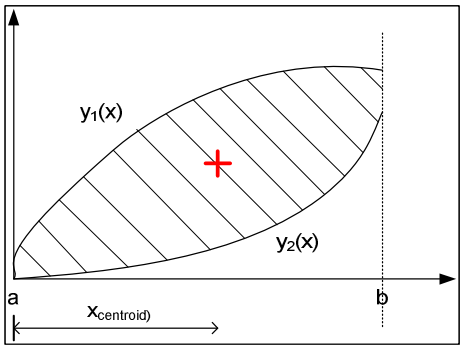

$$x_{centroid} = \frac{\int_a^b x(y_1 - y_2)dx}{\int_a^b (y_1 - y_2)dx}$$

TENSION INTEGRALS 5

	$y*\sigma_{t1}(y)$	$y*\sigma_{t2}(y)$	$y*\sigma_{t3}(y)$	$y*\sigma_{t4}(y)$	$y*\sigma_{t5}(y)$
y^2	3307.65	10.30	-2.43	-0.94	-0.57
y	0.00	1.84	2.65	2.25	1.90

	$\int y*\sigma_{t1}(y)dy$	$\int y*\sigma_{t2}(y)dy$	$\int y*\sigma_{t3}(y)dy$	$\int y*\sigma_{t4}(y)dy$	$\int y*\sigma_{t5}(y)dy$
y^3	1102.55	3.43	-0.81	-0.31	-0.19
y^2	0.00	0.92	1.33	1.13	0.95

COMPRESSION INTEGRALS 3

	$y*\sigma_{c1}(y)$	$y*\sigma_{c2}(y)$	$y*\sigma_{c3}(y)$	$y*\sigma_{c4}(y)$	$y*\sigma_{c5}(y)$
y^8	0	0	0	0	0
y^7	0	0	0		
y^6	0	0	0		
y^5	0	0	0		
y^4	0	-3480036.7	0		
y^3	0	-496.1	0		
y^2	3307.7	3439.3	0		
y	0	0	41.4		

MOMENT ARMS MOMENT ARMS MOMENT ARMS M

	$\int y*\sigma_{c1}(y)dy$	$\int y*\sigma_{c2}(y)dy$	$\int y*\sigma_{c3}(y)dy$	$\int y*\sigma_{c4}(y)dy$	$\int y*\sigma_{c5}(y)dy$
y^9	0	0	0	0	0
y^8	0	0	0		
y^7	0	0	0		
y^6	0	0	0		
y^5	0	-696007.3	0		
y^4	0	-124.0	0		
y^3	1102.6	1146.4	0		
y^2	0	0	20.7		

TENSION MOMENT ARMS

If $y_{t0} \le y_t < y_{t1}$ $\quad y_t =$ 0.112 m

$$Z_{t1} = \frac{\int_0^y y*\sigma_{t1}(y)dy}{\int_0^y \sigma_{t1}(y)dy} = 0.075 \text{ m}$$

If $y_{t1} \le y_t < y_{t2}$

$$Z_{t1} = \frac{\int_0^{y_{t1}} y*\sigma_{t1}(y)dy}{\int_0^{y_{t1}} \sigma_{t1}(y)dy} = 0.000 \text{ m}$$

$$Z_{t2} = \frac{\int_{y_{t1}}^y y*\sigma_{t2}(y)dy}{\int_{y_{t1}}^y \sigma_{t2}(y)dy} = 0.061 \text{ m}$$

If $y_{t2} \le y_t < y_{t3}$

$$Z_{t1} = \frac{\int_0^{y_{t1}} y*\sigma_{t1}(y)dy}{\int_0^{y_{t1}} \sigma_{t1}(y)dy} = 0.000 \text{ m}$$

$$Z_{t2} = \frac{\int_{y_{t1}}^{y_{t2}} y*\sigma_{t2}(y)dy}{\int_{y_{t1}}^{y_{t2}} \sigma_{t2}(y)dy} = 0.034 \text{ m}$$

$$Z_{t3} = \frac{\int_{y_{t2}}^y y*\sigma_{t3}(y)dy}{\int_{y_{t2}}^y \sigma_{t3}(y)dy} = 0.088 \text{ m}$$

COMPRESSION MOMENT ARMS

If $y_{c0} \le y_c < y_{c1}$ $\quad y_c = h-y =$ 0.013 m

$$Z_{c1} = \frac{\int_0^{y_c} y*\sigma_{c1}(y)dy}{\int_0^{y_c} \sigma_{c1}(y)dy} = 0.009 \text{ m}$$

If $y_{c1} \le y_c < y_{c2}$

$$Z_{c1} = \frac{\int_0^{y_{c1}} y*\sigma_{c1}(y)dy}{\int_0^{y_{c1}} \sigma_{c1}(y)dy} = 0.004 \text{ m}$$

$$Z_{c2} = \frac{\int_{y_{c1}}^{y_c} y*\sigma_{c2}(y)dy}{\int_{y_{c1}}^{y_c} \sigma_{c2}(y)dy} = 0.010 \text{ m}$$

If $y_{c2} \le y_c < y_{c3}$

$$Z_{c1} = \frac{\int_0^{y_{c1}} y*\sigma_{c1}(y)dy}{\int_0^{y_{c1}} \sigma_{c1}(y)dy} = 0.004 \text{ m}$$

$$Z_{c2} = \frac{\int_{y_{c1}}^{y_{c2}} y*\sigma_{c2}(y)dy}{\int_{y_{c1}}^{y_{c2}} \sigma_{c2}(y)dy} = 0.012 \text{ m}$$

$$Z_{c3} = \frac{\int_{y_{c2}}^{y_c} y*\sigma_{c3}(y)dy}{\int_{y_{c2}}^{y_c} \sigma_{c3}(y)dy} = 0.015 \text{ m}$$

MOMENT ARMS MOMENT ARMS MOMENT ARM

If $y_{t3} \le y_t < y_{t4}$

$$Z_{t1} = \frac{\int_0^{y_{t1}} y * \sigma_{t1}(y)dy}{\int_0^{y_{t1}} \sigma_{t1}(y)dy} = 0.000 \text{ m}$$

$$Z_{t2} = \frac{\int_{y_{t1}}^{y_{t2}} y * \sigma_{t2}(y)dy}{\int_{y_{t1}}^{y_{t2}} \sigma_{t2}(y)dy} = 0.034 \text{ m}$$

$$Z_{t3} = \frac{\int_{y_{t2}}^{y_{t3}} y * \sigma_{t3}(y)dy}{\int_{y_{t2}}^{y_{t3}} \sigma_{t3}(y)dy} = 0.163 \text{ m}$$

$$Z_{t4} = \frac{\int_{y_{t3}}^{y} y * \sigma_{t4}(y)dy}{\int_{y_{t3}}^{y} \sigma_{t4}(y)dy} = 0.190 \text{ m}$$

If $y_{t4} \le y_t < y_{t5}$

$$Z_{t1} = \frac{\int_0^{y_{t1}} y * \sigma_{t1}(y)dy}{\int_0^{y_{t1}} \sigma_{t1}(y)dy} = 0.000 \text{ m}$$

$$Z_{t2} = \frac{\int_{y_{t1}}^{y_{t2}} y * \sigma_{t2}(y)dy}{\int_{y_{t1}}^{y_{t2}} \sigma_{t2}(y)dy} = 0.034 \text{ m}$$

$$Z_{t3} = \frac{\int_{y_{t2}}^{y_{t3}} y * \sigma_{t3}(y)dy}{\int_{y_{t2}}^{y_{t3}} \sigma_{t3}(y)dy} = 0.163 \text{ m}$$

$$Z_{t4} = \frac{\int_{y_{t3}}^{y_{t4}} y * \sigma_{t4}(y)dy}{\int_{y_{t3}}^{y_{t4}} \sigma_{t4}(y)dy} = 0.592 \text{ m}$$

$$Z_{t5} = \frac{\int_{y_{t4}}^{y} y * \sigma_{t5}(y)dy}{\int_{y_{t4}}^{y} \sigma_{t5}(y)dy} = 0.515 \text{ m}$$

If $y_{C3} \le y_C < y_{C4}$

$$Z_{c1} = \frac{\int_0^{y_{c1}} y * \sigma_{c1}(y)dy}{\int_0^{y_{c1}} \sigma_{c1}(y)dy} = 0.004 \text{ m}$$

$$Z_{c2} = \frac{\int_{y_{c1}}^{y_{c2}} y * \sigma_{c2}(y)dy}{\int_{y_{c1}}^{y_{c2}} \sigma_{c2}(y)dy} = 0.012 \text{ m}$$

$$Z_{c3} = \frac{\int_{y_{c2}}^{y_{c3}} y * \sigma_{c3}(y)dy}{\int_{y_{c2}}^{y_{c3}} \sigma_{c3}(y)dy} = 1.372 \text{ m}$$

$$Z_{c4} = \frac{\int_{y_{c3}}^{y_c} y * \sigma_{c4}(y)dy}{\int_{y_{c3}}^{y_c} \sigma_{c4}(y)dy} = \text{\#DIV/0! m}$$

If $y_{C4} \le y_C < y_{C5}$

$$Z_{c1} = \frac{\int_0^{y_{c1}} y * \sigma_{c1}(y)dy}{\int_0^{y_{c1}} \sigma_{c1}(y)dy} = 0.004 \text{ m}$$

$$Z_{c2} = \frac{\int_{y_{c1}}^{y_{c2}} y * \sigma_{c2}(y)dy}{\int_{y_{c1}}^{y_{c2}} \sigma_{c2}(y)dy} = 0.012 \text{ m}$$

$$Z_{c3} = \frac{\int_{y_{c2}}^{y_{c3}} y * \sigma_{c3}(y)dy}{\int_{y_{c2}}^{y_{c3}} \sigma_{c3}(y)dy} = 1.372 \text{ m}$$

$$Z_{c4} = \frac{\int_{y_{c3}}^{y_{c4}} y * \sigma_{c4}(y)dy}{\int_{y_{c3}}^{y_{c4}} \sigma_{c4}(y)dy} = \text{\#DIV/0! m}$$

$$Z_{c5} = \frac{\int_{y_{c4}}^{y_c} y * \sigma_{c5}(y)dy}{\int_{y_{c4}}^{y_c} \sigma_{c5}(y)dy} = \text{\#DIV/0! m}$$

CALCULATION CALCULATION CALCULATIO

SUMMARY

COMPRESSION	σ_{c5} [MPa]	-	ε_{c5}	0.5	y_{c5} [m]	4.545
	σ_{c4} [MPa]	-	ε_{c4}	0.4	y_{c4} [m]	3.636
	σ_{c3} [MPa]	-	ε_{c3}	2.727	y_{c3} [m]	2.727
	σ_{c2} [MPa]	-	ε_{c2}	0.002	y_{c2} [m]	0.018
	σ_{c1} [MPa]	-	ε_{c1}	0.001	y_{c1} [m]	0.006
Origin	σ_{t0} [MPa]	0	ε_0	0	Y_0 [m]	0
TENSION	σ_{t1} [MPa]	1.85	ε_{t1}	6.1524E-05	y_{t1} [m]	-0.001
	σ_{t2} [MPa]	2.5	ε_{t2}	0.007	y_{t2} [m]	-0.064
	σ_{t3} [MPa]	2	ε_{t3}	0.0296	y_{t3} [m]	-0.269
	σ_{t4} [MPa]	1.35	ε_{t4}	0.1056	y_{t4} [m]	-0.960
	σ_{t5} [MPa]	0	ε_{t5}	0.3656	y_{t5} [m]	-3.324

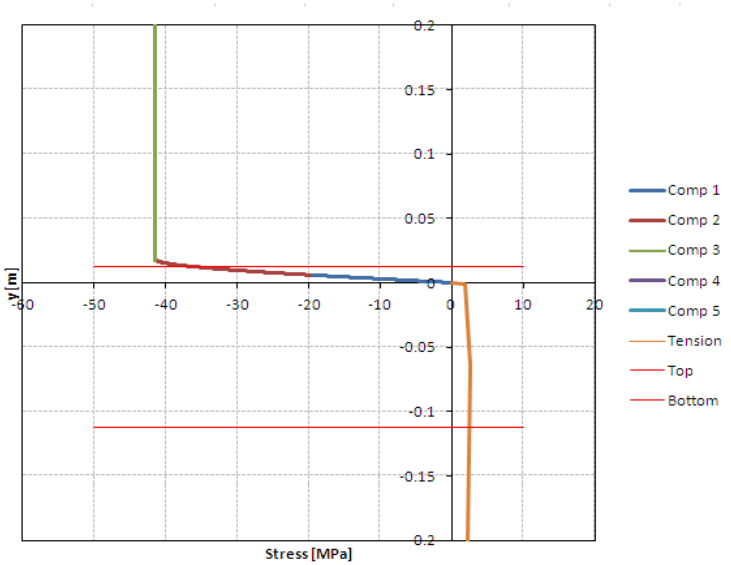

Top and bottom borders of section

Value to shift border downwards (δ)		0.0497	m

LIMITS:

TOP

x	y
10	0.013
-50	0.013

BOTTOM

x	y
10	-0.112
-50	-0.112

Distance to neutral axis (y_n = h/2+δ)			0.112	m
TEST:	$y_n \leq h$	TRUE		

CALCULATION CALCULATION CALCU

SUMMATION OF FORCES

TENSION FORCES [kN]		COMPRESSION FORCES [kN]	
F_{t1}	5206.3	F_{c1}	67.6
F_{t2}	67.8	F_{c2}	64.1
F_{t3}	64.1	F_{c3}	61.9
F_{t4}	68.7		
F_{t5}	101.9		

5	TENSION		
3	COMPRESSION		

TESTS for limits			
$0 \le y < y_{t1}$	FALSE	$0 \le y_c < y_{c1}$	FALSE
$y_{t1} \le y < y_{t2}$	FALSE	$y_{c1} \le y_c < y_{c2}$	TRUE
$y_{t2} \le y < y_{t3}$	TRUE	$y_{c2} \le y_c < y_{c3}$	FALSE
$y_{t3} \le y < y_{t4}$	FALSE		
$y_{t4} \le y < y_{t5}$	FALSE		

CALCULATION OF MOMENTS

MOMENTS [kNm]			
	$0 \le y_c < y_{c1}$	$y_{c1} \le y_c < y_{c2}$	$y_{c2} \le y_c < y_{c3}$
$0 \le y < y_{t1}$	-	-	-
$y_{t1} \le y < y_{t2}$	-	-	-
$y_{t2} \le y < y_{t3}$	-	4.29	-
$y_{t3} \le y < y_4$	-	-	-
$y_{t4} \le y < y_{t5}$	-	-	-